Department of Precision and Microsystems Engineering

Fabrication of polymer nanocomposites for application in luminescent solar concentrators

Jan David Endtz

Report no : 2019.010
Coach : Prof.dr. U. Staufer
Professor : Prof.dr. U. Staufer
Specialisation : Micro and Nano Engineering
Type of report : MSc thesis
Date : 4 March 2019

Fabrication of polymer nanocomposites for application in luminescent solar concentrators

by

Jan David Endtz

to obtain the degree of Master of Science
at the Delft University of Technology,
to be defended publicly on Friday March 15, 2019 at 13:45.

Student number:	4177304	
Project duration:	February, 2018 – March, 2019	
Thesis committee:	Prof. dr. U. Staufer,	TU Delft, supervisor
	Dr. E. Mendes,	TU Delft
	Dr. ir. J. F. L. Goosen,	TU Delft
	Dr. A. Jung,	PHYSEE

An electronic version of this thesis is available at `http://repository.tudelft.nl/`.

TU Delft

Preface

The thesis report that lies before you is the tangible outcome of quite a journey. It has seen many euphoric highs, when the laws of nature finally behaved like they should or when puzzling error messages made way for beautiful plots. It has also seen many lonely lows, with days on end facing seemingly insurmountable problems with little to no progression. Apart from a completely new field of science, I have also learned a lot about myself.

This thesis would not be in its current state without the support of many people. First of all, I would like to thank my supervisors Luigi and Urs for their support in different stages of the project. Luigi always helped me to stay focused on the bigger picture and try new things. Although Urs took over the supervision at a later stage, he has provided many insights and suggestions that changed the scope of the project and made this thesis of a higher quality. I would like to thank Dr. Erik van der Kolk for donating the luminescent nanoparticles that were an essential part of this study. I also owe gratitude to Mike Schellekens from DSM Coating Resins for synthesizing the custom-made amphiphilic copolymers and to Brit Zarin from Polymer Chemistry Innovations for preparing a sample of the compatible matrix polymer. Of course, I would like to thank everybody at PHYSEE for all the fun and support over the last two years. I feel lucky to have been part of their journey, growing from less than ten to more than thirty people while maintaining the open and enjoyable culture. In particular, I want to thank Ana, Joe, Sadiq and David, not only for the insightful discussions during the weekly R&D meetings, but also for making the R&D team so awesome. Furthermore, I would like to thank my parents for listening patiently to my struggles during nightly bike rides and for somehow being able to give useful advice about very unfamiliar topics. I want to thank my housemates for bearing with me when I was at times not the best version of myself. Jasper's presence made the endless hours in the "UB" seem not that bad. Last but not least, I want to thank Richard for always being there for me.

Jan David Endtz
Amsterdam, March 2019

Contents

List of Figures

List of Tables

List of Abbreviations

COC Cyclic Olefin Copolymer

DC Diffusion-controlled

DLS Dynamic Light Scattering

EDL Electrical Double Layer

EDS Energy-dispersive X-ray Spectroscopy

EtOH Ethanol

EHMA 2-Ethylhexyl methacrylate

EO Ethylene oxide

IEP Isoelectric Point

ITC Isothermal Titration Calorimetry

KC Kinetic-controlled

LSC Luminescent Solar Concentrator

MC Mixed kinetic-diffusion-controlled

MEK Methyl Ethyl Ketone

MPEOMA Methoxy poly(ethylene oxide) methacrylate)

NP Nanoparticle

PDMS Polydimethylsiloxane

PE-b-PEG Polyethylene-block-poly(ethylene glycol)

PEO Poly(ethylene oxide)

PEOMA Poly(ethylene oxide) methacrylate

PEHMA Poly(2-ethylhexyl methacrylate)

PEHMA-stat-PMPEOMA poly(2-ethylhexyl methacrylate)-stat-poly(methoxy polyethylene oxide methacrylate)

PMMA Poly(methyl methacrylate)

PS Polystyrene

RPM Revolutions Per Minute

SEC Size Exclusion Chromatography

SEM Scanning Electron Microscopy

WLI White Light Interferometry

XRD X-ray Diffraction

YAG Yttrium Aluminum Garnet

1 Introduction

1.1. Motivation

According to a recent report by the International Energy Agency, buildings accounts for 30% of the final energy consumption worldwide [1]. Nearly two-thirds of this energy use is supplied by fossil fuels,[1] representing 28% of global energy-related CO_2 emissions. At the same time, the global energy demand in buildings is expected to rise by 50% in 2050, driven by a growing population, a doubling of building floor area and increased access to energy in developing countries. Therefore, increasing the energy efficiency of buildings is crucial to keep on track with the global climate ambitions set forth in the Paris Agreement[2]. Although solar photovoltaic (PV) systems have become increasingly more cost effective—showing an astonishing 61 percent decline in system costs between 2010 and 2017 [3]—the potential of PV systems in the commercial buildings sector remains largely untapped. Conventional rooftop PV systems alone are often unable to provide self-sufficient office buildings, because the rooftop surface area of these buildings is usually limited with respect to the floor area. It is becoming increasingly clear that in order to move towards energy neutral building designs, the facade of a building has to be transformed into a functional structural element. In line with the growing trend of using glass as a structural element, several building-integrated PV (BIPV) windows have emerged, mounted with for example semi-transparent thin film solar cells or conventional solar cells equally spaced apart. However, all of these designs obstruct to some extent a clear view and alter the aesthetics of a building, thus far limiting their large-scale application in the built environment. Moreover, solar cells operate most efficiently in direct sunlight, whereas most light in the built environment is diffuse as a result of scattering and reflection by clouds or any surrounding objects. The potential societal impact of power-generating windows that do not compromise on aesthetics and function well in both direct and diffuse light is huge. One technology that could enable the design of such windows is the luminescent solar concentrator (LSC), which can transform conventional glass into a transparent, colorless, power-generating structural element. This research focuses on a universal, low-cost and scalable fabrication method for a luminescent coating—the engine behind the LSC.

1.2. Luminescent solar concentrators

The concept of LSCs dates from as early as the 1970s and initially led to a great number of patents, which were never successfully commercialized due to the drop in oil prices in the 1980s [4–6]. LSCs operate by absorbing solar radiation and re-emitting it at a different wavelength—a process called photoluminescence. A schematic representation of the working principle of an LSC is shown in Figure 1.1. Part of the light emitted in the LSC is trapped inside the waveguide by total internal reflection, which is a result of the difference in the refractive index between the waveguide material and the surrounding air. In this way, an LSC concentrates solar radiation collected over its entire surface area onto a small area at its perimeter, where it is readily converted into electricity by solar cells. LSCs offer several advantages over conventional PV technology:

- LSCs greatly reduce the amount of required PV material due to the concentration of light at the edges.

[1] When the traditional use of biomass is excluded, this share rises to more than 80%.

[2] The Paris Agreement, signed in 2015 by 55 countries that account for an estimated 55% of global greenhouse gas emissions, aims to respond to the threat of climate change by keeping the global temperature rise below 2 °C above pre-industrial levels [2].

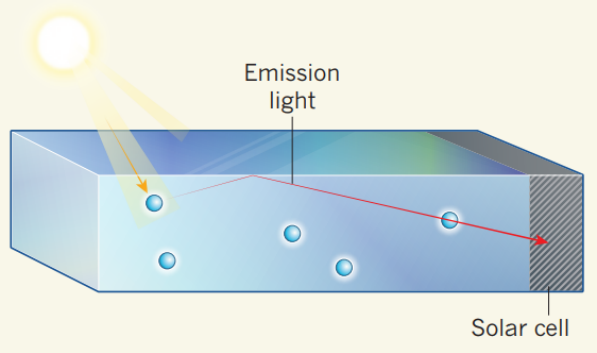

Figure 1.1: Working principle of a luminescent solar concentrator. Light is absorbed by luminescent centers and re-emitted towards the edges, where it is converted into electricity by solar cells. Reproduced from [11].

- LSCs can be made fully transparent and colorless by controlling the absorption and emission spectra of the luminescent material.
- LSCs can collect both direct and diffuse irradiance [7], thereby eliminating the need for expensive solar tracking equipment.
- The narrow-bandwidth emission of the luminescent material can be matched with the band gap of the attached solar cells, which significantly increases their energy conversion efficiency.

LSCs can be designed either by directly incorporating luminescent material into a waveguide, as depicted in Figure 1.1, or by applying a luminescent thin film on top of a waveguide. The advantage of the latter—known as a thin-film LSC—is that a glass pane can be transformed into an LSC simply by applying a coating, thus allowing easy integration into the glass manufacturing process. A thin film of luminescent material can be deposited directly onto a substrate (e.g., by sputter deposition) or luminescent material can be incorporated into a polymer matrix, which is then coated onto a substrate. While sputter deposition offers the advantage of being widely used in industry, there are several reasons to explore polymeric luminescent films.

First of all, incorporating luminescent material in a polymer matrix provides more control over the refractive index of the film. For efficient waveguiding, it is crucial that the refractive index of the film is similar to the refractive index of the substrate. If the interference effects are discounted, the fraction of light trapped inside the film—instead of being guided by the waveguide—depends on the refractive index mismatch by [8]:

$$F_{\text{film}} = \sqrt{\frac{n_{\text{film}}^2 - n_{\text{sub}}^2}{n_{\text{film}}^2}} \tag{1.1}$$

If the refractive index of the film is much larger than the substrate, a significant part of the emitted light will be trapped inside the film only. Any light propagating solely in the film is rapidly lost due to the interface scattering losses in the extremely thin layer [9]. Most polymers have a refractive index similar to glass, which can therefore lead to more efficient waveguiding with respect to high-index sputtered films. In addition, the polymer matrix protects the luminescent material from the outside environment and thus opens the way for using materials sensitive to moisture or oxygen. Moreover, polymeric nanocomposite films open up the possibility to alternative synthesis routes for luminescent materials. For example, while certain halides have proven to be promising host materials for luminescent ions [10], their corrosive properties inhibit the application of these materials in a sputter deposition process. Instead, nanomaterials can be synthesized by a variety of methods, such as sol-gel, hydrothermal or microemulsion methods.

1.3. Rayleigh scattering

In order to obtain an optically clear nanocomposite film, the scattering effects induced by any embedded luminescent material have to be minimized. The intensity of light scattered by spherical particles much smaller than the wavelength of the scattered light can be estimated using Rayleigh scattering theory. The Rayleigh scattering cross section σ_{R} is given by [12]:

$$\sigma_{\text{R}} = \frac{8\pi}{3}\left(\frac{2\pi}{\lambda}\right)^4 a^6 \left[\frac{(n_{\text{p}}/n_{\text{m}})^2 - 1}{(n_{\text{p}}/n_{\text{m}})^2 + 2}\right]^2 \tag{1.2}$$

a is the particle radius, λ is the wavelength of the scattered light in the medium and n_{m} and n_{p} are the refractive indices of the medium and the particles. The fraction of scattered light is equal to σ_{R} times the number of particles per unit volume.

Note that when the refractive indices of the particles and the matrix are exactly equal, there is no scattering and the film appears optically clear. However, matching the refractive indices is far from trivial, because the refractive indices of all materials vary differently with the wavelength of light—a phenomenon known as chromatic dispersion [13]. The scattering intensity is equal to the size of the particles to the power six. In order to minimize the scattering losses as the emitted light propagates through the nanocomposite film, it is crucial to keep the size of the luminescent particles as small as possible.

Organic dye molecules and quantum dots typically have a size ranging from just a few angstroms to a few nanometers and consequently do not cause any visible scattering. However, as will be discussed in Section 2.1, their luminescent properties are typically unfavorable for application in large-scale LSCs. Inorganic rare-earth doped phosphors have promising luminescent characteristics and can be obtained in sizes ranging from the micrometer to the nanometer scale depending on the synthesis method. Without refractive index matching, particles with a mean diameter of only one hundred nanometers can cause already severe scatting losses [14]. Therefore, it is essential that the luminescent particles in the polymer nanocomposites are dispersed as isolated nanosized objects. This thesis research focuses on integrating inorganic rare-earth-doped nanoparticles into a polymer matrix to obtain transparent, clear and luminescent polymer nanocomposite thin films. In Section 2.1, the motivation for selecting rare-earth-doped nanoparticles is discussed in more detail. Incorporating nanoparticles inside a polymer matrix can be a very challenging process, as the high surface energy of nanoparticles often leads to irreversible agglomeration upon direct mixing. The attractive interparticle forces responsible for this behavior are described in Section 2.2. Two stabilization strategies commonly used to suppress these attractive forces are discussed in Sections 2.3 and 2.4. In Section 2.5, important parameters for the preparation of nanocomposite films are outlined, finally leading to the research question of this study in Section 3.1. The plans for the experimental phase, consisting of the approach, the planning and the identified risks are discussed in Sections 3.2, 3.3 and 3.4.

2

Literature Survey

2.1. Luminescent materials

Luminescent materials are the engine behind LSCs and—as their name might suggest—work on the principle of photoluminescence. Luminescent materials adsorb light and then re-emit this light with a different wavelength. Typically, some energy is lost in the process and the emitted photon has a longer wavelength (i.e., lower energy) than the adsorbed photon.[1] For the design of a transparent and colorless LSC with maximum energy output, the luminescent material should fulfill several requirements. Ideally, the luminescent material needs to have:

- a broad absorption band, allowing maximum solar energy conversion while avoiding a colored tint;
- high absorption efficiency;
- a large Stokes shift, eliminating self-absorption losses caused by an overlap between the emission and absorption spectra;
- a high quantum yield, defined as the ratio of the number of photons emitted to the number of photons absorbed by the luminescent center;
- emission at wavelengths below the band gap energy of the PV cell (e.g., < 1107 nm for crystalline silicon solar cells) and above the visible spectrum (> 700 nm);
- high photostability to ensure long-term operation.

Over the last decades, various types of luminescent material have been explored and optimized with respect to their performance in LSCs. They can be divided into three categories: organic dyes, quantum dots and rare-earth elements.

2.1.1. Organic dyes

Organic dyes are organic molecules that absorb light due to their specific planar molecular structure. From the earliest stages of LSC research in the 1970s, organic dyes have been studied due to their high quantum yield, high absorption efficiency and miscibility with organic matrices. In fact, the quantum yield of some contemporary organic dyes has even been shown to reach up to unity [15]. The disadvantages of organic dyes include, in general, their small Stokes shifts, narrow absorption spectra and their low photostability. The small Stokes shift of organic dyes causes considerable **self-absorption losses** (see the second and third plots in Figure 2.1), thereby limiting their performance in large-area LSCs. Moreover, organic dyes are prone to photodegradation, which reduces their performance over time [16].

[1] The opposite effect, in which the adsorption multiple low-energy photons lead to the emission of one photon with a shorter wavelength, also extsts and is known as upconversion.

2.1.2. Quantum dots

Quantum dots (QDs) are nanocrystals typically made from semiconducting materials. Because their size is in the order of the de Broglie wavelength of the electron, electrons are confined in the semiconductor in a similar way to orbital electrons in atoms. Due to their crystalline structure, QDs are more stable than organic dyes [17]. The band gap of QDs—determining both their absorption onset and emission peak—can be engineered by altering their composition as well as their size. By combining materials with different band gaps in so-called core-shell structures, QDs can be designed to have a larger Stokes shift than organic dyes [18] (see the bottom two plots in Figure 2.1). However, large-scale QD-based LSCs often still suffer from **self-absorption losses** due to the low quantum yield of QDs, which is typically in the order of $0.1 - 0.6$ [19, 20]. The low quantum yield results in the fact that every time an emitted photon is absorbed by another QD, there is a significant chance that no photon is re-emitted. Another disadvantage is that QDs absorb more light in the lower end of the spectrum, thereby typically leading to LSCs with a reddish tint. Moreover, there has been increased concern about the **toxicity** of some QDs, which has limited their application on a large scale [21]. Still, at the time of writing, a QD-based LSC holds the record optical efficiency of 8.1% for a 10 cm^2 device, which translates into an electrical power conversion efficiency of 2.2% [22].

2.1.3. Rare-earth elements

Rare-earth (RE) metals are a group of chemical elements that show characteristic luminescence depending on the filling of their 4f electron shell. In contrast to what their name suggests, most of them are relatively abundant on Earth. The luminescence of RE ions is caused by the excitation and relaxation of their orbital electrons by means of absorbing and emitting photons. RE-doped materials—often referred to as phosphors—typically have **high photostability** and can be tuned to have a **large Stokes shift** and **broad absorption band** (see the first plot in Figure 2.1), thus making them promising materials for LSC applications [23]. RE ions are found either as a complex—surrounded by organic ligands—or doped into inorganic host matrices, which play an active role in the luminescence process by enabling energy transfer to the RE ions [24]. By controlling the valency of the RE ion and the composition of the host material, RE-doped materials can be designed to have a broad absorption band and a narrow emission peak. Common host materials include oxides, borates, phosphates, nitrides, oxynitrides, silicates, sulfides, selenides and halides.

2.1.4. Conclusion

The small Stokes shifts of organic dyes and QDs lead to self-absorption losses that limit the performance of LSCs—especially in large-scale devices. Moreover, their relatively narrow absorption bands limit the amount of solar energy that can be harvested and often lead to colored LSCs. RE-doped luminescent materials may be designed to have a broad absorption band in the visible spectrum and a narrow emission peak in the near-infrared spectrum, as can be seen in the absorption and emission spectra of CaI_2:Tm^{2+} given in Figure 2.1. These characteristics allow for colorless films with high absorption, while eliminating the problem of self-absorption. Therefore, this thesis research will focus on RE-doped nanoparticles, in particular those consisting of oxide-containing host materials. As will be addressed in Section 2.2.1, the presence of oxide ions on the surface of nanoparticles introduces binding sites that are beneficial to their stabilization.

2.2. Agglomeration

The ability to disperse isolated nanoparticles is crucial to obtaining non-scattering transparent films. However, nanoparticles have a natural tendency to reduce their effective surface area by forming agglomerate structures. In this section, the different types of agglomerates as well as the theory behind their formation is discussed.

2.2.1. Surface chemistry

Due to their extremely small size, nanoparticles have a relatively large surface area, which is exposed to and interacts with the environment. A thorough understanding of the surface chemistry is therefore crucial to dispersing nanoparticles in a medium. This thesis research will mainly focus on **metal oxide compounds**, which are typically used in the design of commercial phosphors (e.g. in the LED industry) due to their ability to stably host RE ions in their lattice structure [24]. The surface chemistry of metal oxides is characterized by their **high degree of surface hydroxylation**, which can be exploited to control the interaction of metal oxide particles with their surroundings [25]. The hydroxyl groups ($-OH$) present on the particle surface typically participate in hydrogen bonding, acid-base reactions or electrostatic interactions [26]. The formation of

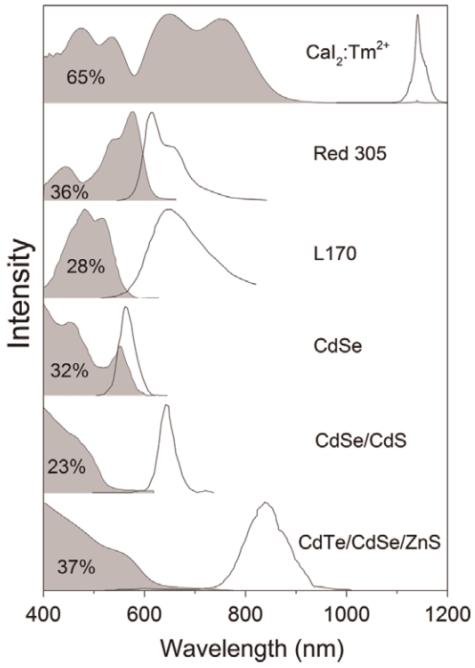

Figure 2.1: Absorption (in grey) and emission (in white) spectra of a rare-earth doped phosphor (CaI_2:Tm^{2+}), two types of organic dyes (Red 305 and L170) and three types of quantum dots (CdSe, CdSe/CdS and CdTe/CdSe/ZnS). The percentages indicate the part of the solar spectrum that can theoretically be absorbed. Reproduced from [10].

these surface hydroxyl sites occurs through dissociative chemical adsorption of water molecules. Metal oxide surfaces typically terminate in oxide ions rather than metal ions due to their large size and low polarizing power [27]. The oxide ions on the surface contain what are known as dangling bonds: unsatisfied valences due to insufficient coordination to the lattice metal ions. In other words, the oxide atoms do not have enough neighboring metal atoms to share their electrons with and therefore possess a surplus of unpaired electrons. The ability to donate an electron pair makes the surface oxide ion extremely reactive: in the presence of a water molecule it acts as a strong Lewis base to form two hydroxyl groups:

$$-\mathrm{O} + \mathrm{H_2O} \longrightarrow -\mathrm{OH\,(a)} + -\mathrm{OH\,(b)} \tag{2.1}$$

where (a) and (b) are the conjugate acid of the surface oxide ion and the conjugate base of the water molecule. The resulting hydroxyl groups form a bilayer on the metal oxide surface. This mechanism of surface hydroxylation was first proposed by Tamura, Mita, Tanaka and Ito [28]. The authors attributed the surface hydroxylation to exposed oxide ions rather than to metal ions, as they found that the hydroxyl site density does not depend on the valency of the metal oxide. Apart from hydroxyl groups, other active sites could be present on the particle surface depending on the environment, such as methoxy ($-\mathrm{OCH_3}$), amino ($-\mathrm{NH_2}$) or carboxyl ($-\mathrm{COOH}$) groups.

2.2.2. Types of agglomerates

Depending on the synthesis and processing conditions, nanoparticles can form either "hard" or "soft" agglomerates [29]. The distinction between hard and soft agglomerates is based on the strength of the interparticle bonds, which keep primary particles together in agglomerate structures. Soft agglomerates are held together by relatively weak van der Waals forces and can, to some extent, be broken down by mechanical deagglomeration methods such as milling, high-shear mixing or ultrasonication [26]. The formation of hard agglomerates on the other hand is typically irreversible, as the particles form strong interparticle bonds [30]. The terms "agglomerate" and "aggregate" are often used interchangeably in literature, underpinned by conflicting definitions of national and international standards [31]. Throughout this text the term "agglomerate" will be used for the soft agglomerate type: an assemblage of particles that are loosely bound at their corners or edges. The terms "aggregate" or "hard agglomerate" are reserved for particles rigidly bound by fusion, sintering or growth. Most powders of course contain a combination of both types in different proportions and a distinction between them can only be made qualitatively. Hard agglomerates are generally formed due to

one of the following factors:

- High temperature synthesis steps such as pyrolysis or calcination often cause partial sintering of the material, so resulting in strong interparticle necks [32].
- Hydroxyl groups present on the particle surfaces promote the formation of hydrogen bonds between particles, which can subsequently lead to irreversible agglomeration [33].
- Drying of a colloid (nanoparticles dispersed in a liquid) to obtain nanopowder generates capillary forces, which can lead to the formation interparticle necks due to the precipitation of dissolved species at the particle contact points [34].

For this reason, high-temperature sintering and drying of a colloid should generally be avoided during nanoparticle processing. The extent to which aggregation occurs when preparing nanopowder depends on the drying technique [35]. However, one of the major issues associated with drying nanoparticles is that **nanopowders generally cannot be redispersed as primary particles**. Zhang et al [36] studied the dispersibility of several commercially available oxide nanopowders (TiO_2, Fe_2O_3, ZnO, NiO and SiO_2) in water employing ultrasonication, chemical dispersants and acidic solutions. They found that none of them could be completely dispersed as primary particles, showing an average particle size of several hundred nanometers. Yeap [33] reviewed the formation of hard agglomerates in nanopowders and concluded that the introduction of a chemical stabilizer is essential to preventing the formation of hard agglomerates during the drying process.

2.2.3. Van der Waals forces

Nanoparticles that are in close proximity are attracted to each other through van der Waals forces, which arise from interactions between permanent or fluctuating dipoles. The total of van der Waals forces between atoms and molecules consists of three contributions:

- The *orientation* or *Keesom* forces, which originate from electrostatic interaction between two permanent dipoles or charges.
- The *induction* or *Debye* forces, in which a permanent dipole or charge in one atom induces a dipole in another atom.
- The *dispersion* or *London* forces, which arise when an instantaneous dipole in one atom—resulting from the instantaneous position of the electrons around the nucleus— induces a dipole in another nearby atom.

Since the electric field of an induced dipole is inevitably aligned with the electric field of the inducing dipole, Debye and London forces are always attractive. London forces are present between all atoms and molecules and generally dominate the other two interactions, except for small highly polar molecules like water [37]. Even though van der Waals forces are not as strong as electrostatic forces or hydrogen bonding interactions, they play a central role in the agglomeration of nanoparticles. The van der Waals interaction energy V_{vdW} between two spheres with radii R_1 and R_2 separated by distance D was first derived by Hamaker [38] and is equal to:

$$W_{\mathrm{vdW}} = -\frac{A}{6}\left\{\frac{2R_1R_2}{(2R_1+2R_2+D)D} + \frac{2R_1R_2}{(2R_1+D)(2R_2+D)} + \ln\frac{(2R_1+2R_2+D)D}{(2R_1+D)(2R_2+D)}\right\} \tag{2.2}$$

where A is known as the *Hamaker constant*. The Hamaker constant is a material-dependent parameter, which increases with the contrast in dielectric properties between the nanoparticles and the medium in which they are dispersed. When two particles are very close together, the equation can be simplified to the short-distance limit [37]:

$$W_{\mathrm{vdW}} = -\frac{A}{6D}\left(\frac{R_1R_2}{R_1+R_2}\right) \tag{2.3}$$

which is valid only when the separation distance is much smaller than the particle radii ($D \ll R_1, R_2$). When D is large relative to R_1 and R_2—as is the case with nanoparticles at relatively large separations—equation 2.2 simplifies to [37]:

$$W_{\mathrm{vdW}} = -\frac{16AR_1^3R_2^3}{9D^6} \tag{2.4}$$

Note that the van der Waals interaction energy is proportional to D^{-6} at the long-distance limit and to D^{-1} at the short-distance limit, making van der Waals forces particularly dominant when particles are closer together. As $D \to 0$, at the point where two atoms of neighboring particles are separated by a distance known as the van der Waals distance—equal to the sum of their van der Waals radii (typically ~ 1Å)— the interaction becomes repulsive rather than attractive due to the overlapping of their electron clouds. A simplified approximation for the nonretarded[2] Hamaker constant for two identical materials 1 interacting across a medium 3 is given by [37]:

$$A = \frac{3}{4}kT\left(\frac{\varepsilon_1 - \varepsilon_3}{\varepsilon_1 + \varepsilon_3}\right)^2 + \frac{3h\nu_e}{16\sqrt{2}}\frac{(n_1^2 - n_3^2)^2}{(n_1^2 + n_3^2)^{3/2}} \tag{2.5}$$

where k is the Boltzmann constant (JK^{-1}), T is the absolute temperature (K), ε_1 and ε_3 are the dielectric constants of materials 1 and 3, h is Planck's constant (Js), ν_e is the electronic absorption frequency in the UV (s^{-1}) and n_1 and n_3 are the refractive indices for material 1 and medium 3. The first term on the right hand side of equation 2.5 represents the contribution of the Keesom and Debye forces to the van der Waals interaction energy. This polar contribution is temperature-dependent and can never exceed $3/4kT$ ($\approx 3\times10^{-21}$J at room temperature). The second term gives the London forces contribution, which is typically in the order of 10^{-20}J. Note that the dominant London forces contribution depends on the **refractive index mismatch** between the nanoparticles and the medium. Bergström [39] calculated the nonretarded Hamaker constants of 31 different inorganic materials across vacuum, water and dodecane ($C_{12}H_{26}$) with the full Lifshitz theory, which is somewhat more advanced than the approximation given by equation 2.5. For SiO_2, the nonretarded Hamaker constant across vacuum, water and dodecane equals to 6.50×10^{-20}, 0.46×10^{-20} and 0.14×10^{-20}J. As the contrast in the dielectric properties between the SiO_2 particles and the intervening media decreases, the Hamaker constant gets smaller. Therefore, the van der Waals interaction energy between the particles is less in organic media such as dodecane than in water or air. Based on these findings, one might expect that nanoparticles are more easily stabilized in organic solvents than in water. However, the presence of free ions in aqueous solutions can introduce repulsive electrostatic interactions that balance the van der Waals forces, as will be discussed in Section 2.3. Note that since the Hamaker constant given by equation 2.5 is always positive, the **the totality of van der Waals forces is always attractive** for two identical materials interacting across a medium. Therefore, some form of repulsive interaction is needed to stabilize nanoparticles dispersed in a liquid.[3] Although van der Waals forces are essential to describing the phenomenon of agglomeration, several other intermolecular forces exist that can contribute to the net interaction energy, such as depletion, solvation, double layer and steric forces [37] [39]. Stabilization strategies typically involve the interaction of ions (for electrostatic stabilization) or molecules (for steric stabilization) with the surface of nanoparticles. The methods of electrostatic and steric stabilization are discussed in Sections 2.3 and 2.4.

2.2.4. Conclusion

Metal oxides are widely used for the fabrication of luminescent materials due to their ability to stably host RE ions in their lattice structure. The surface of metal ion particles is characterized by a high coverage of hydroxyl groups (OH), which interact with the environment and can participate in hydrogen bonding, acid-base reactions or electrostatic interactions. Nanoparticles have a natural tendency to reduce their effective surface area by forming agglomerates, which is often irreversible and should be prevented during nanoparticle processing. The agglomeration is caused by van der Waals forces, which depend on the particle geometry, the separation distance and the contrast in the dielectric properties between the nanoparticles and the intervening liquid medium. The van der Waals interaction is always attractive for two identical materials interacting across a medium. Therefore, some form of stabilization is required to suppress the tendency of nanoparticles to form agglomerates. The two most widely applied stabilization strategies, electrostatic and steric stabilization, are discussed in Sections 2.3 and 2.4.

[2] The Hamaker constant in equation 2.5 does not take into account the retardation effect of dispersion forces. When two atoms are sufficiently far apart, by the time the electric field of the inducing dipole reaches and returns from another atom, the direction of the original instantaneous dipole will have changed. The reduced correlation between the inducing and the induced dipoles at large separations results in a *retarded* attraction which can be up to one order of magnitude weaker ($V_{vdW} \propto D^{-7}$) [37].

[3] In order to obtain a stable dispersion, the net attractive interaction energy should not exceed $1-2kT$ for the particle bonds to be broken up by thermal motion or mechanical agitation [26].

2.3. Electrostatic stabilization

2.3.1. Double layer interaction

Electrostatic stabilization is a result of the **surface charge** (or zeta potential) ψ_0 of the particles. Particles in a liquid can acquire a surface charge due to many phenomena, such as the ionization of its surface groups, the differential dissolution of ions or the adsorption of charged species [26]. The surface charge of metal oxide particles in water typically depends on the pH, which is a measure for the concentration of H^+ ions in the liquid. The hydroxyl groups ($-$OH) on the surface of many divalent and trivalent metal oxides are amphoteric—that is, the hydroxyl groups can react both as an acid and as a base and can thus either donate or accept a proton. A surface charge builds up on the amphoteric oxide (MO) due to the following site-dissociating reactions [40]:

$$\mathrm{MOH} \rightleftharpoons \mathrm{MO^-} + \mathrm{H^+} \tag{2.6}$$

$$\mathrm{MOH_2^+} \rightleftharpoons \mathrm{MOH} + \mathrm{H^+} \tag{2.7}$$

The pH at which the net surface charge of the particle is zero is known as the **isoelectric point** (IEP), which is a material dependent parameter. At a pH higher than the IEP of the material, the hydroxylated surface is deprotonated, giving rise to a negatively charged surface. Inversely, a lower pH leads to a negative surface charge. Any free counterions present in the liquid are attracted to the charged particles, thereby forming an oppositely charged region known as the **electrical double layer** (EDL) that balances the surface charge. The characteristic length or thickness of the EDL is known as the Debye length κ^{-1} and depends solely on the properties of the liquid [37]:

$$\kappa^{-1} = \left(\frac{\varepsilon_\mathrm{r}\varepsilon_0 kT}{2N_\mathrm{A}e^2 I}\right)^{1/2} \tag{2.8}$$

where ε_r is the dielectric constant of the liquid, ε_0 is the permittivity of free space ($\mathrm{C^2\,J^{-1}\,m^{-1}}$), k is the Botzmann constant ($\mathrm{JK^{-1}}$), T is the absolute temperature (K), N_A is the Avogadro constant ($\mathrm{mol^{-1}}$), e is the elementary charge (C) and I is the concentration of free ions in the solution or ionic strength (mM). Both a low dielectric constant and a high ionic strength compress the Debye length and therefore reduce the range of the repulsive interaction [30]. A typical example of agglomeration caused by increasing ionic strength is the drying of a colloid; as the liquid in the colloid evaporates, the concentration of dissolved salts increases and the EDL collapses. For two spherical particles with radii R_1 and R_2 separated by distance D, the repulsive double layer interaction energy is given by [37]:

$$W_\mathrm{EDL} = \left(\frac{R_1 R_2}{R_1 + R_2}\right) Z e^{-\kappa D} \tag{2.9}$$

The interaction constant Z is analogous to the Hamaker constant A used for the van der Waals interaction energy (cf. Equation 2.2) and is equal to:

$$Z = 64\pi\varepsilon_0\varepsilon_\mathrm{r}\left(\frac{kT}{e}\right)^2 \tanh^2\left(\frac{ze\psi_0}{4kT}\right) \tag{2.10}$$

where z is the valency of the electrolyte (e.g., $z = 1$ for a monovalent 1:1 electrolyte such as NaCl). While the derivation of Equations 2.9 and 2.10 outside the scope of this research and not directly relevant, it should be noted that the double layer interaction energy increases as the surface charge and the Debye length increase. French et al. [41] studied the influence of the pH, the ionic strength and the cation valence on the agglomeration kinetics of TiO_2 nanoparticles. At a pH below the IEP of TiO_2 and at low ionic strength, the nanoparticles with a primary size of 4–5 nm formed stable agglomerates with an average diameter of 50–60 nm. Increasing the pH or the ionic strength immediately resulted in micron-sized agglomerates, as did exchanging the monovalent electrolyte for a divalent one with identical pH and ionic strength.

2.3.2. DLVO theory

For the successful electrostatic stabilization of nanoparticles in a liquid, **the electrostatic repulsion has to overcome the attractive van der Waals interaction**. The combined effect of the van der Waals interaction (see Equation 2.2) and double layer interaction (see Equation 2.9) is quantitatively described by the DLVO theory of colloidal stability, named after Derjaguin and Landau [42] and Verwey and Overbeek [43]. A schematic representation of typical DLVO interaction energy diagrams is shown in Figure 2.2. Note that the electrostatic repulsion decays exponentially with the distance ($W_\mathrm{EDL} \propto e^{-D}$), while the van der Waals attraction decays

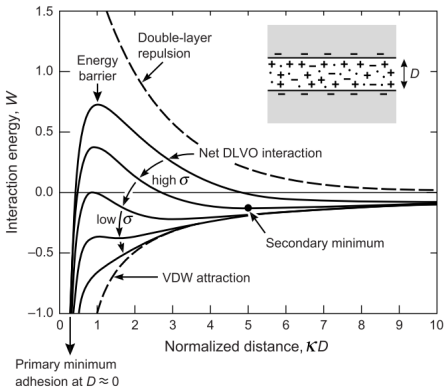

Figure 2.2: Representation of the DLVO interaction energy versus the distance. Reproduced from [37].

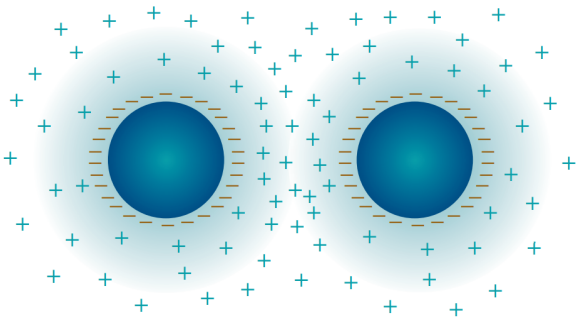

Figure 2.3: Electrostatic stabilization of negatively charged particles. Reproduced from [44].

inversely proportional to the power of the distance ($W_{\mathrm{vdW}} \propto D^{-n}$). Therefore, as $D \to 0$, the van der Waals attraction always dominates, thus resulting in irreversible agglomeration at the primary minimum of the interaction energy. For a high surface charge or surface charge density[4] and low ionic strength—equivalent to a large Debye length—the electrostatic repulsion is high. This results in a high peak of the DLVO interaction energy, referred to as the energy barrier, which the nanoparticles are unable to overcome (see Figure 2.2). If this is the case, the dispersion of nanoparticles is referred to as **thermodynamically stable**. For lower surface charges or more concentrated electrolyte solutions, the energy barrier decreases and a weaker secondary minimum appears. If the particles are unable to overcome this lower energy barrier, they are said to be **kinetically stable** and will either stabilize at the secondary minimum, where reversible adhesion occurs, or stay dispersed in the liquid. Below a certain surface charge or above a critical electrolyte concentration, the net DLVO interaction energy becomes negative and the particles start to agglomerate rapidly. Once this happens, the dispersion is referred to as **unstable**.

Non-aqueous media like hydrocarbons typically have very low dielectric constants, causing the dissociation of electrolytes to be poor and the ionic strength to be negligible. However, while a low ionic strength thus might seem to be beneficial for repulsion, a minimum concentration of free ions is required to ensure a sufficiently large potential gradient at the particle surface. If the electrolyte concentration is too low, the Debye length extends up to the point where particles are positioned inside each other's double layers. Consequently, the electrostatic repulsion in low ε_{r} solvents is often too small to ensure electrostatic stabilization of nanoparticles. Van der Hoeven and Lyklema [46] found that for the electrostatic stabilization in liquids, three regimes of ε_{r} can be distinguished:

- the (semi-)polar regime ($\varepsilon_{\mathrm{r}} \geq 11$), where electrostatic stabilization is easily achieved;
- the low-polar regime ($5 \leq \varepsilon_{\mathrm{r}} \leq 11$), where stabilization is possible if a sufficient amount of dissociated electrolyte is present;
- the apolar regime ($\varepsilon_{\mathrm{r}} \leq 5$), where effective electrostatic stabilization is not possible.

In non-polar solvents and polymer solutions, the repulsive electrostatic interactions between colloidal particles are generally negligible due to the absence of free ions [47]. For this reason, different stabilization methods are required to disperse nanoparticles into common organic polymers. The adsorption of specific molecules on the surface of particles introduces repulsive forces when the particles come into close contact. This method—known as steric stabilization— allows effective stabilization in organic media and is discussed in Section 2.4.

2.3.3. Conclusion

The repulsive double layer interaction between nanoparticles depends on the dielectric constant and the ionic strength of the surrounding liquid, as well as on the geometry, separation distance and surface charge of the particles. Particles in a liquid can be stabilized electrostatically if the double layer repulsion outweighs

[4] The relation between the surface charge ψ_0 and the surface charge density σ is derived by Grahame [45]. For low potentials, the surface charge density is proportional to the surface charge and inversely proportional to the Debye length: $\sigma = \varepsilon_0 \varepsilon \kappa \psi_0$.

the attractive van der Waals interaction. The interplay between the double layer forces and the van der Waals forces is quantitatively described by the DLVO theory. For successful electrostatic stabilization, two conditions have to be fulfilled:

- the **surface charge** on the particles needs to be sufficiently high;
- the **ionic strength** needs to be high enough for a steep potential decay, but not so high that the EDL is compressed completely.

The charging of a surface occurs mainly due to the dissociation of surface groups and can be controlled by changing the pH of the liquid. The dielectric constant of the liquid is important in order obtain a sufficiently high ionic strength, since the dissociation of electrolyte is hampered in liquids with low ε_r. While electrostatic stabilization can be effective for obtaining stable dispersions in (low-)polar liquids, the method is less suitable for dispersing nanoparticles in organic solvents or polymer solutions. In organic media, nanoparticles can be stabilized by adsorbing specific molecules on their surface that introduce repulsive forces. This method is known as steric stabilization and is discussed in Section 2.4.

2.4. Steric Stabilization

As outlined in the previous sections, inorganic nanoparticles tend to form agglomerates when mixed directly into organic solvents or polymers. In such organic media, stable dispersions can be obtained by modifying the surface of the nanoparticles with a stabilizer. Surface modification is a method to hydrophobize the particles by coating them with stabilizer molecules— forming an organic layer containing long aliphatic chains—which adsorb to the surface either by chemical interaction (chemisorption) or physical interaction (physisorption). The organic layers introduce a repulsive interaction between two nanoparticles in close proximity, which opposes the attractive van der Waals force that causes agglomeration. This effect is referred to as steric stabilization and is depicted in figure 2.4. When two atoms of the aliphatic chains adsorbed onto neighboring particles come into close contact with each other, their electron clouds start to overlap. By Pauli exclusion principle, the associated cost in energy causes a strong repulsion between the chains [48]. For sterically stabilized particles, the attractive interparticle van der Waals forces are not strong enough to overcome this repulsion. **Several conditions should be fulfilled for successful stabilization:**

- The stabilizer should be strongly anchored to the surface to prevent desorption during processing and aging.
- The adsorbed organic layer should be thick enough to cause steric repulsion. For this reason, very low molecular weight stabilizers are generally less effective [49].
- The particle surface has to be completely covered with stabilizers. When the surfaces are only partially covered, regions with different polarities are introduced on separate particles. The resulting electrostatic attraction between regions of opposite polarity lead to the formation of agglomerates [50]. This condition is closely related to the kinetics of the stabilizer, which determines how fast a uniform stabilizing layer is formed.
- The aliphatic chains of the stabilizer protruding from the nanoparticle surface have to be compatible with the surrounding organic medium. For coated particles dispersed in a non-solvent, it is energetically favorable to minimize the total surface area of the aliphatic chains in contact with their surroundings. Consequently, besides by contraction of the chains, the nanoparticles minimize their effective total surface area by forming agglomerates [51].

2.4.1. Chemical adsorption

Chemical adsorption or chemisorption involves a chemical reaction of a molecule—also called an adsorptive—with the surface of a nanoparticle, thereby forming strong covalent or ionic bonds. The adsorptive can react with active sites present on the particle surface such as hydroxyl ($-OH$), methoxy ($-OCH_3$), amino ($-NH_2$) or carboxyl ($-COOH$) groups. Alternatively, certain adsorptives can bind directly to surface sites such as metal ions, which act as Lewis acids by accepting an electron pair from the adsorptive [51]. The most commonly applied methods for stabilization by chemisorption are treating the particle surface with a low molecular weight coupling agent and graft polymerization.

Coupling agents
Coupling agents are low molecular weight molecules that improve the interfacial properties between two incompatible materials. On one end, the coupling agent contains a functional group able to form a chemical bond with the surface of an inorganic particle. The other end contains a hydrophobic moiety that interacts well with the organic environment. Coupling agents based on silane, titanate or zirconate react with active sites on the surface and can improve the interfacial compatibility of inorganic nanoparticles in organic media [52]. Typically, methoxy ($-OCH_3$) or ethoxy ($-OCH_2CH_3$) end groups of these coupling agents hydrolyze to form hydrogen bonds with a hydroxylated particle surface. Upon subsequent dehydration, the coupling agent forms a chemical bond with the particle surface. Van Ngo et al. [53] were able to hydrophobize the surface and reduce the average size of ZnO nanoparticles during co-precipitation synthesis by using a trimethoxy silane coupling agent. Alternatively, complexation of the nanoparticle surface with coupling agents such as phosphonic or carboxylic acid is used to hydrophobize particles and improve their dispersion stability [51, 54–56]. The acids strongly coordinate to the surface of metal oxides, substituting any adsorbed molecules—also known as adsorbates—that are occupying a free coordination site of a metal ion. While low molecular weight coupling agents **bind strongly to the particle surface** and can give stable dispersions in liquid media, they usually show **poor interaction with a polymer matrix**. Better compatibility between inorganic particles and a polymer matrix can be obtained by the adsorption of polymeric molecules. This technique allows nanoparticles to be directly incorporated in the polymer matrix and is referred to as graft polymerization.

Graft polymerization
Graft polymerization is a surface treatment in which polymeric molecules are chemisorbed on the nanoparticle surface. Two grafting routes can be distinguished, grafting-*from* and grafting-*to* the nanoparticle.

Grafting-from In the grafting-from method, initiators or monomers are covalently bound to the particle surface after which polymerization is initialized. The surface is usually pretreated by a coupling agent such as silane to introduce functional groups that participate in the polymerization process [57–59]. Common functional groups that are used to bind to an organic resin are vinyl ($-CH=CH_2$), methacryloxy ($CH_2=CCH_3-COO-$), epoxy (a cyclic ether, e.g. $-CHCH_2O$) or amino ($-NH_2$) groups. The grafting efficacy depends on the interaction of these reactive groups with the surrounding organic resin. Zhang et al. [60] showed that SiO_2 nanoparticles modified with methacryloxy(propyl)trimethoxysilane (MPTMS) and vinyltrimethoxysilane (VTMS) could be well dispersed in styrene, while using methyltrimethoxysilane (MTMS) and propyltrimethoxysilane (PTMS) resulted in highly agglomerated particles. Avella et al. [61] grafted polybutylactrylate (PBA) onto $CaCO_3$ nanoparticles treated with vinyltrimethoxysilane (VTMS), after which the particles were dispersed into methylmethacrylate (MMA) phase and polymerization was initiated. SEM analysis revealed that the PBA-grafted $CaCO_3$ particles were homogeneously dispersed into the PMMA matrix, while agglomeration was observed for unmodified particles. Shin et al. [62] grafted poly(ethylene oxide) methacrylate (PEOMA) and poly(propylene oxide) methacrylate (PPOMA) to the surface of silica nanoparticles after pretreatment with vyniltriethoxysilane (VTES) to introduce vinyl groups. The authors measured a lower water vapor absorption—indicating an increase in surface hydrophobicity—and lower zeta potential, indicating a successful surface modification. Coordination complexes with ligands such

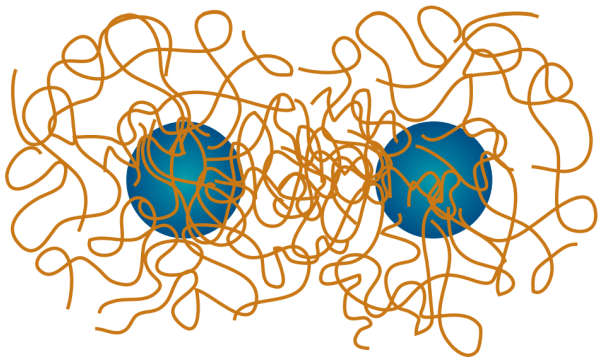

Figure 2.4: Organic layers adsorbed on the particle surfaces prevent agglomeration by introducing repulsive steric forces. Reproduced from [44].

as phosphonic acids that are terminated with polymerizable groups can also be used to increase the compatibility with organic polymers. Noack et al. [55] prepared highly transparent thin film and bulk composite materials using MgF_2 nanoparticles stabilized with vinylphosphonic acid. The undercoordinated magnesium sites on the surface are strongly coordinated by the deprotonated phosphonates, thereby effectively preventing agglomeration by steric repulsion. The copolymerizable vinyl groups increased the compatibility of the particles with the 2-hydroxyethyl methacrylate (HEMA) polymer matrix.

Grafting-to The grafting-to method uses presynthesized polymers that are functionalized with reactive end groups to react with active sites on the nanoparticle surface. Although the grafting-to method allows greater control over the molecular weight of the grafting polymer, the grafting-from method is often preferred, because a low molecular weight modifying agent can penetrate more easily into agglomerate structures than end-functionalized polymers [63]. Apart from chemical grafting, γ radiation can also be used to graft polymers onto nanoparticles by generating active sites on the nanoparticles that can react with vinyl monomers. Irradiation grafting shows some benefits over the chemical method, such as a simplified process, enhanced graft polymer homogeneity and the ability to penetrate previously formed agglomerates [64]. Rong et al. [65] found that under irradiation even some metal nanoparticles can be effectively grafted with polymers despite the low amount of hydroxyl groups present on their surface. In this case, unsaturated atoms resulting form surface defects act as active sites for the grafting.

Conclusion
Graft polymerization is more suitable for fabricating polymer nanocomposites than using low molecular weight coupling agents, because it enhances the compatibility with the polymer matrix. Both stabilization methods rely on a chemical reaction between the stabilizer and the nanoparticle surface, after which a covalent or ionic bond is formed. The strong covalent or ionic attachment of the adsorbate to the surface is often irreversible at ambient temperature and pressure, which is beneficial for the stabilization of nanoparticles in a polymer matrix. However, **two major disadvantages** related to chemical surface modification can be identified:

- A chemical reaction **perturbs the electronic states** of the adsorbate and the nanoparticle surface due to a redistribution of their electron densities [66]. Since the characteristic luminescent properties of rare-earth-doped materials depend on the valency of the dopant ion (see Section 2.1.3), any perturbation of the electronic states should be avoided during processing.

- Chemisorption is **specific to the chemical nature** of the nanoparticle surface, which means that there is a considerable variation between materials and crystal planes. The adsorption efficacy therefore depends on the chemical composition and atomic geography of the nanoparticle surface, thus restricting the universal applicability of the stabilizer.

2.4.2. Physical adsorption

Physical adsorption or physisorption is characterized by physical interaction between the stabilizer molecule and the nanoparticle surface. The attraction is the result of comparatively weak forces such as van der Waals forces, electrostatic interaction and hydrogen bonds. Unlike in chemical bonds, the adsorption is always non-dissociative and reversible. The electronic states are unperturbed, as there is no significant redistribution of electron clouds in the stabilizer molecule or at the particle surface. Physical stabilization is achieved with amphiphiles: molecules that contain both hydrophilic parts that interact with the inorganic particle surface and hydrophobic parts that are compatible with an organic environment. There are **three key parameters** for successful stabilization of nanoparticles in a polymer matrix with amphiphiles. The stabilizer should have [50]:

- high binding strength

- fast adsorption kinetics

- good compatibility with the polymer matrix.

Two types of stabilizers can be distinguished depending on their molecular structure: low molecular weight surfactants and amphiphilic copolymers.

Low molecular weight surfactants

Low molecular weight amphiphiles or surfactants are molecules that contain one or few polar functional groups connected to an aliphatic chain. The polar groups are called anchor groups and interact with the hydrophilic particle surface, while the aliphatic tail protrudes into the organic medium. Surfactants can be classified according to the type of anchor group: anionic, cationic, zwitterionic or nonionic.

Anionic surfactants contain negatively charged anchor groups, such as sulfate ($-SO_4^-$), sulfonate ($-SO_3^-$), phosphate ($-PO_4^{2-}$) or carboxylate ($-COO^-$). Wang et al. [67] successfully stabilized silver nanoparticles in an organic solvent by the addition of different long-chain carboxylates. They found that the particle size can be reduced by increasing the surfactant concentration. Anionic surfactants are typically found in household products such as soaps and detergents, where they are used to form micelles around organic compounds like grease with ther aliphatic tails inward and their polar heads outward. Commonly used anionic surfactants include the soap sodium stearate, ammonium lauryl sulfate (ALS) and sodium lauryl sulfate (SLS).

Cationic surfactants contain anchor groups with a positive charge. They are generally not used in cleansing products, since they bind strongly to skin and hair surfaces which are slightly negatively charged at neutral pH [68]. Instead they are used in fabric softeners, adhering well to the negatively charged fibers and neutralizing their charge. Cationic surfactants are often based on pH-dependent primary, secondary or tertiary amines ($-NH_2$, $-NHR$ or $-NR_2$), which become cationic in acidic solutions, or permanently charged quaternary ammonium cations ($-NR_3^+$). A commonly found cationic surfactants is cetrimonium bromide (CTAB).

Zwitterionic surfactants contain both a negative and a positive ionic group. The formal charges in the molecule cancel each other out, resulting in a zero net charge. Zwitterionic surfactants with permanent formal charges, based on quarternary ammonium cations, are called betaines. Cocamidopropyl betaine is a zwitterionic surfactant often found in cosmetics.

Nonionic surfactants do not carry any formal charge, but bind to a particle surface through van der Waals forces and hydrogen bonds. Typically, their molecular structure contains covalently bonded ether groups ($-O-$) that impart hydrophilic properties to the molecule. The oxygen atoms are able to form hydrogen bonds with surrounding water molecules or hydroxyl groups on the surface of a particle. The ability of nonionic binding groups to adsorb to a wide variety of polar surfaces makes nonionic binding groups the most versatile option.

Due to their small size, low molecular weight surfactants exhibit a high mobility resulting in **fast adsorption kinetics**. They can be used to sterically stabilize nanoparticles in liquid dispersions. However, in polymer nanocomposites, their relatively **low binding strength** can lead to agglomeration during processing or aging. Especially when high-energy processes are used to fabricate the nanocomposite, such as high-shear mixing or extrusion, a low stabilizer binding strength results in desorption [69]. Moreover, the relatively short tails of low molecular weight surfactants do not interact well with the long chains of a polymer matrix, resulting in a **low compatibility**. Lee et al. [70] showed that the dispersion stability of ZrO_2 nanoparticles into polydimethylsiloxane (PDMS) can be enhanced by increasing the molecular weight of the stabilizer tail. Both a higher binding strength and a better compatibility with the polymer matrix can be achieved by using amphiphilic copolymers.

Amphiphilic copolymers

Amphiphilic copolymers are polymeric molecules consisting of both hydrophilic and hydrophobic monomers. Their functionality is determined not only by the chemical composition of the monomers but also by the structural order of the monomers. For **block copolymers**, a block of hydrophilic monomers is covalently attached to a block of hydrophobic monomers, as shown in figure 2.5. Depending on the number of distinct blocks, the copolymer can be classified as diblock, triblock, etc. Block copolymers are typically synthesized by rather complex controlled polymerization techniques that allow polymer synthesis in stages, each containing a different monomer [71]. Copolymers that have a random distribution of monomers instead of ordered blocks are called random or **statistical copolymers**, depicted in figure 2.5. Statistical copolymers can be synthesized by free radical polymerization, which is easily accessible and less expensive [72]. The ability of block copolymers and statistical copolymers to stabilize nanoparticles in a polymer matrix can be completely different, even when the type of monomers they are made up of and their molecular weight are identical. The effectiveness of stabilization is determined by the combined effect of the binding strength, the adsorption kinetics and the compatibility with the polymer matrix.

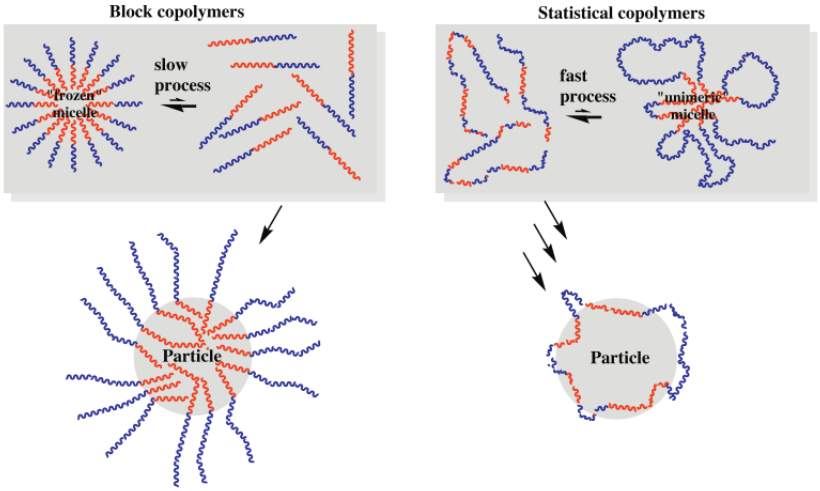

Figure 2.5: Micelle formation and particle adsorption of amphiphilic block and statistical copolymers. Block copolymers tend to form stable "kinetically frozen" micelles, from which unimers cannot easily desorb. Statistical copolymers on the other hand form unstable "unimeric" micelles, thus leading to fast adsorption kinetics. Reproduced from [50].

Binding strength The adsorption of amphiphilic copolymers is stronger than that of low molecular weight surfactants due to their **large number of anchor groups**. While a low molecular weight surfactant is bound to the surface by just one or a few anchor points, the probability for all anchor groups of an amphiphilic copolymer to release simultaneously is much lower. A quantitative experimental study by Chiad et al. [73] compared the adsorption behavior of amphiphilic compounds bearing different types of anchor groups using isothermal titration calorimetry (ITC). They investigated the interaction of several surfactants and amphiphilic statistical copolymers containing nonionic, zwitterionic and acidic anchor groups with SiO_2 nanoparticles in a one-phasic solvent mixture of 1,4-dioxane, ethanol and water. For the nonionic ethylene oxide (EO) anchor groups, which form hydrogen bonds with the hydroxylated SiO_2 surface, the results indicate that the binding strength increases with the number of EO units in the chain. This increase shows a converging trend, which indicates that there is a limit to the number of nonionic anchor groups that can interact with the particle surface. Furthermore, the results show that the bonding strength of a single nonionic EO unit is drastically less than one of its zwitterionic (sulfate betaine) and acidic (phosphate) counterparts. However, in case a sufficient amount of EO units are present in the chain ($n \approx 5$), no significant difference in binding strength was reported. Nonionic binding groups are the most universal option as they can adsorb to a wide variety of polar surfaces. Lastly, the authors found that the adsorption strength of amphiphilic copolymers is up to two orders of magnitude higher than that of their hydrophilic monomers alone. Even though the copolymers in this study consist largely of hydrophobic monomers (85 mol%), the multitude of anchor groups renders their adsorption entropically favorable.

Adsorption kinetics Apart from the binding strength, the effectiveness of stabilization is also dependent on the speed of the adsorption process. The rate of adsorption is directly competing with the rate of nanoparticle agglomeration. The fast adsorption of stabilizers is crucial in order to prevent agglomeration due to partially covered surfaces. The kinetics of the adsorption process are closely related to the **micellization of the stabilizer**. At low stabilizer concentrations, the dissolved amphiphiles are present in the solution as isolated unimers. Above a certain concentration and temperature—known as the critical micelle concentration (CMC) and the Krafft temperature—the stabilizer molecules start to aggregate in the form of micelles: approximately spherical supramolecular assemblies. In a non-polar solvent it is energetically unfavorable for the hydrophilic parts to be in contact with the surroundings, so a micelle is formed with a core of hydrophilic groups and the hydrophobic tails extending out—referred to as a inverse micelle. The unimers in the micelles are in thermodynamic equilibrium with the free unimers in the surrounding medium. A high CMC—indicating a high concentration of free unimers in the solution—is beneficial to the adsorption kinetics. The CMC of amphiphilic copolymers is typically much lower than that of low molecular weight surfactants [74]. For the stabilization of nanoparticles, a high mobility is required for the unimers to quickly adsorb to a nanoparticle surface. Low molecular weight surfactants generally show very fast adsorption ki-

netics due to their high diffusion coefficients, which allows them to rapidly join and desorb from micelles in a diffusion-controlled process. The micelles formed by such surfactants are known as dynamic micelles. However, as discussed in section 2.4.2, the ability of low molecular weight surfactants to prevent agglomeration in a nanocomposite is limited by their low adsorption strength and their incompatibility with polymer matrices. Amphiphilic copolymers have a much lower diffusion coefficient as a result of their large molecular weight, thereby causing the unimer exchange in micelles to be generally much slower. However, comparing the kinetics of statistical and block amphiphilic copolymers shows that they exhibit very different kinetics. Even when their molecular weight and composition are identical, the mere distribution of the monomers in their structure plays an important role in the rate of adsorption. **Block copolymers** tend to from very stable micelles due to the coiling and entangling of their solvophobic blocks in the micelle core, known as **kinetically "frozen" micelles** (see figure 2.5). In-depth reviews on the formation and kinetics of block copolymer micelles are written by Riess [75] and Nicolai, Colombiani and Chassenieux [76]. The formation of frozen micelles is detrimental to the kinetics of adsorption, as the unimers cannot or only very slowly desorb from these frozen micelles—even when their concentration drops below the CMC. This gives nanoparticles a chance to agglomerate before the amphiphilic block copolymers can cover the surface. The exchange kinetics of block copolymer micelles are mainly influenced by three parameters:

- The **interfacial tension** γ between the solvophobic block of the copolymer and the solvent. Minimizing the interfacial tension increases the CMC and prevents the formation of frozen micelles [77]. If one of the blocks of the copolymer is not soluble in the selected solvent, frozen micelles are always formed. The interfacial tension can be estimated by [78]:

$$\gamma_{12} = \gamma_1 + \gamma_2 - 2\Phi\sqrt{\gamma_1\gamma_2} \tag{2.11}$$

  with the constant Φ defined as:

$$\Phi = \frac{4\,(V_1 V_2)^{1/3}}{\left(V_1^{1/3} + V_2^{1/3}\right)^2} \tag{2.12}$$

  where γ_1 and γ_2 are the surface tensions and V_1 and V_2 are the molar volumes of the solvophobic block and the solvent.

- The **length and architecture** of the solvophobic block. Longer chains as well as branched chains exhibit lower mobility due to increased entanglement. The exchange kinetics of a block copolymer is a decreasing function of the degree of polymerization (i.e., the number of monomers in the chain) of its hydrophobic block to the power 2/3 [79].

- The **temperature** of the solvent in which the copolymer is dissolved. If the solvophobic blocks in the core are glassy (below their glass transition temperature), unimer exchange is hampered and the micelles are kinetically frozen [80, 81].

The influence of these three parameters on the kinetics of block copolymer micelle formation has mainly been established on a qualitative level, as existing theories often fail to accurately predict any absolute values. **Statistical copolymers do not form frozen micelles** due to the random order of monomers in their structure. Instead, unstable "unimeric" micelles are formed comprising only a few unimers (see figure 2.5) [50, 82]. Since these unstable micelles can dissociate quickly into unimers that are free to adsorb on a particle surface, statistical copolymers show much faster adsorption kinetics than block copolymers. Khrenov et al. [83] compared the stabilizing effect of statistical and block copolymers with equal molecular weight and composition for the synthesis of ZnO, CdS, $MgCO_3$, Ni and Cu nanoparticles with an inverse emulsion technique, allowing in situ hydrophobization of the particle surface. After redispersing the coated particles in an organic solvent, they analyzed the average particle size and distribution. In all cases, the use of block copolymers resulted in much broader size distributions with an average particle size that was approximately double. In an earlier study, Khrenov et al. [72] investigated the influence of the molecular weight of a statistical amphiphilic copolymer on the size of synthesized particles. To this purpose, ZnO nanoparticles synthesized in an inverse emulsion technique were stabilized by zwitterionic statistical amphiphilic copolymers with different degrees of polymerization. The authors redispersed the stabilized particles into PMMA to obtain transparent nanocomposite films. The use of higher molecular weight copolymers resulted in the formation of larger agglomerates, which can be attributed to a lower chain mobility.

Compatibility with polymer matrix While sufficient binding strength and fast adsorption kinetics allow for the hydrophobization of nanoparticles, these criteria do not ensure homogeneous dispersion in a polymer matrix. In order to fabricate stable polymer nanocomposites, the compatibility between the stabilizer and the matrix is important. As with polymer blends, compatibility results from sufficiently strong interactions between the dissimilar molecules; in this case, the hydrophobic tail of stabilizer tethered to the particle surface—also known as the polymer brush—and the polymer matrix. The importance of compatibility illustrates why the particle-stabilizer-matrix system should be designed as a whole; one universal stabilizer for all types of nanoparticles and polymer matrices does not exist. However, as a rule of thumb, compatibility can often be achieved by matching the chemical composition and the molecular weight of the stabilizer tail with the polymer matrix.

A difference in the **chemical composition** of the stabilizer tail and the matrix can induce phase separation, causing the nanoparticles to agglomerate. Khrenov et al. [84] studied the compatibility of in-situ stabilized ZnO nanoparticles with different polymer matrices. The particles were coated by a statistical copolymer of 2-ethylhexyl methacrylate (EHMA) and dimethylaminoethyl methacrylate betaine (DMAEMA-betaine). The authors found that the particles appeared to be homogeneously dispersed without agglomerates into EHMA and to a slightly lesser extent into PMMA, showing a few small agglomerates. In both cases transparent nanocomposite films were obtained by spin coating. However, large agglomerated were observed in polystyrene (PS), resulting in optically hazy nanocomposite films. The results of the study suggest that in order to achieve complete compatibility, the hydrophobic part of the amphiphilic copolymer should contain the same monomers as the polymer matrix.

Apart from matching the chemical nature, the compatibility is also affected by the **molecular weight** of the stabilizer tail and that of the polymer matrix. Corbierre et al. [85] studied the dispersion of polymer-coated gold nanoparticles in polymer matrices with various molecular weights. Gold nanoparticles capped with PS consisting of 125 repeating units (PS_{125}) were fully dispersed into both low molecular weight ($M_n \approx 2$ kDa or about 19 repeating units) and high molecular weight ($M_n \approx 80$ kDa or about 755 repeating units) PS matrices. Particles covered with 19 repeating PS units (PS_{19}) on the other hand could only be fully dispersed in the low molecular weight matrix. Gold nanoparticles coated with polyethylene oxide (PEO) brushes dispersed in PEO matrices showed similar results. In other words, if the molecular weight of the matrix polymer is substantially higher than that of the copolymer tail, the coated nanoparticles cannot be fully wetted by the matrix, thereby promoting agglomeration. Brush wetting also depends on the grafting density of the stabilizer. For densely coated particles, complete dispersion is generally only achieved when the molecular weight of the brush is greater than the polymer matrix. A less dense packing and the presence of edges between facets of a nanocrystal introduce voids, which can be filled by the polymer chains of the matrix. The presence of voids thus allows for dispersion even when the molecular weight of the matrix is higher than the brush. In the study by Corbierre et al. [85], the PS chains are grafted to the surface at one end and are stretched away from the surface, leading to a high grafting density. For amphiphilic statistical or block copolymers—which bind to multiple sites on the surface and therefore obtain a more stretched out "pancake"-like conformation on the nanoparticle surface [86]—a different behavior is observed. For example, in the study by Khrenov et al. [72], no agglomeration was observed for a statistical amphiphilic copolymer with a molecular weight lower than the polymer matrix ($M_w \approx 21$kDa and $M_w \approx 35$kDa, respectively). This result might be attributed to the less dense packing of the tails, thereby allowing the matrix to fully wet the polymer-covered particles.

2.4.3. Conclusion

The key parameters for successful stabilization of nanoparticles in a polymer matrix are the binding strength of the stabilizer, the kinetics of the adsorption process and the compatibility with the polymer matrix. Although low molecular weight surfactants show a high degree of mobility and can quickly adsorb onto particle surfaces, their binding strength and compatibility with polymer matrices is too low to effectively prevent agglomeration in polymer nanocomposites. Amphiphilic copolymers bind more strongly to a particle surface due to the simultaneous attachment of multiple binding sites. The adsorption kinetics of amphiphilic copolymers can vary greatly depending on their structure and molecular weight. A high molecular weight reduces the mobility of the copolymer and therefore lowers the kinetics of adsorption. Block copolymers tend to form kinetically frozen micelles due to the entangling of the large solvophobic blocks in the micelle center. Such frozen micelles cannot or can only very slowly release unimers, thus inhibiting block copolymers from adsorbing onto a nanoparticle surface. Statistical copolymers on the other hand adsorb much more quickly, because they form small unstable micelles consisting of only a few unimers due to the random order of their hydrophobic and hydrophilic monomers. Since the composition of amphiphilic copolymers can be

easily tuned during their synthesis, their compatibility with different polymer matrices and the interaction with various particle surfaces can be optimized. The compatibility of amphiphilic copolymers with a polymer matrix can be enhanced by matching the both the chemical composition and the molecular weight of its hydrophobic tail with the matrix. In general, statistical amphiphilic copolymers are more effective stabilizers than block copolymers, as evidenced by the observation of smaller agglomerates in polymer nanocomposites.

2.5. Polymer nanocomposites

2.5.1. Matrix parameters

The selection of a suitable polymer matrix is crucial for obtaining transparent nanocomposite films. The hydrophobic tail of the stabilizer should be compatible with the polymer matrix in order to prevent agglomeration, as outlined in section 2.4.2. Although the precise interplay between particles, stabilizer and matrix is complex, chemical matching of the polymer matrix and the stabilizer has proven to be a useful guideline. However, apart from the criteria that allow proper dispersion of nanoparticles, there are also requirements to the material properties of the polymer matrix itself. In this section, some important parameters for the polymer matrix are outlined that affect the performance of the luminescent film.

Transparency High transparency of the polymer matrix is crucial to the performance of the luminescent solar concentrator as well as to the aesthetics. While scattering effects induced by agglomerated particles are often the main cause of turbid films, the polymer matrix itself also induces some losses due to its intrinsic transparency. The transparency of a polymer depends on its degree of crystallinity and its absorbance. Amorphous polymers tend to be transparent, whereas semi-crystalline polymers are typically opaque. The opacity is caused by light scattering at the boundaries between crystalline and amorphous regions, where the material density is lower [87]. While some hydrocarbon polymers are very transparent to visible light, they typically show strong absorption in the near-infrared spectrum due to the molecular vibrations of C–H, C–O and O–H bonds [88, 89]. Perfluorinated polymers, on the contrary, do not show this unwanted absorption, because the vibration frequency of C−F bonds is much further in the infrared spectrum. The transparency of a material is determined by measuring the total transmittance, defined as the ratio of the transmitted light to the incident light [90].

Haze Surface effects and internal structural inhomogeneities in the polymer matrix, such as poorly dispersed particles, dust or air bubbles cause the incident light to diffuse in all directions [91]. If the scattering angle is larger than about 2.5°—known as wide angle scattering—the image loses contrast and the film appears hazy. For haze values below approximately 3% the human eye is unable to detect any loss of quality [92]. The transmission haze is defined by the ratio of light subject to wide angle scattering to the incident light and is measured with a hazemeter [93].

Permeability Rare-earth ions with a valency below their most stable oxidation state are prone to oxidation. When in contact with moisture or oxygen, the ions will oxidize to a higher oxidation state and lose the desired luminescent properties. Incorporating rare-earth doped phosphors in a polymer matrix that acts as a good barrier to oxygen and water vapor is an efficient way to obtain stable nanocomposites. Anesh [94] reviewed the stability of Eu^{2+}-doped strontium aluminate phosphors inside various polymer matrices and concluded that, in general, polyolefins are more suitable for phosphor encapsulation than polyesters or polylactides. The oxygen transmission rate (OTR) and the water vapor transmission rate (WVTR) are measures for the oxygen and water vapor permeability of a material. The OTR and WVTR values of different polymers are of particular interest to the food packaging industry, where they are studied for the development of packaging that can extend the expiration date of fresh products [95]. Coating a nanocomposite film with additional low-permeable barrier layers, such as ethylene vinyl alcohol (EVOH) or cyclic olefin copolymer (COC) can enhance the OTR or WVTR, respectively [52].

Refractive index The refractive index is a material-dependent dimensionless number that describes the relative speed of light in a medium. On the interface between two distinct materials, the ratio of their refractive indices determines the extent to which the path of light is refracted. For efficient waveguiding, the refractive index mismatch between the luminescent film and the waveguide material should be minimized. Ideally, all light is directly coupled into the waveguide, through which it is transported to the edges with maximum light

transport efficiency. However, a difference in refractive index causes part of the light to be trapped inside the film, where it quickly loses intensity due to surface scattering effects [96].

Linear thermal expansion coefficient The coefficient of linear thermal expansion α is a measure for how much a material expands in length upon an increase in temperature. A mismatch of the thermal expansion coefficients of the polymer film and the substrate leads to thermal stresses at elevated temperatures, which might cause cracking of the film [97].

Relative temperature index A characteristic property of amorphous thermoplastic polymers is that they transform from a brittle glassy state into a viscous state at a certain temperature, known as the glass transition temperature T_g. This behavior is not observed in a crystalline polymer phase. Instead, crystalline regions undergo an actual phase transition at their melting point, which is always higher than the glass transition temperature of amorphous regions. The relative temperature index (RTI) is a measure for the maximum acceptable temperature below which critical properties of the polymer are not significantly degraded over the reasonable life time [98].

2.5.2. Dispersion methods

The main challenge in nanocomposite fabrication is to prevent the introduction of agglomerates during processing and obtain a homogeneous dispersion of isolated nanoparticles in the matrix. Surface modification of the nanoparticles prior to mixing generally enhances the dispersion state and the compatibility with the polymer matrix. Commonly used dispersion methods are melt mixing, solution mixing and in situ polymerization.

Melt mixing One rather straightforward way to disperse particles inside a matrix is by directly mixing them with a polymer melt. Upon heating, polymer pellets form a viscous liquid in which the particles can be dispersed using a high shear force mixer. Due to the strong tendency of uncoated nanoparticles to agglomerate, it is difficult to obtain a homogeneous dispersion of isolated particles using melt mixing [99]. Although high shear forces are exerted on the material during melt compounding, agglomerates often do not completely break apart. In addition, the poor interaction between the particles and the matrix leads to deteriorated material properties [50]. Premodification of the nanoparticle surfaces can enhance the compatibility with the matrix and allow for nanocomposites with homogeneously dispersed particles [64, 84]. Nanocomposite films can be fabricated by extrusion, a common polymer processing technique in which the polymer is melted by pressing the material under high pressure through the screws of an extruder. The dispersion of nanoparticles added in the extrusion process is influenced by the temperature, rotation speed and time of the extrusion [52, 57]. Melt mixing can be advantageous because it eliminates the need for toxic solvents and it facilitates processing on an industrial scale.

Solution mixing The limitations of melt mixing can be overcome if both the particles and the polymer are dispersed or dissolved in a solvent prior to mixing, which allows mixing on a molecular level [59]. If a polar solvent is used, electrostatic stabilization may suppress agglomeration (see Section 2.3.2). Alternatively, the nanoparticles can be hydrophobized and dispersed in a nonpolar solvent that is able to dissolve the matrix polymer. As discussed in Section 2.4.2, the adsorption of amphiphilic copolymers can inhibit agglomeration and improve the adhesion between the nanoparticles and the matrix. After agitating the mixture by stirring or sonication, nanocomposite films can be prepared by for example spin coating, dip coating or spray coating.

In situ polymerization Instead of mixing nanoparticles into a polymer melt or polymer solution, the particles can also be dispersed into liquid monomers or a combination of monomers. The nanocomposite is then formed in situ after initiation of the polymerization reaction. In order for the nanoparticles to be fully dispersed in the monomer and interact well with the polymer matrix, surface hydrophobization of the particles is generally required before mixing. A grafting-from reaction (see Section 2.4.1) is simply a form of in situ polymerization in which the surface modifying agent is an initiator or a monomer. In this way, the nanoparticles participate in the polymerization reaction and become part of the polymer network. In situ polymerization is a useful method for polymers that do not melt or easily dissolve.

2.5.3. Conclusion

Not all polymers are suitable binders for the fabrication of efficient thin film LSCs. Apart from compatibility with the stabilizer adsorbed to the nanoparticle surface, the matrix polymer has meet some important criteria. Most importantly, the polymer should be highly transparent for the visible spectrum and for the wavelength of light emitted by the phosphor. In general, amorphous polymers are more transparent than semi-crystalline polymers due to the absence of light-scattering crystallite boundaries. For phosphors that are unstable under ambient conditions, the permeability of the polymer to water and oxygen becomes important. A polymer binder that has a similar refractive index to the substrate it is deposited onto is beneficial for the light guiding efficiency. With respect to the long-term operation of the LSC, the coefficient of linear thermal expansion and the maximum allowable service temperature of the matrix polymer also have to be taken into account.

Nanocomposites are commonly fabricated by melt mixing, solution mixing or in situ polymerization. Melt mixing does not require any solvents and is suitable for industrial-scale processing. Although melt mixing techniques typically exerts high shear forces on the particles which to some extent break up agglomerates, functionalization of the nanoparticle surfaces is required to fully prevent agglomeration and enhance compatibility with the polymer matrix. Solution mixing allows the nanoparticles and the polymer solution to be mixed on a molecular level, thereby resulting in homogeneous dispersions. This method requires the nanoparticles to be stabilized in a solvent that dissolves the matrix polymer prior to mixing with the polymer. Stabilization can be achieved by the adsorption of amphiphilic molecules, which bind to the particles through their polar parts while their nonpolar parts provide compatibility with the polymer matrix. In situ polymerization is simply a form of solution mixing in which the particles are dispersed in a liquid monomer and the adsorbed amphiphile participates in the polymerization reaction. In all cases, the surface of inorganic nanoparticles has to be functionalized to obtain the best results and is therefore a key step in the fabrication. A solution mixing process allows for easy fabrication of nanocomposite thin films by spin coating and is therefore favored over the other techniques.

3

Research Plan

3.1. Research question

The aim of this thesis project is to develop a universal method for the fabrication of rare-earth doped luminescent polymer nanocomposite films. The performance LSCs based on nanocomposite films depends, among other things, on the the size and distribution of the incorporated nanoparticles. Since the loss due to the scattering of light by the particles depends strongly on their size, it is crucial keep the nanoparticles as isolated nanoscopic objects. The main challenge concerning the incorporation of inorganic nanoparticles into polymer matrices is to prevent agglomeration. The incompatibility of inorganic nanoparticles with organic media typically leads irreversible agglomeration upon direct mixing. This problem can be overcome by functionalizing the particle surface with amphiphilic molecules. The function of the amphiphiles is to stabilize the nanoparticles during the phase transfer from polar to nonpolar (organic) solvents and simultaneously compatibilize them with the polymer matrix. In the previous sections we have seen that oxide-containing inorganic nanoparticles accumulate a surface charge in polar solvents and can be electrostatically stabilized by selecting a suitable solvent or adjusting the concentration of ions in the solution. For the transfer to organic media, amphiphilic copolymers—and in particular amphiphilic *statistical* copolymers—are the best candidates if both effective stabilization in the organic solvent and compatibility with the polymer matrix are required. Binding groups that adsorb through physical interactions (i.e. van der Waals forces, hydrogen bonds and electrostatic interaction) are favored over chemically adsorbing groups. This is because they suffer less from material and crystallographic specificity and do not perturb the electronic states of the particle surface, which might interfere with the valence state of the luminescent ions on the nanoparticle surface. The lack of specificity renders the amphiphilic copolymers applicable to a wide variety of inorganic nanoparticles—especially in the case of nonionic binding groups—and not only the type that happens to be studied in this research. The material properties of the amphiphilic copolymers and the process variables of the phase transfer are expected to influence the successful stabilization and dispersion of the nanoparticles. Therefore, the main research question of this study is as follows:

> How can inorganic rare-earth doped luminescent nanoparticles be homogeneously dispersed as isolated nanoscopic objects in a polymer matrix using amphiphilic copolymers to obtain transparent, clear and luminescent nanocomposite films?

The main research question can be divided into the following sub-questions:

- How can inorganic rare-earth doped luminescent nanoparticles be stably dispersed into a polar solvent?
- What is the influence of the composition, molecular weight and concentration of the amphiphilic copolymers on the size of the nanoparticles after the phase transfer to a nonpolar solvent?
- Which process variables of the phase transfer affect the agglomeration of the nanoparticles?
- What is the effect of the composition and molecular weight of the amphiphilic copolymers on the dispersion of the nanoparticles into a polymer matrix?

3.2. Approach

In this section, the approach for the experimental phase will be outlined. First, the selection of materials for the experiments is substantiated. The method of dispersing the nanoparticles and preparing thin films is discussed next. Thereafter, all variable parameters during the experiments are outlined and lastly the characterization methods.

3.2.1. Materials

Because of the large amount of interactions involved, the nanoparticle-amphiphile-matrix system has to be designed as a whole. The selected combination of nanoparticles, amphiphiles and polymer matrices is explained below.

Nanoparticles

For sufficient binding of the amphiphilic copolymers with the nanoparticles, it is important that the nanoparticle surface has a high degree of surface binding sites. Oxides typically have hydroxylated surfaces (see section 2.2.1), which allow the formation of relatively strong hydrogen bonds with amphiphilic molecules. Since the working principle applies to all oxides, the functionality of the amphiphiles can be tested on commercially available metal oxide nanoparticles first.

Al_2O_3

Alumina (Al_2O_3) nanoparticles are used in industry as a filler to enhance the toughness, fire resistance, antifriction properties and insulating properties. They are commercially available in the form of a powder or a colloid. The refractive index of Al_2O_3 is significantly higher than that of common polymers, leading to increased scattering and higher interparticle attraction. The density of surface hydroxyl sites is relatively high [28], which increases the amount of anchor points for the stabilizer, but also the chance of agglomeration due to interparticle hydrogen bonding [100]. Interestingly, Zhou et al. [101] increased the emission intensity of YAG:Ce phosphor powder by coating it with Al_2O_3 using atomic layer deposition (ALD) in a fluidized bed reactor. Al_2O_3 nanoparticles will be used as a starting point, because they are relatively cheap and the mechanism of stabilization is similar to luminescent nanoparticles with hydroxylated particles. The experiments conducted with the Al_2O_3 nanoparticles are outlined in Section 6.1.1.

$Ba_3(PO_4)_2$:Mn^{5+}

Manganese-doped barium phosphate $\left(Ba_3(PO_4)_2{:}Mn^{5+}\right)$ shows strong luminescent emission in the near-infrared—centered around 1191 nm—and finds application in fluorescent imaging of tissues in vivo [102]. Unfortunately, hydrocarbon polymers show strong light absorption around 1200 nm due to excitation of the C−H bond vibrations [88]. The presence of these vibrational centers might cause luminescence quenching of $Ba_3(PO_4)_2{:}Mn^{5+}$ nanoparticles, leading to a low quantum yield [103]. Nanoparticles of this material are synthesized by PHYSEE and are available to use in the experiments. The experiments performed with the $Ba_3(PO_4)_2{:}Mn^{5+}$ nanoparticles are described in Section 6.1.2.

SiAlON:Sm^{2+}

One of the other nanomaterials that PHYSEE is trying to synthesize is a ceramic material made from silicon (Si), aluminum (Al), oxygen (O) and nitrogen (N), doped with samarium ions in their 2+ valency state. SiAlON:Sm^{2+} originated as a material for the sputter deposition process, since the SiAlON host is widely used in the coating industry. Sm^{2+} has a broad absorption band in the visible spectrum and a sharp emission peak around 700 nm, on the verge of the spectral sensitivity of the human eye. Several exploratory experiments have been conducted with the SiAlON:Sm_3^+ particles, which is described in Section 6.1.3.

YAG:Ce

Cerium-doped yttrium aluminate garnet ($Y_3Al_5O_{12}{:}Ce^{3+}$ or YAG:Ce) shows a characteristic bright green luminescence and is commonly used as a phosphor for white light-emitting diodes (LED) [104] [105]. Pradal et al. [106] studied the influence of thermal treatment on the size distribution, zeta potential and quantum yield of YAG:Ce nanoparticles. They were able to obtain stable aqueous dispersions of particles with a mean size of around 30 nm and a quantum yield of 15%. However, the quantum yield can be increased significantly by lowering the Ce^{3+} concentration [107]. In the lab, several grams of (possibly severely agglomerated) YAG:Ce nanopowder is currently available. The YAG:Ce nanoparticles turned out to be the best option throughout this thesis research, as is explained in Section 6.1.4.

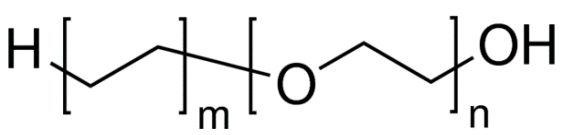

Figure 3.1: Structural formula of PE-b-PEG: a diblock copolymer of ethylene (m) and ethylene oxide (n). Reproduced from [108].

M_n (g/mol)	~575	~875	~920	~1400
wt% EO	20%	20%	50%	50%
m (units)	16.4	25	16.4	25
n (units)	2.2	3.6	10	15.5

Table 3.1: Number average molecular weight and composition of commercially available PE-b-PEG stabilizers.

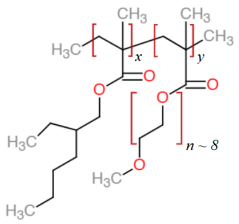

Figure 3.2: Chemical structure of the amphiphilic statistical copolymers of PEHMA (x) and MPEOMA (y).

Copolymer	MPEOMA fraction (mol%)	M_n (kDa)
A	5	19.0
B	10	28.6
C	15	32.9

Table 3.2: Molar fraction of polar MPEOMA monomers in the chain and molecular weight of the amphiphilic copolymers.

Amphiphilic copolymers

Chemical stabilization methods will be avoided due to their chemical specificity and potential perturbation of electronic states (see section 2.4.1). As summarized in section 2.4.3, amphiphilic copolymers have proven to be effective stabilizers for a wide range of nanoparticles and polymer matrices. The selection of suitable amphiphilic copolymers for the experiments is unfortunately limited by their commercial availability, as their synthesis is outside of the scope of this work. Although statistical copolymers—which are preferred over block copolymers for nanoparticle stabilization—are typically easier to synthesize, it turned out that they are very hard to come by. Instead, the commercially available block copolymer PE−b−PEG with varying molecular weight and composition was initially selected. Later on in the project, the more suitable statistical copolymers PEHMA-stat-PMPEOMA were used.

PE-b-PEG

Polyethylene-block-polyethylene glycol (PE-b-PEG) is an amphiphilic diblock copolymer of ethylene and ethylene oxide, which is used in industry as emulsifier, lubricant, mold release agent and thickening agent. A graphic representation of its molecular structure is given in figure 3.1, where m and n denote the number of ethylene units and ethylene oxide (EO) units respectively. The EO units act as nonionic anchor groups, forming hydrogen bonds with hydroxylated nanoparticle surfaces. In order to study the influence of the molecular weight and the composition of the stabilizer on the dispersion stability, different types of PE−b−PEG will be used (see table 3.1). Depending on the composition, PE-b-PEG is soluble in polar as well as non-polar solvents such as toluene. Unfortunately, the crystalline nature of the PE-b-PEG copolymers turned out to them unsuitable for the fabrication of transparent nanocomposites, as is explained in Section 6.2.2.

PEHMA-stat-PMPEOMA

Due to the unsuitability of the PE-b-PEG copolymers, a new type of amphiphilic copolymer had to be found in the course of the project. Statistical copolymers of poly(2-ethylhexyl methacrylate) and methoxy polyethylene oxide methacrylate (PEHMA-stat-PMPEOMA) were synthesized upon request by DSM Coating Resins. The molecular structure of the copolymers is shown in Figure 3.2. Three different types were synthesized with a varying fraction of polar MPEOMA binding groups (5, 10 and 15 mol%). The characteristics of the copolymers are listed in Table 3.2. The reason for the selection of these particular copolymers and the experiments that were conducted are outlined in Section 6.2.3.

Matrix polymers

Apart from compatibility with the amphiphilic copolymer, the polymer matrix has to fulfill the requirements outlined in section 2.5.1. A comparison of various common polymers with respect to these requirements is given in table 3.3. As the waveguiding substrate material is not yet known, the thermal expansion and refractive index are left out of the selection for now. In fact, they are quite similar for most organic polymers

	CYTOP	COC	PMMA	PET	PETG	PC	PS	PVC	PP	LDPE	HDPE
Crystallinity	Am.	Am.	Am.	Semi/Am.	Am.	Am.	Am.	Am.	Semi	Semi	Semi
Transmittance (%)	95	91	93	90	91	89	90	85	90	80	80
Haze (%)	-	0.4	1.0	0.6	0.3	1.0	1.0	3.0	11.0	1.3	6.0
RTI (°C)	108	130	70	80	63	100	75	50	100	80	100
OTR ($cm^3 \cdot mil/100in^2 \cdot day$)	921	100	12	13	25	300	300	11	240	500	185
WVTR ($g \cdot mm/100in^2 \cdot day$)	0.4	0.3	3.6	1.2	1.2	7.4	79.0	3.0	0.3	1.0	0.3
LTEC ($10^{-5}K^{-1}$)	7.4	6	5	6	8	7	6	5	6	10	6
Refractive index	1.34	1.53	1.49	1.57	1.57	1.58	1.59	1.53	1.49	1.52	1.53

Table 3.3: Comparative chart of common polymers on various parameters that affect the performance of the luminescent film. The OTR and WVTR coefficients are under atmospheric pressure. Data acquired from [95, 109–116].

(as opposed to for example perfluorinated polymers). More polymers have been considered than shown in table 3.3, but have been omitted for various reasons that rendered them impractical (e.g., biodegradability and commercial availability). Concluding from the comparative table, CYTOP, cyclic olefin copolymer (COC), polymethyl methacrylate (PMMA), polyethylene terephthalate (PET) and glycol-modified polyethylene terephthalate (PETG) appear to be the most suitable polymers. Several notes should be added to this outcome. First, the extremely high transparency of CYTOP might outweigh the disadvantage of its fairly high oxygen transmission rate, which can be compensated for by adding an extra barrier layer (see section 2.5.1). Secondly, PET in its natural state is an opaque semi-crystalline polymer. Transparent PET can only be obtained by rapidly cooling the molten polymer below its glass transition temperature—or alternatively by stretch blow molding, which is used for the production of PET bottles. Moreover, PET is very difficult to dissolve in common solvents [117]. PETG is produced by replacing glycol with a bigger building block that inhibits crystallization, resulting in a transparent amorphous material that is also more easily dissolved. In the end, the decisive factor for the selection of a polymer matrix is compatibility with the selected stabilizer (see section 2.4.2), yielding COC as the best option for PE-b-PEG. For the PEHMA-stat-PMPEOMA copolymers that were used later in the project, matrix polymers of PEHMA and PMMA were selected. The matrix polymers that were acquired for this project are listed in Table 3.4.

COC

COC are a group of polymers synthesized by copolymerization of ethylene and cyclic monomers such as norbornene, which is a combination known under the brand name TOPAS. The molecular structure of COC is shown in Figure 3.3a. COC is used for the production of optical components due to its excellent optical properties. It is soluble in common non-polar solvents such as toluene, allowing preparation of thin films by spin-coating. As a result of the polyethylene chains in its molecular structure, COC forms homogeneous polymer blends with polyethylene. Therefore, it is expected that the PE-b-PEG stabilizer is to some extent compatible with a COC matrix, depending on its molecular weight and composition. The experiments that have been conducted with COC are described in Section 6.3.

Ou and Hsu [118] prepared COC/fumed silica nanocomposites containing 1 to 15 wt% SiO_2 nanoparticles by solution blending using tetrahydrofuran (THF) solvent. They found that the SiO_2 particles could be dispersed in the COC matrix without large agglomerates, showing a transmittance of higher than 85% for a SiO_2 content up to 10 wt%. Dorigato et al. [119] studied the effect of the particle dimensions on the thermal, mechanical and optical properties of 2 wt% filled COC/fumed silica nanocomposites prepared by melt mixing. The authors showed that the nanocomposites containing the smallest primary particle size (7.8 nm) provided the highest transmittance. However, the transmittance of these nanocomposites was still drastically lower—at around 50% of pure COC. Using the same melt mixing technique and the exact same particles, Roy et al. [120] succeeded in preparing transparent nanocomposites with a transmittance of up to 82% up to a silica content of 3 wt%. The difference might be attributed to pre-drying of the particles, as well as to different mixing equipment and parameters.

PEHMA

The PEHMA-stat-PMPEOMA copolymers acquired later in the project were not expected to be compatible with COC. Therefore, they were used in combination with the chemically similar matrix polymer poly(2-ethylhexyl methacrylate) (PEHMA). The molecular structure of PEHMA is shown in Figure 3.3b. The reader is referred to Section 6.3.1 for more elaborate information on their selection. The experiments conducted with nanocomposites of PEHMA are described in Section 6.3.

Polymer type	Abbreviation	M_w (kDa)	Acquired from
Cyclic olefin copolymer (TOPAS 5013)	COC	N/A	TOPAS Advanced Polymers
poly(2-ethylhexyl methacrylate)	PEHMA	850–1500	Polymer Chemistry Innovations, Inc.
poly(methyl methacrylate)	PMMA	120	Sigma-Aldrich

Table 3.4: Matrix polymers that were used for the fabrication of polymer nanocomposite films.

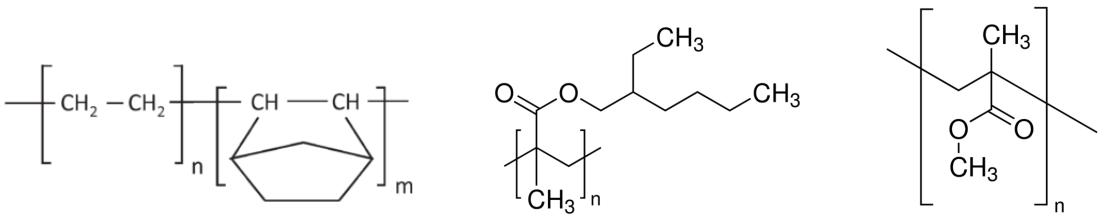

(a) (b) (c)

Figure 3.3: Molecular structures of (a) COC, which is a copolymer of ethylene (n) and norbornene (m), (b) PEHMA and (c) PMMA. Images reproduced from: (a) [119], (b) [121] and (c) [122].

PMMA
The PEHMA-stat-PMPEOMA copolymers were also tested in combination with poly(methyl methacrylate) (PMMA). The molecular structure of PMMA is shown in Figure 3.3c. More information about the selection of PMMA and the experiments conducted with nanocomposites of PMMA are described in Section 6.3.

Optional: CYTOP
If amphiphilic copolymers with fluorophilic functional groups could have been acquired during the project, the plan was to extend the scope of the research to fluoropolymers. These polymers would especially be suitable for the near-infrared emitting $Ba_3(PO_4)_2$:Mn^{5+} nanoparticles (see Section 3.2.1). This is because C−F bond vibrations are excited at wavelengths further in the infrared than C−H bonds, rendering fluoropolymers very efficient waveguides for near-infrared light [88]. Dispersing nanoparticles in a perfluoropolymer requires a stabilizer with fluorophilic functional groups. Unfortunately, fluorinated amphiphilic copolymers are very specific and complex materials and could not be obtained.

Due to the substitution of carbon-hydrogen with higher energy carbon-fluorine bonds, fluoropolymers have some unique properties. They typically have high chemical, thermal and degradation stability, as well as a low refractive index, surface tension and dielectric constant [123]. The term fluoropolymer is used for partially fluorinated polymers, whereas perfluoropolymers do not have any carbon-hydrogen bonds in their molecular structure. CYTOP is the brand name of an amorphous perfluoropolymer made by cyclopolymerization of perfluoro-3-butenyl-vinyl ether (PBVE) [124]. Due to its amorphous structure, CYTOP exhibits exceptional transparency and good solubility in specific fluorinated solvents. Stelzig et al. synthesized in situ functionalized silver and copper nanoparticles using laser ablation in tetrahydrofuran (THF) with statistical amphiphilic terpolymers bearing fluorinated side chains [125]. The stabilized particles could be successfully redispersed into different THF-soluble fluoropolymers without forming agglomerates.

3.2.2. Methods

Inorganic nanoparticles are typically dispersed in polar solvents due to their hydrophilic surfaces. However, both the polar solvent and the hydrophilic nanoparticles are generally incompatible with organic polymer matrices. Compatibilization of the entire system—including the solvent—is therefore crucial to obtain nanocomposites without agglomerates. The challenge that arises is how to transfer inorganic nanoparticles to an organic matrix polymer while preventing agglomeration in the process. The method used to accomplish this is divided into three steps: i) dispersing the nanoparticles in a polar solvent, ii) phase transfer of the nanoparticles to a nonpolar solvent and iii) mixing the nonpolar nanodispersion with matrix polymers and applying the mixture as a thin film.

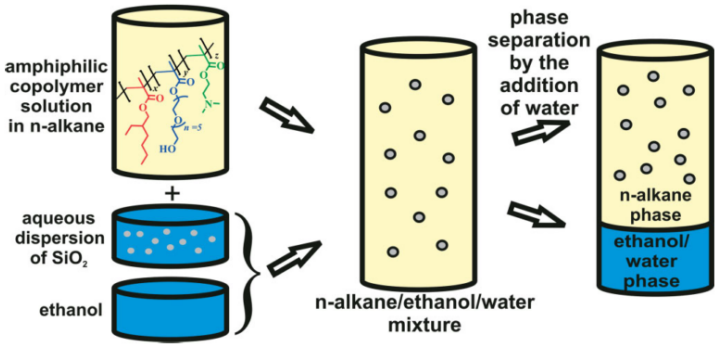

Figure 3.4: Surface modification and transfer of inorganic nanoparticles from an aqueous solution to a non-polar solvent using the monophasic solvent mixture procedure. Reproduced from [127].

Dispersion in polar solvent

The nanoparticles are first dispersed in a polar solvent to obtain electrostatically stable nanodispersions. If necessary, the pH of the liquid or the solvent can be adjusted to increase the dispersion stability. The experiments that were conducted on dispersing the nanoparticles in polar solvents are outlined in Section 6.1.

Phase transfer to nonpolar solvent

The polar nanodispersions cannot be mixed directly with nonpolar media, as this either leads to phase separation or rapid agglomeration of the nanoparticles. One way to overcome this challenge is by using a combination of polar and nonpolar solvents to obtain a hybrid monophasic solvent mixture that is still able to dissolve the amphiphilic copolymers. This simple strategy, developed by Jonschker et al. [126], is depicted schematically in figure 3.4. First, the amphiphilic copolymer is dissolved in a nonpolar solvent and the aqueous dispersion of nanoparticles is diluted with ethanol, which are then mixed together. By finding the exact balance of polar and non-polar components, the addition of ethanol closes the miscibility gap to create a multicomponent monophasic solvent mixture. In the solvent mixture, the polar groups of the amphiphilic copolymer now adsorb to the inorganic nanoparticle surface. By adding additional water the phases again separate, effectively transferring the hydrophobized particles to the nonpolar solvent. Stelzig, Klapper and Müllen [127] were able to transfer silica (SiO_2), alumina (Al_2O_3) and ceria (CeO_2) nanoparticles to a nonpolar solvent without the formation of agglomerates using this approach. In addition, the authors prepared highly transparent SiO_2/polyurethane (PU) nanocomposite films, showing a homogeneous distribution of particles with a particle size well below 100 nm. This strategy is only effective if the amphiphilic copolymer is soluble in both the nonpolar solvent and the solvent mixture. Also, a sufficient amount of hydrophilic anchor groups is necessary to ensure interaction with the particle surfaces. These requirements translate into a minimum concentration of the hydrophobic and hydrophilic contents of the copolymer, which is suggested to be around ~70 mol% and ~5 mol%, respectively [127]. A major advantage of this approach is that the formation of micelles by the amphiphilic block copolymers in an optimized solvent mixture is likely to be suppressed, as the interfacial tension between the polar block and the solvent is lower. Additionally, the process is easy to scale up and is environmentally friendly, as the solvents can be recycled after phase separation.

The YAG:Ce nanoparticles used throughout the project were found to be stable in ethanol, as described in Section 6.1.4. As a result, the nanodispersion can be directly mixed with the nonpolar phase and the ethanol can simply be evaporated. The adapted version of the monophasic solvent mixture process that was used during the project is explained in Section 6.2.1. The phase transfer experiments that have been conducted are outlined in Section 6.2 and in the paper in Chapter 4.

Thin film preparation

After the nanoparticles are successfully stabilized in a nonpolar solvent, the stable nanodispersion can be mixed with matrix polymers dissolved in the same solvent. The resulting mixture will be spin-coated onto glass substrates to form polymer nanocomposite films. The preparation and characterization of the nanocomposite films is outlined in Section 6.3 as well as in the paper in Chapter 4.

Variable parameters
Multiple parameters are varied in the process to study their influence on the success of stabilization, including:

- the type of nanoparticles
- the type of amphiphilic copolymers
- the type of matrix polymers
- the molecular weight and composition of the amphiphilic copolymers
- the concentration of the amphiphilic copolymers
- the volume fractions of solvents in the solvent mixture
- the phase transfer process parameters (e.g., temperature, agitation, sonication)
- the spin coating parameters (e.g., viscosity of the liquid, spin speed, acceleration)

3.2.3. Characterization

In order to study the influence of these variable parameters on the state of agglomeration, it is important to characterize the samples in every step of the process. In liquids, the particle size can be analyzed by dynamic light scattering. When the nanocomposites are incorporated into polymer films, one has to resort to scanning electron microscopy or white light interferometry to study the particles and the structure of the nanocomposite films. The optical properties of the films, such as the transmittance, haze and luminescence intensity can be characterized by spectrophotometry and fluorescence spectroscopy.

Dynamic light scattering
Dynamic light scattering (DLS) is a tool to analyze the size distribution of small particles (in the range of 1 nm to 10 μm) in a liquid. Due to Rayleigh scattering, a light beam incident on the particles scatters in all directions. The particles in the liquid constantly undergo Brownian motion and their mean displacement in a certain time interval depends on their size. The light that scatters on these particles undergoes constructive or destructive interference, thereby causing the light intensity to fluctuate over time. By analyzing this fluctuation, information on the particle size distribution can be deduced. DLS is frequently used in literature to study the size distribution of nanoparticles in solution [30, 33, 36, 41, 56, 60, 72, 73, 83, 84, 128] as well the formation of micelles [50, 71, 75, 82]. DLS is a useful tool to study the agglomeration state of nanoparticles before and after transfer to a nonpolar solvent (see Section 3.2.2), as well as the potential formation of micelles by the amphiphilic copolymers.

DLS is most reliable for monodisperse particle size distributions. For polydisperse and multimodal size distributions, the interpretation of the results becomes more involved. Rayleigh scattering intensity is proportional to the particle size to the power six. Since larger particles in the dispersion scatter much more light than the smaller particles, the particle distributions based on the scattering intensity emphasize the larger particles. Additionally, DLS can compute the particle size distributions by volume or by number, known as the volume distribution and number distribution. This corrects for the emphasis on larger particles by showing the relative volume or relative number of particles of a given size rather than the relative intensity of light scattered by these particles. The volume and number distributions are calculated from the intensity distribution and therefore the intensity distribution is closest to what is actually measured. The conversion is valid only when the particles are much smaller than the wavelength of the laser or the parameters for Mie scattering theory are well-known (i.e., the refractive index and absorbance), provided that the measurement data meets the quality criteria.

Scanning electron microscopy
The particle size in the prepared thin films can be analyzed by scanning electron microscopy (SEM), which creates an image of a sample by scanning the surface with a high-energy beam of electrons. Although the resolution is slightly lower than for transmission electron microscopy (TEM), SEM allows three-dimensional imaging with a nanoscale resolution. In order to study electrically insulating samples—such as organic polymers—an thin layer of conductive material must be applied to prevent an accumulation of surface charge from distorting the image. SEM is a commonly used method in literature for analyzing particle size and distribution in nanocomposite films [61, 62, 84, 106, 118, 127, 129].

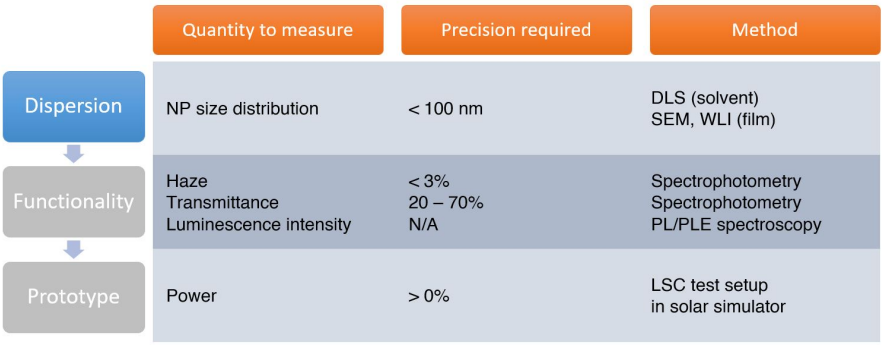

Figure 3.5: Quantities to measure during the three original experimental phases, as well as their required precision and method of characterization.

White light interferometry
White light interferometry makes use of light interference effects to measure the surface profile of a sample, producing 3D images of the surface with sub-nanometer precision. It is a useful tool to analyze the smoothness and thickness of the spin coated polymer films. Moreover, it might provide information about the effect that the embedded nanoparticles have on the morphology of the films.

Spectrophotometry
Spectrophotometry is a method to measure the optical properties of a sample as a function of the wavelength. It is a useful tool to measure the transmission and haze of the nanocomposite films, indicating to what extent the nanoparticles have agglomerated in the polymer matrix [70, 120, 130, 131]. UV-vis spectrophotometers can record the absorption spectra of luminescent samples [18, 19, 67, 84, 85, 105, 132–138], while Fourier transform infrared (FTIR) spectrophotometers can measure the vibrational absorption of the organic bonds [72, 83, 118, 139, 140].

Spectrofluorometry
Spectrofluorometry or fluorescence spectroscopy is a method to analyze the luminescence of a sample. A high intensity light source passes through a filter to excite the sample at a certain wavelength, after which the emission—also passing though a filter—is recorded. A spectrofluorometry setup is commonly used to measure the photoluminescence (PL) or photoluminescence excitation (PLE) spectra of a sample by fixing the excitation filter or the emission filter, respectively [18, 81, 102, 105, 134, 136, 137, 141, 142].

3.3. Planning

The initial and final timeline are discussed in Section 7.3. Originally, the experimental plan was divided into three different phases, each of which was concluded with a well-defined milestone or deliverable based on a measurable quantity. The quantities of interest, as well as their required precision and method of characterization are show in Figure 3.5. As will be explained in Section 7, the project focus has mostly been narrowed to the first phase due to multiple unforeseen circumstances.

Dispersion
The first phase is focused on controlling the dispersion of nanoparticles in both a solvent and the film and was originally planned to comprise about 60% of the total time. During this phase, the influence of the type and concentration of the stabilizer and nanoparticles as well as the process parameters on the size distribution of the nanoparticles will be thoroughly studied. As a general guideline, non-scattering films can usually be obtained when the particle clusters are not larger than 100 nm [14]. In reality, the amount of scattering induced by the particles depends on several additional parameters, including the refractive index mismatch, the particles concentration and the wavelength (see Equation 1.2 in Section 1.3).

Original plan: Functionality
Once the size distribution of dispersed nanoparticles can be controlled, the second phase will focus on the functionality of the nanocomposite film. To this end, the nanoparticle size and loading and the film thickness will be related to the optical performance of the film: the haze, the transmittance and the luminescence

intensity. For windows, the recommended maximum allowable haze—below which the human eye is unable to detect any loss of quality—is equal to 3% [92]. The minimum transmittance for uncoated windows should be between 82% and 78%, depending on the thickness [92]. Windows with applied low emissivity (low-E) coatings typically have a visible light transmittance of 20% to 70% [143]. As the luminescent particles absorb light in the visible spectrum, there is a trade-off between the transmittance and the luminescence intensity of the film. The measured luminescence intensities can be compared qualitatively for samples with similar transmittance.

Original plan: Prototype
The last phase will focus on optimization of the optical performance and the development of a prototype. An LSC test setup with connected solar modules is available at PHYSEE to which the glass substrates with spin coated nanocomposite films can be attached. The electrical power output can be studied in the solar simulator at PHYSEE.

3.4. Risk mitigation

Before the experimental phase, several risks were identified that might cause agglomeration of the nanoparticles in the organic solvent or unsuccessful dispersion in the the polymer matrix. The anticipated risks are outlined in this section. In hindsight, the compatibility indeed turned out to be a serious issue. The risk has been mitigated by shifting towards a new type of amphiphilic copolymer and corresponding matrix polymers, as described in Sections 6.2.3, 6.3.1 and 7.2.

Frozen micelle formation
First and foremost, there is high risk ineffective stabilization due to the formation of kinetically frozen micelles by the block copolymer PE-b-PEG (see section 2.4.2). Unimers cannot or only very slowly desorb from these stable micellar structures, giving the nanoparticles time to agglomerate in the solvent mixture. On the other hand, using a concentration of PE-b-PEG below the CMC might be too low for effective stabilization. This risk can be mitigated in several ways. First of all, minimizing the interfacial tension between the PEG and the solvent mixture by the addition of ethanol increases the CMC and reduces the formation of frozen micelles. Secondly, selecting a lower chain length of PEG reduces the entanglement and therefore the stability of the frozen micelles. Also, the temperature should always be kept higher than the glass transition temperature of the PE-b-PEG copolymers. Above all, the risk of frozen micelle formation should be mitigated completely by using statistical amphiphilic copolymers. The search for commercially available statistical copolymers should be a continuous process throughout the experimental phase.

Incompatibility
There is a risk of incompatibility between the PE-b-PEG stabilizer and the COC matrix. As discussed in section 2.4.2, nanoparticles can sometimes not be fully wetted by the matrix if the molecular weight of the stabilizer is much lower than the polymer matrix, leading to agglomeration. The molecular weight of the commercially available COC (TOPAS) is not specified, but it is expected to be much higher than the commercially available grades of PE-b-PEG. Moreover, the molecular structures of COC and PE-b-PEG are only partially similar. Even though COC is known to be miscible with polyethylene (PE), it is unsure whether it is compatible with PE-b-PEG. This risk can be mitigated by finding a higher molecular weight stabilizer and a corresponding matrix polymer. For example, a diblock copolymer of polystyrene and poly(ethylene glycol) with a molecular weight of $20-30$ kDa is commercially available (and very expensive) [144]. Again, statistical copolymers would be the preferred option.

Vibrational quenching
The excitation of molecular vibrations in the polymer matrix quenches the luminescence if the emission of the phosphor is in the same frequency range. For example, the presence of C−H bonds causes hydrocarbon polymers—including COC—to strongly absorb light with a wavelength around 1200 nm, which is very close to the characteristic 1191 nm emission of $Ba_3(PO_4)_2{:}Mn^{5+}$. The overlap between emission and vibrational excitation might cause total quenching of the emission or lead to complete absorption before it reaches the edges of the substrate. This risk can be mitigated by either using a phosphor that emits at a shorter wavelength, or by selecting a polymer matrix that does not absorb in the near infra-red (such as perfluoropolymers).

4

Scientific Paper

4.1. Summary

The integration of luminescent nanoparticles into transparent polymer matrices opens the way to affordable, scalable and efficient luminescent solar concentrators (LSCs). A key challenge in the fabrication is to prevent agglomeration of the nanoparticles as this will drastically reduce the performance due to scattering effects. In this paper, luminescent YAG:Ce nanoparticles were successfully incorporated into poly(2-ethylhexyl methacrylate) (PEHMA) matrices without any notable agglomeration to form fully transparent nanocomposite thin films. The fabrication method involves an easy, universal and scalable three-step procedure: i) dispersion of the inorganic particles in a polar solvent, ii) phase transfer of the polar nanodispersion to an organic solvent with dissolved amphiphilic statistical copolymers and iii) mixing the organic nanodispersion with a compatible polymer and spin coating the solution.

In order to obtain transparent nanocomposite films, it is essential that the nanoparticles are dispersed in the matrix as isolated, nanoscopic objects. Stabilization of the NPs during the phase transfer process is therefore a crucial step in the procedure. The polar parts of the amphiphilic copolymers adsorb to the hydroxylated YAG:Ce NP surfaces through van der Waals forces and prevent agglomeration by sterically stabilizing the particles. The nonpolar parts ensures compatibility of the particles with the polymer matrix during the fabrication of the nanocomposite.

The rate of nanoparticle agglomeration during the phase transfer process is directly competing with the rate of adsorption of the amphiphilic copolymers. The adsorption rate is ultimately limited by the rate of transport of the amphiphiles to the NP surface, but can be severely hampered by kinetic effects during the binding step. These kinetic effects are described by the adsorption rate constant, which depends exponentially on the temperature and the activation energy for adsorption. In order to prevent agglomeration, it is crucial to maximize the adsorption rate constant and thereby shift the controlling mechanism of adsorption from kinetic-controlled to diffusion-controlled.

Three amphiphilic statistical copolymers of PEHMA and MPEOMA (PEHMA-stat-PMPEOMA) were studied containing 5, 10 and 15 mol% of MPEOMA binding groups. The nonionic binding groups were selected because of their applicability to a wide range of inorganic nanoparticles. In toluene, rapid adsorption of all the studied amphiphilic copolymers was found to be hampered by kinetic effects, leading to a significant increase in particle size during the phase transfer process. It is suggested that the low adsorption rate constant is the result of steric shielding of the MPEOMA binding groups due to intramolecular self-assembly of the amphiphilic copolymers. When the affinity of the polar binding groups with the solvent system is low, the nonpolar EHMA moieties form a protective shell shielding them from the solvent—and from a nearby NP surface. The inaccessibility of the binding groups poses a structural barrier to the adsorption process, which is represented by a high activation energy. The state of agglomeration was found to be influenced by three process parameters that together determine the success of stabilization: the amphiphile concentration, the solvent temperature and the solvent composition.

Increasing the solvent quality for the MPEOMA groups by the addition of ethanol to the solvent system drastically improved the efficiency of stabilization. To a lesser extent, the temperature was also found to influence the measured particle size after the phase transfer process. The effect of the temperature is expected to be two-fold. Elevating the temperature increases the average kinetic energy of the amphiphilic molecules

and thereby improves their chance to overcome the energy barrier to adsorption. In addition, a higher temperature favors the solvent quality for the binding groups, thereby reducing the effect of steric shielding. Increasing the amphiphile concentration is beneficial up to a certain point, after which intermolecular interactions start to play a role. Moreover, the beneficial effect of increasing the concentration is much lower for kinetic-controlled adsorption processes. By carefully tuning the solvent composition, the temperature and the amphiphile concentration, EtOH/YAG:Ce nanodispersions were successfully transfered to toluene without any noticeable agglomeration of the YAG:Ce particles. Although the activation energy was found to decrease with increasing PMPEOMA fraction, no significant difference in performance was observed between the three copolymers. The findings prove that the fraction of polar binding groups in the copolymer is not important as long as a sufficient amount is present.

In this paper, a theoretical approach is presented to relate the kinetics of the agglomeration and adsorption process to the state of agglomeration after the phase transfer. The theoretical model shows excellent agreement with the experimental observations. By comparing the experimental data with the model, it is possible to identify the controlling mechanism of adsorption and obtain order-of-magnitude estimates of the kinetic rate constants and the activation energies of the copolymers in the studied system. In the case of diffusion-controlled adsorption, the model accurately predicts the minimum amphiphile concentration required to prevent agglomeration.

In addition, a simple method is developed to identify the optimal solvent composition by minimizing the difference in Hansen solubility parameters between the binding groups of the amphiphile and the solvent system. At the optimal solvent composition and the corresponding maximum temperature, the limiting kinetic effects were completely eliminated. In general, the following procedure is recommended for the transfer NPs to a nonpolar solvent: i) identify the amphiphile concentration that gives the best results in the nonpolar solvent, ii) identify the optimal solvent composition by adding varying volume fractions of a miscible polar liquid and iii) close to the boiling point of the solvent mixture, identify the lowest concentration required for stabilization.

The stabilized toluene/YAG:Ce nanodispersions were mixed with various transparent polymers to prepare nanocomposite solutions for spin coating. It has been demonstrated that the compatibility of the amphiphilic copolymers with the polymer matrix is of vital importance. Similar to blends of incompatible polymers, phase separation was observed either in the solution mixture or in the nanocomposite. The copolymers were clearly incompatible with solutions of COC, forming a phase separated liquid. In the case of PMMA, seemingly homogeneous solutions were obtained, but spin coating the solution resulted in turbid nanocomposite films. The turbidity decreased significantly for copolymers with higher MPEOMA fractions, indicating that the compatibility with the polymer matrix can be promoted by including a certain fraction compatible moieties in the structure of the amphiphilic copolymer. By dispersing the particles into PEHMA matrices, which is identical to the nonpolar part of the copolymers, fully transparent nanocomposite films were obtained with haze values similar to pure PEHMA films ($< 1\%$). SEM images revealed that the nanoparticles were homogeneously dispersed without any notable agglomeration during the fabrication.

Due to the necessary centrifugation step in processing nanopowders, the YAG:Ce content was too low ($\sim$0.1 wt%) to measure any luminescent output. However, following the exact same procedure, luminescent NPs obtained from colloidal synthesis methods would allow for the fabrication of nanocomposite films with much higher particle fractions. Since the MPEOMA groups in the copolymer strongly bind to the hydroxylated NP surface, it is expected that the procedure described in this article can be applied to any type of metal oxide NPs and possibly even to other polar nanomaterials.

Excellent compatibility with the desired matrix polymer can be obtained by carefully matching the chemical structures of the amphiphilic copolymer and the matrix polymer. The procedure described in this article therefore opens up the possibility to integrate a wide variety of inorganic luminescent nanoparticles into many types of matrix polymers. The simple, cheap and scalable method allows for the fabrication of efficient polymer nanocomposite LSCs.

Stabilization of inorganic luminescent nanoparticles in organic media for the fabrication of polymer nanocomposites

Jan David Endtz, Urs Staufer, Luigi Sasso
Delft University of Technology, Mekelweg 2, 2628 CD Delft, the Netherlands

4.2. Abstract

The integration of luminescent nanoparticles into transparent polymer matrices opens the way to affordable, scalable and efficient luminescent solar concentrators. A key challenge in the fabrication is to prevent agglomeration of the nanoparticles as this will drastically reduce the performance due to scattering effects. The incompatibility of inorganic nanoparticles with organic media typically leads irreversible agglomeration upon direct mixing. In this article, inorganic luminescent $Y_3Al_5O_{12}$:Ce^{3+} nanoparticles are transfered from a polar to a nonpolar solvent without any noticeable agglomeration using amphiphilic statistical copolymers as stabilizing agents. The process parameters that determine the success of stabilization are studied both theoretically and experimentally and a general procedure is proposed to find the optimal conditions for the phase transfer process. The importance of compatibility between the amphiphilic copolymers and the polymer matrix was demonstrated by integrating the stabilized nanoparticles into various polymer matrices. Fully transparent polymer nanocomposite thin films were prepared without any sign of agglomeration. The simple, universal and scalable method presented in this article allows for the fabrication of nanocomposite luminescent solar concentrators using a wide variety of luminescent materials and polymers.

4.3. Introduction

The global buildings sector accounts for 30% of the final energy consumption [1]. Nearly two-thirds of this energy use is supplied by fossil fuels, representing 28% of global energy-related CO_2 emissions [1]. Not surprisingly, increasing the energy efficiency of buildings one of the key challenges of the global climate ambitions set forth in the Paris Agreement [2]. One particularly promising development in this field is the design of luminescent solar concentrators (LSCs), which can transform conventional glass into transparent, colorless, power-generating structural elements. LSCs operate by absorbing solar radiation and re-emitting it at a different wavelength towards the edges of the device, where it is readily converted into electricity by solar cells. Rare-earth doped inorganic compounds are promising luminescent materials for LSC applications due to their potential high photostability, high quantum yield, broad absorption band and low self-absorption [10, 13, 23].

This paper focuses on a universal, simple and scalable method for the fabrication of luminescent polymer nanocomposite films—the engine behind the LSC. The ability to disperse the inorganic luminescent nanoparticles (NPs) in the polymer matrix as isolated nanoscopic objects is crucial to avoiding excessive scattering losses. However, keeping NPs as individual nanoscopic objects is not trivial as they have a natural tendency to reduce their surface energy by forming agglomerates. The primary goal of this study is to investigate the efficacy of various amphiphilic statistical copolymers for the stabilization of inorganic luminescent NPs in matrix polymers. The material and process parameters that affect the formation of agglomerates are identified and their influence is studied both theoretically and experimentally in order to set guidelines for the fabrication of luminescent polymer nanocomposite films.

NPs suspended in a liquid continuously move around in a random manner as a result of collisions with the molecules of the surrounding medium—a process known as Brownian motion. When two isolated NPs come in close proximity, they are attracted to each other through the van der Waals forces arising from the electrostatic interaction between their dipoles. The strength of these forces depends predominantly on the geometry of the particles, the separation distance and the contrast in the dielectric properties between the NPs and the intervening liquid medium [37]. For two identical materials interacting across a medium, the van der Waals interaction is always attractive. Therefore, some form of stabilization is required to suppress the formation of agglomerates. Stabilization strategies usually involve the interaction of ions (for electrostatic stabilization [26, 30, 40, 41, 46, 145, 146]) or molecules (for steric stabilization [48, 50, 70, 72, 83, 84, 127]) with the surface of NPs. While electrostatic stabilization can be effective for obtaining stable dispersions in polar solvents, the method is unsuited for nonpolar solvents or polymer solutions, where the electrostatic interactions between colloidal particles are generally negli-

gible due to the absence of free ions [47].

In nonpolar media, inorganic NPs can be stabilized by the adsorption of amphiphilic molecules—a process known as steric stabilization [49]. Amphiphiles or stabilizers bind to the hydrophilic surface of inorganic NPs with their polar moieties, while their nonpolar parts provide compatibility with the organic environment and introduce steric repulsion between the encapsulated NPs. Successful stabilization of NPs in a polymer matrix depends on three key parameters [50]: i) the binding strength of the amphiphile to the NP surface, ii) the kinetics of the adsorption process and iii) the compatibility of the amphiphile with the matrix polymer.

Stabilizers that are not strongly bound to the surface risk being desorbed during the fabrication of nanocomposites, leading to agglomeration and a loss of transparency. The adsorption of stabilizers to the particle surface occurs through the formation of either chemical or physical bonds. Chemical adsorption methods based on graft polymerization [57–59] or using coupling agents [52–56] typically yield strong covalent or ionic bonds, but are limited by material and crystallographic specificity and could perturb the electronic states of the particle surface [51, 66]. Physical adsorption on the other hand is the result of comparatively weak interactions such as van der Waals forces, electrostatic attraction or hydrogen bonding. As a result, physically adsorbing stabilizers typically adsorb to a wide variety of inorganic materials.

Depending on their molecular weight, physically adsorbing stabilizers can be classified as low molecular wight surfactants or amphiphilic copolymers. Low molecular weight surfactants contain only one or several polar groups and generally suffer from low binding strength [69, 70]. Higher molecular weight amphiphilic copolymers, on the other hand, are more compatible with polymers and bind strongly to a particle surface due to the large amount of hydrophilic monomers functioning as binding sites [73]. Although the individual bonds are comparatively weak, the probability of all binding groups being cleaved simultaneously is extremely low.

The kinetics of amphiphile adsorption directly competes with the rate of NP agglomeration and must be sufficiently high to stabilize the dispersion. The adsorption kinetics of amphiphilic copolymers varies greatly depending on their structure and molecular weight. Amphiphilic block copolymers, consisting of covalently attached blocks of hydrophobic and hydrophilic monomers, tend to aggregate to form "kinetically frozen" micelles due to the entangling of the more solvophobic blocks in the micelle center [75–77, 79, 80, 147]. Block copolymer unimers typically cannot or only slowly desorb from these stable micellar structures, preventing them from adsorbing to the NPs. Statistical copolymers, on the other hand, do not form stable micelles due to the random order of hydrophilic and hydrophobic monomers in their chains, thus allowing much faster adsorption kinetics [50, 82, 83].

In a polymer matrix, sufficient compatibility is required between the encapsulated NPs and the matrix polymer to prevent phase separation. As with polymer blends, compatibility results from sufficiently strong interactions between the polymer chains. The compatibility of an amphiphilic copolymer with a matrix polymer is favored by chemical similarity, both in terms of the chemical composition and the molecular weight [84, 85]. Considering the three key parameters for stabilization—the binding strength, the adsorption kinetics and the compatibility—amphiphilic statistical copolymers are considered to be the best candidates for the fabrication of polymer nanocomposites [50, 83].

4.4. Materials and methods

Materials

Luminescent $Y_3Al_5O_{12}:Ce^{3+}$ (yttrium aluminum garnet doped with cerium, YAG:Ce) nanopowder with a primary particle size of 15–40 nm was acquired and kindly supplied by Dr. Erik van der Kolk. Poly(methyl methacrylate) (PMMA) ($M_w \sim 120$ kDa) and all solvents were purchased from Sigma Aldrich and were used as received. Poly(2-ethylhexyl methacrylate) (PEHMA) ($M_n \sim 850-1500$ kDa) was kindly supplied by Polymer Chemistry Innovations, Inc. Cyclic olefin copolymer (COC, TOPAS 5013) was acquired from TOPAS Advanced Polymers. The poly(2-ethylhexyl methacrylate)-stat-poly(methoxy polyethylene oxide methacrylate) (PEHMA-stat-PMPEOMA) amphiphilic statistical copolymers with MPEOMA fractions of 5, 10 and 15 mol% (M_n = 19.0, 28.6 and 32.9 kDa as calculated by size exclusion chromatography against PMMA standards) were synthesized on request and kindly supplied by DSM Coating Resins.

Characterization

The particle size distribution and average hydrodynamic particle diameter in the dispersions was measured by dynamic light scattering (DLS) using a Zetasizer Nano ZS. The film thickness and surface topography were analyzed by white light interferometry (WLI) using a Bruker 3D Optical Microscope. Haze measurements were performed using a PerkinElmer LAMBDA 950 UV/Vis Spectrometer. The polymer nanocomposite films were treated with oxygen plasma in a Diener Femto plasma cleaner and made conductive for SEM analysis by sputtering a

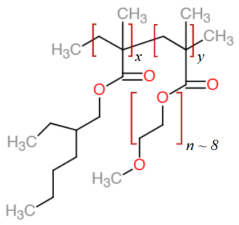

Figure 4.1: Chemical structure of the amphiphilic statistical copolymers of PEHMA (x) and MPEOMA (y) used in this study.

Copolymer	MPEOMA fraction (mol%)	M_n (kDa)
A	5	19.0
B	10	28.6
C	15	32.9

Table 4.1: Molar fraction of polar MPEOMA monomers in the chain and molecular weight of the amphiphilic copolymers.

thin film of Au/Pd (~ 6nm) on top with a SC7620 sputter coater. The size and distribution of the particles in the nanocomposite films were analyzed in a JEOL JSM-6010LA scanning electron microscopy (SEM). Elemental analysis was conducted by energy dispersive X-ray analysis (EDS) in the same instrument.

Dispersion of nanoparticles in ethanol

The surface of metal oxides such as YAG is typically characterized by a high density of hydroxyl groups [27, 28]. Metal oxides build up a surface charge depending on the pH due to the dissociation of surface sites, allowing for electrostatic stabilization [26, 40]. Moreover, the hydroxyl groups function as binding sites for amphiphilic molecules [57, 59, 148]. SEM analysis revealed that the YAG:Ce nanopowder was heavily agglomerated with agglomerate sizes up to 100 µm.

The nanopowder was dispersed in ethanol (EtOH) and placed in a Fisher Scientific FB 15046 ultrasonic bath for 30 minutes at 240W. The suspension was centrifuged for 5 minutes at 13,000 rpm in a Eppendorf 5415 centrifuge to remove the remaining agglomerates. The resulting EtOH/YAG nanodispersions were measured by DLS and shown to have a unimodal size distribution and an average hydrodynamic diameter between 60 – 70nm. The nanodispersions showed no sign of agglomeration for several weeks, indicating that the particles are electrostatically stabilized in EtOH. The concentration of the particles in EtOH was estimated to be ~ 0.007 vol% by comparing the scattered light intensity measured by DLS to that of a polystyrene (PS) standard with the same average particle diameter in water. The difference in scattered light intensity due to the difference in optical properties of the particles (YAG:Ce and PS) and of the liquids (EtOH and water) was accounted for by scaling the measured intensities using Rayleigh scattering theory:

$$I \propto \left[\frac{(n_p/n_m)^2 - 1}{(n_p/n_m)^2 + 2} \right]^2 \tag{4.1}$$

where n_p and n_m are the refractive indices of the particles and the medium.

Transfer of nanoparticles to toluene

Various concentrations of the amphiphilic PEHMA-stat-PMPEOMA copolymers (see Figure 4.1 and Table 4.1) were dissolved in solvent mixtures of toluene and ethanol in various volumetric ratios. The solvent mixtures were heated in 2mL vials on a hot plate while the temperature was measured with a liquid-in-glass thermometer. At the desired temperature, the EtOH/YAG:Ce nanodispersion was pipetted into the liquid and the mixture was heated until the EtOH had evaporated.

Preparation of nanocomposite thin films

The toluene/YAG:Ce nanodispersions were mixed with 30 wt% solutions of COC, PMMA or PEHMA in toluene to obtain mixtures with a total polymer concentration of 10 wt%. The mixtures were agitated by mechanical stirring for 1 hour to ensure proper mixing. Nanocomposite thin films with a thickness of 1 – 2 µm we prepared by spin coating the mixtures on square 25 mm^2 microscope slides with a spin speed of 3000 RPM using a POLOS SPIN150i spin coater.

4.5. Results and discussion

4.5.1. Agglomeration and adsorption kinetics

In order to incorporate the ethanol-dispersed YAG:Ce NPs into a polymer matrix, the NPs first need to be transferred to a nonpolar solvent that is able to dissolve the polymer. However, when the YAG:Ce/EtOH dispersion is directly added to a nonpolar phase, the electrostatic repulsion between the NPs vanishes instantly and the NPs rapidly agglomerate to form micron-sized structures. By dissolving a sufficient amount of a suitable amphiphile in the nonpolar phase, the agglomeration can be suppressed to obtain a stable dispersion. For successful stabilization—meaning that the particle size before and after the phase transfer is approximately equal—the rate of amphiphile adsorption has to be much higher than the rate of nanoparticle agglomeration.

The agglomeration rate of particles in a liquid was first described by Smoluchowski and depends on the

frequency of collisions [149]. The collision frequency constant of spherical particles with diameters d_i and d_j due to both Brownian motion and shear flow is estimated from [149–151]:

$$K_{ij} = \left[\frac{2kT}{3\mu} \left(2 + \frac{d_i}{d_j} + \frac{d_j}{d_i} \right) + \frac{\overline{G}}{6} \left(d_i + d_j \right)^3 \right] \tag{4.2}$$

where k is the Boltzmann constant, T is the absolute temperature, μ is the dynamic viscosity of the medium and $\overline{G}$ is the mean shear rate due to agitation of the fluid. It is important to note that the Brownian motion contribution to the collision frequency only depends on the relative size of the particles, whereas the shear flow contribution depends strongly on their absolute size. Assuming that every collision results in adhesion and that all NPs are initially identical in size, the rate of reduction in the total number particles per unit volume N is determined by [151]:

$$\frac{\mathrm{d}N}{\mathrm{d}t} = -\left(K_\mathrm{B} N^2 + K_\mathrm{S} N \right) \tag{4.3}$$

The parameters K_B and K_S are the rate constants for agglomeration due to Brownian motion and shear, approximated by:

$$K_\mathrm{B} = \frac{4kT}{3\mu} \tag{4.4}$$

and

$$K_\mathrm{S} = \frac{3\overline{G}\phi}{\pi} \tag{4.5}$$

where ϕ is the volume concentration of NPs. Solving equation 4.3 subject to the initial condition $N = N_0$ at $t = 0$, gives the agglomeration time t_ag:

$$t_\mathrm{ag} = \ln \left[\frac{K_\mathrm{B} N_0 + K_\mathrm{S} (N_0 / N)}{K_\mathrm{B} N_0 + K_\mathrm{S}} \right] K_\mathrm{S}^{-1} \tag{4.6}$$

For nanoscopic particles, the effect of agitation is negligible even at extremely high shear rates as the shear contribution depends on the absolute particle size (see Equation 4.2). When the contribution of shear flow to the collision frequency is neglected, the solution to equation 4.3 reduces to:

$$t_\mathrm{ag} = \frac{3\mu}{4kTN_0} \left(\frac{N_0}{N} - 1 \right) \tag{4.7}$$

The agglomeration rate of the nanoparticles is directly competing with the rate of amphiphile adsorption. The adsorption of amphiphiles to the NP surface occurs through the same basic mechanism as agglomeration. Assuming that the amphiphiles are spherical in shape, both in solution and in the adsorbed state, the fractional surface coverage of amphiphiles is estimated by [151]:

$$\theta = \frac{n_\mathrm{a}}{4n_\mathrm{p}} \left(\frac{d_\mathrm{s}}{d_\mathrm{p}} \right)^2 \tag{4.8}$$

where n_s and n_p are the number of adsorbed stabilizer molecules and particles per unit volume, and d_s and d_p are the diameters of the stabilizer molecules and the particles. The surface coverage Γ expressed in moles per unit surface area is given by:

$$\Gamma = \frac{n_\mathrm{a}}{N_\mathrm{A} A_\mathrm{p} n_\mathrm{p}} \tag{4.9}$$

where A_p is the surface area of a single particle. By setting $\theta = 1$ and combining Equations 4.8 and 4.9, we find a relation for the maximum surface coverage:

$$\Gamma_\mathrm{m} = \frac{4}{N_\mathrm{A} \pi d_\mathrm{s}^2} \tag{4.10}$$

After some time, the particle surfaces become saturated with adsorbed molecules, which are blocking surface sites and thereby limit the adsorption rate. Taking this saturation effect into account, the fractional surface coverage can be estimated using [152]:

$$\theta(t) = 1 - \exp\left\{ -\frac{c_0 D_\mathrm{s}}{k_\mathrm{a} \Gamma_\mathrm{m}^2} \left[\exp\left(\frac{k_\mathrm{a}^2 \Gamma_\mathrm{m}^2 t}{D_\mathrm{s}} \right) \operatorname{erfc}\left(k_\mathrm{a} \Gamma_\mathrm{m} \sqrt{\frac{t}{D_\mathrm{s}}} \right) + 2 k_\mathrm{a} \Gamma_\mathrm{m} \sqrt{\frac{t}{D_\mathrm{s} \pi}} - 1 \right] \right\} \tag{4.11}$$

where the function $\operatorname{erfc}(x)$ denotes the complementary error function given by $(2/\sqrt{\pi}) \int_x^\infty e^{-t^2} \mathrm{d}t$, c_0 is the initial molar concentration of the amphiphile, k_a is the adsorption rate constant and D_s is the diffusion coefficient of the amphiphile given by the Stokes-Einstein relation:

$$D_\mathrm{s} = \frac{kT}{3\pi\mu d_\mathrm{s}} \tag{4.12}$$

The kinetics of the adsorption process is approximately determined by the slowest step, which is known as the rate-determining step. The kinetics can be either diffusion-controlled (DC), kinetic-controlled (KC) or mixed kinetic-diffusion-controlled (MC) [153]. For purely DC adsorption, the molecular binding of the amphiphile to the particle surface occurs infinitely fast relative to diffusion of the amphiphiles to the particle surface. In other words, the kinetics of the adsorption process is limited by the rate of amphiphile transport and all amphiphile-particle collisions result in successful adsorption of the amphiphile. In the DC limit, $k_\mathrm{a} \to \infty$ and Equation 4.11 converges to [152]:

$$\theta(t) = 1 - e^{-2(c_0/\Gamma_\mathrm{m}) \sqrt{D_\mathrm{s} t / \pi}} \tag{4.13}$$

By rearranging Equation 4.13, the time required to reach a fractional surface coverage θ by diffusion-controlled adsorption is estimated by:

$$t_\mathrm{dc} = \frac{\pi \Gamma_\mathrm{m}^2}{4 D_\mathrm{s} c_0^2} \ln^2 (1 - \theta) \tag{4.14}$$

For KC adsorption, the kinetics is purely determined by limiting kinetic effects at the particle surface. The rate of adsorption is quantified by the adsorption rate constant k_a, which is analogous to the reaction rate constant for chemical reactions. The value of k_a is typically estimated by fitting experimental data of the adsorption process with kinetic models, of which the Lagergren pseudo-first-order model and the Ho pseudo-second-order model are often used in literature [154, 155]. Second-order models tend to form a better fit for chemisorption processes involving covalent or ionic bonds, but their rate constant is a complex function of the initial adsorbate concentration [155]. On the contrary, pseudo-first-order models typically fit well with physisorption processes and can be applied to higher adsorbate concentrations. Except for the concentration of the species involved and the order of the adsorption process, k_a accounts for all factors that affect the adsorption rate in a KC process, including the temperature and the properties of the solvent. In the KC limit, Equation 4.11 reduces to [152]:

$$\theta(t) = 1 - e^{-k_a c_0 t} \tag{4.15}$$

By rearranging Equation 4.15, the time required to reach a surface coverage θ when the adsorption is limited by kinetic effects is estimated by:

$$t_{kc} = \frac{\ln\left[1/(1-\theta)\right]}{k_a c_0} \tag{4.16}$$

In the intermediate MC adsorption regime, kinetic and diffusive effects are competing and the parameter t_{mc} can be estimated through numerical analysis of Equation 4.11.

Now we have a quantitative description of both the rate of nanoparticle agglomeration and the rate of amphiphile adsorption, it is interesting to compare them. The characteristic time t_{ag95} after which 95% of the initial number of NPs has agglomerated—so that the number of agglomerates is only 5% of the initial number of nanoparticles—can be estimated by setting N_0/N equal to $100/5 = 20$ in equations 4.6 and 4.7. The characteristic times t_{dc95}, t_{kc95} and t_{mc95} after which 95% of the NP surfaces are covered with amphiphiles through DC, KC or MC adsorption, respectively, are estimated by setting $\theta = 0.95$ in Equations 4.14, 4.15 and 4.11. It is useful to introduce the dimensionless parameters τ to describe the ratio between the characteristic adsorption and agglomeration times:

$$\tau_{dc} = \frac{t_{dc95}}{t_{ag95}} \propto \frac{N_0}{d_s^3 c_0^2} \tag{4.17}$$

$$\tau_{kc} = \frac{t_{kc95}}{t_{ag95}} \propto \frac{N_0 T}{k_a c_0 \mu} \tag{4.18}$$

$$\tau_{mc} = \frac{t_{mc95}}{t_{ag95}} \tag{4.19}$$

The parameter τ without subscript will be used when the mechanism of adsorption is irrelevant. Evidently, for the successful stabilization of NPs during the phase transfer, the time required for reaching a nearly complete surface coverage of amphiphiles should be well below the time required for nearly all NPs to agglomerate. The parameter τ is thus a measure for the stabilization kinetics: stabilization becomes more effective as $\tau \to 0$.

The analytical method presented in this section is useful to understand how various parameters influence the stabilization process, such as the particle concentration, the the amphiphile concentration, the size of the amphiphiles and the adsorption rate constant. However, it should be noted that the outcome only serves as a simplified, qualitative estimation. In practice, both the agglomeration and the adsorption process depend on a complex balance of interactions between the particles, the amphiphiles and the solvent molecules that does not allow a simple analytical description. The assumptions and approximations that were necessary to derive the above relations leave several important aspects out of consideration, such as the size distribution of the NPs, the chemical composition of the amphiphiles and their interaction with the solvent.

4.5.2. Conformation of copolymers in solution

Polymer molecules in solution continuously change shape due to Brownian motion and typically adopt a coiled shape as a result of their conformational entropy. In the absence of specific intramolecular interactions, the subunits are randomly distributed in a conformation known as a random coil, which can be regarded to be more or less spherical when averaged over all conformations. The instantaneous shape of a random coil, however, more closely resembles an ellipsoid [156, 157]. The size and shape of a polymer chain of a given molecular weight in solution depends on a variety of factors, including steric effects, electrostatic interactions between the subunits and, importantly, the affinity of the subunits with the surrounding solvent [158]. The affinity of a polymer with a solvent—also referred to as the solvent quality—can be described in terms of the Flory Huggins interaction parameter χ. For strictly nonpolar systems, χ can be approximated by [159]:

$$\chi \approx 0.34 + \frac{V_S}{RT}(\delta_P - \delta_S)^2 \tag{4.20}$$

where V_S is the molar volume of the solvent, R is the gas constant and δ_P and δ_S are the Hildebrand solubility parameters of the polymer and the solvent. The critical value of χ, below which no phase separation occurs, depends on the degree of polymerization: typically polymers only dissolve for $\chi \leq 0.5$

and low molecular weight liquids are only miscible for $\chi \leq 2$. In order to ensure high affinity between the polymer and the solvent, a small difference between δ_P and δ_S is a necessary, but not sufficient requirement. In the derivation of Equation 4.20, it is assumed that no polar and hydrogen bonding interactions are present between the substances involved. Even for combinations of polymer and solvent for which $\delta_P \approx \delta_S$, compatibility is only achieved when the polar and hydrogen bonding interactions are approximately equal. For this reason, it is useful to decompose the Hildebrand solubility parameter δ into three vector components known as the Hansen solubility parameters, which are associated with three types of interaction forces [160]:

$$\delta = \sqrt{\delta_d^2 + \delta_p^2 + \delta_h^2} \tag{4.21}$$

where δ_d is the dispersion force component, δ_p is the polar component and δ_h is the hydrogen-bonding component. The Hansen solubility parameter components of many common solvents have been determined experimentally. For substances with unknown solubility parameters, the components can be estimated from the contributions of the structural groups to the total cohesive energy and molar volume of the molecule. Hoftyzer and Van Krevelen [159] developed a method that allows to estimate the solubility parameters of polymers based on their molecular structure with an accuracy of 10%. The fact that the solubility parameters can be predicted from the chemical structure is consistent with the rule of thumb that the compatibility of substances is favored by chemical similarity. Lindvig et al. [161] proposed an extension to the Flory-Huggins model based on the Hansen solubility parameters. According to the authors, the interaction parameter between a polymer and a solvent can be estimated using:

$$\chi = C\frac{V_S}{RT}\left[(\delta_{d,P} - \delta_{d,S})^2 + \frac{(\delta_{p,P} - \delta_{p,S})^2}{4} + \frac{(\delta_{h,P} - \delta_{h,S})^2}{4}\right] \tag{4.22}$$

where the correction constant C has been fitted to experimental data. The optimum value of C was found to be equal to 0.6 for several acrylate and acetate polymers in nonpolar and hydrogen bonding solvents [161]. The value of χ will be used to compute the dimensions of the amphiphilic copolymer chains in solution.

The extent to which a polymer chain in solution expands due to the excluded volume effect can be described by the expansion factor:

$$\alpha_R = \sqrt{R^2}/\sqrt{R_0^2} \tag{4.23}$$

where $\sqrt{R^2}$ denotes the root-mean-square end-to-end distance of the chain and the subscript 0 refers to the ideal or unperturbed chain dimensions, which may be written in terms of the number of segments N and the effective bond length a [162]:

$$\sqrt{R_0^2} = N^{1/2} a \tag{4.24}$$

The effect of the solvent quality on the expansion of the coil is described by the Flory equation [163]:

$$\alpha_R^5 - \alpha_R^3 = 2C_M\left(\frac{1}{2} - \chi\right)M^{1/2} \tag{4.25}$$

where the parameter C_M is given by [163]:

$$C_M = \left(27/2^{5/2}\pi^{3/2}\right)\left(\overline{v}^2/N_A^2 V_0\right)\left(R_0^2/M\right)^{-3/2} \tag{4.26}$$

Here $\overline{v}$ is the polymer partial specific volume, N_A is Avogadro's constant and V_0 is the molecular volume of the solvent. The factor R_0^2/M is characteristic for the type of polymer and thus C_M is independent of the molecular weight [163].

For very large values of z, the asymptotic solution to Equation 4.25 for the expansion factor α_R is given by [164]:

$$\alpha_R^5 = (2\pi/3)^{1/2} z \tag{4.27}$$

with

$$z = \left(4/3^{3/2}\right) C_M\left(\frac{1}{2} - \chi\right)M^{1/2} \tag{4.28}$$

It is important to note that the asymptotic solution is only valid for large values of z—that is, for high molecular weight polymers in exceptionally good solvents. As the polymer approaches the theta state (where $\chi \to 1/2$ and $\alpha_R \to 1$), various expansions of α_R^2 have been proposed that provide a more accurate description of the swelling behavior [164].

Estimation of the expansion coefficients of the amphiphilic copolymers using Equations 4.25 or 4.27 is impossible without the availability of experimental data. It is possible, however, to derive an expression for the proportionality between, on the one hand, the dimensions of the coil $\sqrt{R^2}$ and, on the other hand, the polymer-solvent interaction parameter χ and the molecular weight M. Taking the asymptotic solution for large values of z given by Equation 4.27, the expansion factor is proportional to:

$$\alpha_R \propto \left(\frac{1}{2} - \chi\right)^{1/5} M^{1/10} \tag{4.29}$$

Using Equations 4.23 and 4.24 and assuming furthermore that the number of segments in a chain is directly proportional to its molecular weight, we find:

$$\sqrt{R^2} \propto \left(\frac{1}{2} - \chi\right)^{1/5} M^{3/5} \tag{4.30}$$

It follows that the coil dimensions are only weakly dependent on the solvent quality, whereas the molecular weight has a more pronounced influence.

The theory presented in this section so far is based on statistical mechanics and is especially valid for homopolymers of high molecular weight. For amphiphilic copolymers, the complex interplay of interactions—both between the chemically different subunits and between the subunits and the solvent—often results in the formation of thermodynamically stable structures that do not necessarily resemble random coil conformations. Similar to the way surfactants in selective solvents aggregate to form intermolecular micellar structures, individual amphiphilic copolymer macromolecules assume conformations that can be regarded as intramolecular micelles [165]. The clustering of functional groups in such intramolecular micelles has a pronounced effect on the adsorption kinetics, which will be discussed in the subsequent sections. Their morphology does not only depend on the quality of the solvent and the molecular weight; it is also affected by the fraction, distribution and mutual incompatibility of the chemically different subunits [166–168]. In good solvents, the copolymer chain is swollen and adopts an expanded coil conformation that is typically ellipsoidal. As the solvent quality decreases, the swollen chain contracts and segregated microdomains appear due to the repulsion between the hydrophilic and the hydrophobic groups. These microdomains function as intramolecular micelles, effectively shielding the more solvophobic groups from the solvent. In poor solvents, the microdomains merge to form a large aggregated core and the macromolecule is said to be in a collapsed state. The shape of the core depends on a balance between the interfacial free energy and the core free energy [166, 169]. Clearly, the minimum of the interfacial free energy is attained for a spherical conformation. However, if the functional groups are distributed over the chain, a spherical conformation is generally not possible without the inclusion of both types of moieties in the core. The resulting repulsion between the dissimilar groups causes the free energy of the core to increase. As a result, the minimum of the total free energy generally corresponds to nonspherical shapes of the core that allow better segregation of the dissimilar groups. For amphiphilic copolymers with functional groups distributed over the chain, the core typically approaches an elongated cylindrical shape as the chain length or repulsive interaction between the groups increases [166, 167]. A better understanding of the influence of the solvent quality on the accessibility of the functional groups can be obtained by performing either Monte Carlo or molecular dynamics simulations of the intramolecular self-assembly.

4.5.3. Influence of amphiphile concentration on particle size

Figure 4.2 shows the influence of the amphiphile concentration c_0 on the measured hydrodynamic particle diameter d_h after the phase transfer from ethanol to toluene. In the experiment, 5 vol% of EtOH/YAG:Ce nanodispersion was added to 2mL of toluene with various concentrations of dissolved copolymer at 100°C. The values of d_h clearly decrease with increasing copolymer concentration and initially appear to follow a linear trend when plotted on logarithmic scales. In order to understand the behavior, we are interested to compare the experimental data with the proposed theory on the kinetics of stabilization presented earlier. Recalling from Equations 4.17 and 4.18, the stabilization parameter and the amphiphile concentration are related by:

$$\tau_{dc} \propto c_0^{-2} \tag{4.31}$$

$$\tau_{kc} \propto c_0^{-1} \tag{4.32}$$

Th parameter τ thus follows a power law relation with the amphiphile concentration and the exponent depends on the controlling mechanism of adsorption. A useful feature of power law relations is that they form straight lines when plotted on logarithmic scales, with a slope equal to the exponent of the power law. For DC and KC adsorption the slope is thus equal to:

$$\frac{\Delta \ln(\tau_{dc})}{\Delta \ln(c_0)} = -2 \tag{4.33}$$

$$\frac{\Delta \ln(\tau_{kc})}{\Delta \ln(c_0)} = -1 \tag{4.34}$$

For MC adsorption, the slope converges on both sides to these two limiting values and can be found by numerical analysis of Equation 4.19. The difference in slope between τ_{dc} and τ_{kc} is visualized in Figure 4.3. The details on the computation of τ will be discussed later in this section. The measured values of d_h on logarithmic scales were analyzed by a linear regression model, which showed a good correlation ($R^2 > 0.94$) with the data for all copolymers. This leads to the belief that τ and d_h are indeed related and that the controlling mechanism for adsorption can be identified by comparing their slopes. It would thus be useful to find a direct relationship between d_h and τ. Intuitively, it might seem reasonable τ and d_h are directly proportional. However, the relationship between τ and the particle size is not entirely straightforward. The reason for this is that the kinetics of stabilization is dynamic: the value of τ decreases while the NPs are agglomerating, which effectively impedes further agglomeration. Let us assume that at a sufficiently high amphiphile concentration, the stabilization is effective and d_h is close to the size before the

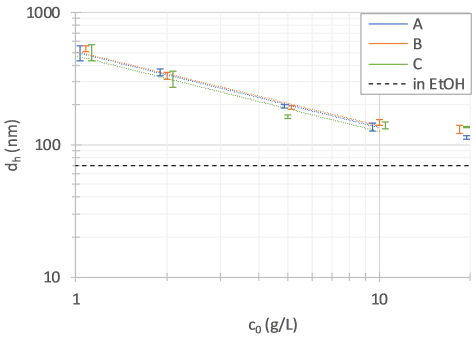

Figure 4.2: Average hydrodynamic diameter of the YAG:Ce particles after phase transfer to toluene versus the concentration of amphiphilic copolymer A (blue), B (orange) or C (green). The dotted line represents the average particle size in EtOH before the phase transfer.

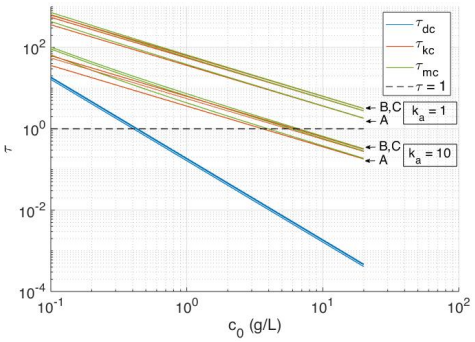

Figure 4.3: Dimensionless stabilization time parameter plotted against the amphiphile concentration for DC (blue), KC (orange) and MC (green) adsorption of copolymers A, B and C with $k_a = 1$ and $k_a = 10$. The dotted line represents the value of $\tau = 1$, where the characteristic agglomeration and adsorption times are equal.

phase transfer. If the amphiphile concentration is now reduced, the particles have a greater chance to collide and agglomerate before they are fully covered with amphiphiles—represented by an increase in τ. The concentration-dependence of τ is stronger for DC adsorption than for KC adsorption, as was shown in Equations 4.33 and 4.34. Regardless of the controlling mechanism, however, τ is directly proportional to the particle concentration N_0. While the particles are agglomerating, the reduction in N_0 thus gradually reduces τ—compensating for the initially higher value of τ due to lowering the amphiphile concentration. In other words, at a certain state of agglomeration, the kinetics of the stabilization process proceeds as if the amphiphile concentration were not reduced. By equating both effects on τ, we can estimate the average increase in particle size that corresponds with a certain reduction in amphiphile concentration. The number of primary particles in an agglomerate and its size are related by a power law relation [170]:

$$N_p = k\left(\frac{R_g}{a}\right)^{D_f} \tag{4.35}$$

where N_p is the number of primary particles in the agglomerate, k is the scaling pre-factor, R_g is the radius of gyration of the agglomerate, a is the radius of the primary particles and D_f is the mass fractal dimension. The fractal dimension quantitatively describes the morphology of agglomerates and can take on values between 1 and 3 for chain-like to compact agglomerates [171]. Monte-Carlo simulations have shown that the value of D_f depends on the primary particle size and the interparticle interaction energy [170]. The fractal dimension increases when the interparticle interaction energy is low, allowing the particles to form more compact structures. The interaction energy is represented by the Hamaker constant and depends mainly on the contrast in dielectric properties between the particles and the surrounding medium [37, 39]. As a result, the interaction energy between metal oxides particles is typically lower in nonpolar liquids. The fractal dimension of the YAG:Ce NPs in toluene is thus expected to be relatively high. D_f has also been shown to decrease with broadening of the primary particle size distribution [172]. Using transmission electron microscope images, Kanniah et al. found that agglomerates of TiO_2 and CeO_2 nanoparticles in ethanol with various average primary particle sizes have D_f values between 1.65–1.82 and 1.62–1.74, respectively [173]. For diffusion-limited agglomeration (i.e., most particle collisions result in adhesion), agglomerates typically have a porous structure with D_f values around 1.75–1.8 [173]. Recognizing that the average number of primary particles in the agglomerates N_p is inversely proportional to the total number of isolated particles in the fluid N_0, it follows that:

$$N_0 \propto R_g^{-D_f} \tag{4.36}$$

Since τ is directly proportional to N_0, the increasing agglomerate size and its reducing effect on τ are related by:

$$d_h \propto \tau^{-1/D_f} \tag{4.37}$$

The relationship between d_h and c_0 is found by equating their opposing effects on τ. Inserting the inverse of Equations 4.31 and 4.32 into Equation 4.37, we find the following relationships depending on the controlling mechanism of adsorption:

$$d_h \propto \left[\left(c_0^{-2}\right)^{-1}\right]^{-1/D_f} \propto c_0^{-2/D_f} \quad \text{for DC} \tag{4.38}$$

$$d_h \propto \left[\left(c_0^{-1}\right)^{-1}\right]^{-1/D_f} \propto c_0^{-1/D_f} \quad \text{for KC} \tag{4.39}$$

The exponents correspond to the slopes of straight lines if d_h is plotted against c_0 on logarithmic scales.

The slope of d_h versus c_0 is thus simply approximated by the slope of τ divided by the fractal dimension:

$$\frac{\Delta \ln(d_h)}{\Delta \ln(c_0)} = \frac{1}{D_f} \frac{\Delta \ln(\tau)}{\Delta \ln(c_0)} \tag{4.40}$$

Assuming that D_f is approximately equal to 1.8, the predicted slopes are equal to:

$$\frac{\Delta \ln(d_h)}{\Delta \ln(c_0)} = -\frac{2}{D_f} \approx -1.11 \quad \text{for DC} \tag{4.41}$$

$$\frac{\Delta \ln(d_h)}{\Delta \ln(c_0)} = -\frac{1}{D_f} \approx -0.56 \quad \text{for KC} \tag{4.42}$$

Table 4.2 lists the slopes of the regression lines plotted in Figure 4.2, which have been fitted to the measured values of d_h for copolymer concentrations between 1 and 10 gL^{-1}. The slopes can be compared to the estimated range of exponents to identify the controlling mechanism of adsorption. In the studied system, the slopes of the regression lines are close to the estimated KC adsorption limit. This indicates that the adsorption process is severely limited by kinetic effects during the binding step. Apparently, the probability of adsorption of the copolymers upon collision with a NP surface in toluene is low.

Copolymer	$\frac{\Delta \ln(d_h)}{\Delta \ln(c_0)}$	R^2
A	-0.57	0.979
B	-0.56	0.983
C	-0.57	0.942

Table 4.2: Slope and coefficient of determination of the regression lines of the measured hydrodynamic diameters versus the copolymer concentration on logarithmic scales.

For copolymer concentrations higher than 10 gL^{-1}, the observed slopes flatten and the goodness of fit of the regression line decreases. It is well known that the controlling mechanism of adsorption shifts towards KC adsorption with increasing concentration [174]. One would thus expect the slope for all copolymers to shift towards the KC limit until the initial particle size is obtained. In reality, increasing the concentration becomes progressively less effective, until the particle size is no longer significantly affected and at some point even starts to increase. The beneficial effect of increasing the amphiphile concentration is thus limited to a certain functional concentration range. This effect can be explained by the appearance of intermolecular interactions between the copolymer molecules as their coils start to overlap. Expanded polymer molecules in solution start to contract as the concentration increases due to the overlapping of neighboring coils. The coils approach their ideal dimensions at volume fractions as low as 0.05–0.20 [175]. Not surprisingly, the overlapping of coils already starts to occur at even lower volume fractions. Based on an estimation of the molar volume of the studied copolymers, a concentration of 20 gL^{-1} roughly corresponds to a volume fraction of 0.02. Overlapping of coils is thus likely to occur in the studied concentration range. Presumably, this results in intermolecular structures that hamper the mobility of the individual molecules and reduce the accessibility of the MPEOMA groups to the NP surface.

Overall, there appears to be little difference in the behavior of the three copolymers. If anything, there is a slight variation in their slope over the studied concentration range. The slope at low concentrations initially appears to be slightly steeper for the copolymers with higher MPEOMA fractions. This might indicate that there is a slight increase in the adsorption rate constant k_a with increasing MPEOMA fraction. It is conceivable that the presence of more MPEOMA groups in the copolymers increases the probability of binding upon collision with a NP surface. This is represented by a higher k_a, which reduces the kinetic limitations and slightly steepens the slope. This theory is further supported by the fact that at high copolymer concentrations, the slope flattens more rapidly for copolymers with larger MPEOMA fractions. It is energetically favorable for the hydrophilic MPEOMA groups on neighboring copolymer molecules to stick together as their coils start to overlap. It is therefore likely that the intermolecular interactions are stronger for copolymers containing more MPEOMA groups, causing less effective stabilization as the concentration increases.

In order to estimate k_a of the copolymers, we need to relate the measured slope of d_h to the slope of τ_{mc} as a function of k_a. The slope of τ_{mc} on logarithmic scales is computed by numerical analysis using:

$$\frac{\Delta \ln(\tau_{mc})}{\Delta \ln(c_0)} = \frac{\ln\left(\frac{\tau_{mc,(c_0+\Delta c_0)}}{\tau_{mc,c_0}}\right)}{\ln\left(\frac{c_0+\Delta c_0}{c_0}\right)} \tag{4.43}$$

Recalling from Equation 4.40 that the slopes of τ and d_h are related through the fractal dimension, the predicted slope of d_h is then approximated by:

$$\frac{\Delta \ln(d_h)}{\Delta \ln(c_0)} = \frac{1}{D_f} \frac{\ln\left(\frac{\tau_{mc,(c_0+\Delta c_0)}}{\tau_{mc,c_0}}\right)}{\ln\left(\frac{c_0+\Delta c_0}{c_0}\right)} \tag{4.44}$$

Figure 4.4 shows the predicted values of the slope of d_h as a function of the adsorption rate constant k_a for the range of copolymer concentrations that was fitted by the linear regression. As expected, the controlling mechanism of adsorption gradually shifts from KC to DC with increasing k_a. By comparing the experimentally obtained slopes to the slopes predicted by numerical analysis, it is possible to obtain an order-of-magnitude estimate of the k_a values in the studied system. The dotted line in Figure 4.4 represents

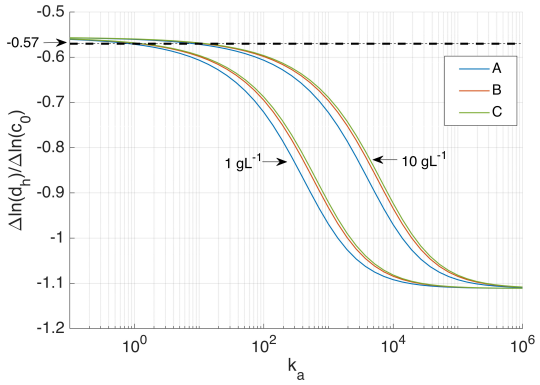

Figure 4.4: Estimated slope of $\ln(d_h)$ as a function of $\ln(c_0)$ for MC adsorption computed by Equation 4.44 plotted against the adsorption rate constant k_a for amphiphilic copolymer A (blue), B (orange) or C (green) with $c_0 = 1$ and 10 gL^{-1}. The parameters used in the simulation are $D_f = 1.8$, T=100°C and ϕ_{EtOH}=5 vol%.

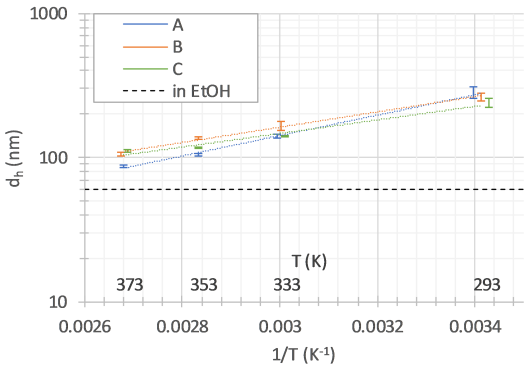

Figure 4.5: Average hydrodynamic diameter of the YAG:Ce particles after phase transfer to toluene versus the reciprocal temperature of the nonpolar phase with amphiphilic copolymer A (blue), B (orange) or C (green). The dotted line represents the average particle size in EtOH before the phase transfer.

a slope of −0.57. For all copolymers, the values of k_a are estimated to be close to $10^0 - 10^1$ $m^3\,mol^{-1}\,s^{-1}$. It should be stressed that this estimation method depends strongly on the fitting of the experimental data as well as on the fractal dimension, which has not been determined experimentally for the studied system. Therefore, the estimates of k_a should be considered as no more than an educated guess. The numerical results predict that the value of k_a increases linearly with c_0 when the slope is constant. However, by definition, k_a should not depend on c_0 in the absence of any intermolecular interactions. Instead, the concentration affects the controlling mechanism of adsorption and thereby the slope of the regression line. Since increasing c_0 gradually shifts the controlling mechanism towards KC adsorption, the slope of the regression line should in fact flatten with increasing c_0. As a result, the slope at a copolymer concentration of 10 gL^{-1} should be less steep than the slope at 1 gL^{-1}—even without the effect of coil overlapping. By taking this difference in slope into account, the estimated values of k_a at different concentrations become closer to the middle of the estimation range. Therefore, more accurate estimates of k_a could be obtained by considering the shift in controlling mechanism with concentration. This requires the experimentally obtained slope to be accurately determined in a narrow concentration range.

Figure 4.3 shows the computed parameters τ_{dc}, τ_{kc} and τ_{mc} for the copolymers as a function of the copolymer concentration. The dimensions of the copolymer molecules in solution were scaled to the experimentally obtained size of similar amphiphilic copolymers by Stelzig et al. [127]. The scaling takes into account the proportionality relations for the molecular weight and the solvent quality, as given by Equation 4.30. Interestingly, there is not much difference between the values of τ_{dc} computed for the different copolymers. Although the copolymers differ in molecular weight and thus in dimensions, the effect of molecular size is largely compensated by the difference in molar concentration. The model predicts that the point $\tau_{dc} = 1$, at which DC adsorption becomes faster than agglomeration, is reached at a concentration around 0.4 gL^{-1}. If the system were governed by DC adsorption, successful stabilization of the NPs would be expected not far from this concentration. Nevertheless, none of the studied copolymers was able to preserve the initial NP size during the phase transfer process over the entire studied concentration range. Clearly, the behavior of this system is not well described by DC adsorption kinetics. This observation is consistent with the observed slopes of the regression lines, which implied that the adsorption is limited by kinetic effects. That is to say, the adsorption rate constants k_a for this system are simply too low to fully prevent agglomeration of the NPs within the functional concentration range.

In order to illustrate the limitations of kinetic effects, the computed parameters τ_{kc} and τ_{mc} are also plotted in Figure 4.3 using k_a values in the estimated range of $k_a = 1$ to $k_a = 10$ for all three copolymers. Although the kinetic constants only serve as rough estimates, some interesting characteristics can be discerned from the simulation results. It is evident that increasing the value of k_a reduces the kinetic limitations and thereby decreases τ_{kc}. Since the adsorption process is close to the KC limit, the values of τ_{mc} and τ_{kc} are nearly identical. The estimated range of k_a values seem to describe the observed behavior reasonably well, indicating a value of $\tau = 1$ around the higher end of the studied concentration range. Moreover, it should be noted that the slope of τ_{dc} is twice as steep. While a DC process would reach the

point of ten times faster adsorption than agglomeration around 1 gL^{-1}, this point is never reached for KC adsorption over the entire studied concentration range.

The kinetics of stabilization is always limited by the slowest step in the adsorption process. Even when the binding step occurs infinitely fast, the rate of adsorption can never be faster than the rate of diffusion of the copolymer molecules to the surface. Therefore, as k_a increases and τ_{kc} approaches τ_{dc}, the controlling mechanism of adsorption shifts towards DC adsorption, as evidenced by the changing slope of τ_{mc}. When the concentration is increased, the negative slope of τ_{mc} decreases until it approaches the KC adsorption limit. The concentration at which the the change in slope starts to occur depends on the value of k_a; the change in slope is more pronounced when τ_{kc} is close to τ_{dc}. In order to successfully stabilize the NPs during the phase transfer, the k_a value of the system needs to be improved. Both the temperature and the composition of the solvent were found to play a key role in the kinetic effects.

4.5.4. Influence of temperature on particle size

The temperature at which the phase transfer takes place influences the stabilization kinetics in multiple ways. It directly affects Brownian motion—both of the NPs and the copolymer molecules—through the diffusion constant. Increasing the temperature also lowers the dynamic viscosity of the fluid, which in turn further enhances diffusion. However, if the agglomeration and adsorption process are both governed by diffusion, the temperature would affect both processes more or less equally. In practice, elevating the temperature was found to significantly increase the efficiency of stabilization, as shown in Figure 4.5. It should be noted that the values of d_h in this figure are plotted against reciprocal temperature. In the experiment, 5 vol% of EtOH/YAG:Ce nanodispersion was added to a toluene phase containing 20 gL^{-1} of dissolved copolymer at various temperatures. Clearly, the adsorption process is limited by kinetic effects, which are directly influenced by the temperature. The value of k_a is related to the temperature via an empirical relationship known as the Arrhenius equation:

$$k_a = Ae^{-\frac{E_a}{RT}} \tag{4.45}$$

where A is the pre-exponential factor related to the number of the collisions, R is the gas constant, T is the temperature and E_a is the activation energy. The activation energy represents the energy barrier to adsorption, which can be imposed by chemical, physical and structural interactions [176]. Since the adsorption of nonionic binding groups does not involve an energy barrier due to a chemical reaction or electrostatic repulsion, E_a is the minimum energy required for overcoming any steric effects in order to adsorb. The factor $e^{-E_A/(RT)}$ varies between zero and unity and describes the proportion of all collisions having sufficient energy to overcome the energy barrier—or the probability of adsorption upon collision, if you will. As the temperature increases, the amphiphiles posses more kinetic energy to overcome the adsorption barrier and the value of k_a increases exponentially.

The values of E_a and A are typically determined by plotting the natural logarithm of k_a versus reciprocal temperature, after values of k_a at different temperatures have been obtained experimentally. This is convenient because exponential functions form straight lines on a semi-log plot with a logarithmic scale on the y-axis and a linear scale on the x-axis. Taking the natural logarithm of Equation 4.45, we obtain:

$$\ln(k_a) = -\frac{E_a}{R}\left(\frac{1}{T}\right) + \ln(A) \tag{4.46}$$

where $-E_a/R$ is simply the slope of a straight line when $\ln(k_a)$ is plotted against reciprocal temperature. In other words, the slope is determined by:

$$\frac{\Delta \ln(k_a)}{\Delta\left(T^{-1}\right)} = -\frac{E_a}{R} \tag{4.47}$$

Even without experimental data on k_a, however, it is still possible to obtain estimates of E_a from the measured values of d_h. It follows from Equation 4.46 that the temperature-dependence of k_a depends on E_a: the higher the value of E_a, the steeper the slope. This temperature-dependence can be used to estimate the E_a values of the copolymers. Let us first assume that E_a does not depend on the temperature. In Section 4.5.3 it was concluded that the adsorption rate of all three copolymers in toluene is mainly governed by kinetic effects—even at temperatures as high as 100°C. Combining Equations 4.18 and 4.45, we find that τ_{kc} is related to T by:

$$\tau_{kc} \propto T k_a^{-1} \propto T A^{-1} e^{\frac{E_a}{RT}} \tag{4.48}$$

Since T occurs in the exponent, the influence of T on τ_{kc} is in most practical cases dominated by the exponential term. Similar to Equation 4.47, the slope of $\ln(\tau_{kc})$ plotted against T^{-1} between two temperatures T and $T+\Delta T$ is determined by:

$$\frac{\Delta \ln(\tau_{kc})}{\Delta\left(T^{-1}\right)} = \frac{\ln\left(\frac{\tau_{kc,T+\Delta T}}{\tau_{kc,T}}\right)}{\frac{1}{T+\Delta T} - \frac{1}{T}} = \frac{\ln\left(\frac{T+\Delta T}{T}\right) - \frac{E_a \Delta T}{RT(T+\Delta T)}}{\frac{1}{T+\Delta T} - \frac{1}{T}} \tag{4.49}$$

By computing the slope on a semi-log plot, the pre-exponential factor A is factored out of the equation and the slope of τ_{kc} is only a function of the temperature and the activation energy. If we can now

find a relationship between τ_{kc} and d_h, the slope of the measured d_h values can be directly related to E_a for the given system. We know that lowering the temperature increases τ_{kc} and causes the particles to agglomerate. The process of agglomeration—associated with a declining particle concentration N_0—in turn benefits the stabilization kinetics by decreasing τ_{kc}. The relation between T and d_h can be found by equating their opposing effect on τ_{kc}. Recalling the proposed effect of d_h on τ from Equation 4.37 and inserting the opposing effect of T on τ_{kc} gives:

$$d_h \propto \left[(\tau_{kc})^{-1}\right]^{-1/D_f} \propto \tau_{kc}^{1/D_f} \tag{4.50}$$

The slope of $\ln(d_h)$ plotted against T^{-1} can thus simply be estimated by:

$$\frac{\Delta \ln(d_h)}{\Delta\left(T^{-1}\right)} = \frac{\Delta \ln\left(\tau_{kc}^{1/D_f}\right)}{\Delta\left(T^{-1}\right)} = \frac{1}{D_f}\frac{\Delta \ln(\tau_{kc})}{\Delta\left(T^{-1}\right)} \tag{4.51}$$

The experimentally obtained slopes of d_h plotted against T^{-1} on a semi-logarithmic scale are listed in Table 4.3. Equating the experimentally obtained slopes to Equation 4.51 and solving numerically for E_a yields the estimated values of the activation energies, which are listed in the same table. The lower and upper bounds of E_a correspond to the numerical results for $T = 293$K and $T = 373$K, respectively.

Copolymer	$\frac{\Delta \ln(d_h)}{\Delta(T^{-1})}$	R^2	Estimated E_a $\left(\mathrm{kJ\,mol^{-1}}\right)$
A	1629.1	0.988	28.2 – 28.8
B	1222.5	0.978	21.7 – 22.4
C	1082.4	0.959	19.5 – 20.2

Table 4.3: Slope and coefficient of determination of the regression lines of the measured hydrodynamic diameters versus the reciprocal temperature on a semi-logarithmic scale. The activation energy E_a is estimated from the slope using Equation 4.51.

The slight difference between the upper and lower bounds of E_a originates from a predicted decrease of the slope with increasing temperature. While the slope of $\ln(k_a)$ versus T^{-1} is constant, the additional term T in Equation 4.48 introduces a slight linear decrease of the slope. More precise estimates of E_a can therefore be obtained by accurately determining the slope between small temperature increments.

Some interesting conclusions can be drawn from the estimated activation energies. Although the activation energies are significant, they appear to correspond with those typically associated with physisorption [177]. This means that the MPEOMA groups indeed most likely bind to the hydroxylated particle surfaces through noncovalent interactions. Moreover, the E_a values clearly decrease with increasing MPEOMA fraction. This observation gives a valuable insight on the nature of the energy barrier to adsorption. Since the studied copolymers are nonionic and adsorption does not require any covalent bonds to be broken, it is suggested that E_a is mainly related to steric shielding of the MPEOMA binding groups. The steric shielding is a result of the way amphiphilic copolymer chains fold in solution. The positions that the subunits assume inside the coil depends on their interaction with the solvent, as well as on the fraction, distribution and incompatibility of the chemically distinct subunits [166–168]. If the interaction of the hydrophilic MPEOMA groups with the solvent and the EHMA groups is poor, they concentrate in clusters, surrounded by an envelope of hydrophobic EHMA moieties that shield them from the solvent—and from a nearby NP surface. The steric shielding of the binding groups poses a structural barrier to the adsorption process. Chiad et al. [73] found that even moderate steric shielding of hydrogen-bonding PEO groups leads to a dramatic decrease in interaction with a NP surface. This means that the interaction of the copolymers with the NP surface is directly influenced by the affinity of the subunits groups with the solvent. Since the nonpolar EHMA groups have more affinity with toluene than the hydrophilic MPEOMA groups, a shell of EHMA groups sterically shields the binding groups from the adsorption sites on the NP surface. It is easy to imagine that increasing the MPEOMA to EHMA ratio allows more binding groups to assume positions close to the outer shell, thereby reducing the effect of steric shielding. As a result, copolymer molecules with higher MPEOMA fractions are expected to have lower activation energies.

In the derivation presented above, it was assumed that E_a is independent of the temperature. However, the temperature affects the conformation of the copolymers through the interaction parameter χ, as was shown in Equation 4.22. It is important to note that increasing the temperature simultaneously influences all intramolecular interactions, as well as the interactions of the subunits with the solvent. In fact, the Hansen solubility parameters themselves are also temperature-dependent quantities. Their temperature-dependence varies for different substances and is related to the coefficient of thermal expansion [178]. Changing the temperature thus causes the conformation of the copolymer molecules to change in a rather complex manner. Overall, it is likely that increasing the temperature benefits the compatibility between the distinct subunits and between the subunits and the solvent. This results in less steric shielding of the binding groups as the temperature increases, ans thus a decrease in the activation energy. The decreasing value of E_a results in an overestimation of the effect of the temperature on k_a and thus in overestimated values of E_a.

While the influence of the temperature on all the relevant interaction parameters χ in the system can be estimated, the exact relation between these χ parameters and E_a is unknown. Nonetheless, as the effect of increasing temperature is present for all copolymers in the experiment, the observed relative difference in activation energy is still expected to hold.

A more detailed understanding of the adsorption process of the copolymers can be obtained by analyzing the thermodynamic profile of the interactions. In order for the amphiphiles to spontaneously adsorb onto the NP surface, the change in the Gibbs free energy ΔG has to be negative. The free energy change is a function of the change in enthalpy and entropy, as described by the Gibbs-Helmholtz equation:

$$\Delta G = \Delta H - T\Delta S \tag{4.52}$$

The change in enthalpy ΔH is related to the strength of the noncovalent interactions of the amphiphiles with the surface compared to the those with the solvent. The entropy term ΔS reflects the changes in the solvation entropy and the conformational entropy of the amphiphiles. Chiad et al. [73] determined the thermodynamic profile of the interaction of several amphiphilic statistical copolymers as well as their monomers with the surface of SiO_2 NPs using isothermal titration calorimetry (ITC). The PEHMA-stat-PPEOMA copolymers that were studied by the authors are nearly identical to the copolymers used in this study (cf. PEHMA-stat-PMPEOMA) and are thus expected to behave in a similar fashion. The authors found that PEOMA monomers and PEHMA-stat-PPEOMA copolymers both showed a dominant negative ΔH, indicating that the adsorption process is exothermic and governed by physisorption. The energetic gain due to the interaction with the surface is balanced by an entropic loss as the molecules bind to the surface. In both cases ΔS was found to be negative, caused by a loss in translational and conformational freedom of the adsorbed molecules. However, in the case of the amphiphilic copolymers the negative ΔS is almost completely compensated, resulting in a much higher adsorption strength. This means that high molecular weight amphiphilic copolymers bear a large entropic advantage over low molecular weight amphiphiles. Still, as a result of the entropically unfavorable interaction, ΔG increases with an increase in temperature—ultimately leading to the point at which adsorption is unfavorable [179]. The beneficial effect of increasing the temperature on the adsorption kinetics is thus restricted to a functional temperature range. This range is larger for high molecular weight amphiphiles, which have a less pronounced negative entropy. Still, the beneficial effect of increasing the temperature is limited to the boiling point of the substances involved—in this case toluene which has a boiling point around 110°C.

Even while heating the toluene phase up to 100°C increases the k_a value of the system, the effect is not enough to prevent agglomeration of the nanoparticles. In order to increase k_a even more and push the adsorption kinetics towards a DC process, the activation energy needs to be reduced. Earlier in this section it was proposed that E_a is related to steric shielding of the MPEOMA binding groups, caused by the unfavorable interactions with both the solvent and their EHMA counterparts. This suggests that E_a can be reduced by adjusting the solvent composition in a way that increases the solvent quality for the MPEOMA groups.

4.5.5. Influence of solvent composition on particle size

In order to increase the solvent quality for the polar MPEOMA groups and possibly reduce the effect of steric shielding, the polarity of the solvent was increased by the addition of ethanol. In the experiment, 5 vol% of the EtOH/YAG:Ce nanodispersion was added to solvent mixtures of toluene with different volume fractions of EtOH, all containing a fixed amphiphile concentration of 20 gL^{-1} and heated to a temperature of 80°C. Figure 4.6 shows that the measured hydrodynamic diameter decreases rapidly as the volume fraction of EtOH of in the solvent system increases from 5 to 20 vol%, after which the particle size remains more or less constant.

It is suggested that the observed decreasing trend results from a conformational change of the copolymer molecules related to the composition of the solvent mixture. In general, two distinct conformational changes are likely to play a role in the adsorption kinetics: swelling of the macromolecules and intramolecular self-assembly. The size of the macromolecules in solution mainly affects the kinetics of DC adsorption, as was shown in Equation 4.17. Intramolecular self-assembly results from the segregation of chemically different subunits and affects the energy barrier to adsorption, which is important for KC adsorption. The influence of the solvent composition on both conformational changes can be described in terms of the interaction parameter χ with the solvent.

Figure 4.7 shows the values of χ computed using Equation 4.22 for the copolymers as well as for the MPEOMA functional groups as a function of the volume fraction of EtOH in the solvent mixture at 80°C. In a nonpolar medium such as toluene, it is energetically favorable for the polar MPEOMA moieties to minimize their interaction with the solvent. This is supported by the relatively large value of χ for MPEOMA groups in pure toluene, as shown in Figure 4.7. Not surprisingly, copolymer A—containing the

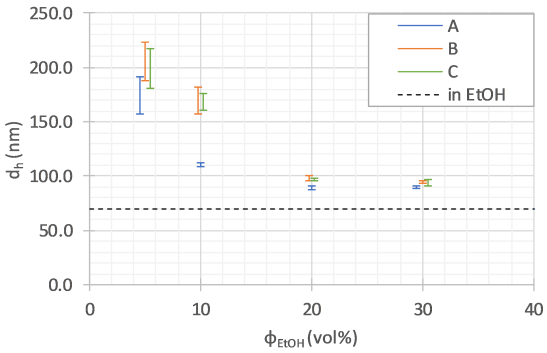

Figure 4.6: Average hydrodynamic diameter of the YAG:Ce particles after the phase tranfer to toluene versus the volume fraction of EtOH in the nonpolar phase with amphiphilic copolymer A (blue), B (orange) or C (green). The dotted line represents the average particle size in EtOH before the phase transfer.

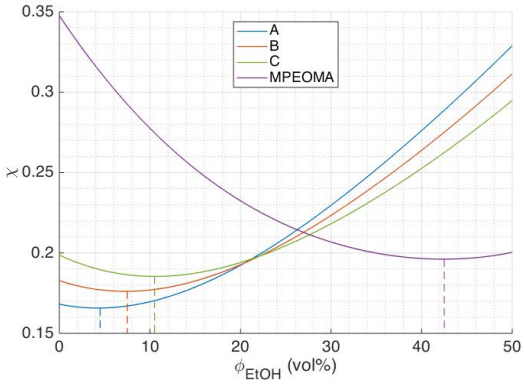

Figure 4.7: Interaction parameters between the solvent and copolymer A (blue), B (orange), C (green) and the MPEOMA monomer (purple) versus the volume fraction of EtOH in the nonpolar phase.

lowest fraction of MPEOMA units—has a higher affinity with the solvent in pure toluene than copolymer B and C. This trend is gradually reversed by increasing the EtOH fraction, which increases the polarity of the solvent mixture.

The degree of swelling of polymers in solution is related to the affinity of the macromolecules with the solvent, as was shown in Equation 4.30. The ideal solvent composition for all three copolymers lies in the region around approximately 5–10 vol% EtOH. Maximum swelling of the macromolecules is thus expected in this range. If the adsorption kinetics were governed by diffusion, the most efficient transfer of NPs would be observed around the ideal solvent compositions. On the contrary, agglomeration is mainly observed at EtOH volume fractions lower than 20 vol%. Clearly, the degree of swelling of the copolymer coils is not an important parameter for the adsorption kinetics in the system under consideration. Consistent with earlier observations, this means the adsorption kinetics in toluene is not controlled by diffusion, but limited by kinetic effects. On the other hand, the correlation between the interaction parameter χ of the MPEOMA groups and d_h is striking. Comparing Figure 4.6 and 4.7, both are observed to decrease rapidly as the EtOH fraction is increased until they reach a broad minimum. It thus seems that the limiting kinetic effects (i.e., steric shielding of the binding groups) are strongly influenced by the affinity of the binding groups with the solvent.

Protic solvents such as EtOH have a pronounced effect on the coil conformation of PEO-containing polymers, because they can participate in hydrogen bonding [180]. It is suggested that the formation of hydrogen bonds with EtOH molecules in the solvent mixture reduces the hydrophilic attraction between the MPEOMA groups. As a result, the confinement of MPEOMA groups to hydrophilic clusters inside the coil becomes energetically less favorable as the EtOH fraction increases. This allows more freedom for the MPEOMA groups to assume positions in the envelope of the coil, thereby increasing their accessibility to binding sites on the NP surface. In other words, improving the solvent quality for the binding groups increases the kinetic rate constant k_a by lowering the activation energy for adsorption E_a. As was shown in Section 4.5.3, an increase in k_a significantly increases the adsorption kinetics of KC processes. From Equation 4.22, we know that χ follows a power law relation centered around the solvent composition associated with the smallest difference in Hansen solubility parameters. It is therefore suggested that the optimal solvent composition for similar NP phase transfer process is easily determined by minimizing the difference between the solubility parameters of the binding groups and the solvent mixture.

For solvent mixtures containing 30 vol% EtOH, the NPs could be transferred without any noticeable agglomeration by adjusting the amphiphile concentration. The average particle size was observed to further decrease from ~90 nm to ~70 nm by decreasing c_0 from 20 gL^{-1} to 1 gL^{-1}. As was suggested section 4.5.3, this effect might be attributed to intermolecular interactions arising from the overlapping of coils as the concentration increases. The fact that such intermolecular interactions are present at lower copolymer concentrations for solvent mixtures containing higher EtOH fractions agrees with the proposed theoretical explanation on intermolecular self-assembly of the macromolecules. Due to the interaction with EtOH molecules, the MPEOMA groups become free to assume positions in the outer shell of the coils. At the same time, this increases their interaction with MPEOMA groups on neighboring coils

once they start to overlap. It is therefore expected that the effect intermolecular interactions is more pronounced at lower copolymer concentrations when the EtOH fraction is high. Successful transfer of NPs without any increase in particle size was observed for c_0 as low as 0.5 gL^{-1}, below which rapid agglomeration was observed. The minimum concentration is close to the predicted concentration of 1 gL^{-1} for $\tau_{dc} = 1$ with $\phi_{EtOH} = 30$ vol%. Note that this concentration is slightly higher than the predicted concentration for $\tau_{dc} = 1$ in Figure 4.2, because the contraction of the copolymer chains at high EtOH fractions negatively affects the kinetics of DC adsorption. The close agreement with the model for DC adsorption supports the theory that increasing the solvent quality for the binding groups increases the kinetic rate constant k_a and thereby shifts the controlling mechanism for adsorption from KC to DC.

4.5.6. Fabrication of nanocomposite thin films

In order to study the dispersion and stability of the particles in a polymer matrix, nanocomposite thin films were prepared by spin coating. After phase transfer of the particles using copolymer concentrations of 20 gL^{-1}, the toluene/YAG:Ce nanodispersions were mixed with various transparent polymers dissolved in toluene. Solutions containing 10 wt% polymer were spin coated on 25 mm^2 microscope slides to form polymer nanocomposite films with a thickness of $1-2$ µm. The nanocomposite films were imaged by scanning electron microscopy (SEM) to analyze the size and distribution of the particles. The three different polymers were tested for the preparation of nanocomposite films: cyclic olefin copolymer (COC, also known by the brand name TOPAS), poly(methyl methacrylate) (PMMA) and poly(2-ethylhexyl methacrylate) (PEHMA).

TOPAS is a highly transparent amorphous polymer produced by copolymerization of cyclic monomers such as norbornene with ethylene. Due to is excellent optical properties and high glass transition temperature it is often used for the fabrication of optical components. Mixing of the toluene/YAG:Ce nanodispersion with polymer solutions of TOPAS resulted in phase separated liquids, as is shown in Figure 4.8a. Evidently, the chemical compatibility between TOPAS and the PEHMA-stat-PMPEOMA copolymers is too low to obtain a homogeneous solution.

The amphiphilic copolymers were expected to be more compatible with methacrylic polymers such as PMMA—also known as acrylic glass due to its similar refractive index and high optical transmittance. Indeed, seemingly homogeneous solutions were obtained after mixing the toluene/YAG:Ce nanodispersions with PMMA, as shown in Figure 4.8b. However, spin coating of the solutions resulted in turbid films with haze values up to 12% (see Figures 4.8d and 4.8e). White light interferometry measurements revealed the PMMA nanocomposite films had moonlike surfaces with craters up to 1 µm deep. The Rq surface roughness was measured to be significantly higher than reference films of pure PMMA. The observations may be explained by the apparent incompatibility between PEHMA and PMMA. While PMMA is to some extent plasticized by the rubbery PEHMA, the two phases are essentially immiscible [181]. Both the high surface roughness and the presence of boundaries between the separate phases promote diffuse scattering of the incoming light, leading to hazy films. The haze was observed to be lower in a central area of the films, growing in size for copolymers with higher MPEOMA fractions. In the center, haze values of less than 2% were measured for copolymers B and C. The lower haze in the center suggests that the phase separation is to some extent suppressed by a fast transition to the glassy state during spin coating, comparable to a quenching process. Moreover, growing of the low-haze region with increasing MPEOMA fraction in the copolymer indicates that the presence of MPEOMA favors the miscibility between between the two phases. It should be noted that the amphiphilic copolymer content in the nanocomposites was quite high (~13.3 wt%) and significantly better results might be obtained when lower concentrations are used.

Mixing the toluene/YAG:Ce nanodispersions with PEHMA, which is identical to the nonpolar part of the amphiphilic copolymers, resulted in homogeneous solutions (Figure 4.8c) and fully transparent nanocomposite films (Figure 4.8f). The haze of all three copolymer samples was measured to be well below 1%, similar to spin coated reference samples of both pure PEHMA and PEHMA with copolymer but without NPs. It should be noted that the NP concentration in the measured films is low (~0.1 wt%) and higher haze values might be observed when the particle content is increased. In all cases, the Rq surface roughness was measured to be significantly higher than those of reference samples. The inclusion of particles thus appears to affect the morphology of the thin films. Since the interferometer has a sub-nanometer vertical resolution and is able to distinguish features with lateral dimensions down to 200 nm, it is conceivable that the measured increase in Rq results from particles protruding from the film.

The particles in the nanocomposite films are clearly visible as bright spots in SEM images and appeared to be homogeneously distributed in the PEHMA matrices (Figures 4.9a, 4.9b and 4.9c). The bright spots were not present in the reference sample consisting of pure PEHMA (Figure 4.9d). Energy-

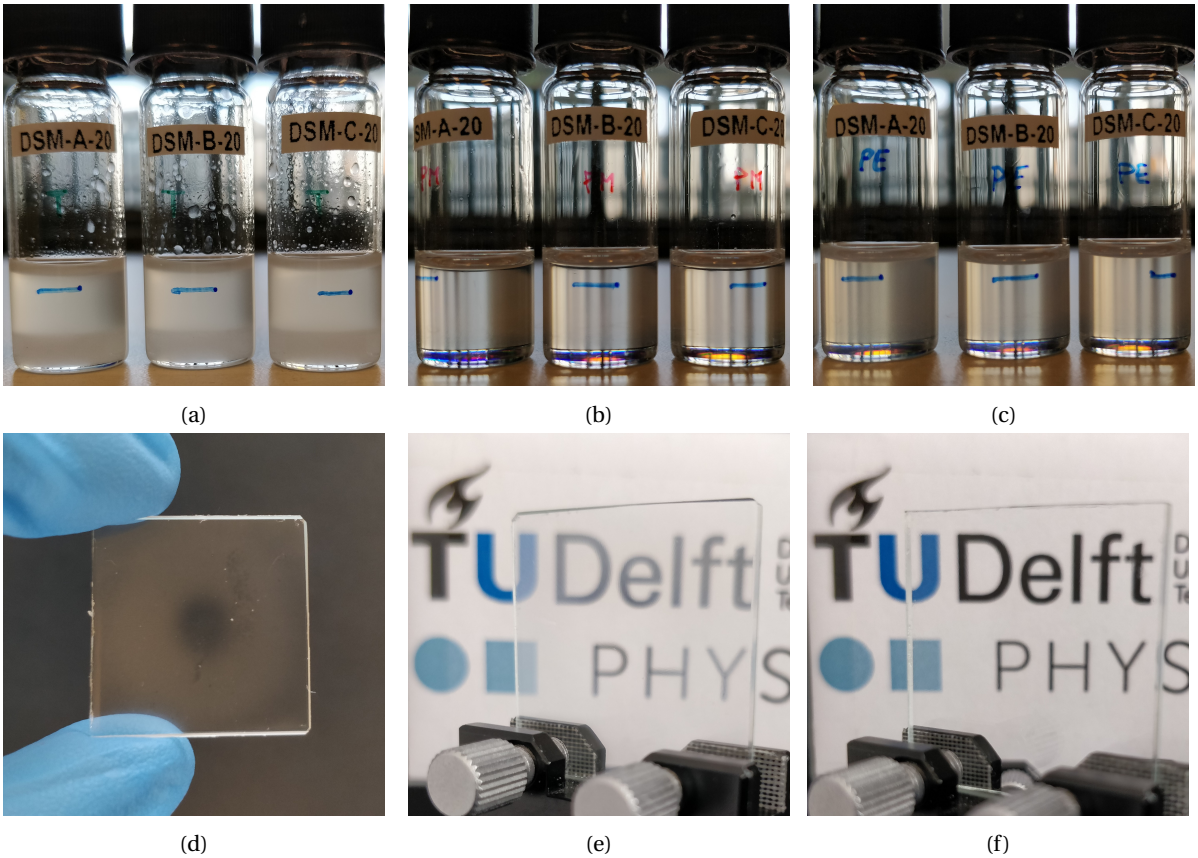

(a) (b) (c)

(d) (e) (f)

Figure 4.8: Toluene/YAG:Ce(A/B/C) nanodispersions mixed with 30 wt% solutions of (a) COC, (b) PMMA and (c) PEHMA in toluene. (d) PMMA/YAG:Ce(A) film showing the typical clear center and a hazy corona. (d) PMMA/YAG:Ce(A) films appear turbid, while (e) PEHMA/YAG:Ce(A) films are very clear.

dispersive X-ray spectroscopy (EDS) measurements identified the presence of yttrium and aluminum in the bright spots, thereby confirming that the visualized spots are indeed YAG:Ce particles. The particles appeared to be mainly rodlike in shape with dimensions ranging from about 50 to 250 nm. No significant difference in particle size was observed between the three different copolymer samples. The dimensions correspond well with the particle size distributions measured by DLS before mixing with the polymer (Figure 4.10). We can therefore conclude that no significant agglomeration occurred during the fabrication of the nanocomposite films.

Surface treatment of the nanocomposite films with oxygen plasma prior to SEM imaging was found to facilitate the detection of the particles. This was especially true for EDS, which was unable to detect any aluminum or yttrium content without prior surface treatment. The oxygen plasma is able to break organic bonds and etches away a small layer of PEHMA from the top of the film, leaving the particles exposed. A part of the surface of the nanocomposites with copolymer A, B and C was treated for 1, 2 and 3 minutes, respectively. As a result, the particles are clearly more visible in the latter two films. Due to the necessary centrifugation of the heavily agglomerated YAG:Ce nanopowder, the NP content in the films was too low (~0.1 wt%) to measure any luminescence output.

Wrinkling of the surface was observed in all films, but was found to be more prominent in the nanocomposites containing higher MPEOMA fractions in the copolymer. The wrinkles appear to be the result of the SEM analysis, as they worsen with increasing exposure time and electron beam intensity. Moreover, they were not observed in the interferometry measurements. Surface wrinkling usually occurs in multilayer systems containing a rigid layer on top of a soft elastic foundation and is related to a strain mismatch between the layers [182]. Typically, the wrinkling is caused by buckling of the top layer as a result of either stress relaxation, compression, cooling or solvent evaporation in the polymer layer. However, surface wrinkling due to heating has also been observed, for example for a bilayer of aluminum/polystyrene on a silicon substrate [183]. It is therefore generally accepted that any force can cause wrinkling of the surface, as long as it induces inter-

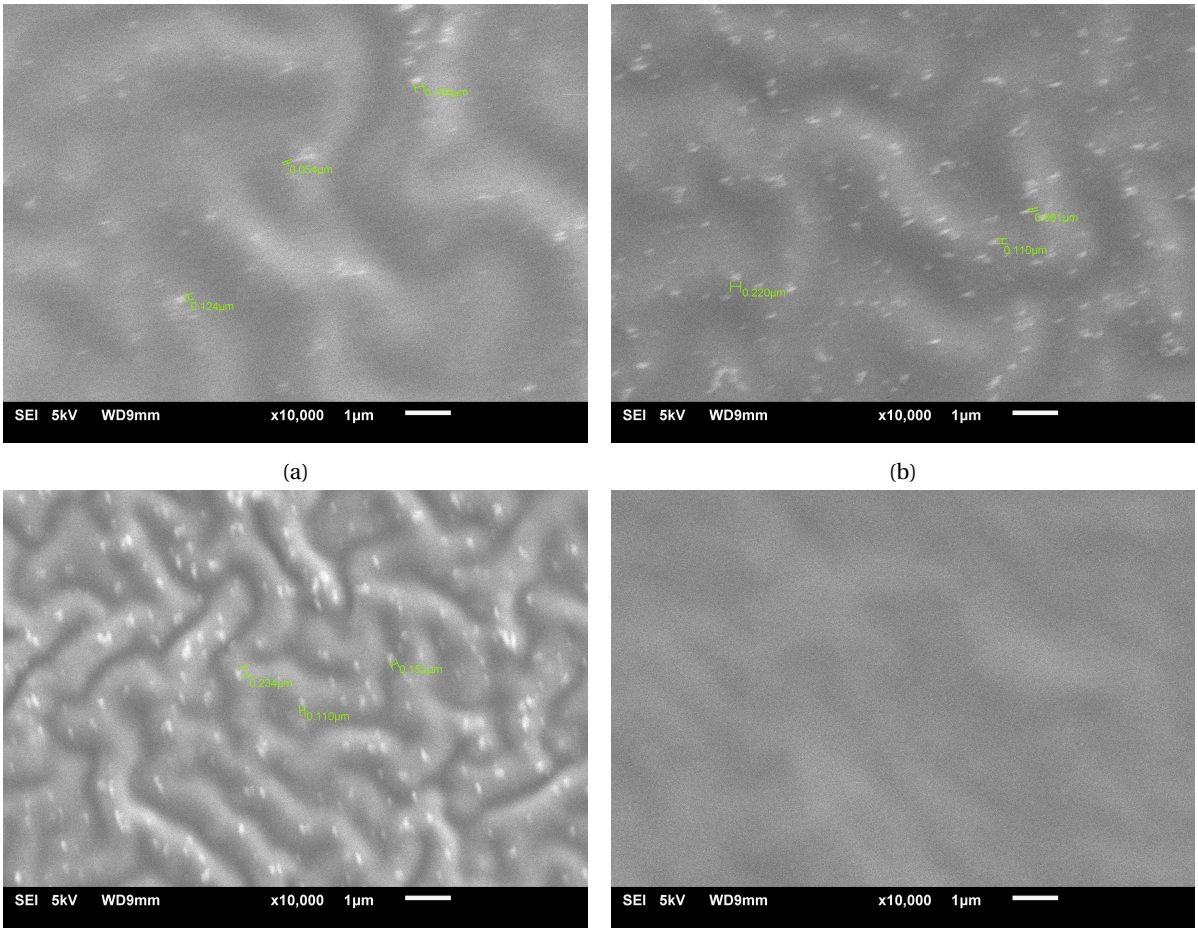

(a) (b)

(c) (d)

Figure 4.9: SEM image of PEHMA/YAG:Ce nanocomposite films with (a) copolymer A, (b) copolymer B and (c) copolymer C and of (d) a PEHMA reference film.

nal stresses that exceed a critical value [182]. In the present study, a 6 nm rigid layer of Au/Pd was sputtered on top of the PEHMA film to make the samples conductive for SEM analysis. The wavelength of the wrinkles depends on a variety of factors, including the elastic modulus and Poisson's ratio of both layers the thickness of rigid layer. A wavelength of several hundred nanometers to several micrometers, which is observed in the PEHMA nanocomposites, is a typical wavelength range for a metal coating on a polymeric layer [184]. It is therefore suggested that the highly focused electron beam of the SEM induces stresses in the multilayer system, thermal or otherwise, causing the Au/Pd film to buckle. The inclusion of higher MPEOMA content in the nanocomposite films—1.3, 2.7 and 3.7 wt% for copolymer A, B and C, respectively—seemingly favors the strain mismatch between the layers.

4.6. Conclusion

A key challenge in the fabrication of polymer nanocomposite LSCs is to minimize the size of the embedded luminescent nanoparticles in order to reduce scattering losses. However, the inherent incompatibility of inorganic nanoparticles with organic media leads to agglomeration. Inorganic nanoparticles can be transfered to organic media with the help of nonionic amphiphilic copolymers, which bind strongly to a wide variety of inorganic nanoparticles and prevent agglomeration through steric stabilization. In the phase transfer process, it is crucial that the rate of amphiphile adsorption to the nanoparticle surface is faster than the agglomeration rat of the nanoparticles.

In this paper, the influence of the amphiphile concentration, the temperature and the solvent composition on the success of stabilization was studied both experimentally and theoretically. Increasing the amphiphile concentration is beneficial to the adsorption kinetics, but is not sufficient to prevent agglom-

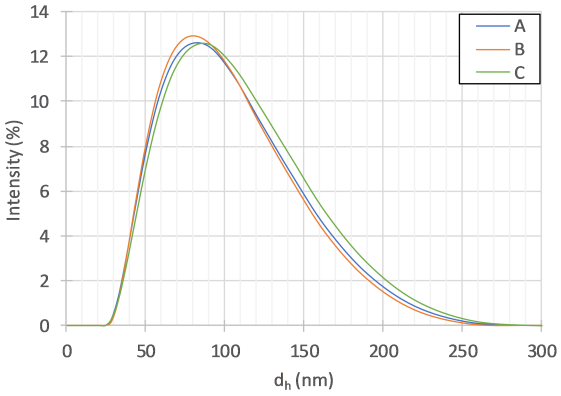

Figure 4.10: Size distributions of YAG:Ce NPs in toluene stabilized by copolymers A (blue), B (red) and C (green) prior to mixing with PEHMA.

eration if the adsorption process is limited by kinetic effects. Kinetic effects due to steric shielding of the binding groups can be eliminated by adding ethanol to the nonpolar phase and increasing the temperature. By careful tuning of these three parameters, it was found that agglomeration of the nanoparticles can be fully suppressed. Without any prior knowledge of the system, the following procedure is recommended for the transfer of inorganic nanoparticles to a nonpolar solvent: i) identify the amphiphile concentration that gives the best results in the nonpolar solvent, ii) identify the optimal solvent composition by adding varying volume fractions of ethanol to the nonpolar solvent and iii) close to the boiling point of the solvent mixture, identify the lowest concentration required for stabilization.

The experimental procedure can be simplified by theoretically estimating the optimal parameters in advance. The optimal ethanol content can be predicted by matching the Hansen solubility parameters of the polar binding group of the amphiphile with those of the solvent mixture. In this optimal solvent system, the kinetic effects due to steric shielding of the binding groups is minimized. The minimum amphiphile concentration can then be estimated by computing the nanoparticle agglomeration rate and the diffusion-controlled amphiphile adsorption rate.

Using this procedure, luminescent $Y_3Al_5O_{12}$:Ce^{3+} nanoparticles were successfully incorporated into poly(2-ethylhexyl methacrylate) (PEHMA) matrices without any sign of agglomeration. Here, the chemical structure of the amphiphilic copolymers plays a crucial role. The copolymers should provide sufficient interaction with the nanoparticles as well as compatibility with the matrix polymer. The fraction of polar binding groups in the amphiphilic copolymers is not crucial as long as a sufficient amount is present. For the PEHMA-stat-PMPEOMA copolymers used in this study, a fraction of 5 mol% MPEOMA already provided sufficient interaction with the particle surface. Compatibility with the polymer matrix is ensured by matching the chemical structures of the matrix polymer and the nonpolar part of the amphiphiloic copolymer. However, the inclusion of a small amount of compatible monomers in their molecular structure favors the compatibility. In case the of the incompatible combination of PEHMA-based copolymers with a PMMA matrix, a fraction of 15 mol% MPEOMA in the copolymer already significantly reduces the incompatibility.

The procedure described in this article opens up the possibility to integrate a wide variety of inorganic luminescent nanoparticles into any type of organic medium, including polymers. The simple, universal and scalable method allows for the fabrication of transparent luminescent polymer nanocomposites for application in luminescent solar concentrators.

5

Theoretical Framework

This chapter serves to outline the framework for the theoretical model that was presented in Chapter 4 and was used to describe the nanoparticle stabilization behavior. The inputs to this model include, among other things, the amphiphile-solvent interaction parameter and the dimensions of the amphiphilic copolymer chains in solution, which are discussed Section 5.1. The inputs to the model and the assumptions that were made are outlined in Section 5.2, along with a brief overview of the implications of the model.

5.1. Amphiphile-solvent interaction

5.1.1. Solubility

The solubility of a polymer in a given solvent depends mainly on the chemical structure of both substances. In general, solvents are able to dissolve polymers that have a similar chemical structure. The solubility is closely related to the cohesive properties of the substances involved, which can be expressed in terms of their solubility parameters. The Hildebrand solubility parameter of a substance is defined as the square root of the cohesive energy divided by its molar volume [159]:

$$\delta = \left(\frac{E_{\text{coh}}}{V} \right)^{1/2} \tag{5.1}$$

The cohesive energy is a measure for the cohesive properties of a substance, and is defined as the increase in internal energy per mole if all intermolecular interactions are removed. The affinity of a polymer with a solvent—also referred to as the solvent quality—can be described in terms of the Flory Huggins interaction parameter χ. For strictly nonpolar systems, χ can be approximated by [159]:

$$\chi \approx 0.34 + \frac{V_{\text{S}}}{RT} \left(\delta_{\text{P}} - \delta_{\text{S}} \right)^2 \tag{5.2}$$

where V_{S} is the molar volume of the solvent, R is the gas constant and δ_{P} and δ_{S} are the Hildebrand solubility parameters of the polymer and the solvent. The lower the value of χ, the higher the compatibility between the substances. The critical value of χ, below which no phase separation occurs, depends on the degree of polymerization: typically polymers only dissolve for $\chi \leq 0.5$ and low molecular weight liquids are only miscible for $\chi \leq 2$. The influence of χ on the swelling of polymer coils in solution is treated in Section 5.1.2. In order to ensure high affinity between the polymer and the solvent, a small difference between δ_{P} and δ_{S} is a necessary, but not sufficient requirement. In the derivation of Equation 4.20, it is assumed that no polar and hydrogen bonding interactions are present between the substances involved. Even for combinations of polymer and solvent for which $\delta_{\text{P}} \approx \delta_{\text{S}}$, compatibility is only achieved when the polar and hydrogen bonding interactions are approximately equal. For this reason, it is useful to decompose the Hildebrand solubility parameter into three vector components known as the Hansen solubility parameters, which are associated with three types of interaction forces [160]:

$$\delta = \sqrt{\delta_{\text{d}}^2 + \delta_{\text{p}}^2 + \delta_{\text{h}}^2} \tag{5.3}$$

where δ_{d} is the dispersion force component, δ_{p} is the polar component and δ_{h} is the hydrogen-bonding component. The smaller the difference in solubility parameters, the higher the compatibility between two

	δ	δ_d	δ_d	δ_d
Solvents				
toluene	18.2	18.0	1.4	2.0
ethanol	26.5	15.8	8.8	19.4
PE-b-PEG				
B575	17.9	16.7	0.6	6.6
B875	17.7	16.8	0.5	5.7
B920	18.6	17.0	0.7	7.4
B1400	18.4	17.1	0.6	6.9
PEHMA-stat-MPEOMA				
A	18.0	16.9	0.0	6.3
B	18.2	17.0	0.0	6.6
C	18.4	17.1	0.0	7.0

Table 5.1: Hildebrand and Hansen solubility parameters (in $MPa^{1/2}$) of the solvents and amphiphilic copolymers used in this study.

substances. The Hansen solubility parameter components of a wide range of solvents have been determined experimentally [160]. For substances with unknown solubility parameters, the components can be estimated from the contributions of the structural groups to the total cohesive energy and molar volume of the molecule. The fact that the solubility parameters can be predicted from the chemical structure is consistent with the rule of thumb that the compatibility between substances is favored by chemical similarity. Hoftyzer and Van Krevelen [159] developed a method that allows estimation the Hansen solubility parameters of polymers with an accuracy of 10%. Using this approach, the Hansen solubility parameters of the PE-b-PEG and PEHMA-stat-PEOMA copolymers used in this thesis research have been estimated. The solubility parameters of the amphiphilic copolymers as well as the solvents used in this study are listed in Table 5.1. The Hildebrand solubility parameter of a solvent mixtures can be determined by averaging the Hildebrand solubility parameters of the separate solvents by volume. In other words, the Hildebrand solubility parameter of a mixture of solvents 1 and 2 is equal to:

$$\delta_{12} = \phi_1\delta_1 + \phi_2\delta_2 \tag{5.4}$$

where ϕ is the volume fraction of the solvent. To determine the Hansen solubility parameters, is it useful to introduce the following fractional parameters [160]:

$$f_d = \frac{\delta_d}{\delta_d + \delta_p + \delta_h} \tag{5.5}$$

$$f_p = \frac{\delta_p}{\delta_d + \delta_p + \delta_h} \tag{5.6}$$

$$f_h = \frac{\delta_h}{\delta_d + \delta_p + \delta_h} \tag{5.7}$$

The fractional parameters represent the contribution of the individual Hansen solubility parameters to the total Hildebrand solubility parameter. The sum of the fractional parameters is always equal to 1. Similar to the Hildebrand solubility parameter, the fractional parameters of a solvent mixture can be computed by:

$$f_{d_{12}} = \phi_1 f_{d_1} + \phi_2 f_{d_2} \tag{5.8}$$

$$f_{p_{12}} = \phi_1 f_{p_1} + \phi_2 f_{p_2} \tag{5.9}$$

$$f_{h_{12}} = \phi_1 f_{h_1} + \phi_2 f_{h_2} \tag{5.10}$$

By combining Equations 5.3–5.10, we find the following relations for the Hansen solubility parameters of a solvent mixture:

$$\delta_{d_{12}} = \frac{f_{d_{12}}\delta_{p_{12}} + f_{d_{12}}\delta_{h_{12}}}{1 - f_{d_{12}}} \tag{5.11}$$

$$\delta_{p_{12}} = \frac{f_{p_{12}}\delta_{d_{12}} + f_{p_{12}}\delta_{h_{12}}}{1 - f_{p_{12}}} \tag{5.12}$$

$$\delta_{h_{12}} = \sqrt{\delta_{12}^2 - \delta_{d_{12}}^2 - \delta_{p_{12}}^2} \tag{5.13}$$

Since the three Hansen solubility parameters of the solvent mixture are the only unknowns, they can be computed by numerically solving Equations 5.11–5.13.

Whether or not a polymer is soluble in a solvent can be predicted by computing the difference in Hansen solubility parameters $\Delta\delta$ between the copolymer and the solvent [159]:

$$\Delta\delta = \left[(\delta_{d,P} - \delta_{d,S})^2 + (\delta_{p,P} - \delta_{p,S})^2 + (\delta_{h,P} - \delta_{h,S})^2\right]^{1/2} \tag{5.14}$$

where the subscripts P and S denote the polymer and the solvent. The Hansen solubility parameters can be plotted in a three-dimensional solubility space—with δ_d, δ_p and δ_h on the axes–to obtain a graphical representation of the solubility behavior. For good solubility, the value of $\Delta\delta$ must be smaller than some interaction radius R, which is specific to the type of polymer. It should be noted that the solubility parameter is defined for polymers in the amorphous state at room temperature. For highly crystalline polymers, the concept of the solubility parameter is only valid at temperatures higher than 90% of their melting point [159].

Lindvig et al. [161] proposed an extension to the Flory-Huggins model based on the Hansen solubility parameters. According to the authors, the interaction parameter between a polymer and a solvent can be estimated using:

$$\chi = C\frac{V_S}{RT}\left[(\delta_{d,P} - \delta_{d,S})^2 + \frac{(\delta_{p,P} - \delta_{p,S})^2}{4} + \frac{(\delta_{h,P} - \delta_{h,S})^2}{4}\right] \tag{5.15}$$

where the correction constant C has been fitted to experimental data. The optimum value of C was found to be equal to 0.6 for several acrylate and acetate polymers in nonpolar and hydrogen bonding solvents [161].

5.1.2. Chain dimensions

Dilute polymer solutions

The simplest model used to describe the dimension of a polymer chain in solution is known as the ideal chain model, which treats the position of the subunits as a random walk and neglects any type of interaction between subunits. For real chains, however, the conformation is influenced by intrachain interactions. For example, two segments of a polymer chain cannot simultaneously occupy the same position in space, thereby leading to the generation of an excluded volume. The extent to which a polymer chain in solution expands due to the excluded volume effect can be described by the expansion factor:

$$\alpha_R = \frac{\sqrt{R^2}}{\sqrt{R_0^2}} \tag{5.16}$$

where $\sqrt{R^2}$ denotes the root-mean-square end-to-end distance of the chain and the subscript 0 refers to the ideal or unperturbed chain dimension, which may be written in terms of the number of segments N and the effective bond length a:

$$\sqrt{R_0^2} = N^{1/2}a \tag{5.17}$$

An expression for the expansion factor of a single polymer chain in dilute solution was introduced by Flory in 1953 [163]:

$$\alpha^5 - \alpha^3 = 2C_M\psi\,(1 - \Theta/T)\,M^{1/2} \tag{5.18}$$

where ψ is the entropy parameter, Θ is the theta temperature, T is the absolute temperature, M is the polymer molecular weight and the parameter C_M is given by [163]:

$$C_M = \left(27/2^{5/2}\pi^{3/2}\right)\left(\overline{v}^2/N_A^2V_0\right)\left(R_0^2/M\right)^{-3/2} \tag{5.19}$$

Here $\overline{v}$ is the polymer partial specific volume, N_A is Avogadro's constant and V_0 is the molecular volume of the solvent. Since R_0^2/M is a characteristic constant of the polymer, C_M is independent of the molecular weight [163]. The factor $\psi\,(1 - \Theta/T)$ represents the quality of the solvent and can also be expressed in terms of the Flory-Huggins interaction parameter χ [163]:

$$\psi\,(1 - \Theta/T) = \frac{1}{2} - \chi \tag{5.20}$$

Some important qualitative characteristics of the expansion factor can already be deduced from Equation 5.21. In the fist place, improving the quality of the solvent leads to a greater expansion coefficient. It follows from Equation 5.20 that both reducing the polymer-solvent interaction parameter χ and increasing the temperature T results in an expansion of the chain. The solvent is referred to as a good solvent for values of $\chi < 0.5$ and a poor solvent for values of $\chi > 0.5$, while at $\chi = 0.5$ the solvent is known as an ideal or theta solvent. Equivalently, a temperature below or above Θ corresponds to a poor or good solvent. At $T = \Theta$ or $\chi = 0.5$, the solvent quality factor in Equation 5.18 becomes equal to 0 and α reduces to 1. In other words, in an ideal solvent there is no excluded volume effect and the chain dimension is equal to that of ideal chain described by the random walk model. Secondly, the expansion factor in Equation 5.18 increases slowly with the molecular weight. Therefore, the size of a real chain in solution increases more rapidly with the molecular weight than an ideal chain. In fact, the end-to-end distance of a polymer chain $\sqrt{R^2}$ is proportional to N^{ν}, where $\nu = 1/2$ for and ideal chain and $\nu \approx 3/5$ for an excluded volume chain in a good solvent [162].

Many different expansions of α_{R}^2 have been proposed to describe the behavior of α in the form of an approximate closed expression. One expression that provides a fairly satisfactory description is known as the modified Flory equation and is given by [164]:

$$\alpha_{\mathrm{R}}^2 = 1 + 1.33z + 2.67z^2 + 9.78z^3 \tag{5.21}$$

with

$$z = \left(4/3^{3/2}\right) C_M \left(\frac{1}{2} - \chi\right) M^{1/2} \tag{5.22}$$

Because the series is very slowly convergent, the validity of Equation 5.21 is confined to small values of z or equivalently, nearly ideal solvents. For large values of z, the asymptotic solution for α (i.e., high molecular weight polymers in good solvents) is given by:

$$\alpha_R^5 = (2\pi/3)^{1/2} z \tag{5.23}$$

The expansion factor may also be described in terms of the root-mean-square radius of gyration $\sqrt{S^2}$, which has a direct relation to the solution properties:

$$\alpha_{\mathrm{S}} = \frac{\sqrt{S^2}}{\sqrt{S_0^2}} \tag{5.24}$$

The relationship between the end-to-end distance and the radius of gyration depends on the value of z and is given by [164]:

$$\frac{\langle R^2 \rangle}{\langle S^2 \rangle} = 6\left(1 + \frac{2}{35}z - ...\right) \tag{5.25}$$

For ideal chains with $z = 0$, the relation simplifies to:

$$\langle R^2 \rangle = 6\langle S^2 \rangle \tag{5.26}$$

Due to the lack of experimental data available for the copolymers used in this study, an accurate estimation of the expansion coefficient using Equations 5.21 or 5.23 is impossible. It is possible, however, to derive an expression for the proportionality between, on the one hand, the coil dimension $\sqrt{R^2}$ and, on the other hand, the solvent quality $(1/2 - \chi)$ and the molecular weight M. Taking the asymptotic solution for large values of z given by Equation 5.23, the expansion factor is proportional to:

$$\alpha_{\mathrm{R}} \propto \left(\frac{1}{2} - \chi\right)^{1/5} M^{1/10} \tag{5.27}$$

Using Equations 5.16 and 5.17 and assuming furthermore that the number of segments in a chain is directly proportional to its molecular weight, we find:

$$\sqrt{R^2} \propto \left(\frac{1}{2} - \chi\right)^{1/5} M^{3/5} \tag{5.28}$$

Semidilute polymer solutions

The theory presented in this section so far falls within the framework of the two-parameter theory, which provides a useful description of the behavior of flexible-chain polymers of high molecular weight in dilute solutions, where coils do not overlap. For concentrated polymer solutions and stiff chains, however, this theory will break down. As the polymer concentration is increased, the coils start to overlap and the coil swelling gradually diminishes due to the screening of the excluded volume effect. An expression for the asymptotic result of α for polymer chains in semidilute solutions in good solvents was proposed in the form of [185, 186]:

$$\alpha_{\mathrm{R}}^2 = 0.932\left(\frac{1}{2}-\chi\right)^{1/4}\phi^{-1/4} \tag{5.29}$$

where ϕ is the polymer volume fraction. It should be noted that as might be expected for semidilute solutions, the effect of the solvent quality on the chain swelling is diminished. It follows from Equation 5.29 that the end-to-end distance of the chain is now approximately proportional to:

$$\sqrt{R^2} \propto \left(\frac{1}{2}-\chi\right)^{1/8} \tag{5.30}$$

A polymer chain in the melt (i.e., $\phi = 1$) behaves as an ideal chain. The explanation for this property of polymers—known by the Flory theorem—is that in the melt the chain is densely surrounded by identical segments, and therefore the interactions on the chain are equivalent in all directions. As the polymer concentration is increased from a dilute solution to a melt, the proportionality of the coil size $\sqrt{R^2}$ thus gradually changes from $N^{3/5}$ to $N^{1/2}$. For many polymer solutions, the chains reach the ideal coil dimensions at volume fractions as low as 0.05–0.20, independent of the molecular weight [175]. Unsurprisingly, the overlapping of coils thus occurs already at very low polymer concentrations. The coils start to overlap when the overall concentration of chain segments in the solution is equal to the concentration of the segments in the coil, known as the overlap concentration c^*:

$$c^* \propto \frac{N}{\langle R\rangle^3} \propto N^{1-3\nu} \tag{5.31}$$

It follows that in good solvents with $\nu \approx 3/5$, the overlap concentration is proportional to $N^{-4/5}$. The overlap concentration can be estimated using [175]:

$$c^* = \frac{6^{3/2} M_{\mathrm{w}}}{8 N_{\mathrm{A}} \langle R\rangle^3} \tag{5.32}$$

where M_{w} is the weight-average molecular weight of the polymer. Due to the lack of experimental data for the amphiphilic copolymers used in this study, it is not possible to estimate their overlap concentrations directly. However, we can find reference expressions for the overlap concentrations of comparable polymers. In fact, the molecular weight of the PEHMA-stat-PMPEOMA copolymers was calculated using size exclusion chromatography (SEC), which bases the computed molecular weight on the hydrodynamic volume relative to that of PMMA. In reality, the copolymers will have a significantly higher hydrodynamic volume than a corresponding PMMA polymer with a similar molecular weight due to the relatively high molar volume of the EHMA and MPEOMA subunits (a factor of 2.4 and 4.3 greater than that of PMMA respectively). While this means that the SEC measurement likely overestimates the molecular weight of the copolymers, the predicted molecular weights correspond to the hydrodynamic volumes occupied by PMMA chains. Since the overlap concentration is a result of the volume occupied by the coils, it is reasonable to assume that computing the overlap concentration for PMMA will provide an adequate estimate. The overlap concentration for PMMA can be estimated to be approximately equal to [187]:

$$c^*_{\mathrm{PMMA}} \approx 8.69 \times 10^5 M_{\mathrm{w}}^{-0.79}\,[\mathrm{g/L}] \tag{5.33}$$

By inserting the molecular weight of the PEHMA-stat-PMPEOMA copolymers in Equation 5.33, we find a value for c^* approximately one order of magnitude higher than the concentrations that were required for the successful stabilization of the YAG:Ce NPs. Therefore, over the concentration range of amphiphiles used in this study, we assume that the coils are in dilute solution and that their dimensions are dominated by the excluded volume effect. In other words, the coil dimensions are expected to scale according to the proportionality relation given by Equation 5.28. The actual swelling of the copolymers in the dilute solution is expected to be slightly less than the swelling predicted by this relation, which is valid for large values of z only (i.e., high molecular weight polymers in exceptionally good solvents). In reality, the proportional effect of the solvent quality on chain dimensions $\sqrt{R^2}$ will most likely be somewhere between $(1/2-\chi)^{1/5}$ and $(1/2-\chi)^{1/8}$, depending on the concentration of the polymer.

5.2. Stabilization kinetics

The reader is referred to Section 4.5.1 in the paper for the existing theories on the kinetics of nanoparticle agglomeration and amphiphile adsorption. These theories allow for a quantitative description of both processes, provided that a number of parameters are known. These input parameters are:

- The size of the particles. The particle size used in the model is the number-weighted average particle diameter measured by DLS.
- The concentration of the particles. The particle concentration is estimated by comparing the scattering intensity to that of a reference standard with identical average size, as is explained in Section 6.1.4.
- The size of the amphiphiles. The size of the amphiphilic copolymer coils in solution is estimated by applying the scaling laws derived in Section 5.1.2 to the experimentally obtained size of similar amphiphilic copolymers in [127].
- The concentration of amphiphiles.
- The temperature of the solvent.
- The viscosity of the solvent. The temperature-dependence of the viscosity is taken into account. The effect of the addition of ethanol to the toluene phase is neglected. This is justified, because a volume fraction of 33 vol% EtOH in the solvent mixture only decreases the viscosity by 3% with respect to that of pure toluene [188].

A number of simplifying assumptions is made in the derivation of these theories, which are summarized here for completeness. The assumptions are that:

- The dispersed nanoparticles and their agglomerates are spherical in shape.
- The colloid is monodisperse. That is to say, all particles in the dispersion are equal in size.
- Every collision between nanoparticles results in adhesion (i.e., agglomeration).
- The effect of shear flow on the agglomeration is negligible.
- The amphiphilic copolymer coils are spherical in shape, both in solution and in the adsorbed state.

At the end of Section 4.5.1, a new parameter is introduced to describe the ratio of the competing processes of nanoparticle agglomeration and amphiphile adsorption, namely the stabilization kinetics parameter τ. The parameter τ is computed with the input parameters mentioned previously in this section. The purpose of τ is to link the input parameters to the measured average particle diameter d_h after the phase transfer process. However, since τ is a dimensionless quantity—defined as the ratio of a characteristic agglomeration time to a characteristic adsorption time—and d_h is in units of length, a direct comparison between the two parameters is not straightforward. A new theory was developed to find a direct, proportional relationship between d_h and τ. The relation states that:

$$d_\mathrm{h} \propto \tau^{-1/D_\mathrm{f}} \tag{5.34}$$

The derivation of this relation is presented in the paper in Section 4.5.3. Taking into account the assumptions mentioned above, it should be stressed that this relation is of course a simplification of reality and mainly serves to promote a better understanding of the behavior. Using this relation, the input parameters that are used to compute τ—such as the amphiphile concentration c_0 and the temperature T—are now proportionally related to d_h. The derivation of the relations linking c_0 and T to d_h are presented in Sections 4.5.3 and 4.5.4 of the paper, respectively. Although these relations were presented in the context of a phase transfer process using PEHMA-stat-MPEOMA copolymers, they are in principle valid for a wide range of systems involving the simultaneous agglomeration of particles and adsorption of molecules onto their surface. Finally, the Flory-Huggins interaction parameter χ of the amphiphiles in various solvent systems was modeled using the theory presented in Section 5.1.1. The information that can be obtained by relating c_0, T and χ to d_h is summarized below. The MATLAB code that was used to compute this information is given in Appendix D.

Amphiphile concentration
By comparing the theoretical relation between c_0 and d_h with experimental data, the controlling mechanism of adsorption can be predicted. That is, it allows to predict whether the adsorption rate is likely to be determined by the diffusion rate of the amphiphiles to the nanoparticle surface (diffusion-controlled, DC) or whether it is more likely limited by kinetic effects during the binding to the particle surface (kinetic-controlled, KC). For DC adsorption, the model allows to estimate the minimum amphiphile concentration required for successful adsorption. The proposed relation between c_0, τ and d_h was found to provide fairly good description of the stabilization behavior, both in terms of predicting the controlling mechanism and estimating the minimum amphiphile concentration.

Temperature
The temperature should only influences d_h for KC adsorption, in which case the adsorption rate is strongly dependent on the adsorption rate constant k_a. Increasing the temperature causes k_a to increase exponentially, thereby reducing the rate-limiting kinetic effects and gradually shifting the controlling mechanism towards DC adsorption. In a similar way to the amphiphile concentration, T was related to d_h via τ. Comparing this relation to experimental data allows for the estimation of the activation energy E_a. In the case of amphiphilic copolymer that bind through noncovalent interactions, E_a is suggested to arise from steric shielding of the binding groups. Although the estimated values of E_a of the copolymers in the system were not verified by measurements, their relative difference was found to agree qualitatively with the expected behavior.

Solvent composition
Kinetic effects that limit the adsorption of the copolymers can also be eliminated by a change in the composition of the solvent mixture. The solvent quality for a substance is described in terms of the Flory-Huggins interaction parameter χ, which was computed for the amphiphilic copolymers as a function of the solvent composition. Although no mathematical relation was proposed, the parameter χ of the binding groups was observed to be closely related to d_h. The computation of χ proves to be a simple and effective method for selecting a suitable solvent composition without the need for any experimental work.

6

Lab Report

6.1. Nanoparticle dispersion in polar solvents

Directly mixing inorganic nanoparticles (NPs) into organic media typically results in severe and practically irreversible agglomeration. In polar media, however, they can be stabilized by introducing sufficient electrostatic repulsion between the particles. The theory behind electrostatic stabilization was outlined in Section 2.3. The stable polar nanodispersion can subsequently be transferred to a nonpolar phase by the adsorption of amphiphilic molecules, which prevent agglomeration through steric forces. The criteria for effective steric stabilization were discussed in Section 2.4. Obtaining a stable nanodispersion in a polar solvent is thus a crucial first step towards transferring the NPs to an organic medium. Three different types of metal oxide NPs were evaluated: Al_2O_3, $Ba_3(PO_4)_2$:Mn^{5+} and $Y_3Al_5O_{12}$:Ce^{3+} (YAG:Ce). More information about these specific materials and the reason behind their selection can be found in Section 3.2.1. Electrostatic stabilization is the result of repulsive electrostatic forces between particles with a charged surface. The surface charge that accumulates on the NP surface depends on the pH of the liquid in which the particles are dispersed. Therefore, the stability of the nanoparticles was studied in water with various concentrations of hydrogen chloride (HCl) or sodium hydroxide (NaOH) to control the pH. The hydrodynamic particle size distribution and average particle size in the dispersions was measured by dynamic light scattering (DLS). Unfortunately, the DLS returned faulty zeta potential measurements during the period that the tests described in this section were performed. As a result, the effect of the surface charge on the stability could not be studied. Most likely, the problem was caused by dirty electrodes.

6.1.1. Al_2O_3

Method

A 20 wt% dispersion of Al_2O_3 NPs in water (H_2O/Al_2O_3) with an average size of 30 nm was acquired from US Research Nanomaterials, Inc. and used as received. The particle concentration is too high to study the average particle size in the dispersion by dynamic light scattering (DLS) due to the appearance of multiple scattering effects. The dispersion was diluted with ultrapure water (18 $M\Omega \cdot cm$) as well as with ultrapure water containing a varying concentration of HCl to study the influence of electrostatic repulsion on the size and stability of the nanoparticles. The particle size distribution and the average hydrodynamic diameter were measured by DLS using a Malvern Zetasizer Nano ZS. The isoelectric point (IEP) of Al_2O_3 NPs has been determined in literature and is close to a pH of 7.1 [146]. Therefore, diluting the H_2O/Al_2O_3 nanodispersion with ultrapure water (pH≈7) is expected to result in severe agglomeration. Conversely, using a diluent with a pH that deviates sufficiently from the IEP should lead to a small average particle size and longer stability of the nanoparticles.

Results

The H_2O/Al_2O_3 nanodispersion appears as a white, milky liquid. An image of the nanodispersion diluted with ultrapure water is shown in Figure 6.1. The measured average particle size and the pH of the diluted nanodispersions are listed in Table 6.1. As expected, the measured pH of the liquid increases with the addition of water. Up to a certain concentration, diluting seems to have little effect on the measured average particle size. Initially only the 10,000x diluted dispersion showed a small increase in particle size. The dilution was found

Dilution	Concentration (ppm)	pH	Average hydrodynamic diameter (nm)		
			Same day	One week	One week + sonication
100x	2000	4.5	153	152	148
1000x	200	5.1	151	292	145
10,000x	20	5.7	172	1059	798

Table 6.1: Average hydrodynamic diameter and pH of the liquid after diluting the H_2O/Al_2O_3 nanodispersion with ultrapure water.

Figure 6.1: H_2O/Al_2O_3 nanodispersion diluted with ultrapure water: 100x (right), 1000x (middle) and 10,000x (left).

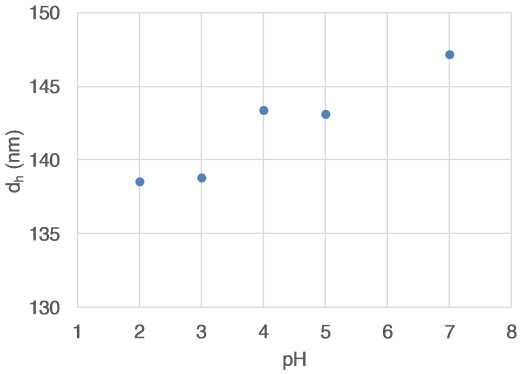

Figure 6.2: Average hydrodynamic diameter of the Al_2O_3 NPs in H_2O:HCl diluents with varying pH values.

to affect the long-term stability of the nanoparticles. While the 100x diluted dispersion did not show any sign of agglomeration after 1 week, the particle size of the more diluted samples increased significantly. The agglomeration of the 1000x diluted sample could be reversed by ultrasound treatment, whereas the 10,000x diluted sample showed irreversible agglomeration. The results might indicate that the particles are stabilized by electrostatic forces. The more the particles are diluted with water, the closer the pH of the dispersion approaches the IEP. This reduces the surface charge on the particles and thereby promotes agglomeration. However, it cannot be ruled out that other additives are present in the supernatant that contribute to the stabilization of the NPs. A more thorough understanding of the nature of stabilization can be obtained by studying the effect of varying the pH of the diluent. It should be noted that the particle concentration in the 10,000x diluted sample is close to the detection limit of the DLS. Measuring samples with very low particle concentrations can give inaccurate results due to number fluctuations. Therefore, a dilution of 1000x was selected for further experiments, having a particle concentration sufficient for accurate DLS measurements while minimizing the effect of the supernatant.

Surprisingly, the pH of the diluent was found to have barely any effect on the mean size of the Al_2O_3 NPs, as shown in Figure 6.2. The nanodispersion was diluted 1000x in solutions of HCl in ultrapure water and sonicated for 10 minutes prior to measurement. The measured average particle size for all pH values was found to be around five times larger than the size reported by the supplier. Ultrasonication of the dispersions had only little effect on the measured particle size. It is likely that the particle size reported by the supplier corresponds to the primary particle size and agglomeration has already occurred to some extent prior to receiving the NPs. The slight decrease in particle size with increasing HCl concentration can be attributed to the increase in ionic strength of the liquid. As the ionic strength increases, the electrical double layer (EDL) is compressed due to a closer packing of ions around the particle. This causes the diffusion speed to increase and can decrease the apparent particle size measured by DLS by up to 10 nm [189]. The limited observed effect of the pH on the mean particle size raised the suspicion that the Al_2O_3 NPs had already received some form of surface treatment, which shields the particles from their environment. Indeed, upon request the supplier disclosed that small amounts of unknown dispersants were used. This means that the state of agglomeration is not merely related to the pH of the liquid; it can equally well be attributed to the desorption of the dispersants. Besides the fact that the acquired particles are technically not nanoparticles (> 100 nm), the presence of unknown dispersants renders the Al_2O_3 particles unsuitable for further research. The interaction of the amphiphilic copolymers with the hydroxylated particle surface cannot be studied when such unknown molecules are adsorbed to the surface.

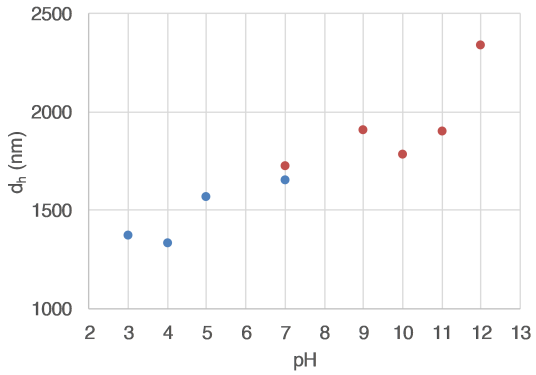

Figure 6.3: Influence of pH on the average hydrodynamic particle size of $Ba_3(PO_4)_2$:Mn^{5+} particles dispersed in solutions of HCl (in blue) and NaOH (in red) in ultrapurewater. 1 mM of KNO_3 electrolyte was added to the solutions indicated in red.

Figure 6.4: $Ba_3(PO_4)_2$:Mn^{5+} powder dispersed in H_2O:HCl diluents with pH values ranging from pH 2 (left) to pH 7 (right).

6.1.2. $Ba_3(PO_4)_2$:Mn^{5+}

Method

$Ba_3(PO_4)_2$:Mn^{5+} particles were synthesized by PHYSEE using a sol-gel method and used as received. The particles were dispersed in ultrapure water with various concentrations of HCl or NaOH to adjust the pH of the dispersion and sonicated for 10 minutes. In the alkaline solutions, 1 mM of potassium nitrate (KNO_3) electrolyte was added to study the influence of the ionic strength on the electrostatic stabilization. If the ionic strength of the liquid medium is too low, the potential gradient at the particle surface is not large enough to provide sufficient electrical double layer (EDL) repulsion. This is typically the case for nonpolar liquids, which have low relative permittivity values are unable to dissolve a substantial concentration of salts. The effect of the ionic strength on the EDL was outlined in Section 2.3.1. It is possible that the ionic strength of the ultrapure, deionized water is too low to allow for electrostatic stabilization, in a similar way to nonpolar liquids. To study this effect, the particles were dispersed in both ultrapure water and ultrapure water with 1 mM KNO_3. While increasing the acid or base concentration should influence the stabilization through the surface charge on the particles, it also affects the ionic strength of the liquid. In order to study the isolated effect of the pH, the difference in ionic strength between the different alkaline pH solutions was decreased by adding 1 mM of KNO_3.

Results

Figures 6.3 shows the effect of the pH of the diluent on the measured average hydrodynamic diameter of the $Ba_3(PO_4)_2$:Mn^{5+} particles. The average particle size showed a clear dependence on the pH, although it remained the micrometre range for all pH values. The particles appear to be most effectively dispersed in acidic diluents. The particle size distribution in the dispersions did not reveal the presence of particles smaller than several hundred nanometers. Centrifugation of the dispersions did not result in nanodispersions with an appreciable particle concentration, as evidenced by extremely low scattering intensity values measured by DLS. The findings indicate that the particles were already heavily and irreversibly agglomerated prior to dispersion. The addition of KNO_3 to the ultrapure water does not appear to affect the particle size much, whcih means that ultrapure water contains sufficient ions for electrostatic stabilization. This can be explained by the fact that ultrapure water easily dissolves carbon dioxide (CO_2) from the atmosphere to form carbonic acid (H_2CO_3), which in turn dissociates into bicarbonate (HCO_3^-) and carbonate (CO_3^{2-}) ions [190]. The amount of scattering is visibly reduced by lowering the pH, as can be seen in Figure 6.4.

Several notes should be added to these observations. First of all, the mean particle size varied significantly between measurements. This indicates that the data quality of the DLS measurements was poor, most likely due to the presence of large particles and high polydispersity. The count rate—which is a measure for the scattering intensity—decreased continuously between successive measurement, probably due to settling of large agglomerates. The scattering intensity was found to reduce drastically at pH 2, almost down to the reference value of pure water. The dispersion in pH 2 also showed a distinct pink tint, which is hardly visible in Figure 6.4. Both observations suggest that the particles dissolve in the highly acidic environment. The

following reaction is proposed for the dissolution of the particles:

$$Ba_3(PO_4)_2\,(s) + 6\,HCl\,(aq) \longrightarrow 3\,BaCl_2\,(aq) + 2\,H_3PO_4\,(aq) \tag{6.1}$$

The pink tint can be explained by the reduction of the manganese ions. Compounds with manganese in its +5 oxidation state are strong oxidizing agents. The Mn^{5+} dopant ions are thus most likely reduced to Mn^{2+}, which is the most stable oxidation state and has a characteristic pale pink color.

6.1.3. SiAlON:Sm^{2+}

Method

Similar experiments to those with $Ba_3(PO_4)_2$:Mn^{5+} have been conducted with multiple batches of SiAlON:Sm^{2+} particles synthesized by PHYSEE. The isoelectric point (IEP) of SiAlON is reported in literature to range between pH 2 to pH 5 depending on the processing conditions [191]. Therefore, the SiAlON:Sm^{2+} particles were dispersed in water with pH 7 and pH 12.

Results

All exploratory studied revealed that the particles were even more agglomerated than $Ba_3(PO_4)_2$:Mn^{5+}. After the ultrasonication and centrifugation steps, the scattering intensity measured by DLS was close to the reference value of water. This indicates that the powder consists mainly of strong, micron-sized aggregates. Most likely, the irreversible agglomeration was caused during the sintering step during their synthesis, which is required to activate the luminescence. It was decided not to proceed with the SiAlON:Sm^{2+} particles.

6.1.4. $Y_3Al_5O_{12}$:Ce^{3+}

Method

$Y_3Al_5O_{12}$:Ce^{3+} (YAG:Ce) nanopowder with an average primary particle size of 25 nm was obtained from ... and kindly supplied by Dr. Erik van der Kolk. The nanopowder was dispersed in solutions of HCl and NaOH in ultrapure water to identify the position of the isoelectric point. The dispersions were placed in an ultrasonic bath to study the effect of the sonication time on the average particle size. The stable dispersions were centrifuged to obtain nanodispersions with a unimodal size distribution. The influence of the centrifugation time was investigated to control the average particle size of the obtained nanodispersion.

Results

The YAG:Ce nanopowder appears as a white solid. Photoluminescence (PL) and photoluminescence excitation (PLE) measurements confirmed that the YAG:Ce powder shows the characteristic blue absorption and yellow/green emission, as shown in figure 6.5. In powder form, the particles were found to be severely agglomerated with agglomerate sizes up to 100 μm, as can be seen in Figure 6.6. Ultrasonic treatment can to some extent break up loose agglomerates, but it was not possible to redisperse the particles in their primary particle size. The effect of the ultrasonication time on the average hydrodynamic diameter of 0.1 wt% YAG:Ce nanopowder dispersed in ultrapure water with 1 mM of KNO_3 is shown in figure 6.7. It should be noted that the dispersions were often too polydisperse to get very reliable results on the average particle diameter. Therefore, the results only serve to identify certain trends in the behavior. Sonication times longer than 20 minutes generally did not result in a significant reduction of the average particle size. In diluents with pH 2, this average particle size was slightly smaller than for diluents with pH 7 and typically required less sonication. The minimum average particle diameter was found to be around 250 nm. Ultrasound treatment was also found to be less effective for lower particle concentrations. Most likely, the amount of collisions in highly diluted samples during sonication is too low to effectively break up agglomerates. More reliable information on the particle size in the dispersions is obtained by analyzing the particle size distributions.

Figure 6.8 shows a typical representation of the measured particle size distribution in pH 2, pH 7 and pH 12. Concluding from the severe agglomeration around pH 12, the IEP of YAG:Ce is located at a strongly alkaline pH and the particles are most effectively dispersed in neutral to acidic diluents. The stability of the particles in neutral environments raised the suspicion that the particles might be stable in ethanol as well. Dispersing the particles directly into ethanol is beneficial for the phase transfer of the YAG:Ce particles to organic solvents, as will be discussed in Section 6.2. Indeed, stable dispersions could be obtained in ethanol by following the same procedure. The dispersions remained stable for long periods of time, showing almost no sign of agglomeration after several weeks. The stable dispersions all showed bimodal or trimodal size distributions, with the smallest peak in the nanometer range. The multimodal distributions can be separated by centrifugation to isolate the smallest peak.

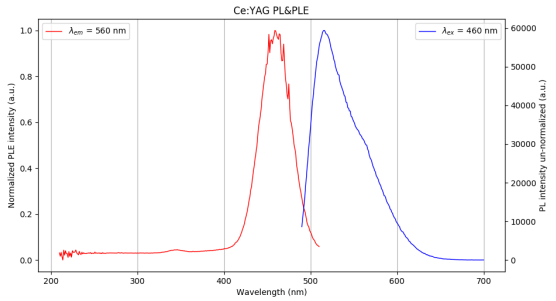

Figure 6.5: Excitation (red) and emission (blue) spectra of the YAG:Ce nanopowder. Measurement was performed by Joe Kao from PHYSEE.

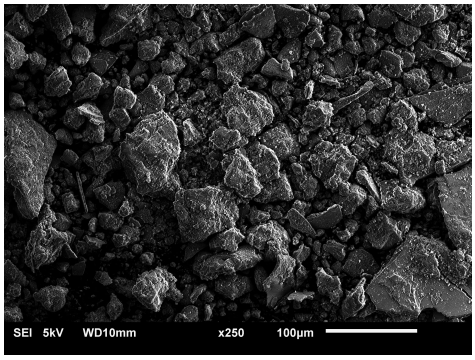

Figure 6.6: SEM micrograph of the agglomerated YAG:Ce nanopowder.

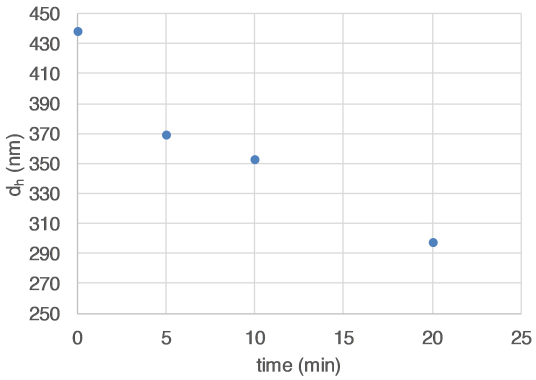

Figure 6.7: Influence of the sonication time on the average hydrodynamic diameter of 0.1 wt% YAG:Ce particles in ultrapure water with 1 mM of KNO_3 (pH=7).

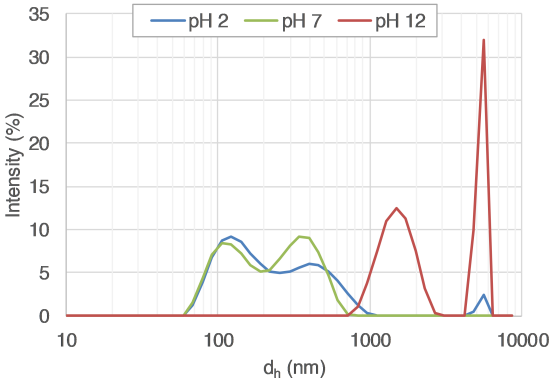

Figure 6.8: Typical particle size distributions of the YAG:Ce nanopowder dispersed in diluents of pH 2 (in blue), pH 7 (in green) and pH 12 (in red) after 10 minutes of sonication. The pH was adjusted by the addition of HCl or NaOH and 1 mM of KNO_3 was added to all solutions.

Centrifugation

The required centrifugation time can be estimated using Stokes' law. According to Stokes' law, the settling velocity of a spherical particle in a liquid due to gravity is equal to [192]:

$$v = \frac{g\left(\rho_p - \rho_l\right) d^2}{18\mu} \tag{6.2}$$

d is the particle diameter, ρ_p and ρ_l are the densities of the particles and the liquid, g is the gravitational acceleration and μ is the viscosity of the liquid. The purpose of centrifugation is to accelerate the settling velocity by introducing a centrifugal force much higher than the gravitational force. The centrifugal acceleration is equal to:

$$a_c = r\omega^2 \tag{6.3}$$

where r is the radius of rotation of the centrifuge and ω is the angular velocity. The angular velocity can be converted to the rotational frequency in rotations per minute (rpm) N_{rpm} by using:

$$\omega = \frac{2\pi N_{rpm}}{60} \tag{6.4}$$

During centrifugation the gravitational acceleration g in Equation 6.2 is substituted by the centrifugal acceleration a_c. The ratio of a_c to g is known as the relative centrifugal force (RCF) (or the "g-force") and is equal to [193]:

$$\mathrm{RFC} = 11.18 r \left(\frac{N_{rpm}}{1000}\right)^2 \tag{6.5}$$

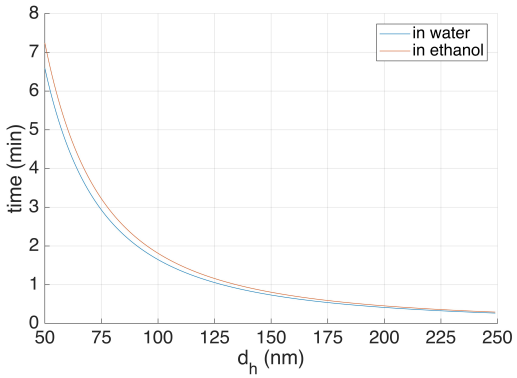

Figure 6.9: Estimated centrigugation time to settle particles with diameter d on the bottom of the centrifuge tube.

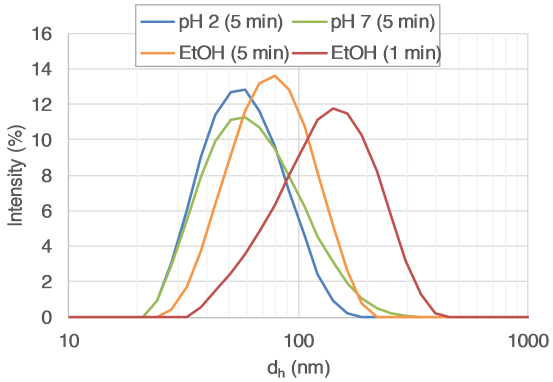

Figure 6.10: Particle size distributions of Yag:Ce nanodispersions in water with pH 2 and pH 7 and ethanol after various centrifugation times.

where r is in units of cm. The average settling velocity is equal to the distance traveled by the particles in a specific period of time:

$$v = \frac{h}{t} \tag{6.6}$$

where, in this case, h is the distance from the top to the bottom of the centrifuge tube and t is the centrifugation time. We can now estimate the centrifugation time required to filter out particles with a diameter d by combining Equations 6.2, 6.3 and 6.6, which gives:

$$t = \frac{18\mu h}{r\omega^2 \left(\rho_\mathrm{p} - \rho_\mathrm{l}\right) d^2} \tag{6.7}$$

In fact, it is more accurate to use the integrated form of Stokes' law, which takes into account the increase in radius of rotation while the particles are settling. The integrated form gives:

$$t = \frac{18\mu \ln\left(r_\mathrm{f}/r_\mathrm{i}\right)}{\omega^2 \left(\rho_\mathrm{p} - \rho_\mathrm{l}\right) d^2} \tag{6.8}$$

where r_i and r_f are the initial and final radius of rotation—or, the distance from the center of the centrifuge to the top of the liquid and to the precipitate. However, due to the small dimensions of the centrifuge tubes, the difference is small.

Figure 6.9 shows the computed centrifugation time versus the particle diameter for the YAG:Ce particles in water and ethanol, using $N_\mathrm{m} = 13{,}000$ rpm, $r = 5$ cm, $\rho_\mathrm{p} = 4560\ \mathrm{kg\,m^{-3}}$ and $T = 25°\mathrm{C}$. The difference in centrifugation time between water and ethanol is negligible. Using Figure 6.9, an indication of the required centrifugation time was obtained. One would expect that the figure allows to select a centrifugation time that settles all particles with a diameter larger than d. In practice, slightly longer centrifugation times were necessary than those predicted by Equation 6.8. It was found that the predicted centrifugation time roughly corresponds to the average particle diameter in the dispersion instead of the maximum particle diameter, as can be seen in figure 6.10. One possible reason for this discrepancy is that Stokes' law is only valid for dilute solutions. This means that it does not account for collisions and any other interparticle interactions that might influence the settling velocity. The size of the YAG:Ce particles in ethanol was observed to be slightly larger than in aqueous dispersions, as can be seen in Figure 6.10. However, this effect might be al least partially attributed to the low ionic strength in ethanol. The low ionic strength expands the EDL, which causes the apparent particle size in DLS to increase by up to 10 nm due to electrostatic interactions between the particles [189]. By dispersing the particles in ethanol with 10 mM of dissolved KNO_3, the average particle size was observed to decrease by approximately 7 nm.

The dispersion process (i.e., the ultrasonication and centrifugation) was found to be highly reproducible. Nanodispersions with unimodal size distributions and average particle diameters between 120 to 30 nm were obtained for centrifugation times ranging from 1 to 45 minutes. Obviously, there is a trade-off between the average particle size and the particle concentration in the dispersion after centrifugation. In order to incorporate an appreciable amount of particles in the polymer films while also ensuring that most particles are

smaller than 100 nm, a centrifugation time of 5 minutes at 13,000 rpm was selected for further experiments. This corresponds to an average hydrodynamic particle diameter of approximately 70 nm.

Concentration
The concentration of the YAG:Ce nanoparticles in the ethanolic nanodispersion was estimated by comparing the measured scattering intensity to that of a calibration standard for DLS with an identical average particle size. The standard that was used is a 1 vol% aqueous dispersion of polystyrene (PS) beads with an average hydrodynamic diameter of 70 nm. The estimated concentration was corrected for the differences in refractive index. The intensity of Rayleigh scattering is proportional to the refractive indices of the particles and the medium:

$$I \propto \left[\frac{\left(n_\mathrm{p}/n_\mathrm{m}\right)^2 - 1}{\left(n_\mathrm{p}/n_\mathrm{m}\right)^2 + 2} \right]^2 \tag{6.9}$$

where n_p and n_m are the refractive indices of the particles (YAG = 1.83, PS = 1.59) and the medium (EtOH = 1.36, H_2O = 1.33). Here the influence of the dopant Ce^{3+} ions on the refractive index of the YAG particles was neglected. The selected refractive indices correspond to those for light with a wavelength of 633 nm, which is the center wavelength of the laser in the DLS. The scattering intensity of the diluted standard was compared with that of EtOH/YAG:Ce nanodispersions containing various initial YAG:Ce concentrations (i.e., before 5 minutes of centrifugation at 13,000 rpm). The scattering intensity increased more or less linearly with the initial YAG:Ce concentration. However, due to the limited amount of YAG:Ce nanopowder available, an initial concentration of 5 wt% (≈ 0.9 vol% in EtOH) was selected for further experiments. After 30 minutes of ultrasound treatment in an ultrasonic bath and 5 minutes of centrifugation at 13,000 rpm to obtain an average particle size of 70 nm, the scattering intensity of the nanodispersion was measured to be equal to that of the diluted H_2O/PS standard with 0.02 vol% PS. Using Equation 6.9, the ratio of the scattering intensity of EtOH/YAG:Ce to that of H_2O/PS is approximately equal to 2.9. Therefore, the concentration of YAG:Ce NPs in ethanol was estimated to be around 0.02/2.9 = 0.007 vol%, which corresponds to 0.032 w/v% or 0.32 $\mathrm{g\,L^{-1}}$. This means that the centrifugation step reduces the concentration by more than a factor 100. It should be noted that the polydispersity of the standard is much lower than that of the EtOH/YAG:Ce nanodispersion, which means that a one-on-one comparison of their average size is not highly reliable. Moreover, the polydispersity also has implications for the average particle size predicted by DLS measurements. As explained in Section 3.2.3, the intensity size distribution emphasizes larger particles in the dispersion. For more polydisperse samples, such as the EtOH/YAG:Ce nanodispersions, the intensity-based analysis by DLS thus likely overestimates the average particle size. Since the intensity of Rayleigh scattering is strongly dependent on the particle size ($I \propto d^6$), the estimated concentration should be regarded as an order-of-magnitude estimate.

6.1.5. Conclusion

In the original research plan, the idea was to start experimenting with a commercially obtained aqueous Al_2O_3 nanodispersion. The reason to start with these nonluminescent nanoparticles is that the synthesis of luminescent inorganic nanoparticles by PHYSEE was not yet completed at the start of this thesis research project. Opting for commercially available aqueous dispersions of inorganic rare-earth doped nanoparticles was not feasible because these are very rare—the few available options typically cost hundreds of euros per milliliter and, moreover, contain functionalized NP surfaces. Since the working principle of the phase transfer process to toluene is identical for all hydroxylated nanoparticles, starting with H_2O/Al_2O_3 nanodispersions would allow for extensive trials before moving on to luminescent particles. Unfortunately, the H_2O/Al_2O_3 nanodispersion acquired at US Research Nanometrials, Inc. turned out to contain unknown dispersants to aid their stabilization in water, which had not been disclosed by the supplier. Besides, the average particle size was measured to be roughly 150 nm in diameter instead of the listed value of 30 nm. For these reasons, no further experiments were conducted with the H_2O/Al_2O_3 nanodispersion.

All batches of $Ba_3(PO_4)_2$:Mn^{5+} nanopowder synthesized by PHYSEE during the course of this project was measured to consist of agglomerated particles an average particle diameter in the micrometer range. Dispersing the particles in diluents with various pH values, followed by extensive ultrasonication and centrifugation did not result in nanodispersions with an appreciable particle concentration. The findings indicate that the agglomeration of the particles had already occurred during the synthesis process and is to a large extent irreversible. At this stage, the particles synthesized by PHYSEE were thus unsuited for the fabrication of polymer nanocomposites.

While the YAG:Ce nanopowder was also observed to contain large agglomerates in SEM analysis, the agglomeration was to some extent reversible. Dispersion studies revealed that in the proper diluents and after

prolonged ultrasonication, multimodal particle size distributions could be obtained with notable peaks in the nanometer range. After filtering out the larger particles by centrifugation, nanodispersions with unimodal particle size distributions were obtained. The necessary centrifugation step is quite a labor-intensive procedure, as the volume of the centrifuge tubes is only 2mL. After centrifugation, much care has to be taken to prevent contamination with agglomerates from the bottom of the tubes while removing the EtOH/YAG nanodispersion with a pipette. In practice, only 1 mL of EtOH/YAG:Ce was obtained per centrifuge tube. The average particle size and the scattering intensity—which combined give an indication of the particle concentration— could be controlled by adjusting the initial YAG:Ce concentration, ultrasonication time and centrifugation time. The particles were found to be stable in acidic and neutral aqueous diluents, as well as in ethanol. Dispersion of the particles in ethanol is beneficial for the phase transfer process, as was discussed in Section 3.2.2. The downside of the centrifugation step is that it drastically reduces the particle concentration—and thereby the luminescence intensity of future polymer nanocomposite films. In spite of this serious drawback, the EtOH/YAG:Ce nanodispersions were the best option to proceed with the project. Unless otherwise stated, the EtOH/YAG:Ce nanodispersions used for further experiments were prepared by dispersing 5 wt% YAG:Ce particles in EtOH, followed by 30 minutes of ultrasound treatment in an ultrasonic bath and 5 minutes of centrifugation at 13,000 rpm. The nanodispersions obtained by following this procedure were highly reproducible. The particles typically had an average hydrodynamic diameter of about 70 nm and the particle concentration was estimated to be around 0.007 vol%. The centrifugation step reduces the particle concentration in the dispersion by more than a factor 100. Higher particle concentrations can possibly obtained by using more advanced deagglomeration methods to break up the agglomerated particles before the centrifugation step, for example with a ball-mill or a powerful ultrasonic probe.

6.2. Phase transfer to nonpolar solvents

The aim of the phase transfer process is to transfer the YAG:Ce nanoparticles that are stably dispersed in ethanol to a nonpolar (organic) solvent, while preserving the initial particle size. Once the nanoparticles are stable in the organic solvent, they be be mixed with the desired polymer to form polymer nanocomposites. The challenge in this procedure is to prevent the nanoparticles from agglomerating during the phase transfer, which inherently occurs when the particles are directly mixed with the organic solvent. In order to prevent this undesired agglomeration, the nanoparticles are stabilized during the phase transfer process using amphiphilic copolymers. Two types of amphiphilic copolymers have been studied in this research: PE-b-PEG block copolymers and PEHMA-stat-PMPEOMA statistical copolymers. The block copolymers turned out to be unsuitable for the fabrication of nanocomposite films and were for that reason not included in the paper. However, they were undoubtedly successful in transferring the nanoparticles to a nonpolar solvent. The experimental work on these block copolymers gave valuable insights on the parameters that are crucial to the phase transfer process. This section aims to do justice on the theoretical and experimental work that has led to a better understanding of the stabilization behavior during the phase transfer process. Ultimately, this groundwork has resulted in the successful transfer of the YAG:Ce nanoparticles to toluene and their incorporation into polymer matrices using the PEHMA-stat-PMPEOMA copolymers, which has been extensively described in the paper. First, however, this section will elaborate on the phase transfer process in monophasic solvent mixtures, which is used throughout this study and is arguably the most crucial step in the fabrication of the nanocomposites.

6.2.1. Monophasic solvent mixture

Ternary solvent mixture

Section 3.2.2 explains the phase transfer procedure of water-dispersed inorganic nanoparticles to nonpolar solvents using a monophasic ternary solvent mixture, which has been developed by Jonschker et al. [126]. In this procedure, an aqueous nanodispersion is diluted with ethanol before being mixed with the nonpolar solvent that contains dissolved amphiphilic copolymers. In this study, toluene has been selected as the nonpolar solvent. Toluene is able to dissolve both the amphiphilic copolymers and the selected matrix polymers. Moreover, the relatively high boiling point of toluene is beneficial for the phase transfer process, as we will see later. The ratio of toluene, ethanol and water needs to be carefully balanced to obtain a monophasic solvent mixture which is able to dissolve the copolymers. In the ternary solvent mixture, the copolymers should adsorb to the nanoparticles before the particles have the chance to agglomerate. When their surfaces are fully covered, the copolymers prevent the nanoparticles from agglomerating through steric forces and the nanoparticles are said to be sterically stabilized. The solvent mixture can be separated again into a nonpolar

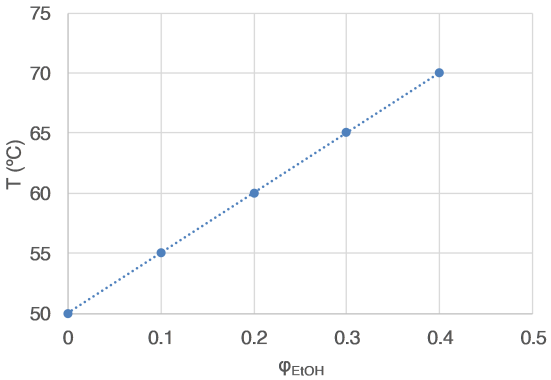

Figure 6.11: Maximum water intake in the monophasic ternary solvent mixtures of toluene, ethanol and water plotted against the ethanol content, both displayed in terms of their volumetric ratio to toluene.

Figure 6.12: Experimental setup for the phase transfer process.

phase containing the stabilized nanoparticles and a polar phase by the addition of water. The ethanol plays a crucial role in the ternary solvent mixture. Because water is immiscible with nonpolar organic solvents such as toluene, the aqueous nanodispersion of nanoparticles cannot be mixed directly with the toluene phase. In order to close the miscibility gap, a medium-polarity cosolvent such as ethanol is required. The ratio of ethanol to toluene determines how much of the aqueous nanodispersion can be incorporated in the monophasic solvent mixture.

The maximum water intake as a function of ethanol content has been studied for various solvent mixtures at room temperature. Figure 6.11 shows the maximum intake of water for solvent mixtures of toluene and ethanol with varying ethanol content. Both the water intake and ethanol content are given in terms of their volumetric ratio to toluene. As expected, a higher EtOH ratio increases the amount of water that can be added before phase separation occurs. The maximum water intake versus EtOH ratio seems to follow a power law relation with an exponent approximately equal to 2. When more water is added, an unstable emulsion is formed which quickly separates into a polar and nonpolar phase. The water intake was observed to increase at elevated temperatures. Increasing the temperature generally improves the miscibility of incompatible solvents, thus allowing more water to be part of the solvent mixture [159].

Initially multiple experiments have been conducted to attempt a successful phase transfer of the YAG:Ce nanoparticles in a ternary solvent mixture. Two variations of the procedure were tested. In the first procedure, the H_2O/YAG:Ce nanodispersions were diluted with ethanol and added to the toluene phase with dissolved PE-b-PEG copolymers. In the second, the ethanol was mixed with the nonpolar phase before the addition of the H_2O/YAG:Ce nanodispersions. Both cases did not result in a successful transfer. In hindsight this could probably be attributed to the PE-b-PEG copolymers that are only effective in specific conditions, as we will see later in this section. More importantly, the separation of the polar and nonpolar phase by the addition of water turned out te be quite a hassle. Often water droplets were present in the nonpolar phase which interfered with the DLS measurements, or the particles were left in the polar phase after the addition of water. The fact that the nanoparticles were also stable in ethanol allowed for the development of an adapted, simpler version of this procedure, which is described next.

Binary solvent mixture

Since the YAG:Ce nanoparticles were found to be stable in ethanol, a simplified procedure for the phase transfer was developed in this thesis research. Instead of balancing ratio of toluene, ethanol and water to obtain a monophasic ternary solvent mixture, a binary solvent mixture of toluene and ethanol was used. Because toluene and ethanol are fully miscible, the binary solvent mixtures are always monophasic and the maximum ethanol content is only limited by the solubility of the amphiphilic copolymers. The experimental setup for the phase transfer process is shown in Figure 6.12. First, vials containing the nonpolar phase with dissolved amphiphilic copolymers are heated to the desired temperature on a hot plate. The hot plate was found to not heat evenly over its surface, as the position of the vials on the hot plate was observed to significantly influence the results. Therefore, the temperature of each vial was measured separately with a construction of clamped thermometers, which is not shown in Figure 6.12. As soon the desired temperature was reached, the

Figure 6.13: PE-b-PEG copolymers dissolved in toluene with a concentration of 10 gL^{-1}, from left to right: B575, B875, B920, B1400.

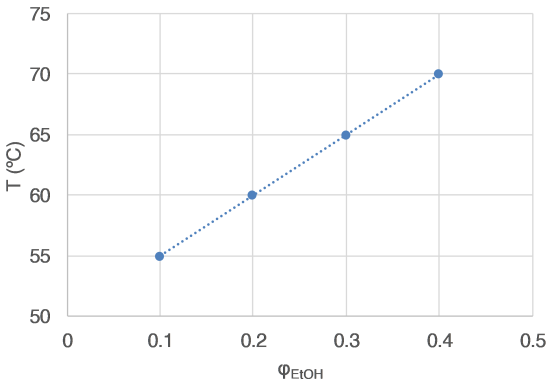

Figure 6.14: Dissolution temperature of B875 plotted against the volume fraction of ethanol in the toluene/ethanol mixture.

EtOH/YAG:Ce nanodispersion was pipetted into the vial. After the copolymers had adsorbed to the nanoparticle surfaces in the resulting mixture, the ethanol was simply evaporated to obtain a pure toluene phase with sterically stabilized nanoparticles. The use of toluene as the nonpolar phase is suitable for this procedure, because it has a much higher boiling point than ethanol (111°C vs. 78°C). Using a binary solvent mixture greatly simplifies the phase transfer procedure and is therefore used throughout this study.

As discussed in Section 2.4.2, the success of stabilization in the solvent mixture depends on the adsorption kinetics of the amphiphilic molecules. Apart from the molecular structure of the copolymers, several other parameters were found to be of crucial importance to the success of stabilization. The most important ones are the concentration of the amphiphilic copolymers, the temperature and the composition of the solvent mixture. Together, these parameters determine whether the nanoparticles are successfully transferred to the nonpolar phase, or agglomerate in the process. The effect of these parameters on the particle size after the phase transfer process was extensively studied for both the PE-b-PEG and the PEHMA-stat-PMPEOMA amphiphilic copolymers. All phase transfer experiments were performed using the same batch of EtOH/YAG:Ce nanodispersion and—as much as possible—under the exact same circumstances in order to compare the behavior and performance of the copolymers. Moreover, many experiments have been conducted to determine the best method for mixing the EtOH/YAG:Ce nanodispersion with the nonpolar phase. For example, it was studied whether adding the nanodispersion in consecutive drops was better than all at once. This was by the way not the case, which is probably related to the fact that physically adsorbing copolymers can form multilayers onto the particle surfaces [66, 86, 148]. The influence of mechanical agitation during the phase transfer, the speed of pipetting, the type of pipette and pipette tip, the volume of the liquid, the size of the flasks and so on were also studied and found have at least some effect. Studying the effect of all these process parameters was necessary to develop a method that was highly reproducible and ruled out most unwanted influences on the measurement results.

6.2.2. PE-b-PEG

The initial research plan involved the use of relatively low molecular weight PE-b-PEG block copolymers, as described in Section 3.2.1. Using block copolymers can be problematic due to the formation of "frozen" micelles that hamper the adsorption kinetics. Moreover, the molecular weight of the block copolymers is much lower than typical matrix polymers, which often leads to agglomeration due to compatibility issues. Both of these phenomena are explained in detail in Section 2.4.2. Still, these copolymers were the most promising commercially available option to start with. Four different types of PE-b-PEG copolymers were studied, which allowed to study the influence of the molecular weight and the ratio of ethylene oxide (EO) functional groups in the structure. The different types are listed in Section 3.2.1 and are named according to their molecular weight in $gmol^{-1}$: B575, B875, B920 and B1400. The EO ratio is equal to 20 wt% for B575 and B875 and 50 wt% for B920 and B1400.

Solubility

Unfortunately, the PE-b-PEG copolymers turned out to unsuitable for the fabrication of polymer nanocomposite films. The main reason for their inadequacy was not necessarily one of the risks mentioned above, but rather their insolubility in toluene at room temperature. In contrast to the product specifications listed by

the supplier, which states that the PE-b-PEG copolymers are soluble in toluene, none of the copolymers actually dissolve at room temperature. Instead, they form non-transparent milky suspensions as shown in Figure 6.13. The insolubility at room temperature can be attributed to the crystalline nature of the PE-b-PEG copolymers. The temperature-dependent phase separation is a characteristic property of surfactants containing polyethoxylate (PEG) chains. The temperature at which the phase separation occurs and the molecules start to flocculate is known as the Krafft temperature.

The dissolution temperature of the PE-b-PEG copolymers was studied experimentally for various solvent mixtures and copolymer concentrations. The concentration of PE-b-PEG did not significantly influence the dissolution temperature over the concentration range that can be reasonably expected for a successful phase transfer (up to 20 gL^{-1}). The solvent composition, on the other hand, was found to play an important role. Figure 6.14 shows the temperature at which B875 was observed to dissolve in various mixtures of toluene and EtOH. The dissolution temperature rises as the volume fraction of EtOH increases, which indicates that the addition of ethanol decreases the solvent quality for the copolymer. In order to understand this behavior, the solubility of the PE-b-PEG copolymers in different solvent mixtures was studied by a theoretical model. The solubility of the PE-b-PEG copolymers in various solvents and solvent mixtures can be described by the Hansen solubility parameters δ_d, δ_p and δ_h of the copolymers and the solvent, as well as by the Flory-Huggins polymer-solvent interaction parameter χ. The reader is referred to Section 5.1.1 for details on the estimation of the Hansen solubility parameters, their graphical representation in a three-dimensional solubility space and the computation of the Flory-Huggins interaction parameter.

In Figure 6.15, the Hansen solubility parameters of PE-b-PEG copolymers are plotted in a three-dimensional solubility space, together with several solvents and solvent mixtures of toluene and ethanol. The dots on the line connecting toluene to ethanol represent solvent mixtures with increments of 10 vol% EtOH. A sphere with interaction radius R is drawn around copolymer B575. Since the value of R specific to PE-b-PEG is unknown, the value of $\Delta\delta$ between B575 and the solvent methyl ethyl ketone (MEK) is chosen as R, which is the solvent with the largest $\Delta\delta$ known to be able to dissolve B575. Given that all four PE-b-PEG copolymers are so close together in the solubility sphere, the results for the other PE-b-PEG types are similar. Therefore, most solvents positioned inside this sphere can be expected to dissolve the PE-b-PEG copolymers. It should be noted that for crystalline polymers such as PE-b-PEG, the concept of the solubility parameter is only valid at temperatures higher than 90% of their melting point [159]. The melting point of the PE-b-PEG copolymers is approximately 100°C, which means that they are expected to show reduced solubility at much lower temperatures. In fact, for temperatures below 50°C the copolymers are no longer soluble in toluene at all, as was shown in Figure 6.11.

The solubility sphere in Figure 6.15 predicts that toluene/ethanol solvent mixtures with up to 60 vol% EtOH should be able to dissolve the PE-b-PEG copolymers at high temperatures. This is relevant, because this means that more of the EtOH/YAG:Ce nanodispersion can be incorporated in a solvent mixture with toluene without precipitation of the copolymers. However, there is a difference in solubility behavior depending on the EtOH fraction. The minimum dissolution temperature increases for higher EtOH fractions, as shown in Figure 6.11. The influence of the solvent composition on the solubility can be explained by analyzing the solvent quality, which is described in terms of the Flory-Huggins interaction parameter χ. Figure 6.16 shows the computed values of χ for the copolymers in the solvent mixture at room temperature as a function of the EtOH fraction in the solvent. In addition, the interaction parameter of the EO functional groups is shown. The polar EO groups clearly have higher affinity with the solvent in toluene/ethanol solvent mixtures than in pure toluene. The solvent quality is optimal in a broad minimum centered around 45 vol% EtOH. Not surprisingly, the optimal value of χ for copolymers B920 and B1400 is found at higher EtOH fractions than for B575 and B875—containing 50 wt% and 20 wt% EO, respectively. The model predicts that the solvent quality for B875 is negatively affected by increasing the EtOH fraction in the solvent mixture. This corresponds with the observations on the dissolution temperature of B875 in Figure 6.14. Elevating the temperature decreases the value of χ, which means that solvent mixtures with a lower solvent quality for B875 need higher temperatures to dissolve the copolymer.

Micellization

A potential problem of using amphiphilic block copolymers for the phase transfer process is that they are notorious for forming stable micellar structures. More details on the formation of so-called "frozen" micelles are given in Section 2.4.2. The formation of micelles can be detrimental to the adsorption kinetics, as the unimers in the micelles are not free to adsorb to the nanoparticle surfaces. Micelles of amphiphilic molecules in nonpolar solvents form by the aggregation hydrophilic groups inside the core and are known as reverse mi-

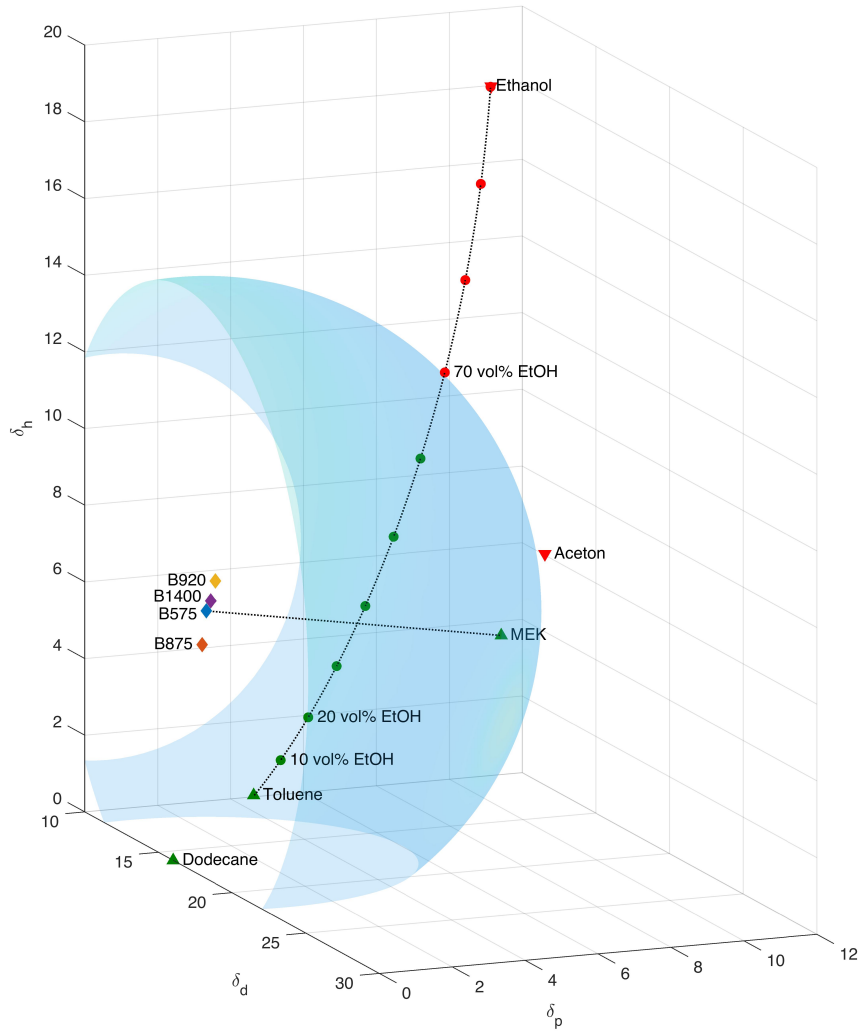

Figure 6.15: Hansen solubility paramters of the PE-b-PEG copolymers and several solvents plotted in a three-dimensional solubility sphere. Solvents inside the sphere (in green) are expected to dissolve the copolymers, while solvents outside the sphere (in red) are not.

celles. Some block copolymers can spontaneously form reverse micelles in selective organic solvents [194]. However, Alexandridis and Andersson found that polyoxyalkylene block copolymers such as PE-b-PEG typically do not spontaneously form reverse micelles in organic solvents, even if the solvent is selective for one of the blocks [195]. For these block copolymers, the formation of reverse micelles requires the addition of small amounts of water and only occurs if the copolymer concentration is sufficiently high. The authors reported that a similar diblock copolymer of poly(butylene oxide) and poly(ethylene oxide) (PBO-b-PEO) with a molecular weight of 1500 $\mathrm{g\,mol^{-1}}$ and 50 wt% EO groups has a critical micelle concentration (CMC) of 3 wt% in xylene (a selective solvent for the PBO blocks) in the presence of small amounts of water. In general, the authors found that the cmc increases as the molecular weight decreases. No clear relation with the concentration of hydrophilic EO groups was observed. The phase transfer procedure used in this study is based on a binary solvent mixture of toluene and ethanol and does not involve any water to induce the formation of reverse micelles. However, it is conceivable that the formation of reverse micelles is promoted by the addition of ethanol. Therefore, the presence of micelles in solvent mixtures with varying ethanol content was studied by DLS.

Figure 6.17 shows DLS measurements of 10 $\mathrm{g\,L^{-1}}$ B575 dissolved in various solvent mixtures of toluene

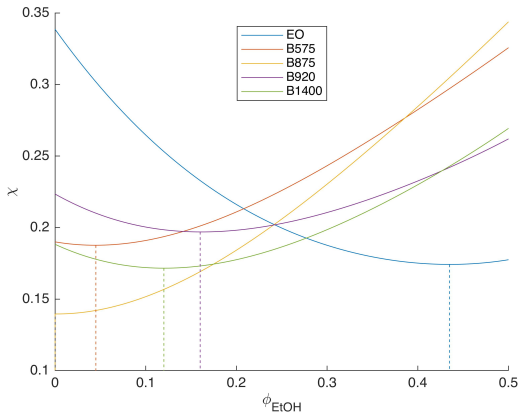

Figure 6.16: Computed values of the Flory-Huggins interaction parameter χ of the PE-b-PEG copolymers and the EO functional groups as a function of the EtOH fraction in the solvent mixture.

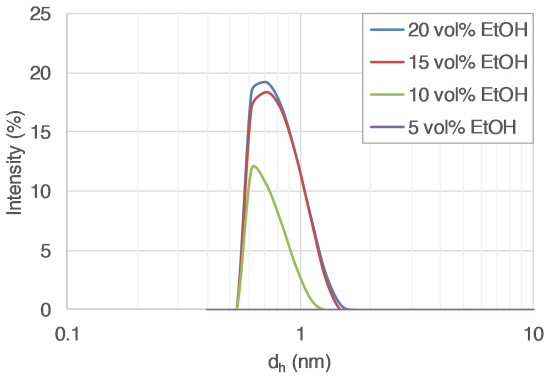

Figure 6.17: DLS measurements of 10 gL^{-1} B575 dissolved in various solvent mixtures of toluene and ethanol. The peaks around 1 nm appear as the EtOH fraction increases, suggesting the formation of reverse micelles.

and ethanol. The appearance of peaks around 1 nm with increasing EtOH volume fraction suggests that the copolymers indeed form reverse micelles in the solvent mixture. The characteristic peaks around 1 nm are observed for all four types of PE-b-PEG when the amount of EtOH is increased and disappear after the evaporation of the EtOH. For B575 and B875 (20 wt% EO) the peaks start to appear at EtOH fractions of 10 vol%, while for B920 and B1400 (50 wt% EO) the peaks are observed at fractions as low as 5 vol%. Moreover, the micelle formation seems to be independent of the stabilizer concentration, as is expected for concentrations above the CMC. It should be noted that the data quality of these DLS measurements is poor and the size distribution results might not be very accurate. This inaccuracy can mainly be attributed to the low scattering intensity of the small micelles, which result in count rates close to the reference value of pure toluene. This means that the samples are extremely sensitive to dust and other contaminants, even after careful filtering of the solvents. The contaminants show as inexplicable peaks at particles sizes ranging from hundreds of nanometers to several microns, which have been left out of Figure 6.17. It is unclear to what extent the presence of micelles hampers the adsorption kinetics during the phase transfer process.

Results

The success of stabilization during the phase transfer process was found to depend mainly on three parameters: the amphiphile concentration, the temperature and the solvent composition. The effect of these parameters on the stabilization kinetics is elaborately described in the paper and Section 5.2. Although the PE-b-PEG copolymers are insoluble at room temperature and therefore unsuitable for the preparation of transparent nanocomposite films, they were certainly successful in the phase transfer process. The influence of the PE-b-PEG concentration, the temperature and the solvent composition on the particle size after the phase transfer was studied.

Amphiphile concentration Figure 6.18 shows the results of an initial set of measurements on the concentration-dependence of the PE-b-PEG copolymers. In the experiment, 5 vol% of the EtOH/YAG nanodispersion was added to the toluene phase with various concentrations of the dissolved copolymers at 90°C. Toluene/YAG:Ce dispersions were obtained after evaporation of the EtOH. Figure 6.18 shows the average hydrodynamic diameters of the particles in the dispersion measured after the phase transfer process. Interestingly, the copolymers were found to show very different behaviors. Copolymers B575 and B875 (both containing 20 wt% PEG) behaved as expected and became more effective when the concentration was increased. The influence of the concentration was clearly visible to the naked eye, as shown in the top figure of Figure 6.19. Below concentrations of 1 gL^{-1}, the copolymers were unable to prevent agglomeration and large flocs were formed. Measurements of the agglomerated samples are not included in Figure 6.18, because the data quality of the DLS measurements was too poor for a reliable determination of the average particle size. The poor data quality can be attributed to the fact that the size of the agglomerates is outside of the measurement range of DLS (maximum 10 µm), as well as to the the high polydispersity of the samples. For copolymers B920 and B1400 (containing 50 wt% PEG) the opposite behavior was observed, as can be seen the bottom

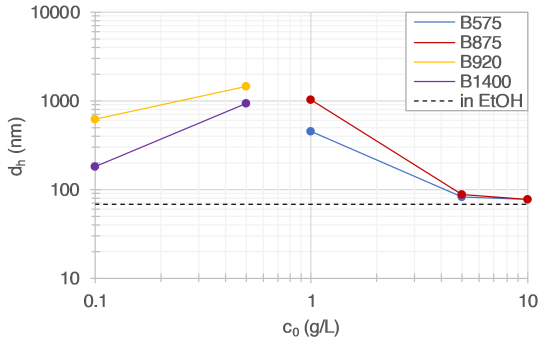

Figure 6.18: Average hydrodynamic diameter of the YAG:Ce particles after the phase transfer using various PE-b-PEG concentrations at 90°C.

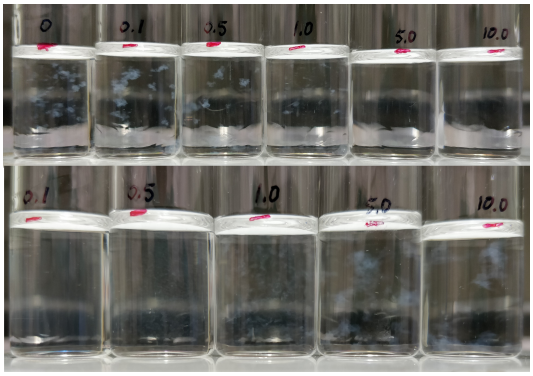

Figure 6.19: Opposite behavior of PE-b-PEG copolymers with 20 wt% and 50 wt% PEG. Top: B875 with $c_0 = 0, 0.1, 0.5, 1, 5, 10$. Bottom: B920 with $c_0 = 0.1, 0.5, 1, 5, 10$.

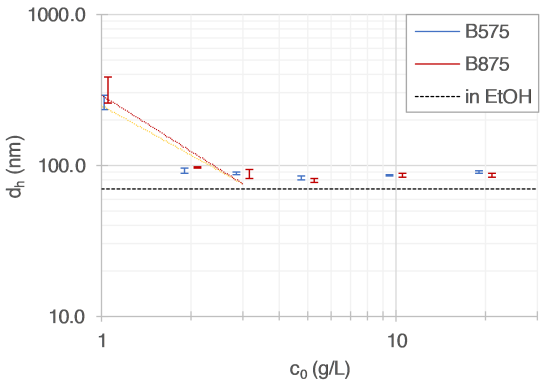

Figure 6.20: Average hydrodynamic diameter of the YAG:Ce particles after the phase transfer for B575 and B875 with varying concentration, for $T = 100$°C and $\phi_{\text{EtOH}} = 5$ vol%.

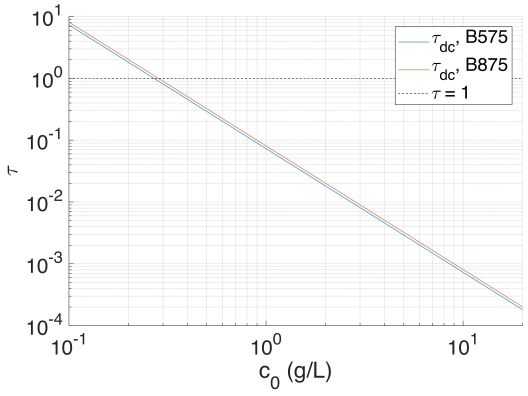

Figure 6.21: Stabilization kinetics paramter τ for DC adorption of copolymers B575 and B875 plotted against the copolymer concentration. The point $\tau = 1$ corresponds to equal rates of amphiphile adsoprtion and nanoparticle agglomeration.

figure of Figure 6.19. The reason for the opposite behavior is not entirely clear. One possible explanation is that copolymers with high PEG content promote bridging flocculation, in which the long PEG tails form molecular "bridges" between particles by simultaneously adsorbing onto multiple particles. Possibly, the bridging effects are more pronounced at higher copolymer concentrations. That being said, typical polymer flocculants are usually of much higher molecular weight [151, 196]. In any case, copolymers B575 and B875 showed much more promising results. As can be seen in Figure 6.18, at high concentrations both copolymers were able transfer the nanoparticles to toluene with practically no agglomeration.[1] Therefore, no further experiments were conducted with copolymers B920 and B1400, and instead copolymers B575 and B875 were studied in more detail.

Figure 6.20 shows the results of the same experiments performed at 100°C with at least 3 samples per concentration. The measurements are displayed as error bars. Both copolymers show a very rapid transition in their stabilization behavior at low concentrations. The strong dependence on the copolymer concentration is an indication of diffusion-controlled (DC) adsorption kinetics, as was explained in Section 5.2. The slope of the regression lines fitted to the measured particle sizes between 1 and 3 gL^{-1} (at 100°C and with 5 vol% EtOH, as shown in Figure 6.20) were found to be -1.1 and -1.2 for B575 and B875, which are close to the predicted value of -1.1 for DC adsorption. It should be mentioned that with an R^2 value of around 0.9, the goodness of fit is much lower than those of the PEHMA-stat-PMPEOMA copolymers, which were governed by kinetic-controlled (KC) adsorption in the same conditions. It should be stressed, moreover, that the slope depends strongly on the concentration range of the regression line. It is much steeper between 1 and 2 gL^{-1} than

[1] It should be noted that the transfer process was found to be extremely temperature-dependent and many trials had preceded these measurements without any success. In fact, these results were only obtained mid June 2019, more than four months after the start of the experimental phase of this thesis research.

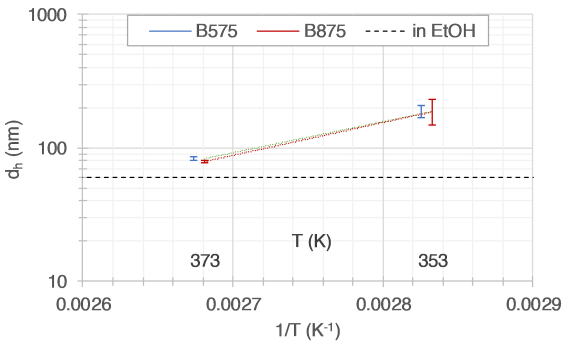

Figure 6.22: Average hydrodynamic diameter of the YAG:Ce particles after the phase transfer for B575 and B875 with varying temperature, for $c_0 = 5$ gL^{-1} and $\phi_{EtOH} = 5$ vol%.

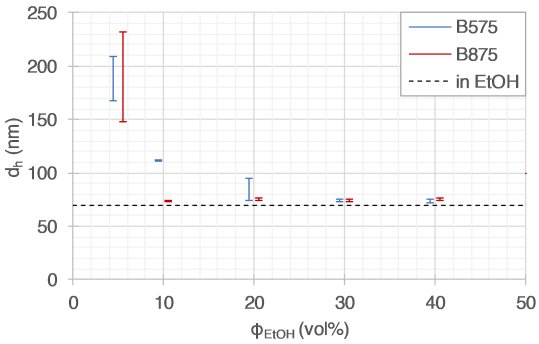

Figure 6.23: Average hydrodynamic diameter of the YAG:Ce particles after the phase transfer for B575 and B875 with varying EtOH fraction, for $c_0 = 5$ gL^{-1} and $T = 80$°C.

between 2 and 3 gL^{-1}. Therefore no definite conclusion can be drawn on the adsorption behavior based on these measurements. More measurements in this narrow concentration range and at various temperatures might provide a better understanding of the behavior.

Figure 6.21 plots the results of the theoretical model on DC stabilization kinetics for copolymers B575 and B875. The model predicts that the point $\tau = 1$, at which the rate of amphiphile adsorption and nanoparticle agglomeration are estimated to be equal, is reached at a concentration of around 0.3 gL^{-1}. The results provide a fairly good estimation of the required copolymer concentration. Effective stabilization is expected when adsorption occurs much faster than agglomeration. The concentration range between 2–5 gL^{-1} where the particles are measured to be effectively stabilized corresponds with $\tau = 10^{-2}$–10^{-3}. In other words, stabilization expected to be when the successful when the adsorption occurs a factor of 100 to 1000 faster than agglomeration. Of course, these predictions are based on numerous assumptions and only serve as a tool to understand the influence of the concentration on the stabilization kinetics.

Temperature The success of stabilization was found to depend strongly on the temperature at which the phase transfer takes place. Figure 6.22 shows the influence of the temperature on the average particle size after the phase transfer process. In the experiment, 5 vol% of EtOH/YAG:Ce nanodispersion was added to the toluene phase with 5 gL^{-1} dissolved B575 and B875 copolymers at 80 and 100°C. The average particle size was measured by DLS after evaporation of the ethanol. The error bars are based on measurements of three separate samples. Agglomeration was found to drastically increase at temperatures of 80°C and below. The temperature dependence is typically indicative of KC adsorption, in which the adsorption rate of the amphiphile is not limited by the rate of amphiphile transport to the nanoparticle surface but rather by kinetics effects during the binding step. One could argue that the decrease in efficacy of the copolymers is related to their crystalline nature, which leads to reduced solubility at lower temperatures. However, as we will see next, temperatures of 80°C were found to be sufficient for successfull stabilization when the solvent composition was altered.

Solvent composition The effect of the EtOH fraction in the solvent mixture during the phase transfer on the average particle size is plotted in Figure 6.23. This time, 5 vol% of EtOH/YAG:Ce nanodispersion was added to solvent mixtures with varying EtOH content containing 5 gL^{-1} B575 or B875 at 80°C. After adding the nanodispersion, the ethanol was evaporated and the resulting average particle size was measured by DLS. The increased polarity of the solvent is clearly beneficial to the phase transfer process, which means that the adsorption process is limited by kinetic effects. The YAG:Ce particles could be transferred to the toluene phase with virtually no observable agglomeration. Comparing the results to the computed interaction parameters in Figure 6.16, the resemblance with χ of the EO functional groups is striking. This suggests that increasing the solvent quality for the functional groups greatly benefits the adsorption kinetics. We suppose that this effect is attributed to steric shielding of the binding groups, either in intramolecular or intermolecular (micellar) structures. In the first case, the polar EO groups are shielded from the toluene solvent by a shell of nonpolar PE. This limits their ability to bind to the hydrophilic YAG:Ce particle upon collision. When the EtOH fraction is increased, the EO moieties become free to assume positions in the outer shell of the copolymer coil, thereby increasing the probability of binding. The same behavior was observed for the PEHMA-

stat-PMPEOMA copolymers in the paper. In the second case, the copolymer molecules are aggregated and kinetically stable in micelles with their polar PEG chains facing inward. Since EtOH is able to form hydrogen binds with the PEG chains in the core, it is conceivable that interaction between the chains in the core becomes weaker. This makes it easier for the molecules to desorb from the micelles, thus allowing them to adsorb to the YAG:Ce particles. Slightly higher volume fractions of EtOH are required for the lower molecular weight B575 than for B875. This might be related to a difference in the intramolecular conformation of the copolymers, which makes it easier for the EtOH molecules to penetrate the larger B875 coils. It is likely that better results can also be expected for copolymers B920 and B1400 by adjusting the polarity of the solvent, but this has not been studied.

Conclusion
With proper tuning of the concentration, temperature and solvent composition, the PE-b-EG copolymers with 20 wt% EO were found to be extremely successful in stabilizing of the YAG:Ce nanoparticles during the phase transfer to toluene. The particles could be transferred without any sign of agglomeration. We can thus conclude that the micellization of these block copolymers is not an issue to the adsorption process. Increasing the temperature ethanol fraction in the solvent mixture was found to be especially beneficial, which indicates that the adsorption of the copolymers is typically limited by kinetic effects. The difference in molecular weight was found to be negligible. Even though the results seem promising, they PE-b-PEG copolymers were of no use for the fabrication of transparent polymer nanocomposites. The nanocomposite films made with toluene/YAG:Ce nanodispersions stabilized the PE-b-PEG copolymers were all nontransparent, as we will see later in this chapter. This is due to the crystallization of the copolymers at temperatures below 50°C, which causes the toluene/YAG:Ce nanodispersions to be turbid at room temperature. This resulted in the search for alternative amphiphilic copolymers, which were eventually found in the form of PEHMA-stat-PMPEOMA.

6.2.3. PEHMA-stat-PMPEOMA

Selection
The realization that the PE-b-PEG copolymers were not going to lead to transparent polymer nanocomposites initiated the search for alternative amphiphilic copolymers that are better suited to the process. As described in 2.4.2, the copolymers should preferably be statistical copolymers to prevent micellization, have sufficient anchor groups to provide strong binding to the particle surface and have sufficiently high molecular weight to provide compatibility with the polymer matrix. The nonpolar part of the copolymers should be compatible with a transparent matrix polymer, while the polar part should be able to adsorb to hydroxylated nanoparticle surfaces. The copolymers should be soluble a high-boiling point solvent that dissolves common organic matrix polymers, such as toluene, as well as in solvent mixtures of this solvent with a medium polarity solvent such as ethanol. Evidently, the copolymers should be transparent, which generally means that they should be amorphous.[2] Besides, we would like to vary at least one parameter of the copolymer—such as the type of binding group, the fraction of polar monomers or the molecular weight—to study its influence on the stabilization of the nanoparticles. Needless to say, no commercially available option was found that meets all of these requirements. At this stage in the project, the synthesis and characterization of these copolymers were outside of the scope of this research. Also within TU Delft I could not find an opportunity acquire such copolymers. That is why I started to reach out to third parties that are specialized in polymer synthesis. Through a contact of PHYSEE I finally got into contact with DSM Coating Resins, a subsidiary of DSM that manufactures a wide range resins for polymeric coatings. The company agreed to make a number of of custom-designed samples of amphiphilic statistical copolymers.

The selection of the right monomers for the design of the amphiphilic copolymers was crucial. The nonpolar part should be compatible with a matrix polymer that is suitable for the preparation of transparent films by solution mixing. An overview of the suitability several common polymers was given in Section 3.2.1. The compatibility between the amphiphilic copolymer and the matrix polymer depends on the similarity in the chemical structure and molecular weight, as was discussed in Section 2.4.2. Therefore, protected polymer brands such as TOPAS and CYTOP with unknown molecular weights and precise molecular structure are not preferred. Polymethacrylates are a class of amorphous thermoplastic polymers that have good optical properties, are widely available and are often found in copolymers. Commercially the most important type of polymethacrylate is poly(methyl methacrylate) (PMMA), which is also known as acrylic glass. A methacrylate monomer with close chemical resemblance to PMMA that DSM Coating Resins had experience with was 2-

[2] The transparency of polymers is related to the scattering of light as it passes through the material. Crystalline polymers are typically opaque, because light scatters on the boudaries of amorphous and crystalline regions.

	mol%/wt% MPEOMA	M_n (kDa)	M_w (kDa)	PDI
Copolymer A	5 / 10	19.0	36.5	1.92
Copolymer B	10 / 20	28.6	44.0	1.53
Copolymer C	15 / 28	32.9	47.9	1.52

Table 6.2: MPEOMA fraction, molecular weight and polydispersity index (PDI) of the synthesized PEHMA-stat-PMPEOMA copolymers.

ethylhexyl methacrylate (EHMA). Amphiphilic copolymers of PEHMA are often encountered in literature and have been shown to work for the in situ stabilization of nanoparticles during their synthesis in inverse emulsion techniques [50, 83, 197, 198] and even for the formation of transparent nanocomposites [84, 127]. The EHMA should be copolymerized with a polar comonomer, preferably one with nonionic moieties, because they can bind to a wide range of polar surfaces. Copolymers with zwitterionic moieties, which contain both a positive and a negatively charged binding group and are also know as betaines, are also effective but more difficult to synthesize [72, 84]. One of the nonionic comonomers that is often found in literature—even in combination with PEHMA—and which has been shown to adsorb to inorganic nanoparticles is poly(ethylene oxide methacrylate) (PEOMA or PEGMA) [50, 73, 74, 125, 127, 197, 198]. About 5–9 EO units in the PEOMA chains are enough to provide equally strong anchoring to hydroxylated metal oxide nanoparticles as acidic or ionic binding groups [73]. The closest available option at DSM Coating resins was methoxy poly(ethylene oxide) methacrylate (MPEOMA), which was available with approximately 8 EO units in the chain (MPEG350MA). Random copolymerization of both monomers results in the amphiphilic statistical copolymer PEHMA-stat-PMPEOMA, which were used throughout the remainder of this project.

The synthesis procedure of the PEHMA-stat-PMPEOMA copolymers allowed for the variation of either the molecular wight or the concentration of the polar moieties. For the selection of the molecular weight, there is a trade-off between the adsorption kinetics and the compatibility with polymer matrices. As was explained in Section 2.4.2, the closer the molecular weight of the amphiphilic copolymer is to the high molecular weight matrix polymer, the better the compatibility. However, comparable amphiphilic copolymers with molecular weights smaller than 28 kDa were more effective for in situ stabilization than those with 70 or 140 kDa [72]. Comparable amphiphilic copolymers that were found to be effective in the fabrication of nanocomposites typically have molecular wights of around 10 kDa [72, 84, 127]. The influence of the molecular weight on the dispersion stability in the nanocomposites can also be studied by varying the molecular weight of the matrix polymer. Therefore, it was decided to synthesize the PEHMA-stat-PMPEOMA copolymers with fixed molecular weight of 10 kDa and vary the concentration of polar moieties. To the best of my knowledge, the effect of concentration of the polar groups on the stabilization of nanoparticles had not yet been reported in literature. Stelzig et al. reported that for the phase transfer procedure involving a monophasic ternary solvent mixture, the amphiphilic copolymers require a minimum of about 70 mol% nonpolar units and about 5 mol% polar units [127]. Therefore, MPEOMA fractions of 5 mol%, 10 mol% and 15 mol% were selected for the synthesis.

The MPEOMA fraction and the molecular wight of the synthesized PEHMA-stat-PMPEOMA copolymers are listed in Table 6.2. The molecular wight of the copolymers turned out to be significantly higher than anticipated. Moreover, there was a variation in molecular weight between the copolymers. Especially copolymer A had a much lower molecular weight than copolymers B and C. It should be noted, however, that the molecular weight of the copolymers was measured by size exclusion chromatography (SEC), which computes the molecular weight based on the hydrodynamic volume relative to that of a PMMA standard. In fact, the molar volume of EHMA and MPEOMA moieties is much higher than that of PMMA—a factor of 2.4 and 4.3 greater, respectively. This means that the SEC measurements likely overestimate the molecular wight of the copolymers. Increasing the concentration of the bulky MPEOMA groups is expected to increase the the overestimation even more. In reality, the molecular weight of the copolymers is thus expected to be lower, and the values listed in Table 6.2 only serve as estimates.

Solubility

The computed Hansen solubility parameters of the PEHMA-stat-PMPEOMA copolymers are close to those of PE-b-PEG, as was shown in Table 5.1. The solubility parameters are plotted in the three-dimensional solubility space in Figure 6.24. A solubility sphere is drawn around copolymer B with an interaction radius R equal to the distance from copolymer B to the solvent methyl ethyl ketone (MEK), which is known to be able to dissolve the copolymers. In spite of the apparent similarity with PE-b-PEG, the solubility behavior of

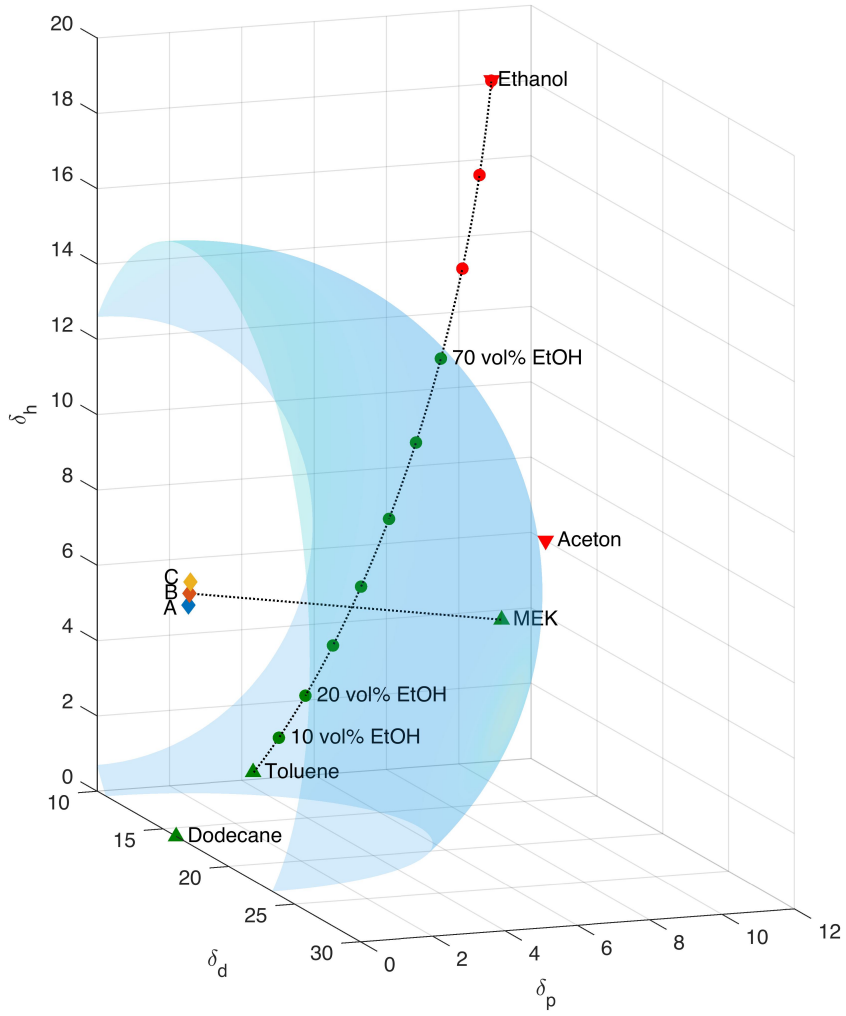

Figure 6.24: Hansen solubility paramters of the PEHMA-stat-PMPEOMA copolymers and several solvents plotted in a three-dimensional solubility sphere. Solvents inside the sphere (in green) are expected to dissolve the copolymers, while solvents outside the sphere (in red) are not.

PEHMA-stat-PMPEOMA is quite different. Because the copolymers are amorphous, they are expected to be soluble at room temperature in all solvents positioned inside the solubility sphere. This is in contrast to the crystalline PE-b-PEG copolymers, which show reduced solubility at temperatures below their melting point. Figure 6.24 shows that the PEHMA-stat-PMPEOMA copolymers should be soluble in binary solvent mixtures of toluene and ethanol with up to 70 vol% EtOH. The interaction parameters χ of the copolymers and the MPEOMA groups are plotted in Figure 6.25. The highest affinity of the MPEOMA groups with the solvent mixture is expected around 40 vol% EtOH.

Results

The same experiments were conducted with PEHMA-stat-PMPEOMA as with PE-b-PEG, which were explained in Section 6.2.2. In other words, the influence of the PEHMA-stat-PMPEOMA concentration, the temperature and the the solvent mixture composition on the particle size after the phase transfer was studied. The results of these experiments are elaborately described in Sections 4.5.3, 4.5.4 and 4.5.5 in the paper, to which the reader is referred. In general, the same trends were observed as for the PE-b-PEG copolymers. That is to say, the particle size was observed to decrease by increasing the copolymer concentration, the tem-

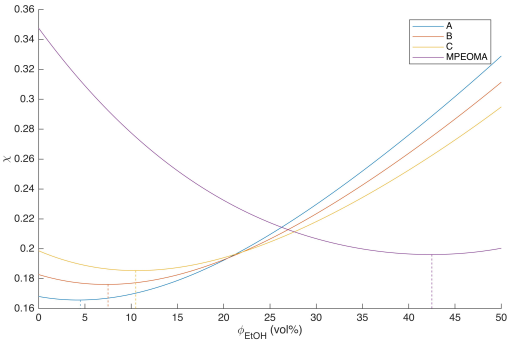

Figure 6.25: Computed values of the Flory-Huggins interaction parameter χ of the PEHMA-stat-PMPEOMA copolymers and the MPEOMA functional groups as a function of the EtOH fraction in the solvent mixture.

perature and the EtOH fraction in the solvent mixture. Furthermore, some theoretical work is presented in the paper to analyze the behavior of the stabilization process. A stabilization kinetics parameter τ was introduced to describe the influence of the copolymer concentration and the temperature on the stabilization kinetics. A new theory was developed to relate the theoretical parameter τ proportionally to the measured average particle diameter d_h. The results indicate that the adsorption of the PEHMA-stat-PMPEOMA copolymers in pure toluene is kinetic-controlled (KC), even at elevated temperatures. This can probably be attributed to the intramolecular conformation of the copolymer molecules in solution, in which the MPEOMA binding groups are sterically shielded by the nonpolar EHMA groups. The rate-limiting kinetic effects clearly reduce by increasing the temperature and can be practically eliminated by adding EtOH to the nonpolar phase prior to the phase transition. By careful tuning of the concentration, temperature and EtOH fraction, the YAG:Ce nanoparticles could be transfered to toluene without any noticeable agglomeration. While this had also been achieved with PE-b-PEG, the advantage of the PEHMA-stat-PMPEOMA copolymers is that they were indeed suitable for the fabrication of transparent nanocomposite films, as we will see in the next section.

6.3. Polymer thin film preparation

The sterically stabilized toluene/YAG:Ce nanodispersions can be mixed with polymers dissolved in toluene to obtain homogeneous solutions. Polymer nanocomposite thin films are then easily obtained by spin coating the solutions onto glass substrates.

6.3.1. Matrix polymers

The compatibility between the amphiphilic copolymers and the matrix polymer determines whether homogeneous films are obtained or whether phase separation occurs. As was explained in Section 2.4.2, compatibility is favored by chemical similarity—both in terms of their molecular structure and their molecular weight. Three different matrix polymers were tested in combination the with the toluene/YAG:Ce nanodispersions stabilized by the PE-b-PEG and PEHMA-stat-PMPEOMA copolymers. The matrix polymers and their molecular weights were listed in Table 3.4 and their molecular structures were depicted in Figure 3.3.

COC

In the original research plan, COC was selected to use in combination with the PE-b-PEG copolymers. Both are copolymers of ethylene and the similarity in their molecular structure was expected to promote compatibility. For more information about COC, the author is referred to Section 3.2.1. Even though the molecular weight of the commercially available COC (TOPAS grade 5013) is not specified and certainly much higher than those of the PE-b-PEG, COC appeared to be matrix polymer with the highest chance of success.

PEHMA

For the newly acquired PEHMA-stat-PMPEOMA copolymers, however, compatibility with COC was not expected due to their low chemical similarity. Instead, methacrylate-based matrix polymers are preferred in combination with these stabilizers. Maximum compatibility is expected with a PEHMA polymer matrix with comparable molecular weight. Unfortunately, PEHMA is not as commercialized as its chemically related fellow polymethacrylate PMMA. While a PEHMA solution in toluene with a molecular weight of ~ 123,000 was

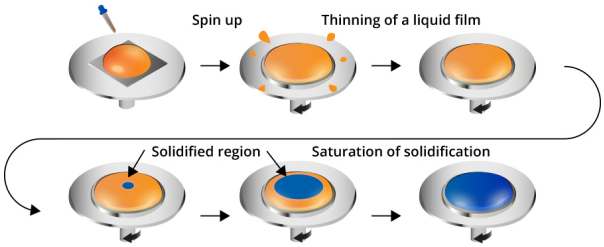

Figure 6.26: Schematic representation of the static dispense spin coating method. Image obtained from [199].

available on Sigma-Aldrich, it was also quite expensive (~300$ per 50 g). One of the only apparent commercial suppliers of PEHMA is a US-based company named Polymer Chemistry Innovations, Inc. After some correspondence the company kindly offered to ship a free sample of their product, which has been used for the fabrication of nanocomposite films in this study. The high molecular weight of the commercial PEHMA at the same time posed an opportunity to study any molecular-weight-related compatibility issues. If the difference in molecular weight would result in inhomogeneous films, there was always the option to go for the Sigma-Aldrich variant with lower molecular weight. Due to the limited commercial use of PEHMA so far, a lot of material properties are still unknown, including optical properties such as its transparency, haze and refractive index. The transparency and haze of PEHMA films were also studied in this research.

PMMA
While maximum compatibility was expected with PEHMA, it was interesting to study whether the PEHMA-stat-PMPEOMA copolymers would also be compatible with its widely-used and chemically related brother PMMA. PMMA is known to have excellent optical properties and could potentially prove to be better suited for transparent polymer nanocomposites than PEHMA. PMMA with a relatively low molecular weight of ~120 kDa was acquired from Sigma-Aldrich and used to fabricate polymer nanocomposite films.

6.3.2. Spin coating thickness

Spin coating is a technique widely used in research and industry for applying thin films on substrates. The process involves depositing a solution of the desired coating material onto a substrate which is then rotated at high velocity, as is depicted in Figure 6.26. After the fluid has spread out evenly over the substrate and the solvent has evaporated, a thin film of the coating material is left on the substrate. The advantage of spin coating is that it can produce very uniform thin films with a thickness ranging from the nanometer up to the micrometer scale. The film thickness depends on the properties of the fluid (such as the viscosity, surface tension and vapor pressure) and on the chosen spin coating parameters. For a given polymer solution, the thickness is inversely proportional to the square root of the spin speed:

$$h \propto \frac{1}{\sqrt{\omega}} = \omega^{-\frac{1}{2}} \tag{6.10}$$

Uniform films can generally be achieved for spin speeds in the range of 1000–6000 rpm, resulting in a thickness variation of a factor $\sqrt{6} \approx 2.4$ for a given solution. The spinning time required for the film to fully dry depends on the vapor pressure of the solvent as well as on the ambient conditions. For most common solvents a spinning time of approximately 30 seconds is enough. The film quality is also affected by the method that is used to dispense the fluid onto the substrate. In the static dispense method, a stationary substrate is fully covered by the fluid before the spinning is initiated, as is shown in Figure 6.26. In the dynamic dispense method, on the other hand, the fluid is pipetted onto the center of an already spinning substrate. While a dynamic dispense typically requires less fluid and shows better reproducibility, it is a difficult to obtain full substrate coverage for low spin speeds or viscous solutions. In this study the static dispense method was used to fabricate the polymer films, because the preparation of polymer films with a thickness in the micrometer range requires quite viscous solutions. In order to get a feeling for controlling the thickness and homogeneity of the polymer films, various solutions of COC were spin coated at different spin speeds.

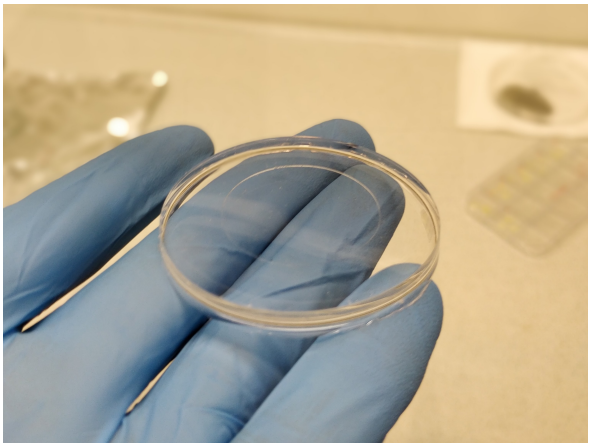

Figure 6.27: PDMS substrate holder for round microscope cover slips.

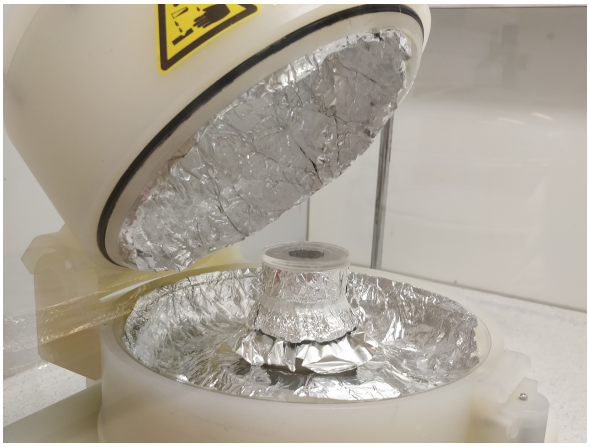

Figure 6.28: The spin coater setup, including the PDMS substrate holder.

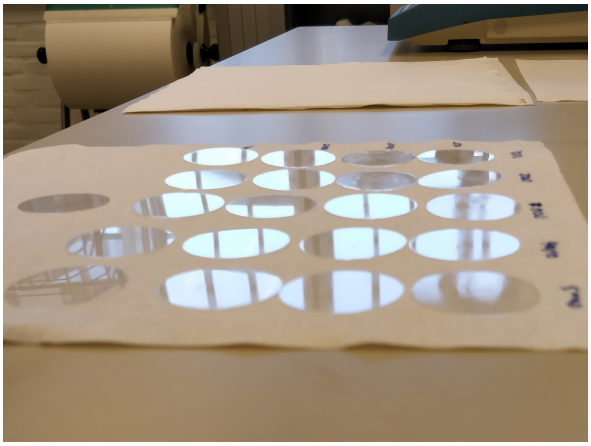

Figure 6.29: COC films spin-coated at various spin speeds and accelerations.

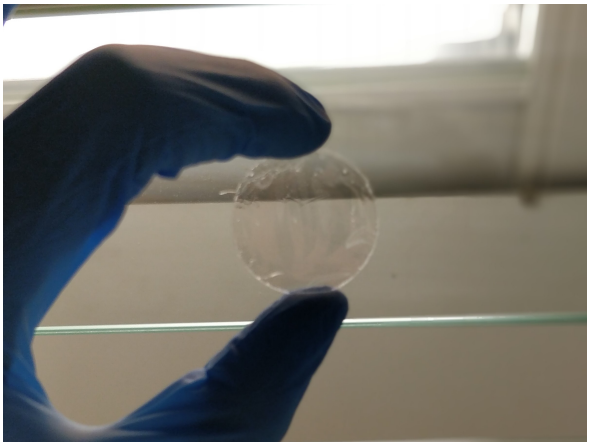

Figure 6.30: Partial delamination of a spin-coated COC film.

Method

TOPAS 5013 COC was dissolved in toluene to obtain 10 wt%, 20 wt% and 30 wt% solutions. A fixed volume of the solutions were pipetted onto ~0.2 µm thick round microscope cover slips to fully cover the substrate, after which the spinning was started. The substrates were placed into specially designed olydimethylsiloxane (PDMS) substrate holders, as shown in Figure 6.27). The substrate holders were fabricated by placing the desired glass substrate (in this case a thin microscope cover slip) in the middle of a petri dish and covering it with PDMS, which was then cured in an oven. The spin coater setup including the PDMS sample holder is shown in Figure 6.28. The spin coater was covered in aluminum foil to prevent the toluene from damaging the polypropylene chuck and spin bowl. The polymer films were prepared at different spin speeds (1000–5000 rpm) with a fixed acceleration of 2000 rpm/s to study the effect of the spin coater parameters on the thickness and homogeneity of the films. The film thickness at different points on the substrate was obtained by removing part of the film and measuring the difference in height using a white light interferometer. In addition, the surface roughness of the film was measured at different points on the substrate.

Results

The spin coated COC films were fully transparent and appeared relatively smooth, as can be seen in Figure 6.29. However, the films had the tendency to fully or partially delaminate from the substrate after some time, especially when using more viscous polymer solutions. The partial delamination of a COC film is shown in Figure 6.30. This effect is probably caused by drying-induced stresses in the polymer film, in combination with poor adhesion of COC to the glass substrate. Pretreatment of the substrate surface with oxygen plasma did not sufficiently increase the adhesion strength to prevent delamination, nor does heating the coated substrate to the glass transition temperature of COC. Presumably, thermal stresses are introduced in the film

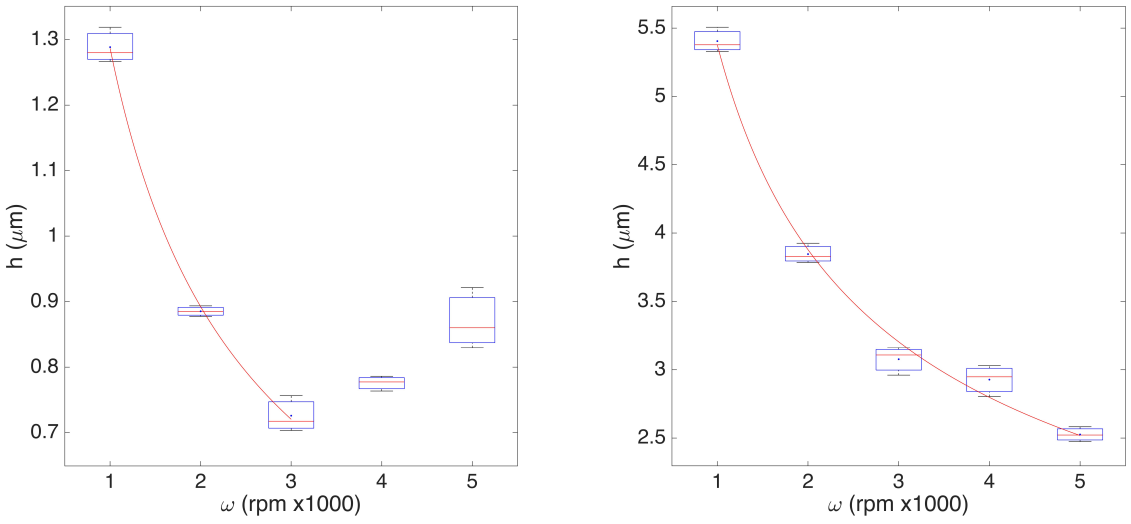

(a) (b)

Figure 6.31: Film thickness plotted against spin speed for (a) 10wt% and (b) 20 wt% soltutions of TOPAS 5013 in toluene.

during cooling down as a result of the mismatch in thermal expansion coefficients between glass and COC. Since COC has a relatively high glass transition temperature of 130°C, cooling the coated substrate down to room temperature introduces a significant amount of stress. The stress deforms the ultrathin glass cover slips, which leads to delamination of the films. No delamination occurred when the films were instead applied to 1 mm thick microscope slides, which were therefore used throughout the remainder of the project.

The thickness of the spin coated films was observed to decrease with increasing spin speed for both 10wt% and 20wt% COC solutions, as shown in Figure 6.31. The exponents of ω in the power law relations that fit the data are equal to -0.53 and -0.47 for 10 wt% and 20 wt%, which are both close to to the exponent of -0.5 predicted by Equation 6.10. The films prepared with a 30wt% COC solution all delaminated completely, which rendered thickness measurements with the white light interferometer impossible. While thickness values of the 20wt% samples show a neat inverse-square-root decline over the entire spin speed range, the 10wt% samples appear to increase in thickness for spin speeds higher than 3000 rpm. The reason for this behavior is not entirely clear. The unexpected results can possibly be attributed the limited reproducibility of spin coating with the static dispense method. The solvent has some time to evaporate after the solution is dispensed onto the substrate, which might lead to variations in viscosity or partial solidification before the spinning is started. It should be noted that the data points correspond to 3 different measurement on one single sample, taken at fixed points between the center and the perimeter. More samples should be prepared to better predictions on the film thickness. However, the experiments show that relatively homogeneous films with a thickness up to a few microns is feasible. This experiment was only performed with COC. Although solutions of PMMA and PEHMA have different fluid properties and therefore different thickness ranges, this experiment has shown that the scaling law of Equation 6.10 holds. Therefore, if the film thickness at one spin speed is known, the thickness at different spin speeds can be reliably predicted.

6.3.3. Preparation of nanocomposite films

Every combination of matrix polymer (PEHMA, PMMA and COC) and toluene/YAG:Ce nanodispersion stabilized with amphiphilic copolymers (A, B, C, B575 and B875) was mixed to study whether homogeneous solutions and nanocomposite thin films could be obtained.

First, a large batch of EtOH/YAG:Ce nanodispersion (~100 mL) was prepared, following the procedure outlined in Section 6.1.4. This process is quite labor-intensive due to the small volume of nanodispersion that can be obtained per centrifuge tube (~ 1 mL), which in addition requires extremely careful pipetting to prevent contamination with agglomerates from the bottom of the tubes. Similar to the phase transfer experiments, however, it is important to prepare all the nanocomposite films from the same nanodispersion.

Next, batches of toluene/YAG:Ce nanodispersions were prepared for every type of amphiphilic copoly-

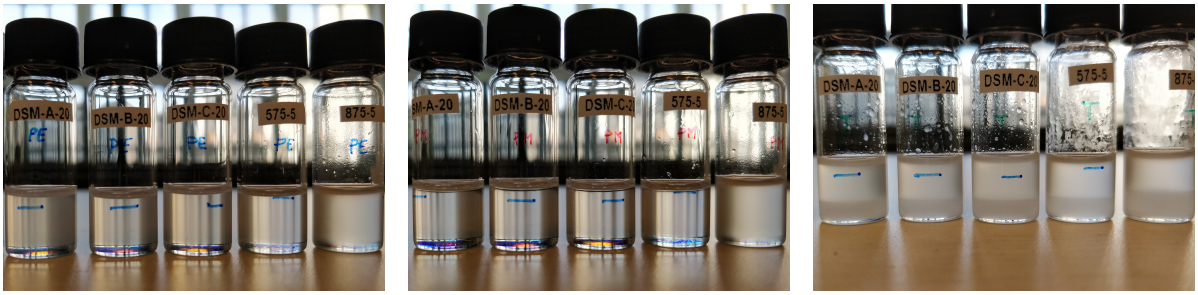

(c) (c) (c)

Figure 6.32: Mixtures of (a) PEHMA, (b) PMMA, (c) COC with toluene/YAG:Ce nanodispersions stabilized with (from left to right) copolymers A, B, C, B575 and B875.

mer. The particle size distribution of these batches is shown in Figure. The batches for A, B, and C were prepared by dissolving 20 gL^{-1} copolymer in toluene, heating up a temperature of 100°C and then adding 40 vol% of EtOH/YAG:Ce nanodispersion. The same procedure was followed for B575 and B875, but with 5 gL^{-1} copolymer and 30 vol% EtOH/YAG:Ce nanodispersion. The benefit of adding a large volume of the nanodispersion to the toluene phase—instead of adding a smaller volume to a solvent mixture of toluene and ethanol— is that a higher particle concentrations is obtained in the nonpolar phase. This makes the particles easier to detect in the nanocomposite films. For the phase transfer experiments described in Section 6.2, however, this method was not preferred as it requires large batches of the labor-intensive EtOH/YAG:Ce nanodispersions. The stabilized toluene/YAG:Ce nanodispersions that are obtained with both methods are similar—at least when using a high copolymer concentrations, high temperature and large EtOH fraction.

Finally, 30 wt% solutions of all matrix polymers were prepared in toluene, which were then diluted with the stabilized toluene/YAG:Ce nanodispersions to obtain in total 15 mixtures (3 matrix polymers times 5 amphiphilic copolymers) with a total polymer concentration of 10 wt%. Typical photographs of these mixtures are shown in Figure 6.32. The PEHMA-stat-PMPEOMA copolymers formed homogeneous solutions with PEHMA and PMMA, but phase separated in the COC solution. The phase separation is most likely the result of poor compatibility between PEHMA-stat-PMPEOMA and COC and could not be reversed by heating the samples. Therefore, spin coating was not possible for this combination. The PE-b-PEG initially appeared to form homogeneous solutions with all matrix polymers. When the mixtures cool down the PE-b-PEG copolymers again crystallize and precipitate. The flocculation is reversible, however, and polymer films could be prepared by reheating the mixtures prior to spin coating. The homogeneous mixtures were spin coated onto glass substrates to form polymer nanocomposite films, using a spin speed of 3000 rpm and an acceleration of 2000 rpm/s. Photographs of all the spin-coated films are displayed in Appendix A.

The concentration of YAG:Ce particles in the nanocomposite film was estimated as follows, taking a PEHMA film with PEHMA-stat-PMPEOMA copolymer as an example. The concentration in the EtOH/YAG:Ce nanodispersion was estimated to be around 0.007 vol% (see Section 6.1.4), which corresponds to to 0.032 w/v% or 0.32 gL^{-1}. After the phase transfer to toluene using 40 vol% EtOH/YAG:Ce, the concentration is equal to $40/100 \cdot 0.32 = 0.13\ gL^{-1}$. The amphiphilic copolymer concentration in the toluene/YAG:Ce nanodispersion is reduced from 20 gL^{-1} to 13.4 gL^{-1} after mixing with the 30 vol% PEHMA solution in toluene. A 10 wt% solution of PEHMA in toluene corresponds to 87.1 gL^{-1}. After evaporation of the solvent, the YAG:Ce particle concentration in the nanocomposite films is then equal to $0.13/(87.1+13.4) \approx 0.13$ wt%.

6.3.4. Transparency and haze

The transmittance and haze of the polymer nanocomposite films were measured using a PerkinElmer Lambda 950 UV/Vis spectrometer. The transmittance is defined as the ratio of the transmitted light to the incident light, while the haze is equal to the ratio of the diffused light to the incident light. For more information about these optical properties and the use of spectrophotometers, the reader is referred to Sections 2.5.1 and 3.2.3.

The measured transmittance and haze are plotted in Figures 6.33 and 6.34. Both quantities were measured in a small area in the center of the films. It should be noted that the measurements have not been corrected for the transmittance and haze of the glass substrates. Therefore, the values correspond to the optical properties of the coated substrates—hereafter called samples—and not solely of the polymer films. That

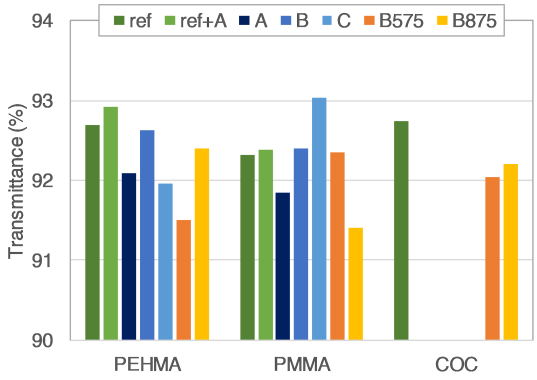

Figure 6.33: Transmittance of the polymer nanocomposite and reference films spin-coated on glass substrates.

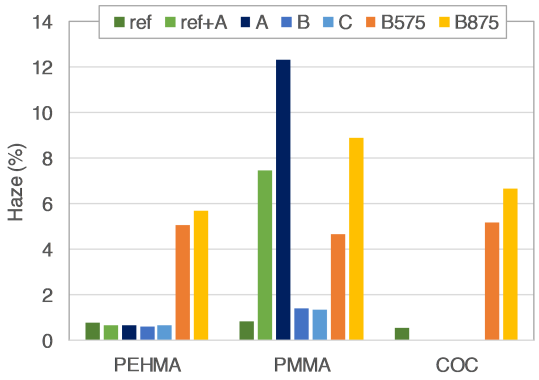

Figure 6.34: Haze of the polymer nanocomposite and reference films spin-coated on glass substrates.

being said, the haze value of glass is typically negligible. Assuming furthermore that the difference in optical properties between the glass substrates are negligible, the measured differences can be attributed to the optical properties of the polymer films. Moreover, it should be stressed that each measurement corresponds to a single sample only. The reason for this is that the entire process to go from YAG:Ce nanopowder to spin-coated films from one single batch is extremely time-consuming. So even though no hard conclusions can be drawn from the results, they certainly give a good indication of the optical properties. The transmittance was found to be close to 92% for all for samples, as can be seen in Figure 6.33. Clearly, the transmittance is not a suitable parameter for comparing the optical performance of the films. When looking at the haze, on the other hand, we can see some notable differences.

First of all, the measured haze values of the pure polymer reference films are very low. The haze values of PMMA and COC are close to the values reported in literature (see Table 3.3), which indicates that the measurement method resembles the standard testing conditions. The haze value of PEHMA—which to the best of my knowledge has not yet been reported in literature—was found to be practically equal to that of PMMA.

The reader is referred to Section 4.5.6 for a discussion about the PEHMA and PMMA nanocomposite films containing the PEHMA-stat-PMPEOMA copolymers. In short, no increase in haze was observed for the PEHMA nanocomposites as is shown in Figure 6.34. This translates into the extremely clear appearance of the films, as can be seen in Appendix A. This observation indicates that the incorporated nanoparticles do not influence the optical properties of the film, which was one of the goals of this research project. It should be stresses, however, that the particle concentration is low (~0.1 wt%) and that higher haze values can be expected for higher concentrations required for functional LSCs. In PMMA, haze values are observed except for in a small area in the center of the films, as was also shown in Section 4.5.6 in the paper. The size of the clear center increases with increasing MPEOMA fraction in the copolymers, as can be seen in Appendix A. Only for copolymer A, part of the films with high haze falls within the measurement area of the spectrometer, which results in a haze value of over 12% in Figure 6.34. Reference samples of PMMA mixed with copolymer A without any nanoparticles give similar results (indicated as "ref+A" in Figure 6.34). This means that the haze can be mainly attributed to the immiscibility of PEHMA and PMMA, which has been reported in literature [181]. The immiscibility was clearly observed by surface analysis methods, which will be discussed in the next section. The concentration of PEHMA-stat-PEHMA in the films was approximately 13 wt%, which is much higher than required for the phase transfer process and less compatibility issues are expected for lower concentrations.

The PE-b-PEG copolymers show high haze values in all matrix polymers, as can be seen in Figure 6.34. The high haze can be attributed to crystallized flocs of the copolymers, which are clearly visible to the naked eye (see Appendix A) as well as by surface analysis methods (see next section). The copolymers crystallize while the nanocomposite solution cools down during spin coating. For this reason, PE-b-PEG is unsuitable for the fabrication of nanocomposite films.

6.3.5. Surface roughness

The surface of the nanocomposite and reference films were analyzed by white light interferometry (WLI) using a Bruker 3D optical microscope. WLI allows to evaluate the thickness of the spin-coated films, which were

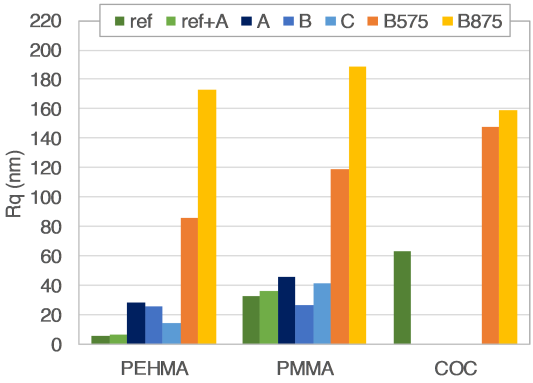

Figure 6.35: Rq surface roughness of the polymer nanocomposite and reference films.

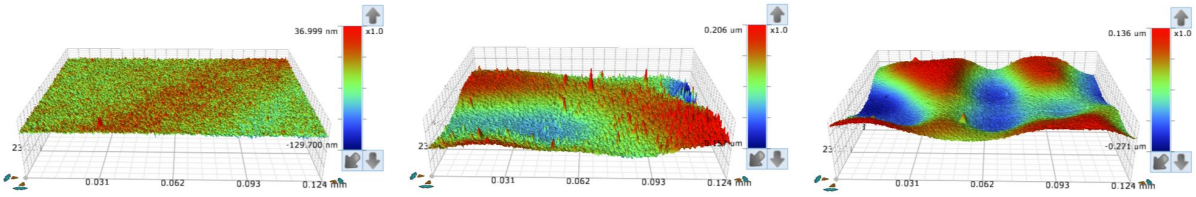

(a) (b) (c)

Figure 6.36: 3D surface profiles of a polymer reference film of (a) PEHMA, (b) PMMA and (c) COC. Note that the scale on the z-axis is different.

measured to be equal to ~1.7 µm for PEHMA and ~1 µm for PMMA and COC. Initially, the reason for analyzing the surface was to see whether the presence of nanoparticles protruding from the film could be detected. WLI can give a lot of information on the characteristics of a surface. First of all, it allows to make 2D and 3D images. Apart from the surface roughness, it is able to compute a lot of interesting surface parameters, such as the number of summits per unit area (Sds). Comparing these surface characteristics of the nanocomposite films to those of the reference films might give an indication of size and distribution of the particles protruding from the film. Unfortunately, no definite trends were observed in the data. This can most likely be attributed to the limited lateral resolution of WLI. Still, some interesting results were obtained by comparing the images and surface roughness of the films to the haze values.

The root mean square surface roughness (Rq) of the films is shown in Figure 6.35. Each measurement corresponds to only one sample and should therefore only serve as an indication of the roughness. The surface roughness of the films is not one-on-one related to the haze of the films. While the reference films all have very low haze values, their surface characteristics are quite different. 3D images of the surface profile at center of the reference films are shown in Figure 6.36. The PEHMA films are much more smooth than those of PMMA, which might be related to its lower glass transition temperature and higher plasticity. The COC films showed a high degree of waviness, which could also be observed with the naked eye.

An exception to this rule are the films containing the PE-b-PEG copolymers, for which the high haze value likely results from the micron-sized flocculated crystals. Figure 6.37 shows a typical 2D and 3D image of these crystals present in the polymer films containing PE-b-PEG. The crystals are observed for both B575 and B875, appear in all three polymer matrices and are present over the entire surface.

Phase separation between the incompatible phases of PMMA and PEHMA-stat-PMPEOMA is clearly observed when analyzing the surface profile. Figure 6.38 shows the 2D surface profiles of a reference film of PMMA ("ref" in Figure 6.35) and of a reference film of PMMA containing the same concentration of copolymer A as was used for the nanocomposite films ("ref+A" in Figure 6.35). No YAG:Ce particles are present in these films, and the differences in the surface profile can be solely attributed to the incompatibility between the phases. The surface profile in the center of the two films are shown in Figure 6.38(a) and 6.38(b). While both surfaces are more or less equally smooth, there appears to be a distinct difference in the surface morphology. The "ref+A" film appeared transparent in the center of the film, similar to Figure 4.8d in the paper. In the hazy part outside of the center, and the surface roughness is much higher (Rq=116 nm) and the sur-

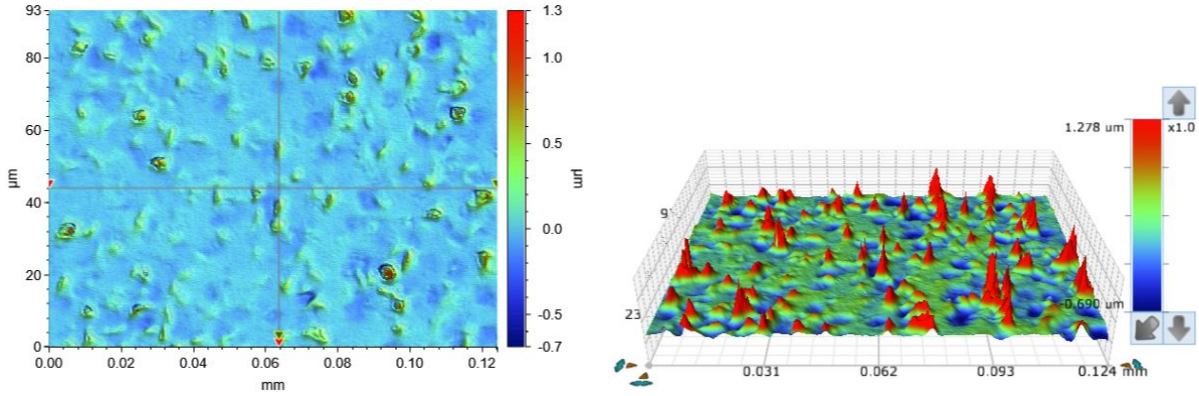

(a) (b)

Figure 6.37: Surface profile in (a) 2D and (b) 3D of a PMMA film with YAG:Ce/B575 at 50x magnification.

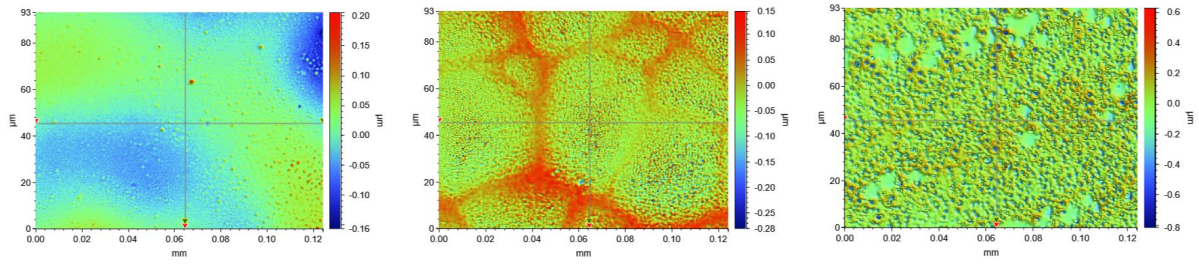

(a) (b) (c)

Figure 6.38: 2D surface profile of (a) the center of a PMMA reference film, (b) the center of a PMMA + copolymer A reference film and (c) the side of a PMMA + copolymer A reference film.

face profile looks like 6.38(c). It appears that the PEHMA-stat-PMPEOMA separates into small islands in the PMMA matrix that diffuse incident light. Phase separation of blends PEHMA and PMMA mixtures into distinct islands has been reported in literature [181]. Presumably, PMMA is more compatible with MPEOMA than with PEHMA, which explains the growth of the low-haze area with increasing MPEOMA fraction in the copolymers.

6.3.6. Particle size and distribution

The nanocomposite samples were analyzed in a scanning electron microscope (SEM) to study the size and distribution of the nanoparticles in the films. The reader is referred to Section 4.5.6 for an explanation of the procedure and SEM images of the PEHMA nanocomposites. In conclusion, the size of the particles corresponded with the particle size distribution in the toluene/YAG:Ce nanodispersion, indicating that no significant agglomeration occurred during the preparation of the films. Moreover, the particles appeared to be homogeneously dispersed in the polymer matrix.

Imaging of the nanoparticles in the films proved to be quite tedious. In order to obtain a resolution high enough to image nanometer-sized features such as the YAG:Ce nanoparticles, a high accelerating voltage is required. However, using high accelerating voltages led to charging effects and damage to the polymer films, even though they were coated by a 6 nm layer of Au/Pd to render them conductive. On the other hand, a high accelerating voltage increases the diffusion volume of the electron beam, especially in the soft polymeric material. This makes the detection of the low concentration of YAG:Ce particles in the film using elemental analysis by electron dispersive X-ray spectroscopy (EDS) very difficult. Applying thicker layers of conductive material reduces the penetration depth of the electron beam and prevents the appearance of charging effects, but also interferes with the results of the EDS measurements. Needless to say, a lot of trial and error was required to find the optimal imaging conditions.

Many attempts were made to image the YAG:Ce nanoparticles in the nanocomposite films and confirm the presence of aluminum and yttrium with EDS. Several parameters were varied to see whether the detec-

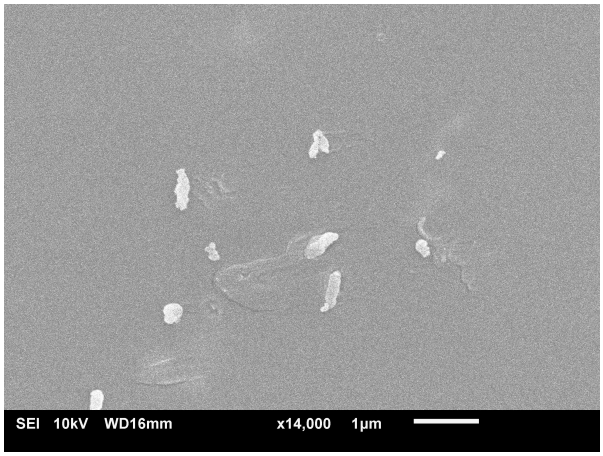

Figure 6.39: SEM image of YAG:Ce/B575 particles in a COC matrix.

tion of the particles could be improved: the particle concentration in the film, the Au/Pd coating thickness, the acceleration voltage, the working distance and the spot size of the electron beam. At best, vague bright spots were observed that— with some imagination—could indeed be the YAG:Ce nanoparticles. According to elemental analysis, the bright spots appeared to contain more oxygen than the darker areas. These observations were not satisfactory, however, since the analysis of low atomic number elements such oxygen by EDS is notoriously inaccurate. Besides, both PEHMA and the MPEOMA groups in the copolymers also contain oxygen, which made it impossible to draw any hard conclusion on the presence of the YAG:Ce particles. The detection problem was not caused by the material or the equipment; the presence of aluminum and yttrium could be easily detected by analyzing the pure YAG:Ce nanopowder stuck to carbon tape. It thus appeared that signal of the particles incorporated inside the nanocomposites was simply too low to be detected.

The turning point came when the samples were first treated with oxygen plasma. The oxygen plasma etches away a small layer of polymer on the surface, leaving the YAG:Ce particles exposed. Suddenly, the bright spots became much more pronounced and the EDS measurements clearly indicated the presence of aluminum and yttrium, as shown in Appendix B. The duration of oxygen plasma treatment was found influence the visibility of the nanoparticles in the SEM. A treatment time of 2 minutes was sufficient for the PEHMA nanocomposite films.

The COC nanocomposites with PE-b-PEG were also analyzed by SEM and showed significantly larger YAG:Ce agglomerates with sizes up to 600 nm, as can be seen in Figure 6.39. This particular film was coated with pure Au at the department of Material Science instead of Au/Pd. The Au coating in combination with the COC matrix allowed for attaining a much higher resolution than was observed for the PEHMA nanocomposites shown in Section 4.5.6. The COC films were much less sensitive to surface wrinkling and radiation damage than the PEHMA films. The surface wrinkling is likely caused by thermal stresses in the multilayer system, as was explained in Section 4.5.6 in the paper. The reduced appearance of surface wrinkling might thus be explained by a lower linear thermal expansion coefficient of COC than that of the rubbery PEHMA.

7 Reflection

7.1. Origin of the project

The idea behind this thesis project originated from the findings of an internship I did at PHYSEE from March until June 2017. During this internship, I had focused on modeling the optical losses in thin-film LSCs. The conversion of sunlight into electrical power by LSCs involves many intrinsic losses, which all need to be addressed individually to optimize the conversion efficiency. One of these fundamental loss mechanisms is the light trapping efficiency, which determines how much light can be trapped by an LSC and is based on the difference in refractive index between the luminescent layer and the surroundings—typically air. In thin-film LSCs, on the other hand, there are three optical pathways for the light that is emitted by the luminescent centers: either it is trapped inside the luminescent thin film, or it is trapped in both the film and the substrate or it escapes through the so-called escape cone. The higher the refractive index of the luminescent thin film compared to the substrate, the more light is trapped in this layer. One can imagine that the light that is trapped inside the thin film has to bounce back an forth many times to reach the edges of the device, which induces considerable interface scattering losses. At the time, the material that PHYSEE envisioned for the luminescent film was known to have a reflective index much higher than glass. The results of the optical modeling indicated that this mismatch would lead to unacceptable losses.[1] In a discussion that followed, we recognized that one way to circumvent this problem would be to encapsulate the luminescent material in a polymeric nanocomposite film. Instead of applying the luminescent material directly onto the glass using a sputter deposition process, nanoparticles of the material can be mixed with transparent polymer matrices and applied as a polymeric coating. This way, the luminescent material can be easily applied to virtually any transparent surface using scalable coating techniques such as spray coating, or for example be integrated into the polymeric interlayer of laminated glass to fabricate power-generating windshields for cars. In other words, the design of luminescent transparent polymer nanocomposites proves to be an exciting and promising field of research. Although PHYSEE had recently started to look into the synthesis of rare-earth doped inorganic particles, they had no experience with integrating them into polymers. For PHYSEE, my project was therefore relevant in the context of kickstarting an alternative coating manufacturing process: stable integration of prefabricated nanophosphors in polymers using wet chemical methods that allow easy scaling up and eliminate some constraints related to sputter deposition (e.g., the dependency on commercial glass manufacturers, the need for conductive and non-hygroscopic host materials, the limited coating thickness, the restriction to flat glass surfaces, waveguide losses through glass, etc). However, in order to obtain transparent luminescent coatings with acceptable losses, it is important that the nanoparticles remain nanosized. Directly dispersing such inorganic nanoparticles into common transparent organic polymers causes them to agglomerate instantly. Therefore, the challenge was to find a way to stabilize the nanoparticles synthesized by PHYSEE and integrate them into a suitable polymer matrix. From a research perspective, the subject was

[1] One other option to reduce the undesirable trapping of light in the thin film is by making use of the wavelike properties of light. In the nanoscopic to microscopic dimensions of the thin film, the emitted light is subject to interference effects and is only allowed to propagate through the film in certain modes. The allowed propagation modes are, among other things, dependent on the film thickness. In the intership, I studied the effect of the film thickness on the optical efficiency using finite-difference time domain (FDTD) electromagnetic simulations. The results predicted the existence of a cut-off thickness around 100 nm, below which light propagation in the film is inhibited and interface scattering losses are avoided. The cut-off thickness is dependent on the refractive indices of the materials, as well as on the wavelength of the propagating light.

equally interesting. To the best of my knowledge, the ex situ stabilization (i.e. stabilization not during synthesis) of inorganic rare-earth doped luminescent nanoparticles and their integration into transparent polymer matrices for application in luminescent solar concentrators has not been reported in literature.

Naturally, the subject was quite different from my background in mechanical engineering. At first sight, one could even argue that the subject falls outside of the scope of the faculty and is better suited for a student in chemical engineering or a related field. However, the subject certainly has some overlap with the mission of the Micro and Nano Engineering (MNE) research group; after all, the aim of the project is to manipulate and analyze objects at the nanometer scale in order to develop functional devices at the macroscopic scale. Now, the challenge was of course to convey my enthusiasm for this subject and find a supervisor willing to embark on the project. After some discussions, Dr. Luigi Sasso agreed to supervise the project and so I joined his research group of Polymer Micro and Nano Manufacturing in September 2017.

7.2. Course of the project

The project started with an extensive literature survey on concepts that were completely new to me at the time, most notably on the topics of nanoparticle agglomeration and stabilization, compatibilization in polymer nanocomposites and polymer science in general. Although not all information turned out to be equally relevant to the research project, the literature survey has been added almost in its entirety to this thesis report in Chapter 2. Besides all the information that is shared in this chapter, the literature survey mainly involved catching up on a lot of textbook-level chemistry. My knowledge of chemistry had largely been neglected since senior year in high school. This initially resulted in an overload of new information and seemingly endless zooming out, before I could finally orient my focus on a suitable research plan and the well-known "gap" in literature. This whole process took somewhat more time than I had anticipated, and I was eager to start the lab phase in February 2018.

The initial research plan was divided into three phases with a distinct focus: dispersion, functionality and prototyping. The goal of the dispersion phase was to disperse the nanoparticles both in a nonpolar solvent and in polymer films, while keeping the average particle size below 100 nm. In the functionality phase, the nanoparticle concentration and size as well as the film thickness would be related to the performance of the films in terms of the transmittance, haze and luminescence intensity. Finally, several films with optimal performance would be integrated into an LSC test setup with solar modules to measure their electrical power output in a solar simulator. In hindsight, these research goals seem somewhat idealistic to say the least. A number of issues were encountered along the way that resulted in a deviation from the original research plan.

To begin with, my project goals were to a large extent dependent on the availability of suitable inorganic luminescent nanoparticles. Around the time I started with the project, PHYSEE had recently taken on a full-time employee focusing on the synthesis of such nanoparticles. The main focus was on SiAlON:Sm^{2+} (the ratio of the elements Si, Al, O and N in the SiAlON host is not specified) and $Ba_3(PO_4)_2$:Mn^{5+}, both of which have a broad absorption band in the visible spectrum and re-emit light with a wavelength of around 700 and 1200 nm, respectively. The synthesis of the nanoparticles was expected to be finished before the end of writing my literature survey, but unfortunately suffered a lot of delay. The nanoparticles were synthesized using a sol-gel method and even though the particle size estimated from X-ray diffraction (XRD) measurements using the Scherrer equation indicated a particle size well below 100 nm, all batches that were tested turned out to be severely agglomerated. The dynamic light scattering (DLS) measurements I performed on the dispersed nanoparticles typically returned average particle sizes in the micrometer range (for example, see Section 6.1.2). Most likely, the drying and sintering step—necessary to activate the luminescence—after the sol-gel synthesis resulted in heavily agglomerated micron-sized powder. Unfortunately, I was unable to break-up and redisperse the agglomerated particles with the lab equipment at my disposal. To the best of my knowledge, there is no commercial supplier of unfunctionalized, inorganic luminescent nanoparticles electrostatically stabilized in a polar solvent—let alone with adsorption and emission properties suitable for LSC applications. Admittedly, this is quite a niche product. The project focus thus shifted towards using the commercially available luminescent YAG:Ce nanopowder that was kindly donated by Dr. Erik van der Kolk. At the same time, this decision represented the first concession to my project goals, namely giving up on developing a prototype. The YAG:Ce particles are not suitable for LSC window applications due to their low Stokes shift (the spectral gap between emission and absorption), their narrow absorption band and their emission in the visible spectrum.

There was a second issue related to the decision to proceed with the YAG:Ce nanopowder. Typically, irreversible agglomeration occurs during the drying step of (unfunctionalized) nanoparticles in order to form a

nanopowder (see Section 2.2.2). Deagglomeration methods such as ultrasonication or even ball-miling cannot redisperse the nanoparticles in their primary particle size. This means that in order to obtain actual nanodispersions, the dispersed YAG:Ce particles had to be centrifuged to filter out agglomerates. As a result, the particle concentration was drastically reduced and difficult to determine—not to mention control. Besides, it was impossible to control the particle size and concentration independently from each other. These unavoidable consequences constituted the second concession to the research goals: the particle concentration could not varied to optimize the functionality of the luminescent nanocomposite films. In fact, the YAG:Ce particle concentration in the nanocomposite films turned out to be too low to even measure any luminescence output. Therefore, the scope of the research was now reoriented towards optimizing the dispersion phase.

The unavailability of required materials was a recurring issue throughout the project. Apart from the very specific requirements for the nanoparticles, the type of amphiphilic copolymers best suited to the process are also very specific. The best candidates for ensuring both a successful phase transfer and compatibility with a polymer matrix are statistical copolymers, as was explained in Section 2.4. Again to the best of my knowledge, the only amphiphilic copolymers that are commercially available are block copolymers, and there is not much to choose.[2] The molecular structure of the selected amphiphilic copolymers in turn determines the choice of matrix polymer, because their compatibility is favored by chemical similarity. In other words, everything hinges on the selection of the amphiphilic copolymer. Although not perfect, the combination of PE-b-PEG copolymers with a COC polymer matrix was deemed the most promising commercially available option at the time. As it turned out, the insolubility of PE-b-PEG at room temperature made them unsuitable for the fabrication of transparent polymer films. It thus seemed like I had to give up on yet another goal, namely the fabrication of a transparent nanocomposite coating. This realization initiated the search for suitable amphiphilic statistical copolymers, which was a continuous process throughout the first four months of the project. I finally got in touch with DSM Coating Resins, who were able and willing to synthesize free samples of these very specific copolymers. Even better, the properties of the copolymers could be almost completely customized to my wishes. This suddenly opened up a lot of opportunities for the remainder of the project and in hindsight this was indeed a tuning point—both in terms of the results that followed and the feeling of lacking control over the project.

One more unforeseen issue was that the phase transfer process turned out to be much more involved than expected. The procedure for the transferring inorganic nanoparticles from a polar to a nonpolar medium appears to be pretty straightforward in literature. In reality, there are many parameters that determine whether agglomeration of the nanoparticles is suppressed or not. As discussed in the paper (Chapter 4), the success of stabilization during the phase transfer was found to depend on three key parameters: the amphiphile concentration, the temperature and the solvent composition. It should be noted that the influence of many other parameters and methods was tested to arrive at this conclusion, most of which were outlined in Section 6.2.1. In itself, the unforeseen complexity of the phase transfer process did not necessarily require a change in the scope of the project. The scope had after all already been narrowed down to the dispersion phase due to the unavailability of suitable nanoparticles. In fact, it provided an excellent opportunity to study the behavior of nanoparticle stabilization in more detail. To the best of my knowledge, the identification of the parameters that are relevant for the stabilization of nanoparticles in a phase transfer process and their influence on the stabilization kinetics has not yet been reported in literature.

7.3. Timeline

The initial and final timeline of the project are shown in Figures 7.1 and 7.2. All together the entire thesis project has taken about 3 months longer than was initially planned. There are a number of reasons that contributed to this delay, which will be discussed in this section.

First of all, I have seriously underestimated the time it takes to do lab work. As an illustration, the first measurement of a successful transfer of YAG:Ce nanoparticles to toluene (i.e., with an average particle size below 100 nm) was dated June 8th 2018, about 4 months after the start of the lab phase. In my original planning, I expected to have full control over the particle size by the beginning of April. Of course, experimental work in its essence is hard to predict and the initial planning is actually more like a guideline telling you when it's time to move to plan B. However, I mainly underestimated the time it takes to get acquainted with doing lab work, before you can even get started. This is true both for learning how to operate new equipment as

[2] The best avalable options at the time were either a single PS-b-PEG copolymer with 2–5% wt% PEG and a molecular weight of 21–31 kDa, or multiple PE-b-PEG copolymers with various PEG weight fractions (20 or 50 wt%) and molecular weights (575–1400 Da).

well as for working in a chemical lab in general. Since I had no daily supervisor or PhD candidate to help out, most of the doubts that I had or the problems I encountered in the lab I needed to solve on my own. Without any prior experience in a chemical lab, everything in the beginning goes extremely slow. From small things like learning how to use a pipette to more general things like learning which parameters might influence the reproducibility of what you are doing. Reproducibility was a major issue during the phase transfer process of the nanoparticles to toluene. In order to compare the behavior and performance of the copolymers, all experiments had to be conducted with the same batch of EtOH/YAG:Ce nanodispersion and under the exact same circumstances. In practice, this resulted in the fact that many experiments had to be redone, again and again, after inconsistencies due to unwanted influences had been discovered.[3] All in all I have done exactly 1018 dynamic light scattering (DLS) measurements throughout the entire project, which take about 5 minutes each—that means a lot of hours of silent contemplation. Although many of these measurements are not shared in this thesis report, they certainly contributed to my understanding of the behavior and to getting a "feeling" for the process. Besides mastering DLS, I learned to use a variety of other techniques to do characterization. To name a few, the nanoparticle size in dispersion was analyzed using dynamic light scattering (DLS), the film thickness and surface roughness with white light interferometry (WLI), the transmission and haze with spectrophotometry and the particle size and distribution in the film with scanning electron microscopy (SEM). Besides getting in touch with the right people (sometimes at other faculties) and following the mandatory trainings, learning how to master each of these machines took a considerable amount of time.

Secondly, the unsuitability of materials put a lot of pressure on my planning. Two of the most important materials for the process turned out to be unsuitable: the nanoparticles and the amphiphilic copolymers. The reasons can be found partly in a lack of experience and partly in a too optimistic research plan, to say the least. Due to the difficulties with the synthesis of luminescent nanoparticles by PHYSEE, an alternative had to be found in an early stage of the project. First the plan was to start out with Al_2O_3 nanoparticles, which should behave similarly to luminescent metal oxide particles. These turned out to be stabilized with unknown dispersants, which made them unsuitable. Finally I decided to proceed with the agglomerated YAG:Ce nanopowder, which needed some processing to finally obtain usable nanodispersions in polar solvents. All in all this resulted in a considerable delay before I could even start with the phase transfer process, which would prove to be equally problematic. The selected PE-b-PEG copolymers were found to be unsuitable for the fabrication of transparent nanocomposite films due to their crystalline nature. In itself, the unsuitability of the PE-b-PEG copolymers did not have to lead to a delay. It would have been possible to narrow the focus to the phase transfer process and study the influences of the concentration, temperature and solvent properties. However, I did not want to give up on the goal of making nanocomposite films. After all, that was the main reason for starting the project in the first place. Focusing only on the phase transfer process, and more specifically on the performance of materials that would not even be suitable anyway, felt like too much of a compromise for sticking to the original timeline. Although I had been warned that things often do not go according to plan in experimental research, this felt like an extremely unsatisfactory conclusion to my master's thesis. Therefore, I put a lot of effort into finding a way out of the impasse by finding new amphiphilic copolymers. Luckily, the search payed off and the statistical copolymers that were synthesized by DSM coating resins worked like a charm, as they were expected to. In hindsight, I believe this delay was worth the added value to the outcome of the project. Moreover, I have learned a lot during this dip in the project, both in my personal attitude towards facing a seemingly unsurmountable problem as well as in terms of reaching out to other people to find a solution.

Lastly, the theoretical part of my work took a considerable amount of time, which was not included in the original research plan. Along the way, the focus of my project shifted from fabricating a functional device towards optimizing the phase transfer process of inorganic nanoparticles to organic media. I found clear empirical trends in the phase transfer process, namely that the process is generally favored by increasing the amphiphile concentration, the temperature and the ethanol content in the solvent mixture. Initially I was not planning to dive deep into the theory of nanoparticle stabilization kinetics—let alone try to contribute to the existing knowledge. However, since this was know the focus of my project, merely stating the empirical findings would not be a strong conclusion. It would be more interesting to get a true understanding of the behavior, which allows then to broaden the findings and come up with a generalized approach that can be used by researchers using different materials. In other words, I needed to find a theoretical basis for the empirical findings, in order to predict the stabilization behavior under different conditions. This meant that I had to dive into the literature on nanoparticle agglomeration and amphiphile adsorption kinetics, which were

[3] A small anecdote to illustrate the unexpected nature of such unwanted influences: one day, after several days of inconsisitent results, I found out that the cause was that the ethanol bottle had been refilled with acetone.

completely new to me. The problem of building a model is that it is difficult to stop; the more you include, the more accurate the model becomes. This resulted in the fact that I spent a lot of time on getting the model to work properly. A fun anecdote in this respect is that I struggled for a very long time with a seemingly horrible equation derived by two Japanese scientist (Equation 4.11), which was published in the reputable Journal of Physical Chemistry B. No matter what I tried, the the equation did not return the expected behavior. In fact, in one limit it converged to a value that was off by a factor π. Indeed, after contacting the authors, it turned out that this was due to a misprint in the equation. As a result, I have the honor to be thanked by the authors in the correction to this paper that was published in the same journal, which I have added in Appendix C.

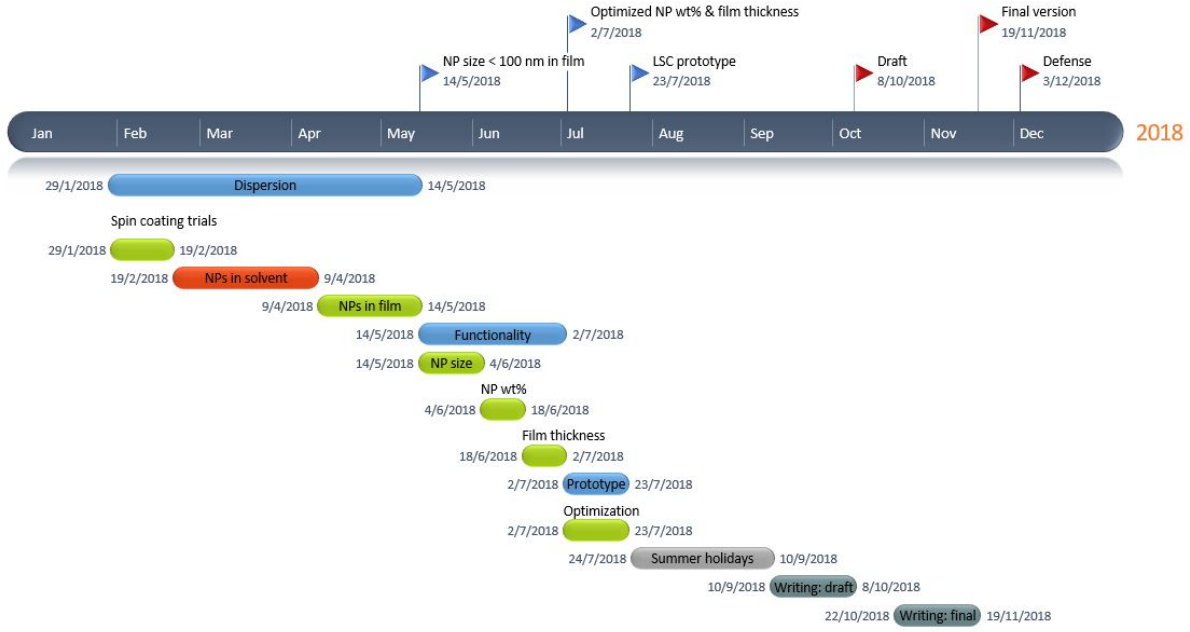

Figure 7.1: Overview of the original timeline.

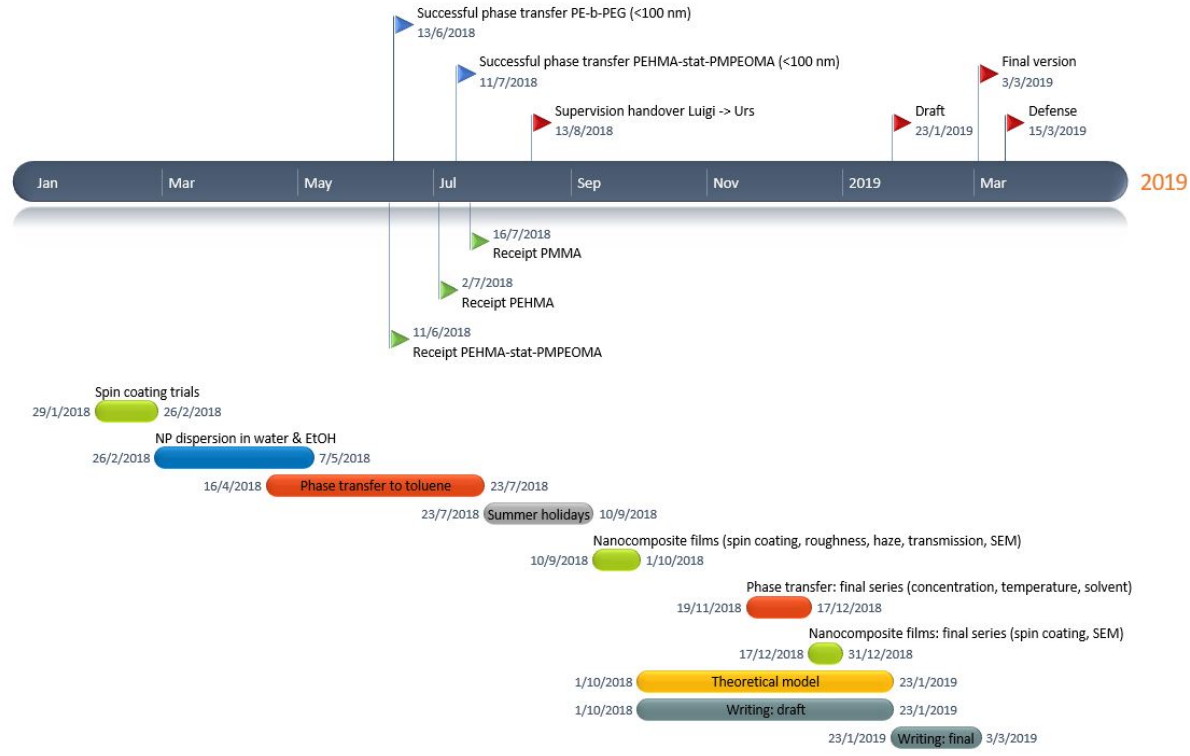

Figure 7.2: Overview of the final timeline.

A

Photographs of nanocomposite films

A.1. PEHMA

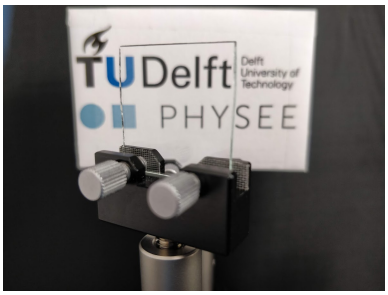

PEHMA reference film.

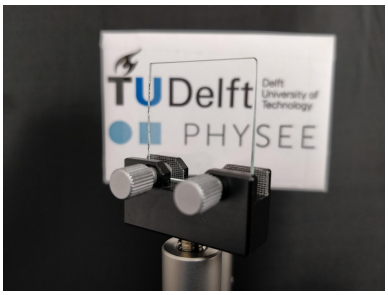

PEHMA + copolymer A.

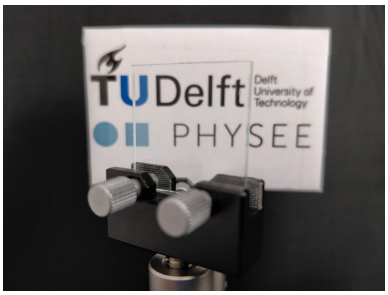

PEHMA + YAG:Ce/A.

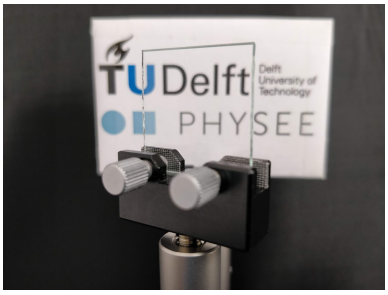

PEHMA + YAG:Ce/B.

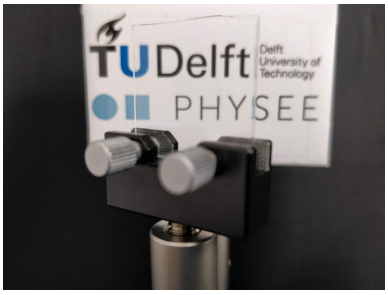

PEHMA + YAG:Ce/C.

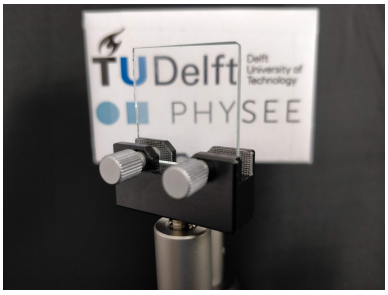

PEHMA + YAG:Ce/B575.

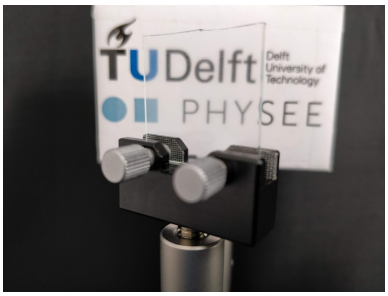

PEHMA + YAG:Ce/B875.

A.2. PMMA

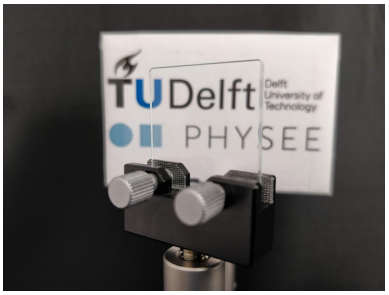

PMMA reference film.

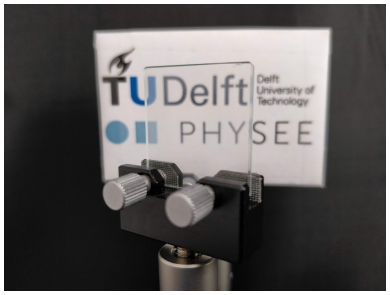

PMMA + copolymer A.

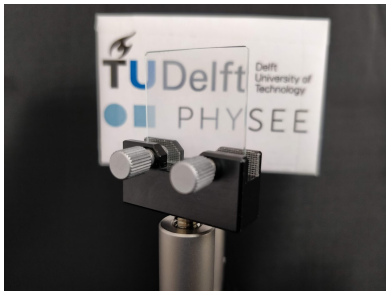

PMMA + YAG:Ce/A.

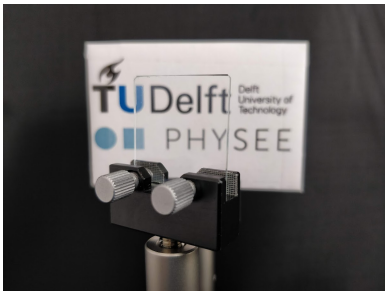

PMMA + YAG:Ce/B.

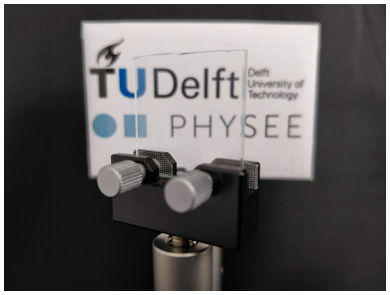

PMMA + YAG:Ce/C.

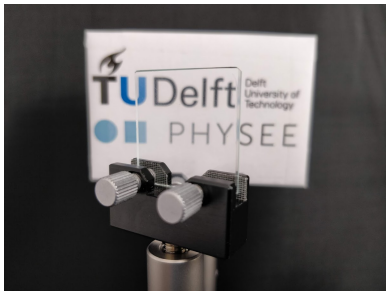

PMMA + YAG:Ce/B575.

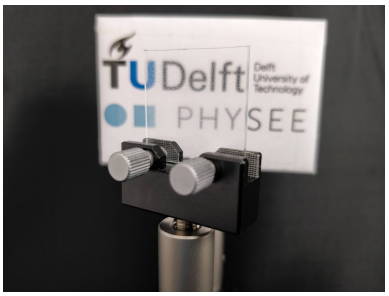

PMMA + YAG:Ce/B875.

A.3. COC

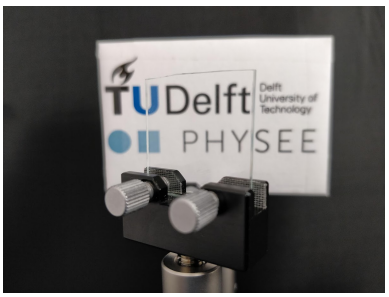

COC reference film.

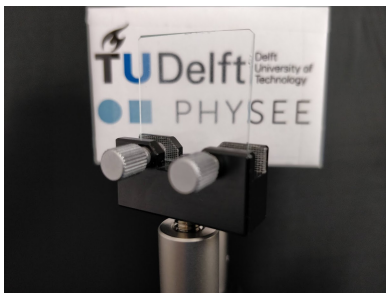

COC + YAG:Ce/B575.

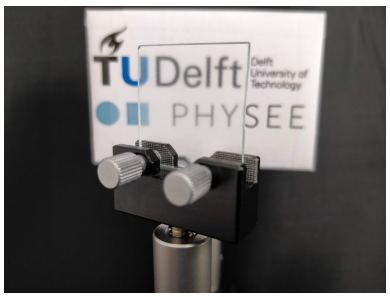

COC + YAG:Ce/B875.

B

EDS measurements

001

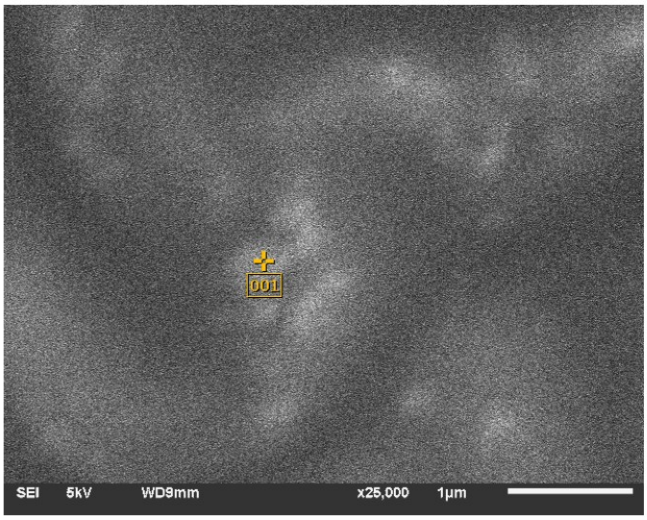

Volt : 5.00 kV
Mag. : x 25,000
Date : 2019/01/14
Pixel : 1280 x 960

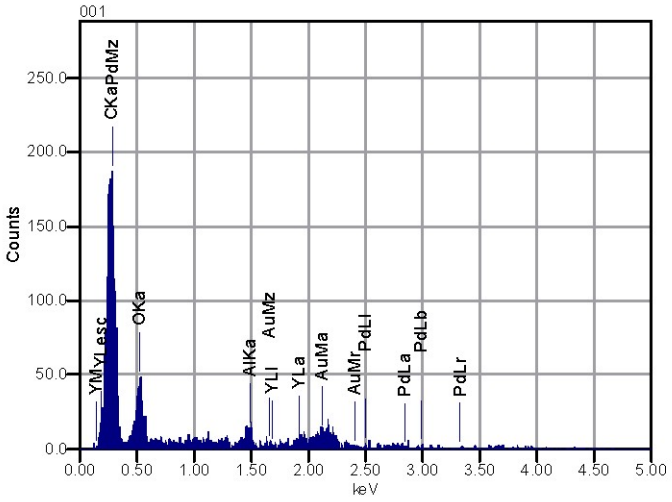

Acquisition Condition
Instrument : 6010LA
Volt : 5.00 kV
Current : ---
Process Time : T1
Live time : 60.00 sec.
Real Time : 60.02 sec.
DeadTime : 0.00 %
Count Rate : 91.00 CPS

Chemical formula	mass%	Atom%	Sigma	Net	K ratio	Line
C*	49.33	80.43	0.21	3961	0.0015886	K
O*	9.29	11.37	0.28	911	0.0010742	K
Al*	4.22	3.06	0.34	505	0.0006037	K
Y*	8.60	1.89	1.92	329	0.0006961	L
Pd*	4.73	0.87	2.04	69	0.0002194	L
Au*	23.84	2.37	2.98	578	0.0013865	M
Total	100.00	100.00				

JEOL EDS System JEOL

EDS measurement of YAG:Ce particle.

002

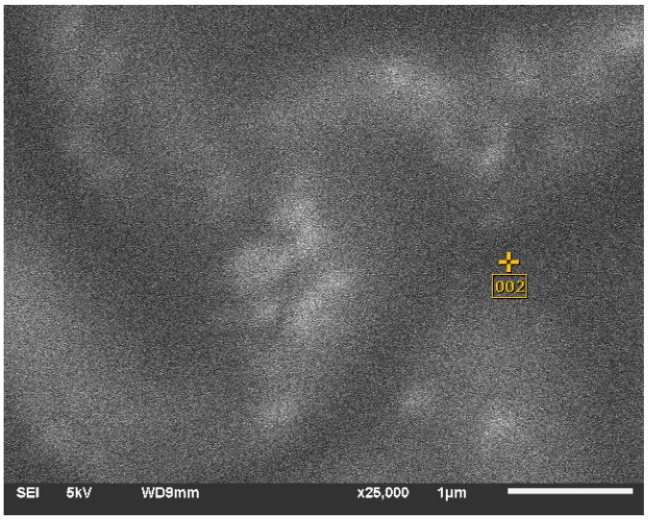

Volt : 5.00 kV
Mag. : x 25,000
Date : 2019/01/14
Pixel : 1280 x 960

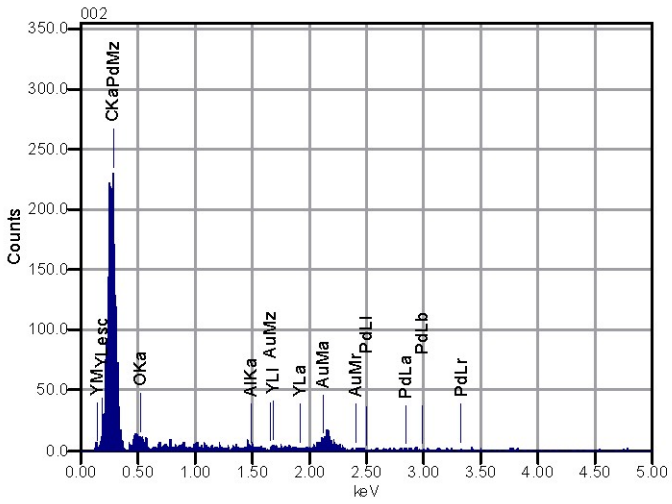

Acquisition Condition
Instrument : 6010LA
Volt : 5.00 kV
Current : ---
Process Time : T1
Live time : 60.00 sec.
Real Time : 60.02 sec.
DeadTime : 0.00 %
Count Rate : 84.00 CPS

Chemical formula	mass%	Atom%	Sigma	Net	K ratio	Line
C	70.19	94.82	0.27	4880	0.0019574	K
O*	1.83	1.86	0.25	128	0.0001513	K
Al*	1.68	1.01	0.33	150	0.0001791	K
Y	nd	nd				L
Pd*	2.14	0.33	2.29	23	0.0000736	L
Au*	24.16	1.99	3.30	438	0.0010520	M
Total	100.00	100.00				

JEOL EDS System JEOL

EDS measuremnt of polymer matrix.

C

Correction to "Diffusion Influenced Adsorption Kinetics"

THE JOURNAL OF PHYSICAL CHEMISTRY B
Addition/Correction
Cite This: J. Phys. Chem. B 2019, 123, 324−324
pubs.acs.org/JPCB

Correction to "Diffusion Influenced Adsorption Kinetics"

Toshiaki Miura and Kazuhiko Seki*

J. Phys. Chem. B **2015**, *119* (34), 10954−10961. DOI: 10.1021/acs.jpcb.Sb00580

The authors regret that there were misprints in eqs 20 and 24. In both equations, $\sqrt{t/D}$ should be written as $\sqrt{t/(D\pi)}$. Equation 20 (the equation in the TOC graphic) should read

$$\Gamma(t) \approx \frac{c_0 D}{k_a \Gamma_m}\left(\exp\left(\frac{k_a^2 \Gamma_m^2 t}{D}\right)\operatorname{erfc}\left(k_a \Gamma_m \sqrt{\frac{t}{D}}\right) + 2k_a \Gamma_m \sqrt{\frac{t}{D\pi}} - 1\right)$$

Equation 24 should read

$$\Gamma(t) = \Gamma_m - \Gamma_m \exp\left\{-\frac{c_0 D}{k_a \Gamma_m^2}\left[\exp\left(\frac{k_a^2 \Gamma_m^2 t}{D}\right)\right.\right.$$
$$\left.\left.\times \operatorname{erfc}\left(k_a \Gamma_m \sqrt{\frac{t}{D}}\right) + 2k_a \Gamma_m \sqrt{\frac{t}{D\pi}} - 1\right]\right\}$$

These corrections do not affect any results including Figures 1−5, discussion, or conclusions. The authors apologize for any inconvenience caused. We thank Mr. Jan David Endtz for drawing our attention to this problem.

Published: December 20, 2018

DOI: 10.1021/acs.jpcb.8b11741
J. Phys. Chem. B 2019, 123, 324−324

D

MATLAB

D.1. Amphiphile-solvent interaction

This script computes the solubility parameters of all the substances and plots the solubility spheres (Figure 6.15 for PE-b-PEG and Figure 6.24 for PEHMA-stat-PMPEOMA). With the solubility parameters it also computes the amphiphile-solvent interaction parameters χ as a function of the ethanol content in the solvent mixture (Figure 4.6 in the paper for PEHMA-stat-PMPEOMA and Figure 6.16 for PE-b-PEG.

```
clear all
close all
clc

%% Parameters
R = 8.3144598;      % gas constant
T = 353;            % temperature (K)
steps = 101;        % number of steps for loop

%% Solubility parameters

% toluene
d_tol   = 18.2;                                     % hildebrand
dd_tol  = 18;                                       % hansen
dp_tol  = 1.4;
dh_tol  = 2;
d_tol_t = sqrt(dd_tol^2 + dp_tol^2 + dh_tol^2);     % hansen total
fd_tol  = dd_tol/(dd_tol+dp_tol+dh_tol);
fp_tol  = dp_tol/(dd_tol+dp_tol+dh_tol);
fh_tol  = dh_tol/(dd_tol+dp_tol+dh_tol);
F_tol   = fd_tol+fp_tol+fh_tol;
V_tol   = 92.14/0.867;                              % molar volume

% % hexane (used for scaling to 2nm copolymer diameter in Steltzig et al. (2008) in hexane/etoh
    mixture)
% d_tol   = 14.9;                                     % hildebrand
% dd_tol  = 14.9;
% dp_tol  = 0.001;
% dh_tol  = 0.001;
% d_tol_t = sqrt(dd_tol^2 + dp_tol^2 + dh_tol^2);     % hansen total
% fd_tol  = dd_tol/(dd_tol+dp_tol+dh_tol);
% fp_tol  = dp_tol/(dd_tol+dp_tol+dh_tol);
% fh_tol  = dh_tol/(dd_tol+dp_tol+dh_tol);
% F_tol   = fd_tol+fp_tol+fh_tol;
% V_tol   = 131.4;

% ethanol
d_etoh = 26.5;                                      % hildebrand
dd_etoh = 15.8;
dp_etoh = 8.8;
dh_etoh = 19.4;
d_etoh_t = sqrt(dd_etoh^2 + dp_etoh^2 + dh_etoh^2); % hansen total
fd_etoh = dd_etoh/(dd_etoh+dp_etoh+dh_etoh);        % fractional parameters
fp_etoh = dp_etoh/(dd_etoh+dp_etoh+dh_etoh);
fh_etoh = dh_etoh/(dd_etoh+dp_etoh+dh_etoh);
F_etoh = fd_etoh+fp_etoh+fh_etoh;
V_etoh = 46.07/0.789;                               % molar volume

% mek
dd_mek = 16.0;
dp_mek = 9.0;
```

```
dh_mek = 5.1;
d_mek_t = sqrt(dd_mek^2 + dp_mek^2 + dh_mek^2);     % hansen total

% aceton
dd_ace = 15.5;
dp_ace = 10.4;
dh_ace = 7.0;
d_ace_t = sqrt(dd_ace^2 + dp_ace^2 + dh_ace^2);     % hansen total

% dodecane
dd_dod = 16.0;
dp_dod = 0.0;
dh_dod = 0.0;
d_dod_t = sqrt(dd_dod^2 + dp_dod^2 + dh_dod^2);     % hansen total

% hexane
dd_hex = 14.9;
dp_hex = 0.0;
dh_hex = 0.0;
d_hex_t = sqrt(dd_hex^2 + dp_hex^2 + dh_hex^2);     % hansen total
V_hex = 131.4;

% water
dd_wat = 15.6;
dp_wat = 16.0;
dh_wat = 42.3;
d_wat_t = sqrt(dd_wat^2 + dp_wat^2 + dh_wat^2);     % hansen total

% THF
dd_thf = 16.8;
dp_thf = 5.7;
dh_thf = 8.0;
d_thf_t = sqrt(dd_thf^2 + dp_thf^2 + dh_thf^2);     % hansen total

% solvent mixture etOH
for i=1:steps
f_tol(i)    = 1 - (i-1)*(1/(steps-1));              % ratio ethanol (0 to 1)
f_etoh(i)   = 1-f_tol(i);
d_mix(i)    = f_tol(i)*d_tol + f_etoh(i)*d_etoh;    % hildebrand mixture
fd_mix(i)   = f_tol(i)*fd_tol + f_etoh(i)*fd_etoh;  % fractional parameters
fp_mix(i)   = f_tol(i)*fp_tol + f_etoh(i)*fp_etoh;
fh_mix(i)   = f_tol(i)*fh_tol + f_etoh(i)*fh_etoh;
F_mix(i)    = fd_mix(i) + fp_mix(i) + fh_mix(i);    % check if = 1

syms dd_mix dp_mix dh_mix
eq1 = dd_mix - (fd_mix(i)*dp_mix + fd_mix(i)*dh_mix)/(1-fd_mix(i)) == 0;        % see section 5.1
eq2 = dp_mix - (fp_mix(i)*dd_mix + fp_mix(i)*dh_mix)/(1-fp_mix(i)) == 0;
eq3 = dh_mix - sqrt(d_mix(i).^2 - dd_mix^2 - dp_mix^2) == 0;
[sol_dd_mix,sol_dp_mix,sol_dh_mix]  = solve(eq1,eq2,eq3,dd_mix,dp_mix,dh_mix);
dd_mix_sol(i)   = double(sol_dd_mix);
dp_mix_sol(i)   = double(sol_dp_mix);
dh_mix_sol(i)   = double(sol_dh_mix);
H_mix(i,:)      = [dd_mix_sol(i),dp_mix_sol(i),dh_mix_sol(i)];
H_mix_t(i)      = sqrt(dd_mix_sol(i)^2+dp_mix_sol(i)^2+dh_mix_sol(i)^2);
end

% topas
dd_coc  = 18;
dp_coc  = 3;
dh_coc  = 2;
d_coc_t = sqrt(dd_coc + dp_coc + dh_coc);   % hansen total


%% Group contributions
% Properties of polymers, Hoftyzer & Van Krevelen (1992)
E_CH3   = 9640;                 % cohesive energy
E_CH2   = 4190;
E_O     = 6290;
E_OH    = 29800;

Fdi_CH3     = 420;              % molar attraction constant
Fdi_CH2     = 270;
Fdi_CH      = 80;
Fdi_C       = -70;
Fdi_O       = 100;
Fdi_OH      = 210;
Fdi_COO     = 390;
Fdi_PEHMA   = 3*Fdi_CH3 + 6*Fdi_CH2 + Fdi_CH + Fdi_C + Fdi_COO;
Fdi_PEOMA   = 2*Fdi_CH3 + 16*Fdi_CH2 + Fdi_C + Fdi_COO + 7.5*Fdi_O;
Fdi_EO      = 2*Fdi_CH2 + Fdi_O;

Fpi_CH3     = 0;
Fpi_CH2     = 0;
Fpi_CH      = 0;
```

```
Fpi_C       = 0;
Fpi_O       = 400;
Fpi_OH      = 500;
Fpi_COO     = 490;
Fpi_PEHMA   = 3*Fpi_CH3 + 6*Fpi_CH2 + Fpi_CH + Fpi_C + Fpi_COO;
Fpi_PEOMA   = 2*Fpi_CH3 + 16*Fpi_CH2 + Fpi_C + Fpi_COO + 7.5*Fpi_O;
Fpi_EO      = 2*Fpi_CH2 + Fpi_O;

Ehi_CH3     = 0;
Ehi_CH2     = 0;
Ehi_CH      = 0;
Ehi_C       = 0;
Ehi_O       = 3000;
Ehi_OH      = 20000;
Ehi_COO     = 7000;
Ehi_PEHMA   = 3*Ehi_CH3 + 6*Ehi_CH2 + Ehi_CH + Ehi_C + Ehi_COO;
Ehi_PEOMA   = 2*Ehi_CH3 + 16*Ehi_CH2 + Ehi_C + Ehi_COO + 7.5*Ehi_O;
Ehi_EO      = 2*Ehi_CH2 + Ehi_O;

% Molar volume (Fedors p.195 in Van Krevelen (1992)
V_CH3       = 33.5;
V_CH2       = 16.1;
V_CH        = -1.0;
V_C         = -19.2;
V_O         = 3.8;
V_OH        = 13.0;
V_COO       = 18.0;
V_PEHMA     = 3*V_CH3 + 6*V_CH2 + V_CH + V_C + V_COO;
V_PEOMA     = 2*V_CH3 + 16*V_CH2 + V_C + V_COO + 7.5*V_O;
V_EO        = 2*V_CH2 + V_O;
V_PMMA      = 2*V_CH3 + V_CH2 + V_COO + V_C;

%% Hildebrand
E_575   = 2.5*(E_O + 2*E_CH2)+ E_OH + (15.9-1)*(2*E_CH2) + E_CH2 + E_CH3;     % cohesive energy
E_875   = 3.9*(E_O + 2*E_CH2)+ E_OH + (24.5-1)*(2*E_CH2)+ E_CH2 + E_CH3;
E_920   = 10.3*(E_O + 2*E_CH2)+ E_OH + (16.1-1)*(2*E_CH2)+ E_CH2 + E_CH3;
E_1400  = 15.7*(E_O + 2*E_CH2)+ E_OH + (24.7-1)*(2*E_CH2)+ E_CH2 + E_CH3;

V_575   = 2.5*(V_O + 2*V_CH2)+ V_OH + (15.9-1)*(2*V_CH2) + V_CH2 + V_CH3;     % molar volume
V_875   = 3.9*(V_O + 2*V_CH2)+ V_OH + (24.5-1)*(2*V_CH2)+ V_CH2 + V_CH3;
V_920   = 10.3*(V_O + 2*V_CH2)+ V_OH + (16.1-1)*(2*V_CH2)+ V_CH2 + V_CH3;
V_1400  = 15.7*(V_O + 2*V_CH2)+ V_OH + (24.7-1)*(2*V_CH2)+ V_CH2 + V_CH3;
V_A     = 86.4*V_PEHMA + 4.4*V_PEOMA;
V_B     = 115.5*V_PEHMA + 13.3*V_PEOMA;
V_C     = 116.3*V_PEHMA + 23.0*V_PEOMA;

% Solubility parameters PE-b-PEG
d_575   = sqrt(E_575/V_575);                % hildebrand
d_875   = sqrt(E_875/V_875);
d_920   = sqrt(E_920/V_920);
d_1400  = sqrt(E_1400/V_1400);

delta_d_mix_575     = abs(d_575 - d_mix);   % delta hildebrand with mixture
delta_d_mix_875     = abs(d_875 - d_mix);
delta_d_mix_920     = abs(d_920 - d_mix);
delta_d_mix_1400    = abs(d_1400 - d_mix);

delta_d_tol_575     = abs(d_575 - d_tol);
delta_d_tol_875     = abs(d_875 - d_tol);
delta_d_tol_920     = abs(d_920 - d_tol);
delta_d_tol_1400    = abs(d_1400 - d_tol);

delta_d_etoh_575    = abs(d_575 - d_etoh);
delta_d_etoh_875    = abs(d_875 - d_etoh);
delta_d_etoh_920    = abs(d_920 - d_etoh);
delta_d_etoh_1400   = abs(d_1400 - d_etoh);

%% Hansen
Fdi_575     = 2.5*(Fdi_O + 2*Fdi_CH2)+ Fdi_OH + (15.9-1)*(2*Fdi_CH2) + Fdi_CH2 + Fdi_CH3;   % molar
    attraction constants (dispersion component)
Fdi_875     = 3.9*(Fdi_O + 2*Fdi_CH2)+ Fdi_OH + (24.5-1)*(2*Fdi_CH2)+ Fdi_CH2 + Fdi_CH3;
Fdi_920     = 10.3*(Fdi_O + 2*Fdi_CH2)+ Fdi_OH + (16.1-1)*(2*Fdi_CH2)+ Fdi_CH2 + Fdi_CH3;
Fdi_1400    = 15.7*(Fdi_O + 2*Fdi_CH2)+ Fdi_OH + (24.7-1)*(2*Fdi_CH2)+ Fdi_CH2 + Fdi_CH3;
Fdi_A       = 86.4*Fdi_PEHMA + 4.4*Fdi_PEOMA;
Fdi_B       = 115.5*Fdi_PEHMA + 13.3*Fdi_PEOMA;
Fdi_C       = 116.3*Fdi_PEHMA + 23.0*Fdi_PEOMA;


Fpi_575_2   = 2.5*(Fpi_O^2 + 2*Fpi_CH2^2)+ Fpi_OH^2 + (15.9-1)*(2*Fpi_CH2^2) + Fpi_CH2^2 + Fpi_CH3
    ^2;
Fpi_875_2   = 3.9*(Fpi_O^2 + 2*Fpi_CH2^2)+ Fpi_OH^2 + (24.5-1)*(2*Fpi_CH2^2)+ Fpi_CH2^2 + Fpi_CH3^2;
Fpi_920_2   = 10.3*(Fpi_O^2 + 2*Fpi_CH2^2)+ Fpi_OH^2 + (16.1-1)*(2*Fpi_CH2^2)+ Fpi_CH2^2 + Fpi_CH3
    ^2;
Fpi_1400_2  = 15.7*(Fpi_O^2 + 2*Fpi_CH2^2)+ Fpi_OH^2 + (24.7-1)*(2*Fpi_CH2^2)+ Fpi_CH2^2 + Fpi_CH3
```

```
    ^2;
Fpi_A       = 86.4*Fpi_PEHMA + 4.4*Fpi_PEOMA;
Fpi_B       = 115.5*Fpi_PEHMA + 13.3*Fpi_PEOMA;
Fpi_C       = 116.3*Fpi_PEHMA + 23.0*Fpi_PEOMA;


Ehi_575     = 2.5*(Ehi_O + 2*Ehi_CH2)+ Ehi_OH + (15.9-1)*(2*Ehi_CH2) + Ehi_CH2 + Ehi_CH3;
Ehi_875     = 3.9*(Ehi_O + 2*Ehi_CH2)+ Ehi_OH + (24.5-1)*(2*Ehi_CH2)+ Ehi_CH2 + Ehi_CH3;
Ehi_920     = 10.3*(Ehi_O + 2*Ehi_CH2)+ Ehi_OH + (16.1-1)*(2*Ehi_CH2)+ Ehi_CH2 + Ehi_CH3;
Ehi_1400    = 15.7*(Ehi_O + 2*Ehi_CH2)+ Ehi_OH + (24.7-1)*(2*Ehi_CH2)+ Ehi_CH2 + Ehi_CH3;
Ehi_A       = 86.4*Ehi_PEHMA + 4.4*Ehi_PEOMA;
Ehi_B       = 115.5*Ehi_PEHMA + 13.3*Ehi_PEOMA;
Ehi_C       = 116.3*Ehi_PEHMA + 23.0*Ehi_PEOMA;


% Hansen solubility parameters  (dispersion, polar & hydrogen bonding)
sym05   = 0.5;
sym1    = 1;
dd_575  = Fdi_575/V_575;
dp_575  = sqrt(Fpi_575_2)/V_575 * sym05;
dh_575  = sqrt(Ehi_575/V_575);
d_575t  = sqrt(dd_575^2 + dp_575^2 + dh_575^2);     % 575 hansen total

dd_875  = Fdi_875/V_875;
dp_875  = sqrt(Fpi_875_2)/V_875 * sym05;
dh_875  = sqrt(Ehi_875/V_875);
d_875t  = sqrt(dd_875^2 + dp_875^2 + dh_875^2);     % 875 hansen total

dd_920  = Fdi_920/V_920;
dp_920  = sqrt(Fpi_920_2)/V_920 * sym05;
dh_920  = sqrt(Ehi_920/V_920);
d_920t  = sqrt(dd_920^2 + dp_920^2 + dh_920^2);     % 920 hansen total

dd_1400 = Fdi_1400/V_1400;
dp_1400 = sqrt(Fpi_1400_2)/V_1400 * sym05;
dh_1400 = sqrt(Ehi_1400/V_1400);
d_1400t = sqrt(dd_1400^2 + dp_1400^2 + dh_1400^2);  % 1400 hansen total

dd_A    = Fdi_A/V_A;
dp_A    = sqrt(Fpi_A)/V_A * sym1;
dh_A    = sqrt(Ehi_A/V_A);
d_At    = sqrt(dd_A^2 + dp_A^2 + dh_A^2);   % A hansen total

dd_B    = Fdi_B/V_B;
dp_B    = sqrt(Fpi_B)/V_B * sym1;
dh_B    = sqrt(Ehi_B/V_B);
d_Bt    = sqrt(dd_B^2 + dp_B^2 + dh_B^2);   % B hansen total

dd_C    = Fdi_C/V_C;
dp_C    = sqrt(Fpi_C)/V_C * sym1;
dh_C    = sqrt(Ehi_C/V_C);
d_Ct    = sqrt(dd_C^2 + dp_C^2 + dh_C^2);   % C hansen total

dd_PEOMA    = Fdi_PEOMA/V_PEOMA;
dp_PEOMA    = sqrt(Fpi_PEOMA)/V_PEOMA * sym1;
dh_PEOMA    = sqrt(Ehi_PEOMA/V_PEOMA);
d_PEOMAt    = sqrt(dd_PEOMA^2 + dp_PEOMA^2 + dh_PEOMA^2);   % MPEOMA hansen total

dd_EO   = Fdi_EO/V_EO;
dp_EO   = sqrt(Fpi_EO)/V_EO * sym1;
dh_EO   = sqrt(Ehi_EO/V_EO);
d_EOt   = sqrt(dd_EO^2 + dp_EO^2 + dh_EO^2);                % EO hansen total



for i = 1:steps
    for j = 1:81
        T(j) = 293 + (j-1);
D_mix_EO(i)     = sqrt( (dd_mix_sol(i)-dd_EO).^2 + (dp_mix_sol(i)-dp_EO).^2 + (dh_mix_sol(i)-dh_EO)
    .^2);       % delta hildebrand
D_mix_575(i)    = sqrt( (dd_mix_sol(i)-dd_575).^2 + (dp_mix_sol(i)-dp_575).^2 + (dh_mix_sol(i)-
    dh_575).^2);
D_mix_875(i)    = sqrt( (dd_mix_sol(i)-dd_875).^2 + (dp_mix_sol(i)-dp_875).^2 + (dh_mix_sol(i)-
    dh_875).^2);
D_mix_920(i)    = sqrt( (dd_mix_sol(i)-dd_920).^2 + (dp_mix_sol(i)-dp_920).^2 + (dh_mix_sol(i)-
    dh_920).^2);
D_mix_1400(i)   = sqrt( (dd_mix_sol(i)-dd_1400).^2 + (dp_mix_sol(i)-dp_1400).^2 + (dh_mix_sol(i)-
    dh_1400).^2);

D_mix_A(i)      = sqrt( (dd_mix_sol(i)-dd_A).^2 + (dp_mix_sol(i)-dp_A).^2 + (dh_mix_sol(i)-dh_A).^2)
    ;
D_mix_B(i)      = sqrt( (dd_mix_sol(i)-dd_B).^2 + (dp_mix_sol(i)-dp_B).^2 + (dh_mix_sol(i)-dh_B).^2)
    ;
D_mix_C(i)      = sqrt( (dd_mix_sol(i)-dd_C).^2 + (dp_mix_sol(i)-dp_C).^2 + (dh_mix_sol(i)-dh_C).^2)
```

```
    ;
D_mix_PEOMA(i)  = sqrt( (dd_mix_sol(i)-dd_PEOMA)^2 + (dp_mix_sol(i)-dp_PEOMA)^2 + (dh_mix_sol(i)-
    dh_PEOMA)^2);

V_mix_id(i,j)   = f_tol(i)*V_tol + f_etoh(i)*V_etoh;  % molar volume mixture (ideal)
X_mix_575(i,j)  = 0.6*V_mix_id(i)/(R*T(j))* ((dd_mix_sol(i)-dd_575).^2 + 0.25*(dp_mix_sol(i)-dp_575)
    .^2 + 0.25*(dh_mix_sol(i)-dh_575).^2);       % chi
X_mix_875(i,j)  = 0.6*V_mix_id(i)/(R*T(j))* ((dd_mix_sol(i)-dd_875).^2 + 0.25*(dp_mix_sol(i)-dp_875)
    .^2 + 0.25*(dh_mix_sol(i)-dh_875).^2);
X_mix_920(i,j)  = 0.6*V_mix_id(i)/(R*T(j))* ((dd_mix_sol(i)-dd_920).^2 + 0.25*(dp_mix_sol(i)-dp_920)
    .^2 + 0.25*(dh_mix_sol(i)-dh_920).^2);
X_mix_1400(i,j) = 0.6*V_mix_id(i)/(R*T(j))* ((dd_mix_sol(i)-dd_1400).^2 + 0.25*(dp_mix_sol(i)-
    dp_1400).^2 + 0.25*(dh_mix_sol(i)-dh_1400).^2);
X_mix_EO(i,j)   = 0.6*V_mix_id(i)/(R*T(j))* ((dd_mix_sol(i)-dd_EO).^2 + 0.25*(dp_mix_sol(i)-dp_EO)
    .^2 + 0.25*(dh_mix_sol(i)-dh_EO).^2);

X_mix_A(i,j)    = 0.6*V_mix_id(i)/(R*T(j))* ((dd_mix_sol(i)-dd_A).^2 + 0.25*(dp_mix_sol(i)-dp_A).^2
    + 0.25*(dh_mix_sol(i)-dh_A).^2);
X_mix_B(i,j)    = 0.6*V_mix_id(i)/(R*T(j))* ((dd_mix_sol(i)-dd_B).^2 + 0.25*(dp_mix_sol(i)-dp_B).^2
    + 0.25*(dh_mix_sol(i)-dh_B).^2);
X_mix_C(i,j)    = 0.6*V_mix_id(i)/(R*T(j))* ((dd_mix_sol(i)-dd_C).^2 + 0.25*(dp_mix_sol(i)-dp_C).^2
    + 0.25*(dh_mix_sol(i)-dh_C).^2);
X_mix_PEOMA(i,j) = 0.6*V_mix_id(i)/(R*T(j))* ((dd_mix_sol(i)-dd_PEOMA).^2 + 0.25*(dp_mix_sol(i)-
    dp_PEOMA).^2 + 0.25*(dh_mix_sol(i)-dh_PEOMA).^2);


% X_hex_A(j) = 0.6*V_hex/(R*T(j))* ((dd_hex-dd_A).^2 + 0.25*(dp_hex-dp_A).^2 + 0.25*(dh_hex-dh_A)
    .^2);  % used for scaling to 2nm copolymer diameter in Steltzig et al. (2008) in hexane/etoh
    mixture
% X_hex_B(j) = 0.6*V_hex/(R*T(j))* ((dd_hex-dd_B).^2 + 0.25*(dp_hex-dp_B).^2 + 0.25*(dh_hex-dh_B)
    .^2);
% X_hex_C(j) = 0.6*V_hex/(R*T(j))* ((dd_hex-dd_C).^2 + 0.25*(dp_hex-dp_C).^2 + 0.25*(dh_hex-dh_C)
    .^2);

end
end

% Distance between solvent and centre of solubility sphere
D_tol_575   = sqrt( (dd_tol-dd_575)^2 + (dp_tol-dp_575)^2 + (dh_tol-dh_575)^2);
D_tol_875   = sqrt( (dd_tol-dd_875)^2 + (dp_tol-dp_875)^2 + (dh_tol-dh_875)^2);
D_tol_920   = sqrt( (dd_tol-dd_920)^2 + (dp_tol-dp_920)^2 + (dh_tol-dh_920)^2);
D_tol_1400  = sqrt( (dd_tol-dd_1400)^2 + (dp_tol-dp_1400)^2 + (dh_tol-dh_1400)^2);
D_tol_B     = sqrt( (dd_tol-dd_B)^2 + (dp_tol-dp_B)^2 + (dh_tol-dh_B)^2);

D_etoh_575  = sqrt( (dd_etoh-dd_575)^2 + (dp_etoh-dp_575)^2 + (dh_etoh-dh_575)^2);
D_etoh_875  = sqrt( (dd_etoh-dd_875)^2 + (dp_etoh-dp_875)^2 + (dh_etoh-dh_875)^2);
D_etoh_920  = sqrt( (dd_etoh-dd_920)^2 + (dp_etoh-dp_920)^2 + (dh_etoh-dh_920)^2);
D_etoh_1400 = sqrt( (dd_etoh-dd_1400)^2 + (dp_etoh-dp_1400)^2 + (dh_etoh-dh_1400)^2);

D_mek_575   = sqrt( (dd_mek-dd_575)^2 + (dp_mek-dp_575)^2 + (dh_mek-dh_575)^2);
D_mek_875   = sqrt( (dd_mek-dd_875)^2 + (dp_mek-dp_875)^2 + (dh_mek-dh_875)^2);
D_mek_920   = sqrt( (dd_mek-dd_920)^2 + (dp_mek-dp_920)^2 + (dh_mek-dh_920)^2);
D_mek_1400  = sqrt( (dd_mek-dd_1400)^2 + (dp_mek-dp_1400)^2 + (dh_mek-dh_1400)^2);
D_mek_B     = sqrt( (dd_mek-dd_B)^2 + (dp_mek-dp_B)^2 + (dh_mek-dh_B)^2);


D_ace_575   = sqrt( (dd_ace-dd_575)^2 + (dp_ace-dp_575)^2 + (dh_ace-dh_575)^2);
D_ace_875   = sqrt( (dd_ace-dd_875)^2 + (dp_ace-dp_875)^2 + (dh_ace-dh_875)^2);
D_ace_920   = sqrt( (dd_ace-dd_920)^2 + (dp_ace-dp_920)^2 + (dh_ace-dh_920)^2);
D_ace_1400  = sqrt( (dd_ace-dd_1400)^2 + (dp_ace-dp_1400)^2 + (dh_ace-dh_1400)^2);

D_dod_575   = sqrt( (dd_dod-dd_575)^2 + (dp_dod-dp_575)^2 + (dh_dod-dh_575)^2);
D_dod_875   = sqrt( (dd_dod-dd_875)^2 + (dp_dod-dp_875)^2 + (dh_dod-dh_875)^2);
D_dod_920   = sqrt( (dd_dod-dd_920)^2 + (dp_dod-dp_920)^2 + (dh_dod-dh_920)^2);
D_dod_1400  = sqrt( (dd_dod-dd_1400)^2 + (dp_dod-dp_1400)^2 + (dh_dod-dh_1400)^2);

D_wat_575   = sqrt( (dd_wat-dd_575)^2 + (dp_wat-dp_575)^2 + (dh_wat-dh_575)^2);
D_wat_875   = sqrt( (dd_wat-dd_875)^2 + (dp_wat-dp_875)^2 + (dh_wat-dh_875)^2);
D_wat_920   = sqrt( (dd_wat-dd_920)^2 + (dp_wat-dp_920)^2 + (dh_wat-dh_920)^2);
D_wat_1400  = sqrt( (dd_wat-dd_1400)^2 + (dp_wat-dp_1400)^2 + (dh_wat-dh_1400)^2);


%% PLOT delta hildebrand amphiphile A/B/C - solvent mixture

figure(1)
plot(f_etoh,D_mix_PEOMA,f_etoh,D_mix_A,f_etoh,D_mix_B,f_etoh,D_mix_C)
hold on
% plot(f_etoh,D_mix_575,f_etoh,D_mix_875)
% plot(f_etoh,D_mix_920,f_etoh,D_mix_1400)
ax = gca;
ax.ColorOrderIndex = 1;
yL = get(gca,'YLim');
plot([f_etoh(D_mix_PEOMA==min(D_mix_PEOMA)) f_etoh(D_mix_PEOMA==min(D_mix_PEOMA))],[min(D_mix_PEOMA)
     yL(1)],'--')
```

```
plot([f_etoh(D_mix_A==min(D_mix_A)) f_etoh(D_mix_A==min(D_mix_A))],[min(D_mix_A) yL(1)],'--')
plot([f_etoh(D_mix_B==min(D_mix_B)) f_etoh(D_mix_B==min(D_mix_B))],[min(D_mix_B) yL(1)],'--')
plot([f_etoh(D_mix_C==min(D_mix_C)) f_etoh(D_mix_C==min(D_mix_C))],[min(D_mix_C) yL(1)],'--')
xlabel('\phi_E_t_O_H')
ylabel('\Delta\delta')
legend('MPEOMA','A','B','C')


%% PLOT delta hildebrand amphiphile B575/B875- solvent mixture

figure(2)
hold on
plot(f_etoh,D_mix_EO,f_etoh,D_mix_575,f_etoh,D_mix_875)
plot(f_etoh,D_mix_920,f_etoh,D_mix_1400)
ax = gca;
ax.ColorOrderIndex = 1;
yL = get(gca,'YLim');
plot([f_etoh(D_mix_EO==min(D_mix_EO)) f_etoh(D_mix_EO==min(D_mix_EO))],[min(D_mix_EO) yL(1)],'--')
plot([f_etoh(D_mix_575==min(D_mix_575)) f_etoh(D_mix_575==min(D_mix_575))],[min(D_mix_575) yL(1)],'
    --')
plot([f_etoh(D_mix_875==min(D_mix_875)) f_etoh(D_mix_875==min(D_mix_875))],[min(D_mix_875) yL(1)],'
    --')
plot([f_etoh(D_mix_920==min(D_mix_920)) f_etoh(D_mix_920==min(D_mix_920))],[min(D_mix_920) yL(1)],'
    --')
plot([f_etoh(D_mix_1400==min(D_mix_1400)) f_etoh(D_mix_1400==min(D_mix_1400))],[min(D_mix_1400) yL
    (1)],'--')

xlabel('\phi_E_t_O_H')
ylabel('\Delta\delta')
legend('EO','575','875','920','1400')

%% PLOT chi amphiphile A/B/C - solvent mixture

figure(3)
hold on
set(gca,'fontsize',16)
plot(f_etoh*100,X_mix_A(:,1),f_etoh*100,X_mix_B(:,1),f_etoh*100,X_mix_C(:,1),f_etoh*100,X_mix_PEOMA
    (:,1))
ax = gca;
ax.ColorOrderIndex = 1;
yL = get(gca,'YLim');
plot([f_etoh(X_mix_A(:,1)==min(X_mix_A(:,1))) f_etoh(X_mix_A(:,1)==min(X_mix_A(:,1)))]*100,[min(
    X_mix_A(:,1)) yL(1)],'--')
plot([f_etoh(X_mix_B(:,1)==min(X_mix_B(:,1))) f_etoh(X_mix_B(:,1)==min(X_mix_B(:,1)))]*100,[min(
    X_mix_B(:,1)) yL(1)],'--')
plot([f_etoh(X_mix_C(:,1)==min(X_mix_C(:,1))) f_etoh(X_mix_C(:,1)==min(X_mix_C(:,1)))]*100,[min(
    X_mix_C(:,1)) yL(1)],'--')
plot([f_etoh(X_mix_PEOMA(:,1)==min(X_mix_PEOMA(:,1))) f_etoh(X_mix_PEOMA(:,1)==min(X_mix_PEOMA(:,1))
    )]*100,[min(X_mix_PEOMA(:,1)) yL(1)],'--')
xlabel('\phi_E_t_O_H (vol%)')
ylabel('\chi')
legend('A','B','C','MPEOMA')


%% PLOT chi amphiphile B575/B875 - solvent mixture

figure(4)
hold on
set(gca,'fontsize',14)
plot(f_etoh,X_mix_EO(:,1),f_etoh,X_mix_575(:,1),f_etoh,X_mix_875(:,1),f_etoh,X_mix_920(:,1),f_etoh,
    X_mix_1400(:,1))
ax = gca;
ax.ColorOrderIndex = 1;
yL = get(gca,'YLim');
plot([f_etoh(X_mix_EO(:,1)==min(X_mix_EO(:,1))) f_etoh(X_mix_EO(:,1)==min(X_mix_EO(:,1)))],[min(
    X_mix_EO(:,1)) yL(1)],'--')
plot([f_etoh(X_mix_575(:,1)==min(X_mix_575(:,1))) f_etoh(X_mix_575(:,1)==min(X_mix_575(:,1)))],[min(
    X_mix_575(:,1)) yL(1)],'--')
plot([f_etoh(X_mix_875(:,1)==min(X_mix_875(:,1))) f_etoh(X_mix_875(:,1)==min(X_mix_875(:,1)))],[min(
    X_mix_875(:,1)) yL(1)],'--')
plot([f_etoh(X_mix_920(:,1)==min(X_mix_920(:,1))) f_etoh(X_mix_920(:,1)==min(X_mix_920(:,1)))],[min(
    X_mix_920(:,1)) yL(1)],'--')
plot([f_etoh(X_mix_1400(:,1)==min(X_mix_1400(:,1))) f_etoh(X_mix_1400(:,1)==min(X_mix_1400(:,1)))],[
    min(X_mix_1400(:,1)) yL(1)],'--')
xlabel('\phi_E_t_O_H')
ylabel('\chi')
legend('EO','B575','B875','B920','B1400','Location','North')

%% PLOT temperature vs chi in solvent mixture for A/B/C

figure(5)
hold on
plot(T,X_mix_A(11,:),T,X_mix_B(11,:),T,X_mix_C(11,:),T,X_mix_PEOMA(11,:))
xlabel('T (K)')
```

```
ylabel('\chi')
legend('A','B','C','MPEOMA')

%% PLOT temperature vs chi in solvent mixture hexane:etoh for A/B/C (for scaling)

figure(5)
hold on
plot(T-273,X_mix_PEOMA(vf,:),T-273,X_mix_A(vf,:),T-273,X_mix_B(vf,:),T-273,X_mix_C(vf,:))
plot(T-273,X_hex_A,T-273,X_hex_B,T-273,X_hex_C)
xlabel('T')
ylabel('\chi')
legend('MPEOMA','A','B','C')


%% PLOT solubility sphere PE-b-PEG

r = D_mek_575;
[x,y,z] = ellipsoid(dd_575,dp_575,dh_575,r,r,r,128);

figure (6)
h = surfl(x, y, z);
set(h, 'FaceAlpha', 0.2, 'FaceColor', [0 1 0], 'EdgeColor', 'none');
shading interp
hold on
scatter3(dd_575,dp_575,dh_575,50,'filled','d')
text(dd_575,dp_575,dh_575-0.1,'B575  ','HorizontalAlignment','right')
scatter3(dd_875,dp_875,dh_875,50,'filled','d')
text(dd_875,dp_875,dh_875,'B875  ','HorizontalAlignment','right')
scatter3(dd_920,dp_920,dh_920,50,'filled','d')
text(dd_920,dp_920,dh_920,'B920  ','HorizontalAlignment','right')
scatter3(dd_1400,dp_1400,dh_1400,50,'filled','d')
text(dd_1400,dp_1400,dh_1400+0.1,'B1400  ','HorizontalAlignment','right')
scatter3(dd_tol,dp_tol,dh_tol,50,'filled','^','MarkerFaceColor',[0 0.5 0])
text(dd_tol,dp_tol,dh_tol,'  Toluene')
scatter3(dd_mek,dp_mek,dh_mek,50,'filled','^','MarkerFaceColor',[0 0.5 0])
text(dd_mek,dp_mek,dh_mek,'  MEK')
scatter3(dd_ace,dp_ace,dh_ace,50,'filled','rv')
text(dd_ace,dp_ace,dh_ace,'  Aceton')
scatter3(dd_dod,dp_dod,dh_dod,50,'filled','^','MarkerFaceColor',[0 0.5 0])
text(dd_dod,dp_dod,dh_dod,'  Dodecane')
scatter3(dd_etoh,dp_etoh,dh_etoh,50,'filled','rv')
text(dd_etoh,dp_etoh,dh_etoh,' Ethanol')
for i=1:6
    point = 1+(steps-1)*i/10;
    scatter3(dd_mix_sol(point),dp_mix_sol(point),dh_mix_sol(point),'filled','MarkerFaceColor',[0 0.5
        0])
end
for i=7:10
    point = 1+(steps-1)*i/10;
    scatter3(dd_mix_sol(point),dp_mix_sol(point),dh_mix_sol(point),'filled','r')
end
text(dd_mix_sol(1+(steps-1)*0.1),dp_mix_sol(1+(steps-1)*0.1),dh_mix_sol(1+(steps-1)*0.1),'  10 vol%
    EtOH')
text(dd_mix_sol(1+(steps-1)*0.2),dp_mix_sol(1+(steps-1)*0.2),dh_mix_sol(1+(steps-1)*0.2),'  20 vol%
    EtOH')
text(dd_mix_sol(1+(steps-1)*0.7),dp_mix_sol(1+(steps-1)*0.7),dh_mix_sol(1+(steps-1)*0.7),'  70 vol%
    EtOH')
plot3([dd_575, dd_mek], [dp_575, dp_mek], [dh_575, dh_mek],'k:', 'LineWidth', 1);
plot3(dd_mix_sol, dp_mix_sol, dh_mix_sol,'k:', 'LineWidth', 1);
grid on
axis equal
xlabel('\delta_d');ylabel('\delta_p');zlabel('\delta_h')
axis([10 30 0 12 0 20])
view([1 0 0])

%% PLOT solubility sphere PEHMA-stat-PMPEOMA

r = D_mek_B;
[x,y,z] = ellipsoid(dd_B,dp_B,dh_B,r,r,r,128);
figure (7)
h = surfl(x, y, z);
set(h, 'FaceAlpha', 0.2, 'FaceColor', [0 1 0], 'EdgeColor', 'none');
shading interp
set(gca,'fontsize',20)
hold on
scatter3(dd_A,dp_A,dh_A,50,'filled','d')
text(dd_A,dp_A,dh_A-0.1,'A  ','HorizontalAlignment','right')
scatter3(dd_B,dp_B,dh_B,50,'filled','d')
text(dd_B,dp_B,dh_B,'B  ','HorizontalAlignment','right')
scatter3(dd_C,dp_C,dh_C,50,'filled','d')
text(dd_C,dp_C,dh_C+0.1,'C  ','HorizontalAlignment','right')
scatter3(dd_tol,dp_tol,dh_tol,50,'filled','^','MarkerFaceColor',[0 0.5 0])
text(dd_tol,dp_tol,dh_tol,'  Toluene')
scatter3(dd_mek,dp_mek,dh_mek,50,'filled','^','MarkerFaceColor',[0 0.5 0])
```

```
text(dd_mek,dp_mek,dh_mek,'  MEK')
scatter3(dd_ace,dp_ace,dh_ace,50,'filled','rv')
text(dd_ace,dp_ace,dh_ace,'  Aceton')
scatter3(dd_dod,dp_dod,dh_dod,50,'filled','^','MarkerFaceColor',[0 0.5 0])
text(dd_dod,dp_dod,dh_dod,'  Dodecane')

scatter3(dd_etoh,dp_etoh,dh_etoh,50,'filled','rv')
text(dd_etoh,dp_etoh,dh_etoh,' Ethanol')
for i=1:7
    point = 1+(steps-1)*i/10;
    scatter3(dd_mix_sol(point),dp_mix_sol(point),dh_mix_sol(point),'filled','MarkerFaceColor',[0 0.5
        0])
end
for i=8:10
    point = 1+(steps-1)*i/10;
    scatter3(dd_mix_sol(point),dp_mix_sol(point),dh_mix_sol(point),'filled','r')
end
text(dd_mix_sol(1+(steps-1)*0.1),dp_mix_sol(1+(steps-1)*0.1),dh_mix_sol(1+(steps-1)*0.1),'  10 vol%
    EtOH')
text(dd_mix_sol(1+(steps-1)*0.2),dp_mix_sol(1+(steps-1)*0.2),dh_mix_sol(1+(steps-1)*0.2),'  20 vol%
    EtOH')
text(dd_mix_sol(1+(steps-1)*0.7),dp_mix_sol(1+(steps-1)*0.7),dh_mix_sol(1+(steps-1)*0.7),'  70 vol%
    EtOH')
plot3([dd_B, dd_mek], [dp_B, dp_mek], [dh_B, dh_mek],'k:', 'LineWidth', 1);
plot3(dd_mix_sol, dp_mix_sol, dh_mix_sol,'k:', 'LineWidth', 1);
grid on
axis equal
xlabel('\delta_d');ylabel('\delta_p');zlabel('\delta_h')
axis([10 30 0 12 0 20])
view([1 0 0])
```

D.2. Stabilization kinetics

This script computes τ as a function of the amphiphile concentration for DC, KC and MC adsorption kinetics (Equations 4.14, 4.16 and 4.11, respectively, and plotted in Figure 4.3 in the paper) using, among other things, the solubility parameters computed in the script of Section D.1.

```
clear all
close all
clc

chi

%% Polymer adsorption kinetics
% Fixed inputs
R_etOH      = 5;        % vol% etOH dispersion
V_tol       = 2;        % volume toluene (mL)
c_p0        = 1e-3;     % concentration polymer (g/mL)
MW          = 19e3;     % MW polymer (g/mol)
c_s_etOH    = 0.007;    % concentration solids in etOH (w/v%) (g/100mL)
T           = 353;      % temperature
G           = 1;        % mean shear rate
theta       = 0.95;     % fractional surface coverage;

% Parameters
vf          = (((R_etOH/100)/1))*(steps-1)+1;   % volume fraction step for loop
d_p         =  2e-9*(MW/10.6e3)^(3/5);          % diameter polymer
d_np        = 15e-9;                            % diameter NP (number-weighted average from DLS)
rho_s       = 4560;                             % density YAG (kg/m3)
kb          = 1.38064852e-23;                   % Boltzmann constant
N           = 6.022140857e23;                   % Avogadro's constant
A1          = -5.878;
A2          = 1287;
A3          = .004575;
A4          = -4.499e-6;
mu          = exp(A1 + A2/T + A3*T + A4*T^2) * 1e-3;    % viscosity toluene (Pa.s)

% Calculate number concentration solids
V_etOH          = V_tol/(100-R_etOH)*(R_etOH);  % volume etOH dispersion (mL)
V_tot           = V_tol + V_tol/(95)*(5);       % total volume (mL)
V_np            = 4/3*pi*(d_np/2)^3;            % volume per NP (m3)
c_s_etOH_gmL    = c_s_etOH/100;                 % concentration solids (w/v% to g/mL)
m_s             = c_s_etOH_gmL*V_etOH;          % total mass solids (g)
m_np            = V_np*rho_s*1000;              % mass per NP (g)
n_s             = m_s/m_np / V_tot;             % number concentration solids (per mL mixture)
n_s_m3          = n_s * 1e6;                    % number concentration solid (per m3 mixture)

% Calculate number concentration polymer (at t=0) & surface coverage if all
% is adsorbed
m_p0        = c_p0*V_tol;               % total mass polymer (g) in toluene
mol_p0      = m_p0 / MW;                % total moles polymer in toluene
```

```
n_p0        = mol_p0 * N / V_tot;       % number concentration polymer (per mL mixture)
n_p0_m3     = n_p0 * 1e6;               % number concentration polymer (per m3 mixture)
mol_p0_m3   = n_p0_m3 / N;              % molar concentration polymer (per m3 mixture)

% Calculate number concentration polymer for max coverage (theta=1)
n_a         = 4*n_s*(d_np/d_p)^2;       % number of adsorbed molecules (per mL mixture)
n_a_m3      = n_a * 1e6;                % number of adsorbed molecules (per m3 mixture)
n_a_np      = n_a/n_s;                  % number of molecules per NP
mol_a_np    = n_a_np / N;               % moles absorbed per NP
mol_a       = n_a / N;                  % moles absorbed (per mL mixture)
mol_a_m3    = mol_a * 1e6;              % moles absorbed (per m3 mixture)
m_a         = mol_a * MW;               % mass absorbed (g) (per mL mixture)
F_mol       = mol_p0_m3/mol_a_m3;       % Factor molar excess stabilizer


%% Adsorption % agglomeration time
% Calculate absorption time (surplus polymer, n_p0 constant)
K_ij        = 8*kb*T/(3*mu) + G/6*(2*d_np)^3;                           % collision frequency
    constant NP-NP
K_sp        = 2*kb*T/(3*mu)*(2+d_p/d_np+d_np/d_p)+ G/6*(d_np+d_p)^3;    % collision frequency
    constant polymer-NP
F_K         = K_sp/K_ij;
A_np        = 4*pi*(d_np/2)^2;                                          % surface area NP (m2)
A_np_m3     = A_np * n_s_m3;                                            % total surface area NPs (m2
    per m3 mixture)
gamma_m     = mol_a_m3 / A_np_m3;                                       % maximum surface coverage (
    mol/m2)
gamma_m2    = 4/(N*A_np)*(d_np/d_p)^2;                                  % maximum surface coverage (
    mol/m2)
D_p         = kb*T/(6*pi*mu*(d_p/2));                                   % diffusion constant polymer
t_dl95      = (-log(1-theta)*gamma_m./(2*mol_p0_m3)).^2 .* pi/(D_p);    % diffusion-limited
    adsorption time (95% adsorbed)

% Calculate agglomeration time
t_ag95      = (20-1)*3*mu/(4*kb*T*n_s_m3);                      % agglomeration time diffusion (95%
    agglomerated)
F_b         = 2;
F_s         = 3;
phi_s_m3    = V_np*n_s_m3;                                      % volume concentration NPs (m3 per
    m3 mixture)
K_b         = 2*kb*T/(3*mu)*F_b;                                % rate constant Brownian
K_s         = G*phi_s_m3/pi*F_s;                                % rate constant shear
t_fl95      = log((K_b*n_s_m3+K_s*20)/(K_b*n_s_m3+K_s))/K_s;    % flocculation time diffusion&shear
    (95% agglomerated)
X_np        = n_s_m3^(-1/3);                                    % average interparticle distance

% Calculate tau
tau         = t_dl95/t_fl95;



%% PLOT tau (DC, KC & MC) vs amphiphile concentration

MW_array            = [19e3 29e3 33e3 19e3 29e3 33e3]; %[575 875];
X_all_T             = [X_mix_A(vf); X_mix_B(vf); X_mix_C(vf); X_mix_A(vf); X_mix_B(vf); X_mix_C(vf)
    ]; %X_mix_575(vf); X_mix_875(vf);
k_a                 = vpa([1 1 1 10 10 10]);
X_75hex_25etoh_B    = 0.15;
for i = 1:6
    disp(i)
    for j = 1:20
        disp(j)

        d_p(i)              = 2e-9*(MW_array(i)/10.6e3)^(3/5)*( (0.5-X_all_T(i))/(0.5-
            X_75hex_25etoh_B) )^0.2;  % diameter polymer
        C_X(i)              = ( (0.5-X_all_T(i))/(0.5-X_75hex_25etoh_B) )^0.2;
        D_p(i)              = vpa(kb*T/(6*pi*mu*(d_p(i)/2)));   % Diffusion constant polymer
        gamma_m2(i)         = vpa(4/(N*A_np)*(d_np/d_p(i))^2);
        c_p0_c(j)           = 1e-4+1e-4*(j-1);                      % concentration polymer in
            toluene (g/mL)
        m_p0_c(j)           = c_p0_c(j)*V_tol;                      % total mass polymer (g) in
            toluene
        mol_p0_m3_c(i,j)    = vpa((m_p0_c(j) / MW_array(i))/V_tol *1e6);          % total moles
            polymer (per m3 mixture)
        mol_a_m3_c(i)       = 4*n_s*(d_np/d_p(i))^2 / N *1e6;
        F_mol_c(i,j)        = mol_p0_m3_c(i,j) / mol_a_m3_c(i);       % Factor of molar excess
            stabilizer

        t_dl95_c(i,j)       = (-log(1-theta)*gamma_m2(i)/(2*mol_p0_m3_c(i,j)))^2 * pi/(D_p(i));    %
             diffusion-limited adsorption time (95% adsorbed)
        t_fl95_c(i,j)       = log((K_b*n_s_m3+K_s*20)/(K_b*n_s_m3+K_s))/K_s;                %
            flocculation time diffusion&shear (95% agglomerated)
        tau_dc_c(i,j)       = t_dl95_c(i,j)/t_fl95_c(i,j);

```

```
        t_kc95_c(i,j)       = log(1/(1-theta))/(k_a(i)*mol_p0_m3_c(i,j));
        tau_kc_c(i,j)       = t_kc95_c(i,j)/t_fl95_c(i,j);
    tic
        syms t_symMC1 t_symMC2
        eqn1                = vpa(theta) - 1 + exp(-mol_p0_m3_c(i,j)*D_p/(k_a(i)*gamma_m2(i)^2)* (
            exp(k_a(i)^2*gamma_m2(i)^2*t_symMC1/D_p(i))*erfc(k_a(i)*gamma_m2(i)*sqrt(t_symMC1/D_p(i
            ))) + 2*k_a(i)*gamma_m2(i)*sqrt(t_symMC1/(D_p(i)*pi))-1))==0;
        t_mc95_c            = zeros(3,20);
        t_mc95_c(i,j)       = solve(eqn1(i),t_symMC1,'Real',true);
        tau_mc_c(i,j)       = t_mc95_c(i,j)/t_fl95_c(i,j);
    toc
    end
end

figure(1)
hold on
for k = 1:length(MW_array)
%     plot(c_p0_c*1e3,t_dl95_c(k,:))
%     plot(c_p0_c*1e3,t_fl95_c(1,:))
    plot(c_p0_c*1e3,tau_dc_c(k,:))
    plot(c_p0_c*1e3,tau_kc_c(k,:))
    plot(c_p0_c*1e3,tau_mc_c(k,:))
    ax = gca;
    ax.ColorOrderIndex = 1;
end
plot(c_p0_c*1e3,ones(1,length(c_p0_c)),'--k')
set(gca, 'XScale', 'log')
set(gca, 'YScale', 'log')
set(gca,'fontsize',20)
grid on
xlabel('c_0 (g/L)')
ylabel('\tau')
title('\tau vs amphiphile concentration')
legend('\tau_d_c','\tau_k_c','\tau_m_c','\tau=1')
% legend('\tau_d_c, B575','\tau_d_c, B875','\tau = 1')


%% PLOT tau (DC) vs temperature

X_all_T             = [X_mix_575(vf,:); X_mix_875(vf,:); X_mix_A(vf,:); X_mix_B(vf,:); X_mix_C(vf,:)
    ];
X_75hex_25etoh_B    = 0.15;
MW_array            = [575 875 19e3 29e3 33e3];

for i = 1:length(MW_array)
    for j = 1:81
    d_p(i,j)        = 2e-9*(MW_array(i)/10.6e3)^(3/5)*((0.5-X_all_T(i,j))/(0.5-X_75hex_25etoh_B) )
        ^0.2;  % diameter copolymer
    mol_p0(i)       = m_p0 / MW_array(i);
    mol_p0_m3_T(i)  = mol_p0(i) * N / V_tot * 1e6 / N;                                          % #
        concentration polymer (per mL mixture)
    gamma_m2_T(i,j) = 4/(N*A_np)*(d_np/d_p(i,j))^2;
    T_T(j)          = 293 + (j-1);
    A1              = -5.878;
    A2              = 1287;
    A3              = .004575;
    A4              = -4.499e-6;
    mu_T(j)         = exp(A1 + A2/T_T(j) + A3*T_T(j) + A4*T_T(j)^2) * 1e-3;                     %
        viscosity (Pa.s)
    K_b_T(j)        = 2*kb*T_T(j)/(3*mu_T(j))*F_b;                                              %
        rate constant Brownian
    D_p_T(i,j)      = kb*T_T(j)/(6*pi*mu_T(j)*(d_p(i,j)/2));                                    %
        diffusion constant polymer

    t_dl95_T(i,j)   = (-log(1-theta)*gamma_m2_T(i,j)/(2*mol_p0_m3_T(i)))^2 * pi/(D_p_T(i,j));   %
        diffusion-limited adsorption time (95% adsorbed)
    t_fl95_T(j)     = log((K_b_T(j)*n_s_m3+K_s*20)/(K_b_T(j)*n_s_m3+K_s))/K_s;                  %
        flocculation time diffusion&shear (95% agglomerated)
    tau(i,j)        = t_dl95_T(i,j)/t_fl95_T(j);
    end
end
figure(2)
hold on
for k = 1:length(MW_array)
% plot(T_T-273,t_dl95_T(k,:))
plot(T_T-273,tau(k,:))
end
% plot(T_T-273,t_fl95_T)
set(gca, 'YScale', 'log')
grid on
xlabel('Temperature (\circC)')
ylabel('\tau')
set(gca, 'YScale', 'log')
set(gca,'fontsize',20)
```

```
title('\tau vs temperature')
legend('\tau_D_C, 575','\tau_D_C, 875','\tau_D_C, A','\tau_D_C, B','\tau_D_C, C' )
% legend('t_a_g_9_5','t_a_d_9_5, 575','t_a_d_9_5, 875','t_a_d_9_5, A','t_a_d_9_5, B','t_a_d_9_5, C'
    )
```

D.3. Controlling mechanism of adsorption

This script computes the estimated slope of $\ln(d_h)$ vs $\ln(c_0)$ for MC adsorption computed by Equation 4.44 as a function of the adsorption rate constant k_a (Equation 4.44 and Figure 4.4 in the paper).

```
close all
clear all
clc

mol_p0_m3_array = vpa([0.05 0.0328 0.0288]);                % molar concentration of A, B & C
D_p_array       = vpa([7.4036e-10 5.7446e-10 5.3160e-10]);  % diffusion constant of A, B & C
gamma_m2_array  = vpa([2.6240e-07 1.5798e-07 1.3528e-07]);  % max surface coverage of A, B & C
c0_array        = [1 10];                                   % c0

for c0 = 1:2        % loop for concentration
    figure(2)
    ax = gca;
    ax.ColorOrderIndex = 1;
    for cp = 1:3    % loop for copolymer
theta           = 0.95;                                 % surface coverage
mol_p0_m3_1     = mol_p0_m3_array(cp)*c0_array(c0);     % molar c0
D_p             = D_p_array(cp);                        % diffusion constant
gamma_m2        = gamma_m2_array(cp);                   % max surface coverage
dc              = 0.001;                                % infinitessimal step
mol_p0_m3       = vpa([mol_p0_m3_1 mol_p0_m3_1+dc]);    % molar c0 and at c0+step
D_f             = 1.8;                                  % fractal dimension

%% Solving KC, DC & MC

% ka_mc = [1e-4 10 1e7];
% ka_sym = vpa(ka_mc(1));
% t_dc0 = (log(1-theta)*gamma_m2./(2*mol_p0_m3(1))).^2 .* pi/(D_p)
% t_dc1 = theta^2*gamma_m2^2*pi/(4*mol_p0_m3(1)^3*D_p)
% t_kc0 = -log(1-theta)/(ka_sym*mol_p0_m3(1))
% syms t_symDC t_symKC
% eqn1 = theta - 1 + exp(-2*(mol_p0_m3(1)/gamma_m2)*sqrt(D_p*t_symDC/pi)) == 0;
% t_dc = solve(eqn1,t_symDC)
% eqn2 = theta - 1 + exp(-ka_sym*mol_p0_m3(1)*t_symKC) == 0;
% t_kc = solve(eqn2,t_symKC)

% % Solving KC
% syms t_symKC1 t_symKC2
% eqn3 = theta - 1 + exp(-ka_sym*mol_p0_m3(1)*t_symKC1) == 0;
% t_kc1 = solve(eqn3,t_symKC1,'Real',true);
% eqn4 = theta - 1 + exp(-ka_sym*mol_p0_m3(2)*t_symKC2) == 0;
% t_kc2 = solve(eqn4,t_symKC2,'Real',true);
% slope_kc0 = (t_kc1./t_kc2)/dc;
%
% % Solving DC
% syms t_symDC1 t_symDC2
% eqn5 = theta - 1 + exp(-2*(mol_p0_m3(1)/gamma_m2)*sqrt(D_p*t_symDC1/pi)) == 0;  % diffusion-
    controlled
% t_dc1 = solve(eqn5,t_symDC1,'Real',true);
% eqn6 = theta - 1 + exp(-2*(mol_p0_m3(2)/gamma_m2)*sqrt(D_p*t_symDC2/pi)) == 0;  % diffusion-
    controlled
% t_dc2 = solve(eqn6,t_symDC2,'Real',true);
% slope_dc0 = (t_dc1./t_dc2)/dc;
%
% % Solving mixed control for erfc(x)
% syms t_sym
% eqn1 = theta - 1 + exp(-mol_p0_m3(1)*D_p/(ka_sym*gamma_m2^2)* ( exp(ka_sym^2*gamma_m2^2*t_sym/D_p)
    *erfc(ka_sym*gamma_m2*sqrt(t_sym/D_p)) + 2*ka_sym*gamma_m2*sqrt(t_sym/(D_p*pi))-1))==0;
% t_mc1 = solve(eqn1,t_sym,'Real',true);
% syms t_sym2
% eqn2 = theta - 1 + exp(-mol_p0_m3(2)*D_p/(ka_sym*gamma_m2^2)* ( exp(ka_sym^2*gamma_m2^2*t_sym2/D_p
    )*erfc(ka_sym*gamma_m2*sqrt(t_sym2/D_p)) + 2*ka_sym*gamma_m2*sqrt(t_sym2/(D_p*pi))-1))==0;
% t_mc2 = solve(eqn2,t_sym2,'Real',true);
% slope_mc0 = (t_mc1./t_mc2)/dc;

% % Approximation for erfc(x)
% a1 = 0.278393;
% a2 = 0.230389;
% a3 = 0.000972;
% a4 = 0.078108;
% syms t_sym
% x1 = ka_sym*gamma_m2*sqrt(t_sym/D_p);
```

```
% erfc1 = 1/(1 + a1*x1 + a2*x1^2 + a3*x1^3 + a4*x1^4)^4;
% eqn1 = theta - 1 + exp(-mol_p0_m3(1)*D_p/(ka_sym*gamma_m2^2)* ( exp(ka_sym^2*gamma_m2^2*t_sym/D_p)*erfc1 + 2*ka_sym*gamma_m2*sqrt(t_sym/(D_p*pi))-1))==0;
% t_mc1 = solve(eqn1,t_sym,'Real',true);
% syms t_sym2
% x2 = ka_sym*gamma_m2*sqrt(t_sym2/D_p);
% erfc2 = 1/(1 + a1*x2 + a2*x2^2 + a3*x2^3 + a4*x2^4)^4;
% eqn2 = theta - 1 + exp(-mol_p0_m3(2)*D_p/(ka_sym*gamma_m2^2)* ( exp(ka_sym^2*gamma_m2^2*t_sym2/D_p)*erfc2 + 2*ka_sym*gamma_m2*sqrt(t_sym2/(D_p*pi))-1))==0;
% t_mc2 = solve(eqn2,t_sym2,'Real',true);
% slope = -sqrt(t_mc1/t_mc2)
% ka_mc = 0.1:0.1:1;

% % Approximation for erfc(x) by Seki
% syms t_sym
% x1 = ka_sym*gamma_m2*sqrt(t_sym/D_p);
% erfc1 = 1 - 2/sqrt(pi)*exp(-x1^2)*(x1+2/3*x1^3);
% eqn1 = theta - 1 + exp(-mol_p0_m3(1)*D_p/(ka_sym*gamma_m2^2)* ( exp(x1^2)*erfc1 + 2*x1-1))==0;
% t_mc1 = solve(eqn1,t_sym,'Real',true);
% syms t_sym2
% x2 = ka_sym*gamma_m2*sqrt(t_sym2/D_p);
% erfc2 = 1 - 2/sqrt(pi)*exp(-x2^2)*(x2+2/3*x2^3);
% eqn2 = theta - 1 + exp(-mol_p0_m3(2)*D_p/(ka_sym*gamma_m2^2)* ( exp(x2^2)*erfc2 + 2*x2-1))==0;
% t_mc2 = solve(eqn2,t_sym2,'Real',true);
% slope = -sqrt(t_mc1/t_mc2)


%% Loops

ka_mc = logspace(-1,6);
for i=1:length(ka_mc)
    ka_sym(i) = vpa(ka_mc(i));
% Solving MC
syms t_symMC1 t_symMC2
eqn1 = theta - 1 + exp(-mol_p0_m3(1)*D_p/(ka_sym(i)*gamma_m2^2)* ( exp(ka_sym(i)^2*gamma_m2^2*t_symMC1/D_p)*erfc(ka_sym(i)*gamma_m2*sqrt(t_symMC1/D_p)) + 2*ka_sym(i)*gamma_m2*sqrt(t_symMC1/(D_p*pi))-1))==0;
t_mc1(i) = solve(eqn1,t_symMC1,'Real',true);
eqn2 = theta - 1 + exp(-mol_p0_m3(2)*D_p/(ka_sym(i)*gamma_m2^2)* ( exp(ka_sym(i)^2*gamma_m2^2*t_symMC2/D_p)*erfc(ka_sym(i)*gamma_m2*sqrt(t_symMC2/D_p)) + 2*ka_sym(i)*gamma_m2*sqrt(t_symMC2/(D_p*pi))-1))==0;
t_mc2(i) = solve(eqn2,t_symMC2,'Real',true);
slope_mc(i) = log((t_mc1(i)./t_mc2(i)))/log(mol_p0_m3(1)/mol_p0_m3(2));
% Solving KC
syms t_symKC1 t_symKC2
eqn3 = theta - 1 + exp(-ka_sym(i)*mol_p0_m3(1)*t_symKC1) == 0;
t_kc1(i) = solve(eqn3,t_symKC1,'Real',true);
eqn4 = theta - 1 + exp(-ka_sym(i)*mol_p0_m3(2)*t_symKC2) == 0;
t_kc2(i) = solve(eqn4,t_symKC2,'Real',true);
slope_kc(i) = log((t_kc1(i)./t_kc2(i)))/log(mol_p0_m3(1)/mol_p0_m3(2));
% Solving DC
syms t_symDC1 t_symDC2
eqn5 = theta - 1 + exp(-2*(mol_p0_m3(1)/gamma_m2)*sqrt(D_p*t_symDC1/pi)) == 0;  % diffusion-controlled
t_dc1(i) = solve(eqn5,t_symDC1,'Real',true);
eqn6 = theta - 1 + exp(-2*(mol_p0_m3(2)/gamma_m2)*sqrt(D_p*t_symDC2/pi)) == 0;  % diffusion-controlled
t_dc2(i) = solve(eqn6,t_symDC2,'Real',true);
slope_dc(i) = log((t_dc1(i)./t_dc2(i)))/log(mol_p0_m3(1)/mol_p0_m3(2));
disp(i)
end

%% PLOT
lim1 = ka_mc;

figure(1)
hold on
plot(lim1,t_mc1)
plot(lim1,t_kc1)
plot(lim1,t_dc1)
set(gca, 'YScale', 'log')
set(gca, 'XScale', 'log')
xlabel('k_a')
% xlabel('k_a^2\Gamma_m^2/D')
% xlabel('Dc_0/(k_a\Gamma_m^2)')
% xlabel('k_a')
ylabel('t_1 (\Gamma/\Gamma_m=0.95)')
% legend('t_m_c_1 (c=c_0)','t_m_c_2 (c=2\cdotc_0)','t_r_c_1 (c=c_0)','t_r_c_2 (c=2\cdotc_0)','t_d_c_1 (c=c_0)','t_d_c_2 (c=2\cdotc_0)')
legend('MC','KC','DC')

figure(2)
hold on
grid on
```

```
plot(lim1,slope_mc/D_f)
set(gca, 'XScale', 'log')
xlabel('k_a')
% ylabel('proportionality coefficient a (t ~ c_0^-^a)')
ylabel('\Deltaln(d_h)/\Deltaln(c_0)')
legend('A','B','C')
    end
    plot([1e-1 1e6],[-0.57 -0.57],'--k','HandleVisibility','off')
end
```

D.4. Activation energy

This script computes the estimated activation energies of copolymer A, B and C from the experimentally obtained slopes of $\ln(d_h)$ vs. $1/T$ (Equation 4.51 in the paper).

```
clear all
close all
clc

% Parameters
R               = 8.314459;             % gas constant
Ea              = 28200;                % activation energy (random)
A               = 353000;               % exponential pre-factor (random)
for i = 1:81
    dT              = 1;                % temperature increment
    T(i)            = 293+dT*(i-1);     % temperature
    T2(i)           = T(i)+dT;
    ka(i)           = A*exp(-Ea/(R*T(i)));                              % adsorption rate constant
        k_a
    ka2(i)          = A*exp(-Ea/(R*(T(i)+dT)));
    slope_k(i)      = log(ka2(i)^(-1)/ka(i)^(-1)) / (1/T2(i)-1/T(i));   % slope ln(k_a) vs 1/T
    tau(i)          = 1/A*exp(Ea/(R*T(i)))*T(i);
    tau2(i)         = 1/A*exp(Ea/(R*T2(i)))*T2(i);
    slope_tau(i)    = log(tau2(i)/tau(i)) / (1/T2(i)-1/T(i));           % slope ln(tau) vs 1/T
    slope_dh(i)     = 1/1.9 * slope_tau(i);
end


syms Ea_sym A_sym H_sym
% solve for Ea with experimentally obtained slope
for k = 1:3
    slope = [1629.1 1222.5 1082.4];         % experimental slopes of copolymers A, B and C
    eqn1 = 1/1.9 * log( (T(2)/T(1) * exp(-Ea_sym*(T(2)-T(1))/(R*T(1)*T(2)))) ) / (1/T(2)-1/T(1)) -
        slope(k)==0;
    Ea_sol1(k) = vpasolve(eqn1,Ea_sym);     % activation energy
    eqn4 = 1/1.9 * (-H_sym*(T(2)-T(1))/(R*T(1)*T(2)* (1/T(2)-1/T(1))) ) - slope(k)==0;
    H_sol(k) = vpasolve(eqn4,H_sym);        % activation enthalpy
end
disp(Ea_sol1');
disp(H_sol');

% solve for pre exponential factor A
for l = 1:3
    ka_est = [40 40 75];
    eqn5 = A_sym*exp(-Ea_sol1(l)/(R*373))==ka_est(l);
    A_sol(l) = vpasolve(eqn5,A_sym);
end
disp(A_sol')

figure(1)
hold on
grid on
plot(T,slope_k)
figure(2)
hold on
grid on
plot(T,slope_tau)
figure(3)
hold on
grid on
plot(T,slope_dh)
```

Bibliography

[1] UN Environment and International Energy Agency. Towards a zero-emission, efficient, and resilient buildings and construction sector. Global Status Report 2017. Technical report, 2017.

[2] United Nations Framework Convention on Climate Change. The Paris Agreement. `http://unfccc.int/paris{_}agreement/items/9485.php`, 2015.

[3] Ran Fu, David Feldman, Robert Margolis, Mike Woodhouse, and Kristen Ardani. U.S. Solar Photovoltaic System Cost Benchmark: Q1 2017. Technical report, National Renewable Energy Laboratory, 2017.

[4] W. H. Weber and John Lambe. Luminescent greenhouse collector for solar radiation. *Applied Optics*, 15(10), 1976.

[5] J. A. Levitt and W. H. Weber. Materials for luminescent greenhouse solar collectors. *Applied Optics*, 16 (10), 1977.

[6] A. Goetzberger and W. Greube. Solar energy conversion with fluorescent collectors. *Applied Physics*, 14 (2), 1977.

[7] A. Goetzberger. Fluorescent solar energy collectors: Operating conditions with diffuse light. *Applied Physics*, 16(4), 1978.

[8] J.W.E. Wiegman and E. van der Kolk. Building integrated thin film luminescent solar concentrators: Detailed efficiency characterization and light transport modelling. *Solar Energy Materials and Solar Cells*, 103, 2012.

[9] P. K. Tien. Light Waves in Thin Films and Integrated Optics. *Applied Optics*, 10(11), 1971.

[10] Otmar M. ten Kate, Karl W. Krämer, and Erik van der Kolk. Efficient luminescent solar concentrators based on self-absorption free, Tm2+ doped halides. *Solar Energy Materials and Solar Cells*, 140, 2015.

[11] Michael Debije. Better luminescent solar panels in prospect. *Nature*, 519(7543), 2015.

[12] A J Cox, Alan J Deweerd, and Jennifer Linden. An experiment to measure Mie and Rayleigh total scattering cross sections. *American Journal of Physics*, 70, 2002.

[13] Dick K G de Boer, Dirk J Broer, Michael G Debije, Wilco Keur, Andries Meijerink, Cees R Ronda, and Paul P C Verbunt. Progress in phosphors and filters for luminescent solar concentrators. *Opt. Express*, 20(S3), 2012.

[14] Walter Caseri. Nanocomposites of polymers and metals or semiconductors: Historical background and optical properties. *Macromolecular Rapid Communications*, 21(11), 2000.

[15] Wilfried G.J.H.M. van Sark, Keith W.J. Barnham, Lenneke H. Slooff, Amanda J. Chatten, Andreas Büchtemann, Andreas Meyer, Sarah J. McCormack, Rolf Koole, Daniel J. Farrell, Rahul Bose, Evert E. Bende, Antonius R. Burgers, Tristram Budel, Jana Quilitz, Manus Kennedy, Toby Meyer, C. De Mello Donegá, Andries Meijerink, and Daniel Vanmaekelbergh. Luminescent Solar Concentrators - A review of recent results. *Optics Express*, 16(26), 2008.

[16] M.A. El-Shahawy and A.F. Mansour. Optical properties of some luminescent solar concentrators. *Journal of Materials Science: Materials in Electronics*, 7(3), 1996.

[17] A.J. Chatten, K.W.J. Barnham, B.F. Buxton, N.J. Ekins-Daukes, and M.A. Malik. A new approach to modelling quantum dot concentrators. *Solar Energy Materials and Solar Cells*, 75(3-4), 2003.

[18] Olga I. Micic, Calvin J. Curtis, Kim M. Jones, Julian R. Sprague, and Arthur J. Nozik. Synthesis and Characterization of InP Quantum Dots. *The Journal of Physical Chemistry*, 98(19), 1994.

[19] Francesco Meinardi, Annalisa Colombo, Kirill A. Velizhanin, Roberto Simonutti, Monica Lorenzon, Luca Beverina, Ranjani Viswanatha, Victor I. Klimov, and Sergio Brovelli. Large-area luminescent solar concentrators based on 'Stokes-shift-engineered' nanocrystals in a mass-polymerized PMMA matrix. *Nature Photonics*, 8(5), 2014.

[20] G. V. Shcherbatyuk, R. H. Inman, C. Wang, R. Winston, and S. Ghosh. Viability of using near infrared PbS quantum dots as active materials in luminescent solar concentrators. *Applied Physics Letters*, 96 (19), 2010.

[21] Melanie Bottrill and Mark Green. Some aspects of quantum dot toxicity. *Chemical Communications*, 47(25), 2011.

[22] Matthew R Bergren, Nikolay S Makarov, Karthik Ramasamy, Aaron Jackson, Rob Guglielmetti, and Hunter Mcdaniel. High-Performance CuInS 2 Quantum Dot Laminated Glass Luminescent Solar Concentrators for Windows. *ACS Energy Letters*, 3(520), 2018.

[23] Michael G. Debije and Paul P. C. Verbunt. Thirty Years of Luminescent Solar Concentrator Research: Solar Energy for the Built Environment. *Advanced Energy Materials*, 2(1), 2012.

[24] Carlos Ruvalcaba Cornejo. Luminescence in Rare Earth Ion-Doped Oxide Compounds. In Jagannathan Thirumalai, editor, *Luminescence - An Outlook on the Phenomena and their Applications*, chapter 03. InTech, Rijeka, 2016.

[25] C G Allen, D J Baker, J M Albin, H E Oertli, D T Gillaspie, D C Olson, T E Furtak, and R T Collins. Surface Modification of ZnO Using Triethoxysilane-Based Molecules. *Langmuir*, 24, 2008.

[26] Bertrand Faure, German Salazar-Alvarez, Anwar Ahniyaz, Irune Villaluenga, Gemma Berriozabal, Yolanda R De Miguel, and Lennart Bergström. Dispersion and surface functionalization of oxide nanoparticles for transparent photocatalytic and UV-protecting coatings and sunscreens. *Sci. Technol. Adv. Mater*, 14, 2013.

[27] H P Boehm. Acidic and Basic Properties of Hydroxylated Metal Oxide Surfaces. *Discussions of the Faraday Society*, 52, 1971.

[28] Hiroki Tamura, Kenya Mita, Akio Tanaka, and Makoto Ito. Mechanism of Hydroxylation of Metal Oxide Surfaces. *Journal of Colloid and Interface Science*, 243, 2001.

[29] Thomas Hanemann and Dorothée Vinga Szabó. *Polymer-nanoparticle composites: From synthesis to modern applications*, volume 3. 2010.

[30] Jingkun Jiang, Ae Günter, Oberdörster Ae, and Pratim Biswas. Characterization of size, surface charge, and agglomeration state of nanoparticle dispersions for toxicological studies. *Journal of Nanoparticle Research*, 11, 2009.

[31] Gary Nichols, Stephen Byard, Mark J. Bloxham, Joanne Botterill, Neil J. Dawson, Andrew Dennis, Valerie Diart, Nigel C. North, and John D. Sherwood. A Review of the Terms Agglomerate and Aggregate with a Recommendation for Nomenclature Used in Powder and Particle Characterization. *Journal of Pharmaceutical Sciences*, 91(10), 2002.

[32] A Teleki, R Wengeler, L Wengeler, H Nirschl, and S E Pratsinis. Distinguishing between aggregates and agglomerates of flame-made TiO 2 by high-pressure dispersion. *Powder Technology*, 181, 2008.

[33] Swee Pin Yeap. Permanent agglomerates in powdered nanoparticles: Formation and future prospects. *Powder Technology*, 323, 2018.

[34] Eric Laarz, Anders Meurk, and Lennart Bergström. Colloidal Processing of Silicon Nitride. In *Silicon-Based Structural Ceramics for the New Millennium, Volume 142*, Westerville, Ohio, 2003. The American Ceramic Society.

[35] I A Rahman, P Vejayakumaran, C S Sipaut, J Ismail, and C K Chee. Effect of the drying techniques on the morphology of silica nanoparticles synthesized via sol–gel process. *Ceramics International*, 34, 2008.

[36] Yang Zhang, Yongsheng Chen, Paul Westerhoff, Kiril Hristovski, and John C Crittenden. Stability of commercial metal oxide nanoparticles in water. *Water Research*, 42, 2008.

[37] Jacob N. Israelachvili. *Intermolecular and Surface Forces*. Academic Press, Waltham, MA, third edition, 2011.

[38] H.C. Hamaker. The London—van der Waals attraction between spherical particles. *Physica*, 4(10), 1937.

[39] Lennart Bergström. Hamaker constants of inorganic materials. *Advances in Colloid and Interface Science*, 70, 1997.

[40] Johnny Widegren and Lennart Bergström. Electrostatic Stabilization of Ultrafine Titania in Ethanol. *Journal of the American Ceramic Society*, 85(3), 2004.

[41] R.A. French, A.R. Jacobson, B. Kim, S.L. Isley, R.L. Penn, and P. Baveye. Influence of Ionic Strength, pH, and Cation Valence on Aggregation Kinetics of Titanium Dioxide Nanoparticles. *Environmental Science and Technology*, 43, 2009.

[42] B Derjaguin and L Landau. Theory of the Stability of Strongly Charged Lyophobic Sols and of the Adhesion of Strongly Charged Particles in Solutions of Electrolytes. *Acta Physicochimica U.R.S.S.*, 14(633-662), 1941.

[43] E.J. Verwey and J.Th.G. Overbeek. *Theory of the stability of lypophobic colloids*. Elsevier Publishing Company INC., Leiden, 1948.

[44] Particle Sciences. Physical Stability of Disperse Systems. `http://www.particlesciences.com/news/technical-briefs/2009/physical-stability-of-disperse-systems.html`, 2009.

[45] David C. Grahame. Diffuse Double Layer Theory for Electrolytes of Unsymmetrical Valence Types. *The Journal of Chemical Physics*, 21(6), 1953.

[46] Ph. C. van der Hoeven and J. Lyklema. Electrostatic Stabilization in Non-Aqueous Media*. *Advances in Colloid and Interface Science*, 42, 1992.

[47] Peidong Yang. *The Chemistry of Nanostructured Materials*. World Scientific Publishing Company, 2011.

[48] Balazs Pinter, Tim Fievez, F Matthias Bickelhaupt, Paul Geerlings, and Frank De Proft. On the origin of the steric effect. *Phys. Chem. Chem. Phys.*, 14, 2012.

[49] D.H. Napper. Steric stabilization. *Journal of Colloid and Interface Science*, 58(2), 1977.

[50] Joseph W Krumpfer, Thomas Schuster, Markus Klapper, and Klaus Müllen. Make it nano-Keep it nano. *Nano Today*, 8, 2013.

[51] Michael A Boles, Daishun Ling, Taeghwan Hyeon, and Dmitri V Talapin. The surface science of nanocrystals. *Nature Materials*, 15, 2016.

[52] Kerstin Müller, Elodie Bugnicourt, Marcos Latorre, Maria Jorda, Yolanda Echegoyen Sanz, José Lagaron, Oliver Miesbauer, Alvise Bianchin, Steve Hankin, Uwe Bölz, Germán Pérez, Marius Jesdinszki, Martina Lindner, Zuzana Scheuerer, Sara Castelló, and Markus Schmid. Review on the Processing and Properties of Polymer Nanocomposites and Nanocoatings and Their Applications in the Packaging, Automotive and Solar Energy Fields. *Nanomaterials*, 7, 2017.

[53] Giang Van Ngo, Margaillan André, Sylvie Villain, Christine Leroux, and Christine Bressy. Synthesis of ZnO nanoparticles with tunable size and surface hydroxylation. *Journal of Nanoparticle Research*, 15 (1), 2012.

[54] Marie-Alexandra Neouze and Ulrich Schubert. Surface Modification and Functionalization of Metal and Metal Oxide Nanoparticles by Organic Ligands. *Monatshefte für Chemie - Chemical Monthly*, 139 (3), 2008.

[55] Johannes Noack, Larissa Schmidt, Hans-Jürgen Gläsel, Monika Bauer, and Erhard Kemnitz. Inorganic-organic nanocomposites based on sol-gel derived magnesium fluoride. *Nanoscale*, 3(11), 2011.

[56] Mustafa M Demir, Kaloian Koynov, Mit Akbey, Christoph Bubeck, Insun Park, Ingo Lieberwirth, and Gerhard Wegner. Optical Properties of Composites of PMMA and Surface-Modified Zincite Nanoparticles. *Macromolecules*, 40, 2007.

[57] R Y Hong and Q Chen. *Dispersion of Inorganic Nanoparticles in Polymer Matrices: Challenges and Solutions*. 2015.

[58] Yuvaraj Haldorai and Jae-Jin Shim. *Fabrication of Metal Oxide–Polymer Hybrid Nanocomposites*. 2015.

[59] Sarita Kango, Susheel Kalia, Annamaria Celli, James Njuguna, Youssef Habibi, and Rajesh Kumar. Surface modification of inorganic nanoparticles for development of organic–inorganic nanocomposites—A review. *Progress in Polymer Science*, 38, 2013.

[60] Sheng-Wen Zhang, Shu-Xue Zhou, Yu-Ming Weng, and Li-Min Wu. Synthesis of SiO 2 /Polystyrene Nanocomposite Particles via Miniemulsion Polymerization. *Langmuir*, 21(6), 2005.

[61] Maurizio Avella, Maria Emanuela Errico, and Gennaro Gentile. PMMA based nanocomposites filled with modified CaCO3 nanoparticles. *Macromolecular Symposia*, 247, 2007.

[62] Youngchan Shin, Deokkyu Lee, Kangtaek Lee, Kyung Hyun Ahn, and Bumsang Kim. Surface properties of silica nanoparticles modified with polymers for polymer nanocomposite applications. *Journal of Industrial and Engineering Chemistry*, 14, 2008.

[63] M Z Rong, M Q Zhang, and W H Ruan. Surface modification of nanoscale fillers for improving properties of polymer nanocomposites: a review. *Material Science and Technology*, 22(7), 2006.

[64] Min Zhi Rong, Ming Qiu Zhang, Yong Xiang Zheng, Han Min Zeng, R Walter, and K Friedrich. Structure–property relationships of irradiation grafted nano-inorganic particle filled polypropylene composites. *Polymer*, 42, 2001.

[65] M. Z. Rong, M. Q. Zhang, H. B. Wang, and H. M. Zeng. Surface Modification of Magnetic Metal Nanoparticles andIts Influence on the Performance of Polymer Composites. *Polymer Physics*, 41(10), 2003.

[66] D.H. Everett. Manual of Symbols and Terminology for Physicochemical Quantities and Units, Appendix II: Definitions, Terminology and Symbols in Colloid and Surface Chemistry. *Pure and Applied Chemistry*, 31, 1972.

[67] Wei Wang, Xiao Chen, and Shlomo Efrima. Silver Nanoparticles Capped by Long-Chain Unsaturated Carboxylates. *The Journal of Physical Chemistry B*, 103(34), 1999.

[68] Ingegard. Johansson and P. Somasundaran. *Handbook for cleaning/decontamination of surfaces*. Elsevier, 2007.

[69] Béla Pukánszky. Polyolefin Composites: Interfacial Phenomena and Properties. In *Handbook of Polyolefins*, chapter 25, . Taylor & Francis Inc, New York, second edition, 2000.

[70] Sangkyu Lee, Hyeon-Jin Shin, Seon-Mi Yoon, Dong Kee Yi, Jae-Young Choi, and Ungyu Paik. Refractive index engineering of transparent ZrO 2 –polydimethylsiloxane nanocomposites. *The Royal Society of Chemistry*, 18, 2008.

[71] By Stephan Förster and Markus Antonietti. Amphiphilic Block Copolymers in Structure- Controlled Nanomaterial Hybrids. *Advanced Materials*, 10(3), 1998.

[72] Victor Khrenov, Markus Klapper, Mathias Koch, and Klaus Mu. Surface Functionalized ZnO Particles Designed for the Use in Transparent Nanocomposites. *Macromolecular Chemistry and Physics*, 206, 2005.

[73] Khalid Chiad, Simon H Stelzig, Radu Gropeanu, Tanja Weil, Markus Klapper, and Klaus Müllen. Isothermal Titration Calorimetry: A Powerful Technique To Quantify Interactions in Polymer Hybrid Systems. *Macromolecules*, 42, 2009.

[74] F. E. Golling, T. Schuster, C. Geidel, L. Mammen, D. Vollmer, K. Müllen, and M. Klapper. The power of perfluorinated amphiphilic polymers at interfaces. In *Advances in Fluorine-Containing Polymers*, volume 1106, chapter 8, . American Chemical Society, 2012.

[75] Gérard Riess. Micellization of block copolymers. *Progress in Polymer Science*, 28, 2003.

[76] Taco Nicolai, Olivier Colombani, and Christophe Chassenieux. Dynamic polymeric micelles versus frozen nanoparticles formed by block copolymers. *Soft Matter*, 6, 2010.

[77] O Théodoly, M Jacquin, P Muller, and S Chhun. Adsorption Kinetics of Amphiphilic Diblock Copolymers: From Kinetically Frozen Colloids to Macrosurfactants. *Langmuir*, 25, 2009.

[78] Robert J. Good, Louis A. Girifalco, and Gerard Kraus. A Theory for Estimation of Interfacial Energies. II. Application to Surface Thermodynamics of Teflon and Graphite. *The Journal of Physical Chemistry*, 62 (11), 1958.

[79] Raoul Zana, Carlos Marques, and Albert Johner. Dynamics of micelles of the triblock copolymers poly(ethylene oxide)–poly(propylene oxide)–poly(ethylene oxide) in aqueous solution. *Colloid and Interface Science*, 123-126, 2006.

[80] Jan Van Stam, Serge Creutz, Frans C De Schryver, and Robert Jé Rô Me. Tuning of the Exchange Dynamics of Unimers between Block Copolymer Micelles with Temperature, Cosolvents, and Cosurfactants. *Macromolecules*, 33(17), 2000.

[81] Yongmei Wang, R Balaji, Roderic P Quirk, and Wayne L Mattice. Detection of the rate of exchange of chains between micelles formed by diblock copolymers in aqueous solution. *Polymer Bulletin*, 28, 1992.

[82] Patrizio Raffa, Diego Armando, Zakarias Wever, Francesco Picchioni, and Antonius A Broekhuis. Polymeric Surfactants: Synthesis, Properties, and Links to Applications. *Chemical Reviews*, 115, 2015.

[83] V Khrenov, F Schwager, M Klapper, M Koch, and K Müllen. The formation of hydrophobic inorganic nanoparticles in the presence of amphiphilic copolymers. *Colloid Polymer Science*, 284, 2006.

[84] V Khrenov, F Schwager, M Klapper, M Koch, and K Müllen. Compatibilization of inorganic particles for polymeric nanocomposites. Optimization of the size and the compatibility of ZnO particles. *Polymer Bulletin*, 58, 2007.

[85] Muriel K Corbierre, Neil S Cameron, Mark Sutton, Khalid Laaziri, and R Bruce Lennox. Gold Nanoparticle/Polymer Nanocomposites: Dispersion of Nanoparticles as a Function of Capping Agent Molecular Weight and Grafting Density. *Langmuir*, 21(13), 2005.

[86] Rigoberto C. Advincula, William J. Brittain, Kenneth C. Caster, and Jürgen Rühe. *Polymer Brushes*. Wiley-VCH, Weinheim, 2004.

[87] Tim Osswald. *Material science of polymers for engineers*. Hanser Publishers, Munich Germany, 2012.

[88] Shinji Ando, Tohru Matsuura, and Shigekuni Sasaki. Perfluorinated polymers for optical waveguides. *American Chemical Society*, 1994.

[89] Nicolas Cinausero, Nathalie Azema, José-Marie Lopez Cuesta, Marianne Cochez, and Michel Ferriol. Impact of modified alumina oxides on the fire properties of PMMA and PS nanocomposites. *Polymers for Advanced Technologies*, 22(12), 2011.

[90] ASTM International. ASTM D1746-15 Standard Test Method for Transparency of Plastic Sheeting. 2015.

[91] R.J. Tabar, C.T. Murray, and R.S. Stein. The Effect of Particle Size on the Haze of Polymer Films. *Journal of Polymer Science: Polymer Physics Edition*, 21, 1983.

[92] D R Bowman, T J Whitney, and M A Huelsman. *Procurement Specification Guidelines for Mass Transit Vehicle Window Glazing*. Report (Transit Cooperative Research Program). National Academy Press, 1996.

[93] ASTM International. ASTM D1003-13 Standard Test Method for Haze and Luminous Transmittance of Transparent Plastics. 2013.

[94] M. P. Anesh, Syed K H Gulrez, A. Anis, H. Shaikh, M. E Ali Mohsin, and S. M. Al-Zahrani. Developments in Eu+2-doped strontium aluminate and polymer/strontium aluminate composite. *Advances in Polymer Technology*, 30, 2014.

[95] Markus Schmid, Kerstin Dallmann, Elodie Bugnicourt, Dario Cordoni, Florian Wild, Andrea Lazzeri, and Klaus Noller. Properties of Whey-Protein-Coated Films and Laminates as Novel Recyclable Food Packaging Materials with Excellent Barrier Properties. *International Journal of Polymer Science*, 7, 2012.

[96] Jan David Endtz. Light propagation in thin film luminescent solar concentrators. *Unpublished*, 2017.

[97] A Liebig, J Donges, M Hietschold, G Beddies, and M Albrecht. Influence of the substrate thermal expansion coefficient on the morphology and elastic stress of CoSb3 thin films. 146(1), 2013.

[98] UL Standard. UL 746B Standard for Polymeric Materials - Long Term Property Evaluations. 2013.

[99] Hua Zou, Shishan Wu, and Jian Shen. Polymer/Silica Nanocomposites: Preparation, Characterization, Properties, and Applications. *Chemical Reviews*, 108(9), 2008.

[100] P. Nordell, S. Nawaz, B. Azhdar, H. Hillborg, and U. W. Gedde. Preparation and characterization of aluminum oxide-poly(ethylene-co-butyl acrylate) nanocomposites. *Journal of Applied Polymer Science*, 125(2), 2012.

[101] Zhi Zhou, Nan Zhou, Xiangyang Lu, Melvin ten Kate, David Valdesueiro, J. Ruud van Ommen, and H. T. (Bert) Hintzen. Performance improvement by alumina coatings on Y3Al5O12:Ce 3+ phosphor powder deposited using atomic layer deposition in a fluidized bed reactor. *RSC Advances*, 6(80), 2016.

[102] RenPing Cao, Xiaoguang Yu, Xinyuan Sun, Chunyan Cao, and JianRong Qiu. Near-infrared emission Ba3(PO4)2:Mn5+ phosphor and potential application in vivo fluorescence imaging. *Spectrochimica Acta Part A: Molecular and Biomolecular Spectroscopy*, 128, 2014.

[103] Angelo Monguzzi, Alberto Milani, Agniezka Mech, Luigi Brambilla, Riccardo Tubino, Carlo Castellano, Francesco Demartin, Francesco Meinardi, and Chiara Castiglioni. Predictive modeling of the vibrational quenching in emitting lanthanides complexes. *Synthetic Metals*, 161(23-24), 2012.

[104] Maria Luisa Saladino, Francesco Armetta, Motshabi A. Sibeko, Adriaan S. Luyt, Delia F. Chillura Martino, and Eugenio Caponetti. Preparation and characterisation of Ce:YAG -polycarbonate composites for white LED. *Journal of Alloys and Compounds*, 664, 2016.

[105] Do Ngoc Chung, Do Ngoc Hieu, Tran Thi Thao, Vo-Van Truong, and Nguyen Nang Dinh. Synthesis and Characterization of Ce-Doped Y 3 Al 5 O 12 (YAG:Ce) Nanopowders Used for Solid-State Lighting. *Journal of Nanomaterials*, 2014, 2014.

[106] Nathalie Pradal, Geneviève Chadeyron, Sandrine Thérias, Audrey Potdevin, Celso V Santilli, and Rachid Mahiou. Investigation on combustion derived BaMgAl10O17:Eu2+ phosphor powder and its corresponding PVP/BaMgAl10O17:Eu2+ nanocomposite. *Dalton transactions (Cambridge, England : 2003)*, 43(3), 2014.

[107] Mario Borlaf, Roman Kubrin, Vladimir Aseev, Alexander Yu Petrov, Nikolay Nikonorov, and Thomas Graule. Deep submicrometer YAG:Ce phosphor particles with high photoluminescent quantum yield prepared by flame spray synthesis. *Journal of the American Ceramic Society*, 100(8), 2017.

[108] Sigma-Aldrich. PEG Diblock Copolymers - Amphiphilic Block Copolymers, .

[109] George Wypych. *Handbook of Polymers 2nd Edtion*. ChemTec Publishing, Toronto, 2nd edition, 2016.

[110] Liesl K Massey. *Permeability Properties of Plastics and Elastomers A Guide to Packaging and Barrier Materials*. Plastics Design Library, Norwich, NY, 2003.

[111] Topas. *Thermoplastic Olefin Polymer of Amorphous Structure (COC)*. Polyplastics Co., Ltd., Tokyo, 2015.

[112] Thermo Fisher Scientific. Plastic Material Selection. https://www.thermofisher.com/nl/en/home/life-science/lab-plasticware-supplies/plastic-material-selection.html.

[113] Omnexus. Polymer Properties & Chemical Resistance of Plastics. https://omnexus.specialchem.com/polymer-properties.

[114] Matbase. Chemical, mechanical, physical and environmental properties of materials. https://www.matbase.com/.

[115] AGC Chemicals. CYTOP Technical Information. http://www.agcce.com/cytop-technical-information/.

[116] Yuri Yampolskii, Ingo Pinnau, and Benny Freeman. *Materials Science of Membranes for Gas and Vapor Separation.* John Wiley & Sons, Chichester, 2006.

[117] Junlong Song, Jing Liang, Xiaomeng Liu, Wendy E Krause, Juan P Hinestroza, and Orlando J Rojas. Development and characterization of thin polymer films relevant to fiber processing. *Thin Solid Films*, 517, 2009.

[118] Cheng-Fang Ou and Ming-Chieh Hsu. Preparation and characterization of cyclo olefin copolymer (COC)/silica nanoparticle composites by solution blending. *Journal of Polymer Research*, 14(5), 2007.

[119] Andrea Dorigato, Alessandro Pegoretti, Luca Fambri, Miroslav Slouf, and Jan Kolarik. Cycloolefin copolymer/fumed silica nanocomposites. *Journal of Applied Polymer Science*, 119(6), 2011.

[120] Sunanda Roy, Tanya Das, Chee Yoon Yue, and Xiao Hu. Transparent cyclic olefin copolymer/silica nanocomposites. *Polymer International*, 63(2), 2013.

[121] Poly(2-ethylhexyl methacrylate) solution average mw ~123,000 by gpc, in toluene | sigma-aldrich. https://www.sigmaaldrich.com/catalog/product/aldrich/182079?lang=en&region=NL, .

[122] Poly(methyl methacrylate) average mw ~120,000 by gpc | sigma-aldrich. https://www.sigmaaldrich.com/catalog/product/aldrich/182230?lang=en&region=NL, .

[123] Marie Pierre Krafft and Jean G. Riess. Chemistry, Physical Chemistry, and Uses of Molecular Fluorocarbon-Hydrocarbon Diblocks, Triblocks, and Related Compounds: Unique "Apolar" Components for Self-Assembled Colloid and Interface Engineering. *Chemical Reviews*, 109(5), 2009.

[124] Hongxiang Teng. Overview of the Development of the Fluoropolymer Industry. *Applied Sciences*, 2(2), 2012.

[125] Simon H. Stelzig, Christin Menneking, Michael S. Hoffmann, Klaus Eisele, Stephan Barcikowski, Markus Klapper, and Klaus Müllen. Compatibilization of laser generated antibacterial Ag- and Cu-nanoparticles for perfluorinated implant materials. *European Polymer Journal*, 47(4), 2011.

[126] G D Jonschker, M D Klapper, M D Koch, J D Pahnke, and S Stelzig. Surface-modified with copolymers particles, 2008.

[127] Simon H. Stelzig, Markus Klapper, and Klaus Müllen. A simple and efficient route to transparent nanocomposites. *Advanced Materials*, 20(5), 2008.

[128] Nathalie Pradal, Geneviève Chadeyron, Audrey Potdevin, Jérôme Deschamps, and Rachid Mahiou. Elaboration and optimization of Ce-doped Y 3 Al 5 O 12 nanopowder dispersions. *Journal of the European Ceramic Society*, 33, 2013.

[129] G. A. Kumar, C. W. Chen, R. Riman, S. Chen, D. Smith, and J. Ballato. Optical properties of a transparent CaF 2: Er 3+ fluoropolymer nanocomposite. *Applied Physics Letters*, 86(24), 2005.

[130] Mei Chee Tan, Swanand D Patil, and Richard E Riman. Transparent Infrared-Emitting CeF 3 :Yb-Er Polymer Nanocomposites for Optical Applications. *Applied Materials & Interfaces*, 2(7), 2010.

[131] Colleen E O'Neil, Scott Taylor, Kumuditha Ratnayake, Swathi Pullagurla, Varshni Singh, and Steven A Soper. Characterization of activated cyclic olefin copolymer: effects of ethylene/norbornene content on the physiochemical properties. *Analyst*, 141, 2016.

[132] Thomas Dienel, Christophe Bauer, Igor Dolamic, and Dominik Brühwiler. Spectral-based analysis of thin film luminescent solar concentrators. *Solar Energy*, 84(8), 2010.

[133] Francesco Meinardi, Samantha Ehrenberg, Lorena Dhamo, Francesco Carulli, Michele Mauri, Francesco Bruni, Roberto Simonutti, Uwe Kortshagen, and Sergio Brovelli. Highly efficient luminescent solar concentrators based on earth-abundant indirect-bandgap silicon quantum dots. 2017.

[134] Yufeng Zhou, Daniele Benetti, Zhiyuan Fan, Haiguang Zhao, Dongling Ma, Alexander O. Govorov, Alberto Vomiero, and Federico Rosei. Near Infrared, Highly Efficient Luminescent Solar Concentrators. *Advanced Energy Materials*, 6(11), 2016.

[135] Anees A. Ansari, Ranvijay Yadav, and S. B. Rai. Enhanced luminescence efficiency of aqueous dispersible NaYF4 :Yb/Er nanoparticles and the effect of surface coating. *RSC Adv.*, 6(26), 2016.

[136] Haiguang Zhao, Yufeng Zhou, Daniele Benetti, Dongling Ma, and Federico Rosei. Perovskite quantum dots integrated in large-area luminescent solar concentrators. *Nano Energy*, 37, 2017.

[137] Haiguang Zhao, Daniele Benetti, Lei Jin, Yufeng Zhou, Federico Rosei, and Alberto Vomiero. Absorption Enhancement in "Giant" Core/Alloyed-Shell Quantum Dots for Luminescent Solar Concentrator. *Small*, 12(38), 2016.

[138] Christian S Erickson, Liam R Bradshaw, Stephen Mcdowall, John D Gilbertson, Daniel R Gamelin, and David L Patrick. Zero-Reabsorption Doped-Nanocrystal Luminescent Solar Concentrators. *ACS Nano*, 8(4), 2014.

[139] Claudia G. Espinosa-González, Fernando J. Rodríguez-Macías, Abraham G. Cano-Márquez, Jasmeet Kaur, Meisha L. Shofner, and Yadira I. Vega-Cantú. Polystyrene composites with very high carbon nanotubes loadings by in situ grafting polymerization. *Journal of Materials Research*, 28(08), 2013.

[140] V M Gun 'ko, E F Voronin, E M Pakhlov, V I Zarko, V V Turov, N V Guzenko, R Leboda, and E Chibowski. Features of fumed silica coverage with silanes having three or two groups reacting with the surface. *Colloids and Surfaces A: Physicochemical and Engineering Aspects*, 166, 2000.

[141] Robert E Draper, David L Reid, Tamil S Sakthivel, Thomas Sammet, Andrew Demko, Eric L Petersen, and Sudipta Seal. Facile nanoparticle dispersion detection in energetic composites by rare earth doped in metal oxide nanostructures. *RSC Advances*, 5, 2015.

[142] Robert D. Breukers, Gerald J. Smith, Hedley L. Stirrat, Adam J. Swanson, Trevor A. Smith, Kenneth P. Ghiggino, Sebastiampillai G. Raymond, Nicola M. Winch, David J. Clarke, and Andrew J. Kay. Light losses from scattering in luminescent solar concentrator waveguides. *Applied Optics*, 56(10), 2017.

[143] 3M United States. 3M Sun Control Window Films, Prestige Series for Commercial. `https://www.3m.com/3M/en{_}US/company-us/all-3m-products/?N=5002385+8710654+3292716662{&}rt=rud`.

[144] Sigma-Aldrich. Poly(styrene)-block-poly(ethylene glycol). `https://www.sigmaaldrich.com/catalog/product/aldrich/686476?lang=en{&}region=NL,`.

[145] Johnny Widegren and Lennart Bergström. The effect of acids and bases on the dispersion and stabilization of ceramic particles in ethanol. *Journal of the European Ceramic Society*, 20(6), 2000.

[146] J. Michael Berg, Amelia Romoser, Nivedita Banerjee, Rema Zebda, and Christie M. Sayes. The relationship between pH and zeta potential of 30 nm metal oxide nanoparticle suspensions relevant to in vitro toxicological evaluations. *Nanotoxicology*, 3(4), 2009.

[147] Ramanathan Nagarajan. Non-equilibrium block copolymer micelles with glassy cores: A predictive approach based on theory of equilibrium micelles. *Journal of Colloid and Interface Science*, 449, 2015.

[148] Bedri Erdem, E. David Sudol, Victoria L. Dimonie, and Mohamed S. El-Aasser. Encapsulation of inorganic particles via miniemulsion polymerization. I. Dispersion of titanium dioxide particles in organic media using OLOA 370 as stabilizer. *Journal of Polymer Science, Part A: Polymer Chemistry*, 38(24), 2000.

[149] M Von Smoluchowski. Drei Vortrage uber Diffusion. Brownsche Bewegung und Koagulation von Kolloidteilchen. *Z. Phys.*, 17, 1916.

[150] David L Swift and S K Friedlandev. The coagulation of hydrosols by Brownian motion and laminar shear flow. Technical report, 1964.

[151] Richard Hogg. Bridging Flocculation by Polymers. *KONA Powder and Particle Journal*, 30, 2013.

[152] Toshiaki Miura and Kazuhiko Seki. Diffusion Influenced Adsorption Kinetics. *J. Phys. Chem. B*, 119, 2015.

[153] Nadezhda L. Filippova. Kinetic-Diffusion-Controlled Adsorption and Desorption Kinetics on Planar Surfaces. *Journal of Colloid and Interface Science*, 206(2), 1998.

[154] S. Lagergren. Zur theorie der sogenannten adsorption gelöster stoffe. *Kungliga Svenska Vetenskapsakademiens. Handlingar*, 24(4), 1898.

[155] Yuh-Shan Ho. Review of second-order models for adsorption systems. *Journal of Hazardous Materials*, 136(3), 2006.

[156] Karel Šolc and Karel Solct. Shape of a Random-Flight Chain. *Radii of Gyration for Random-Flight Chains The Journal of Chemical Physics*, 55, 1971.

[157] Iwao Teraoka. *Polymer Solutions: An Introduction to Physical Properties*. John Wiley & Sons, Inc., New York, USA, 2002.

[158] Wei-Fang Su. Polymer Size and Polymer Solutions. In *Principles of Polymer Design and Synthesis*. Springer, Berlin, Heidelberg, 2013.

[159] D.W. van Krevelen and K. te Nijenhuis. *Properties of polymers*, volume 16. 2009.

[160] Charles M. Hansen. *Hansen Solubility Parameters: A User's Handbook, Second Edition*. CRC Press, Boca Raton, FL, 2007.

[161] Thomas Lindvig, Michael L Michelsen, and Georgios M Kontogeorgis. A Flory-Huggins model based on the Hansen solubility parameters. Technical report, 2002.

[162] M. Doi and S.F. Edwards. *The Theory of Polymer Dynamics*. Clarendon Press, Oxford, 1986.

[163] P.J. Flory. *Principles of Polymer Chemistry*. Cornell University Press, Ithaca, NY, 1953.

[164] Hiromi Yamakawa. *Modern Theory of Polymer Solutions*. Harper & Row, New York, NY, 1971.

[165] Alexei R. Khokhlov and Pavel G. Khalatur. Protein-like copolymers: computer simulation. *Physica A: Statistical Mechanics and its Applications*, 249(1-4), 1998.

[166] Valentina V Vasilevskaya, Pavel G Khalatur, and Alexei R Khokhlov. Conformational Polymorphism of Amphiphilic Polymers in a Poor Solvent. *Macromolecules*, 36, 2003.

[167] Valentina V Vasilevskaya, Alexei A Klochkov, Alexei A Lazutin, Pavel G Khalatur, and Alexei R Khokhlov. HA (Hydrophobic/Amphiphilic) Copolymer Model: Coil-Globule Transition versus Aggregation. *Macromolecules*, 37, 2004.

[168] M D Carbajal-Tinoco, R Ober, I Dolbnya, W Bras, and C E Williams. Structural Changes and Chain Conformation of Hydrophobic Polyelectrolytes. *J. Phys. Chem. B*, 106, 2002.

[169] Pavel G. Khalatur, Alexei R. Khokhlov, Irina A. Nyrkova, and Alexander N. Semenov. Aggregation processes in self-associating polymer systems: A comparative analysis of theoretical and computer simulation data for micelles in the superstrong segregation regime. *Macromolecular Theory and Simulations*, 5(4), 1996.

[170] Xiaoliang Deng, Zhonghui Huang, Wenqiang Wang, and Rajesh N. Davé. Investigation of nanoparticle agglomerates properties using Monte Carlo simulations. *Advanced Powder Technology*, 27(5), 2016.

[171] Nelson Ibaseta and Béatrice Biscans. Fractal dimension of fumed silica: Comparison of light scattering and electron microscope methods. *Powder Technology*, 203(2), 2010.

[172] M. L. Eggersdorfer and S. E. Pratsinis. The structure of agglomerates consisting of polydisperse particles. *Aerosol Science and Technology*, 46(3), 2012.

[173] Vinod Kanniah, Peng Wu, Natalia Mandzy, and Eric A. Grulke. Fractal analysis as a complimentary technique for characterizing nanoparticle size distributions. *Powder Technology*, 226, 2012.

[174] Nitin Kumar, Alexander Couzis, and Charles Maldarelli. Measurement of the kinetic rate constants for the adsorption of superspreading trisiloxanes to an air/aqueous interface and the relevance of these measurements to the mechanism of superspreading. *Journal of Colloid and Interface Science*, 267, 2003.

[175] William W. Graessley. Polymer chain dimensions and the dependence of viscoelastic properties on concentration, molecular weight and solvent power. *Polymer*, 21(3), 1980.

[176] Keith M Carroll, Armin W Knoll, Heiko Wolf, and Urs Duerig. Explaining the Transition from Diffusion Limited to Reaction Limited Surface Assembly of Molecular Species through Spatial Variations. *Langmuir*, 34(1), 2018.

[177] Hendrik Nollet, Murielle Roels, Pierre Lutgen, Paul Van der Meeren, and Willy Verstraete. Removal of PCBs from wastewater using fly ash. *Chemosphere*, 53(6), 2003.

[178] C.M. Hansen and A. Beerbower. Solubility Parameters, 1971.

[179] L.-M. Ackermann, M Klapper, and A Kaiser. Isothermal Titration Calorimetry: A New Tool for the Development of Structure Activity Relationships for Sulphide Scale Control. In *SPE International Conference on Oilfield Chemistry*, 2017.

[180] Ravi Shankar, Rebecca R Klossner, Juan T Weaver, Tsuyoshi Koga, John H Van Zanten, Wendy E Krause, Coray M Colina, Fumihiko Tanaka, and Richard J Spontak. Competitive hydrogen-bonding in polymer solutions with mixed solvents. *Soft Matter*, 5, 2009.

[181] G.G. Cameron and D. Stewart. Spin-label studies of blends of immiscible polymers: 6. Phase morphology in blends of poly(methyl methacrylate) and poly(2-ethyl hexyl methacrylate). *Polymer*, 37(24), 1996.

[182] Juan Rodríguez-Hernández. Wrinkled interfaces: Taking advantage of surface instabilities to pattern polymer surfaces. *Progress in Polymer Science*, 42, 2015.

[183] A. R. Shugurov, A. I. Kozelskaya, and A. V. Panin. Wrinkling of the metal–polymer bilayer: the effect of periodical distribution of stresses and strains. *RSC Advances*, 4(15), 2014.

[184] Alexandra Schweikart, Anne Horn, Alexander Böker, and Andreas Fery. Controlled Wrinkling as a Novel Method for the Fabrication of Patterned Surfaces. In A. Müller and HW. Schmidt, editors, *Complex Macromolecular Systems I. Advances in Polymer Science, vol 227*. Springer, Berlin, Heidelberg, 2009.

[185] M Muthukumar. The Thermodynamics of Polymer Solutions. *J. Chem. Phys.*, 85, 1986.

[186] Peter Cifra and Tomáš Bleha. Variation of the chain dimensions with the concentration and quality of the monomer and polymer solvent. *Polymer*, 34(23), 1993.

[187] Siddarth Srinivasan, Shreerang S. Chhatre, Joseph M. Mabry, Robert E. Cohen, and Gareth H. McKinley. Solution spraying of poly(methyl methacrylate) blends to fabricate microtextured, superoleophobic surfaces. *Polymer*, 52(14), 2011.

[188] Pandharinath S Nikam, Bapu S Jagdale, Arun B Sawant, and Mehdi Hasan. Densities and Viscosities of Binary Mixtures of Toluene with Methanol, Ethanol, Propan-1-ol, Butan-1-ol, Pentan-1-ol, and 2-Methylpropan-2-ol at (303.15, 308.15, 313.15) K. *J. Chem. Eng. Data*, 45, 2000.

[189] Eric Farrell and Jean-Luc Brousseau. Guide for DLS sample preparation. Technical report, Brookhaven Instruments.

[190] C. Nora, S. Mabic, and D. Darbouret. A theoretical approach to measuring pH and conductivity in high-purity water. *Ultrapure Water*, 19(8), 2002.

[191] A. Kudyba-Jansen, M. Muurmans, M. Almeida, J. Laven, H.T. Hintzen, and R. Metselaar. Changes in β-sialon suspension behaviour due to surface oxidation, milling, surfactant and sintering additive. *Ceramics International*, 26(8), 2000.

[192] Paul T Sharpe. Methods of Cell Separation. In *Laboratory Techniques in Biochemistry and Molecular Biology, Volume 18*. Elsevier Science Publishers B.V., Amsterdam, 1988.

[193] Marion LeRoy Jackson. *Soil Chemical Analysis: Advanced Course*. Parallel Press, Madison, Wisconsin, second edition, 2005.

[194] José R Quintana, Maria D Jáñez, Manuel Villacampa, and Issa Katime. Diblock Copolymer Micelles in Solvent Binary Mixtures. 1. Selective Solvent/Precipitant. Technical report, 1995.

[195] Paschalis Alexandridis and Karin Andersson. Reverse Micelle Formation and Water Solubilization by Polyoxyalkylene Block Copolymers in Organic Solvent. *J. Phys. Chem. B*, 101(41), 1997.

[196] R Hogg. The role of polymer adsorption kinetics in flocculation. Technical report, 1999.

[197] Christian Geidel, Markus Klapper, and Klaus Müllen. In situ hydrophobized, shape-anisotropic nanoparticles for composite materials. *Colloid and Polymer Science*, 290(13), 2012.

[198] Kathy Schmidtke, Simon H. Stelzig, Christian Geidel, Markus Klapper, and Klaus Müllen. Complex Inorganic/Organic Core-Shell Particles by an Inverse Emulsion Technique. *Macromolecular Symposia*, 296(1), 2010.

[199] Polos. How to do a sol-gel coating using spin coating technique? `https://www.spincoating.com/en/featured-items/how-to-do-a-sol-gel-coating-using-spin-coating-technique/205/`.